

DERIVATION OF SITE-SPECIFIC UHS BASED ON SIMULATED GROUND
MOTIONS AND ITS PARAMETRIC EFFECTS ON BUILDING FRAGILITY

A THESIS SUBMITTED TO
THE GRADUATE SCHOOL OF NATURAL AND APPLIED SCIENCES
OF
MIDDLE EAST TECHNICAL UNIVERSITY



BY

AIDA AZARI SISI

IN PARTIAL FULFILLMENT OF THE REQUIREMENTS
FOR
THE DEGREE OF DOCTOR OF PHILOSOPHY
IN
CIVIL ENGINEERING

MAY 2016

Approval of the thesis:

**DERIVATION OF SITE-SPECIFIC UHS BASED ON SIMULATED
GROUND MOTIONS AND ITS PARAMETRIC EFFECTS ON BUILDING
FRAGILITY**

submitted by **AIDA AZARI SISI** in partial fulfilment of the requirements for the degree of **Doctor of Philosophy in Civil Engineering Department, Middle East Technical University** by,

Prof. Dr. Gülbin Dural Ünver
Dean, Graduate School of **Natural and Applied Sciences**

Prof. Dr. İsmail Özgür Yaman
Head of Department, **Civil Engineering**

Assoc. Prof. Dr. Ayşegül Askan Gündoğan
Supervisor, **Civil Engineering Dept., METU**

Prof. Dr. Murat Altuğ Erberik
Co-Supervisor, **Civil Engineering Dept., METU**

Examining Committee Members:

Prof. Dr. Ahmet Yakut
Civil Engineering Dept., METU

Assoc. Prof. Dr. Ayşegül Askan Gündoğan
Civil Engineering Dept., METU

Assoc. Prof. Dr. Mustafa Tolga Yılmaz
Engineering Science Dept., METU

Assoc. Prof. Dr. Berna Unutmaz
Civil Engineering Dept., HU

Assoc. Prof. Dr. Özgür Avcı
Civil Engineering Dept., AU

Date: 31/05/2016



I hereby declare that all information in this document has been obtained and presented in accordance with academic rules and ethical conduct. I also declare that, as required by these rules and conduct, I have fully cited and referenced all material and results that are not original to this work.

Name, Last Name: Aida AZARI SISI

Signature:

ABSTRACT

DERIVATION OF SITE-SPECIFIC UHS BASED ON SIMULATED GROUND MOTIONS AND ITS PARAMETRIC EFFECTS ON BUILDING FRAGILITY

Azari Sisi, Aida

PhD. Department of Civil Engineering

Supervisor: Assoc. Prof. Dr. Ayşegül Askan Gündoğan

Co-Supervisor: Prof. Dr. Murat Altuğ Erberik

May 2016, 254 pages

Estimation of seismic demands is essential for the purpose of structural seismic design and analyses. It is significant to obtain reliable ground motion amplitudes to estimate seismic damage on structures in a realistic manner. The ground motion simulation methodologies provide a physical approach to estimate seismic demands in the regions with sparse recording data and scarce networks.

This dissertation consists of two main parts: In the first part, site-specific uniform hazard spectrum (UHS) of Erzincan region in Eastern Turkey is derived based on a

stochastically-generated earthquake catalog and simulated ground motions. During the generation of the catalog, Monte Carlo simulation methodology is employed to determine spatial and temporal distribution of events. The magnitude of each event is obtained through Gutenberg-Richter recurrence relationship. Stochastic point-source and finite-fault simulation methodologies are used to calculate ground motion amplitudes. The effects of near-field forward directivity and alternative site amplification functions are studied on the proposed UHS.

In the second part, the effect of proposed seismic hazard is studied on structural response and fragility. The selected ground motions from the first part are applied for nonlinear time history analyses of equivalent single degree freedom systems (ESDOF). ESDOF systems are developed such that they represent typical low-rise and mid-rise residential buildings in Erzincan. Fragility curves of building groups are then calculated based on demand predictive models. The effects of site conditions, near-field forward directivity, alternative site amplification functions and structural variability are studied on fragility functions.

This study is an alternative approach to estimate seismic hazard for the regions with sparse data in which ground motion prediction equations (GMPE) may not be adequate. The proposed approach produces a regional UHS based on physical properties and complex seismicity parameters. The derived UHS mostly yield lower ground motion amplitudes than classical probabilistic seismic hazard analysis (PSHA) due to large aleatory variability inherent in PSHA. The effects of near-field forward directivity and detailed local site conditions are investigated on seismic hazard and building fragility in a practical manner. Additionally, this study provides a complete simulated ground motion database based on regional characteristics which are applied to perform sensitivity analyses of fragility functions to seismicity parameters.

Keywords: Uniform hazard spectrum, Ground motion simulation, Monte Carlo simulation, Single degree of freedom system analysis, Fragility curves

ÖZ

SENTETİK YER HAREKETLERİ İLE SAHAYA ÖZEL SABİT TEHLİKE SPEKTRUMU ÇIKARILMASI VE BİNA KIRILGANLIK EĞRİLERİ ÜZERİNDEKİ PARAMETRİK ETKİLERİ

Azari Sisi, Aida

Doktora., İnşaat Mühendisliği Bölümü

Tez Yöneticisi: Doç. Dr. Ayşegül Askan Gündoğan

Ortak Tez Yöneticisi: Prof. Dr. Murat Altuğ Erberik

Mayıs 2016, 254 sayfa

Sismik talep tahmini, yapısal sismik tasarım ve analiz için gereklidir. Gerçekçi bir şekilde yapıların sismik hasarını tahmin etmek için, güvenilir yer hareketi elde etmek önemlidir. Yer hareketi simülasyon metodolojileri seyrek veri kaydı ve kıt ağırları olan bölgelerde, sismik taleplerini tahmin etmek için fiziksel bir yaklaşım sağlamaktadır.

Bu tez, iki ana bölümden oluşmaktadır. İlk bölümde, stokastik olarak oluşturulan deprem katalogu ile sentetik yer hareketlerine dayanarak Erzincan bölgesi için sahaya-özel sabit tehlike spektrumu çıkarılmıştır. Monte Carlo simülasyon yöntemi depremlerin zamansal ve mekansal dağılımını tanımlamak için kullanılmıştır. Depremlerin magnitüd dağılımı ise Gutenberg-Richter magnitüd-tekerrür ilişkisi ile türetilmiştir. Yer hareketleri oluşturmak için, stokastik nokta kaynak ve sonlu fay simülasyon yöntemleri uygulanmıştır. Yakın saha ileri yırtılma-yönü ve zemin büyütme fonksiyonları etkileri, önerilen sabit tehlike spektrumu üzerinde incelenmiştir.

Tezin ikinci bölümünde ise, önerilen sismik tehlike değerlendirmesinin etkisi yapısal tepki ve kırılmalık üzerine çalışılmıştır. İlk bölümde seçilen yer hareketleri, tek serbestlik dereceli sistemlerin zaman tanım alanında nonlineer analizi için uygulanmıştır. Tek serbestlik dereceli sistemleri Erzincan'da tipik az ve orta katlı binaları temsil edecek şekilde geliştirilmiştir. Yapı gruplarının kırılmalık eğrileri talep tahmini modellere dayanarak hesaplanmıştır. Kırılmalık eğrileri üzerinde saha koşulları, yakın saha ileri yırtılma-yönü etkisi, detaylı yerel zemin koşulları ve yapısal değişkenlik etkileri araştırılmıştır.

Önerilen yöntem, az veriye sahip olup yer hareketi tahmin denklemlerinin yeterli olmadığı bölgeler için alternatif bir yaklaşımdır. Önerilen yöntem, fiziksel özellikler ve karmaşık sismik parametrelere göre bölgesel sabit tehlike spektrumu üretir. Türetilmiş sabit tehlike spektrumu çoğunlukla klasik olasılıksal sismik tehlike analizinin doğasında olan büyük belirsizlikten dolayı, klasik olasılıksal sismik tehlike analizinden daha küçük yer hareketi değerleri vermektedir. Yakın saha ileri yırtılma-yönü ve ayrıntılı yerel zemin koşullarının etkileri pratik bir şekilde sismik tehlike ve bina kırılmalık üzerinde incelenir. Ayrıca, bu çalışma kırılmalık eğrilerini incelemek için bölgesel özelliklere dayalı tam bir sentetik yer hareketi veritabanı sağlar.

Anahtar kelimeler: Sabit tehlike spektrum, Yer hareketi simülasyonu, Monte Carlo simülasyonu, Tek serbestlik dereceli sistemler analizi, Kırılmalık eğrileri



To the loving memory of my mother

ACKNOWLEDGEMENTS

I owe my deepest gratitude to my supervisor, Assoc. Prof. Dr. Ayşegül Askan Gündoğan, for her guidance, patience and immense knowledge. She gave me encouragement and motivation whenever I needed. It was a great chance to work with her.

I would like to appreciate Prof. Dr. Murat Altuğ Erberik whose valuable guidance, advice and motivation assisted me a great deal during this research.

I am grateful to Prof. Dr. Ahmet Yakut and Assoc. Prof. Dr. Mustafa Tolga Yılmaz for their insightful comment during this dissertation.

I would express my deepest appreciation to my late mother. I am sorry that she cannot see me graduate but her memory is always with me. I would thank my father, my sister and my aunt for their endless love and support. I also thank my little niece, Tara, who made me happy during the difficult times.

My deepest thanks and love belong to my dear husband, Dr. Ayma Hasanpour because of his love, understanding and patience in the most difficult times during this study.

I also owe thanks to Dr. Shaghayaegh Karimzadeh Naghshineh, Fatma Nurten Şişman Dersen, Gizem Can, Barış Ünal and Mustafa Bilal for their endless support and assistance.

I want to thank Saeaideh Nazirzadeh, Vesile Akansel, Başak Varlı Bingöl, Golnesa Karimi, Dr. Abdullah Dilsiz and Dr. Abdullah Sandıkkaya for their friendship and encouragement during this dissertation.

Finally, I express my thanks to Scientific and Technological Research Council of Turkey (TUBITAK) for its financial support throughout this study.

TABLE OF CONTENTS

ABSTRACT	v
ÖZ	vii
ACKNOWLEDGEMENTS	x
TABLE OF CONTENTS	xi
LIST OF FIGURES	xiv
LIST OF TABLES	xxvi
CHAPTERS	
1 INTRODUCTION	1
1.1 General	1
1.2 Literature Review	2
1.3 Objective and Scope	7
2 GROUND MOTION SIMULATION METHODOLOGY	11
2.1 Introduction	11
2.2 Stochastic Point-Source Model	11
2.2.1 Simulation of Acceleration Time History	14
2.2.2 Random Vibration Theory	15
2.2.3 The Source Function	16
2.2.4 The Path Function	18
2.2.5 The Site Function	20
2.3 Stochastic Finite-Fault Model	22
2.4 Calibration of Stress Drop for Point Sources	27
3 CONSTRUCTION OF SITE-SPECIFIC UNIFORM HAZARD SPECTRUM AND GROUND MOTION SELECTION	29
3.1 Introduction	29

3.2 Derivation of Uniform Hazard Spectrum Based on Simulated Ground Motions	30
3.2.1 Study Area.....	30
3.2.2 Methodology	33
3.2.3 Initial Results of the Proposed Methodology and Comparisons with Results from Classical PSHA.....	38
3.3 Sensitivity of the Proposed UHS.....	48
3.3.1 Sensitivity of the Proposed UHS to Near-Field Forward Directivity	48
3.3.2 Sensitivity of the Proposed UHS to Site Amplification Functions	57
3.4 Ground Motion Selection According to the Proposed UHS	67
3.4.1 Methodology	67
3.4.2 Selected Ground Motions.....	69
3.5 Main Findings of Chapter 3	75
4 PREDICTION OF SEISMIC DEMAND BASED ON EQUIVALENT SINGLE DEGREE OF FREEDOM ANALYSES	79
4.1 Introduction	79
4.2 Methodology	80
4.3 ESDOF Response Statistics without Structural Variability	85
4.3.1 Demand Predictive Equations	85
4.3.2 Residual Analyses on Predictive Models with respect to magnitude and distance.....	92
4.4 The Impact of Effective Duration on Displacement Demands	100
4.4.1 Residual Analyses on Demand Predictive Models with Respect to Effective Duration	100
4.4.2 The Impact of Effective Duration on Displacement Demands within PGA Bins.....	101
4.4.3 The impact of Effective Duration on Displacement Demands Resulted from Some Ground Motions with Similar PGAs	106
4.5 The Effect of Seismic Parameters (Other than Effective Duration) on Displacement Demands Resulted from Some Ground Motions with Similar PGAs	110
4.6 ESDOF Response Statistics with Structural Variability	114
4.6.1 Latin Hypercube Sampling Methodology	114
4.6.2 Demand Predictive Equations	115
4.7 Main Findings of Chapter 4	124
5 SENSITIVITY ANALYSIS OF FRAGILITY FUNCTIONS	127
5.1 Introduction	127
5.2 Methodology	127

5.3 The Effect of Site Condition on Fragility Curves	130
5.4 The Effect of Near-Field Forward Directivity on Fragility Curves	134
5.5 The Effect of Site Amplification Functions on Fragility Curves	136
5.6 The Effect of Structural Variability on Fragility Curves	139
5.7 Continuous Fragility Functions	145
5.8 Sensitivity of Estimated Damage to Seismological and Structural Parameters	152
5.8.1 The Effect of Site Amplification and Forward Directivity Pulse on Estimated Damage due to 13 March 1992 Erzincan Earthquake.....	154
5.8.2 The Effect of Site Condition on Estimated Damage due to Ground Motion Scenario with a Specified PGA.....	157
5.9 Main Findings of Chapter 5	158
6 CONCLUSIONS, CONTRIBUTIONS AND FUTURE WORK.....	161
6.1 Summary	161
6.2 Conclusions	163
6.3 Contributions to the Literature	166
6.4 Limitations and Future Work	168
REFERENCES.....	171
APPENDICES	
A. SELECTED GROUND MOTIONS	191
B. RESIDUAL PLOTS OF DEMAND PREDICTION EQUATIONS.....	203
C. VARIATIONS OF DEMAND WITH RESPECT TO EFFECTIVE DURATION	211
CURRICULUM VITAE	249

LIST OF FIGURES

Figures

Figure 1.1. Flowchart for step-by-step procedures in this dissertation	9
Figure 2.1. Schematic representation of source, path and site factors in surface ground motion amplitudes.....	13
Figure 2.2. Flowchart for stochastic time series simulation (Boore, 2003)	14
Figure 2.3. Single corner frequency ω -squared source spectrum proposed by Aki (1967)	17
Figure 2.4. General shape of Q function in log-log space proposed by Aki (1980) ..	19
Figure 2.5. Combination of generic site amplification and different diminution factors (from Boore and Joyner, 1997)	21
Figure 2.6. Rupture propagation on a finite-fault source model and subfaults (Adopted from Hisada, 2008).....	23
Figure 2.7. Dependency of radiated seismic energy on subfault size in finite-fault model (Adopted from Motazedian and Atkinson, 2005)	24
Figure 2.8. Independency of radiated seismic energy of subfault size in finite-fault model based on dynamic corner frequency (Adopted from Motazedian and Atkinson, 2005)	26
Figure 2.9. Misfit ($E(f)$) related to a) PSa b) FAS, and sensitivity index (SI) related to c) PSa d) FAS for point source simulations with different stress drop values with respect to finite-fault model	28
Figure 3.1. Regional map showing the epicenters, rupture zones and the mechanisms of the 1939 and 1992 earthquakes (epicenters are indicated with stars) and strong	

ground motion stations that recorded 1992 Erzincan earthquake are indicated with triangles (Adopted from Askan et al., 2013). The sites, which are used in this study, are indicated with solid circles with site numbers beside them. 30

Figure 3.2. Locations of seismic zones which are defined in Table 3.2. The three sites (S1, S2 and S3) in this study are shown with solid circles. 33

Figure 3.3. Distribution of events in 3000-year stochastic earthquake catalog related to Site 1 35

Figure 3.4. Hazard curves for a) PGA b) PSA (T=0.1 s) c) PSA (T=0.2 s) d) PSA (T=0.5 s) e) PSA (T=0.7 s) f) PSA (T=1.0 s) g) PSA (T=1.5 s) h) PSA (T=2.0 s) and i) UHS of proposed study and classical PSHA for Site 1 39

Figure 3.5. Hazard curves for a) PGA b) PSA (T=0.1 s) c) PSA (T=0.2 s) d) PSA (T=0.5 s) e) PSA (T=0.7 s) f) PSA (T=1.0 s) g) PSA (T=1.5 s) h) PSA (T=2.0 s) and i) UHS of proposed study and classical PSHA for Site 2 40

Figure 3.6. Hazard curves for a) PGA b) PSA (T=0.1 s) c) PSA (T=0.2 s) d) PSA (T=0.5 s) e) PSA (T=0.7 s) f) PSA (T=1.0 s) g) PSA (T=1.5 s) h) PSA (T=2.0 s) and i) UHS of proposed study and classical PSHA for Site 3 41

Figure 3.7. Number of standard deviation of simulated GMIPs from the corresponding median values (Akkar and Bommer, 2010) versus simulated GMIPs for a) PGA b) PSA (T=0.1 s) c) PSA (T=0.2 s) d) PSA (T=0.5 s) e) PSA (T=0.7 s) f) PSA (T=1.0 s) g) PSA (T=1.5 s) and h) PSA (T=2.0 s) for Site 1..... 44

Figure 3.8. Number of standard deviation of simulated GMIPs from the corresponding median values (Akkar and Bommer, 2010) versus simulated GMIPs for a) PGA b) PSA (T=0.1 s) c) PSA (T=0.2 s) d) PSA (T=0.5 s) e) PSA (T=0.7 s) f) PSA (T=1.0 s) g) PSA (T=1.5 s) and h) PSA (T=2.0 s) for Site 2..... 45

Figure 3.9. Number of standard deviation of simulated GMIPs from the corresponding median values (Akkar and Bommer, 2010) versus simulated GMIPs for a) PGA b) PSA (T=0.1 s) c) PSA (T=0.2 s) d) PSA (T=0.5 s) e) PSA (T=0.7 s) f) PSA (T=1.0 s) g) PSA (T=1.5 s) and h) PSA (T=2.0 s) for Site 3..... 46

Figure 3.10. Calibration of parameters in Table 3.4 with respect to 13 March 1992 earthquake (ERC recording) in terms of a) PSv, b) Velocity time series and c) Displacement time series.....	50
Figure 3.11. Observed and simulated ground motions of 13 March 1992 earthquake (ERC recording) with and without considering forward directivity in terms of a) FAS and b) PSa considering parameters of Table 3.4.....	51
Figure 3.12. Hazard curves for a) PGA b) PSA (T=0.1 s) c) PSA (T=0.2 s) d) PSA (T=0.5 s) e) PSA (T=0.7 s) f) PSA (T=1.0 s) g) PSA (T=1.5 s) h) PSA (T=2.0 s) and i) UHS of proposed study with and without near-field forward directivity for Site 254	
Figure 3.13. Contribution of long duration ground motions in a) 2% in 50 years and b) 10% in 50 years hazard levels for Site 2 with and without considering forward directivity	56
Figure 3.14. 1D soil deposit layers on elastic half-space	58
Figure 3.15. 1D Shear wave velocity profile of a) Site 1 and b) Site 3 (Adopted from Askan et al., 2015).....	59
Figure 3.16. Theoretical and generic attenuated site amplification factor as a function of frequency for a) Site 1 and b) Site 3	60
Figure 3.17. Hazard curves for a) PGA b) PSA (T=0.1 s) c) PSA (T=0.2 s) d) PSA (T=0.5 s) e) PSA (T=0.7 s) f) PSA (T=1.0 s) g) PSA (T=1.5 s) h) PSA (T=2.0 s) and i) UHS of the proposed study without soil nonlinearity for Site 1.....	62
Figure 3.18. Hazard curves for a) PGA b) PSA (T=0.1 s) c) PSA (T=0.2 s) d) PSA (T=0.5 s) e) PSA (T=0.7 s) f) PSA (T=1.0 s) g) PSA (T=1.5 s) h) PSA (T=2.0 s) and i) UHS of the proposed study with soil nonlinearity for Site 1	63
Figure 3.19. Hazard curves for a) PGA b) PSA (T=0.1 s) c) PSA (T=0.2 s) d) PSA (T=0.5 s) e) PSA (T=0.7 s) f) PSA (T=1.0 s) g) PSA (T=1.5 s) h) PSA (T=2.0 s) and i) UHS of the proposed study without soil nonlinearity for Site 3.....	64
Figure 3.20. Hazard curves for a) PGA b) PSA (T=0.1 s) c) PSA (T=0.2 s) d) PSA (T=0.5 s) e) PSA (T=0.7 s) f) PSA (T=1.0 s) g) PSA (T=1.5 s) h) PSA (T=2.0 s) and i) UHS of the proposed study with soil nonlinearity for Site 3.....	65

Figure 3.21. Selected recordings, median of selected recordings and UHS related to Site 1 with generic site amplification for return periods of a) 2475 years b) 475 years c) 225 years and d) 75 years.....	70
Figure 3.22. Selected recordings, median of selected recordings and UHS related to Site 1 with theoretical site amplification for return periods of a) 2475 years b) 475 years c) 225 years and d) 75 years	71
Figure 3.23. Selected recordings, median of selected recordings and UHS related to Site 2 without near-field effect for return periods of a) 2475 years b) 475 years c) 225 years and d) 75 years.....	71
Figure 3.24. Selected recordings, median of selected recordings and UHS related to Site 2 with near-field effect for return periods of a) 2475 years b) 475 years c) 225 years and d) 75 years.....	72
Figure 3.25. Selected recordings, median of selected recordings and UHS related to Site 3 with generic site amplification for return periods of a) 2475 years b) 475 years c) 225 years and d) 75 years.....	72
Figure 3.26. Selected recordings, median of selected recordings and UHS related to Site 3 with theoretical site amplification for return periods of a) 2475 years b) 475 years c) 225 years and d) 75 years	73
Figure 4.1. The backbone curve of peak-oriented hysteretic model (Ibarra et al., 2005)	81
Figure 4.2. Schematic illustration of bilinear demand formulation (Adapted from Bai et al., 2011).....	85
Figure 4.3. Variation of maximum displacement demand with respect to PGA and the predictive regression models for Site 1 using generic site amplification.....	86
Figure 4.4. Variation of maximum displacement demand with respect to PGA and the predictive regression models for Site 1 using theoretical site amplification.....	87
Figure 4.5. Variation of maximum displacement demand with respect to PGA and the predictive regression models for Site 2 without near-field forward directivity effect.....	88

Figure 4.6. Variation of maximum displacement demand with respect to PGA and the predictive regression models for Site 2 with near-field forward directivity effect	89
Figure 4.7. Variation of maximum displacement demand with respect to PGA and the predictive regression models for Site 3 using generic site amplification.....	90
Figure 4.8. Variation of maximum displacement demand with respect to PGA and the predictive regression models for Site 3 using theoretical site amplification.....	91
Figure 4.9. Residual plots and the corresponding trend lines related to predictive models of Figure 4.3 (Site 1 using generic site amplification)	93
Figure 4.10. Residual plots and the corresponding trend lines related to predictive models of Figure 4.4 (Site 1 using theoretical site amplification)	94
Figure 4.11. Residual plots and the corresponding trend lines related to predictive models of Figure 4.5 (Site 2 without near-field forward directivity).....	95
Figure 4.12. Residual plots and the corresponding trend lines related to predictive models of Figure 4.6 (Site 2 with near-field forward directivity).....	96
Figure 4.13. Residual plots and the corresponding trend lines related to predictive models of Figure 4.7 (Site 3 using generic site amplification)	97
Figure 4.14. Residual plots and the corresponding trend lines related to predictive models of Figure 4.8 (Site 3 using theoretical site amplification)	98
Figure 4.15. Maximum displacement demand versus effective duration scatters for six PGA bins regarding Site 1 using generic site amplification and MU3C. PGA_m and std. dev stand for mean and standard deviation of PGAs inside each bin, respectively.....	102
Figure 4.16. Ground motions with similar PGAs and considerably different demands which are shown inside elliptic (Site 1 using generic site amplification adapted from Figure 4.3)	107
Figure 4.17. Ground acceleration and displacement demand related to Table 4.11	108
Figure 4.18. Ground acceleration and displacement demand related to Table 4.12	109

Figure 4.19. Ground acceleration and displacement demand related to Table 4.13	109
Figure 4.20. Pseudo-acceleration spectrum and ground velocity related to Table 4.14 (dashed grey line shows the fundamental period of RF2C).....	112
Figure 4.21. Pseudo-acceleration spectrum and ground velocity related to Table 4.15 (dashed grey line shows the fundamental period of MU2B)	112
Figure 4.22. Pseudo-acceleration spectrum and ground velocity related to Table 4.16 (dashed grey line shows the fundamental period of MU3C)	113
Figure 4.23. Variation of maximum displacement demand with respect to PGA and the predictive regression models for Site 1 using generic site amplification.....	116
Figure 4.24. Variation of maximum displacement demand with respect to PGA and the predictive regression models for Site 1 using theoretical site amplification.....	117
Figure 4.25. Variation of maximum displacement demand with respect to PGA and the predictive regression models for Site 2 without near-field forward directivity .	118
Figure 4.26. Variation of maximum displacement demand with respect to PGA and the predictive regression models for Site 2 with near-field forward directivity	119
Figure 4.27. Variation of maximum displacement demand with respect to PGA and the predictive regression models for Site 3 using generic site amplification.....	120
Figure 4.28. Variation of maximum displacement demand with respect to PGA and the predictive regression models for Site 3 using theoretical site amplification.....	121
Figure 5.1. Fragility curves related to Site 2 (solid line) and Site 1 (dashed line)...	131
Figure 5.2. Fragility curves related to Site 3 (solid line) and Site 1 (dashed line)...	133
Figure 5.3. Fragility curves related to Site 2 with (dashed line) and without (solid line) near-field forward directivity	134
Figure 5.4. Displacement demand histories of ESDOFs using 13 March 1992 Erzincan, ERC recording with and without near-field forward directivity.....	136
Figure 5.5. Fragility curves related to Site 1 using generic (solid line) and theoretical (dashed line) site amplification function.....	137

Figure 5.6. Fragility curves related to Site 3 using generic (solid line) and theoretical (dashed line) site amplification function	138
Figure 5.7. Fragility curves related to Site 1 using generic site amplification without (solid line) and with (dashed line) structural variability	139
Figure 5.8. Fragility curves related to Site 1 using theoretical site amplification without (solid line) and with (dashed line) structural variability	140
Figure 5.9. Fragility curves related to Site 2 without near-field forward directivity without (solid line) and with (dashed line) structural variability	141
Figure 5.10. Fragility curves related to Site 2 with near-field forward directivity without (solid line) and with (dashed line) structural variability	142
Figure 5.11. Fragility curves related to Site 3 using generic site amplification without (solid line) and with (dashed line) structural variability	143
Figure 5.12. Fragility curves related to Site 3 using theoretical site amplification without (solid line) and with (dashed line) structural variability	144
Figure 5.13. Continuous fitted fragility curves (dashed line) and discontinuous original fragility curves (solid line) for Site 1 using generic site amplification (without structural variability)	146
Figure 5.14. Continuous fitted fragility curves (dashed line) and discontinuous original fragility curves (solid line) for Site 1 using theoretical site amplification (without structural variability)	146
Figure 5.15. Continuous fitted fragility curves (dashed line) and discontinuous original fragility curves (solid line) for Site 2 without near-field forward directivity (without structural variability)	147
Figure 5.16. Continuous fitted fragility curves (dashed line) and discontinuous original fragility curves (solid line) for Site 2 with near-field forward directivity (without structural variability)	147

Figure 5.17. Continuous fitted fragility curves (dashed line) and discontinuous original fragility curves (solid line) for Site 3 using generic site amplification (without structural variability)	148
Figure 5.18. Continuous fitted fragility curves (dashed line) and discontinuous original fragility curves (solid line) for Site 3 using theoretical site amplification (without structural variability)	148
Figure 5.19. Continuous fitted fragility curves (dashed line) and discontinuous original fragility curves (solid line) for Site 1 using generic site amplification (with structural variability).....	149
Figure 5.20. Continuous fitted fragility curves (dashed line) and discontinuous original fragility curves (solid line) for Site 1 using theoretical site amplification (with structural variability)	150
Figure 5.21. Continuous fitted fragility curves (dashed line) and discontinuous original fragility curves (solid line) for Site 2 without near-field forward directivity (with structural variability)	150
Figure 5.22. Continuous fitted fragility curves (dashed line) and discontinuous original fragility curves (solid line) for Site 2 with near-field forward directivity (with structural variability)	151
Figure 5.23. Continuous fitted fragility curves (dashed line) and discontinuous original fragility curves (solid line) for Site 3 using generic site amplification (with structural variability).....	151
Figure 5.24. Continuous fitted fragility curves (dashed line) and discontinuous original fragility curves (solid line) for Site 3 using theoretical site amplification (with structural variability)	152
Figure 5.25. Damage state definitions on fragility functions in this study.	153
Figure 5.26. MDR variation of three cases related to Site 1 from the reference case which is Site 1 using generic site amplification and without structural variability (S1/G/wo-sv).....	155

Figure 5.27. MDR variation of three cases related to Site 2 from the reference case, which is Site 2 without forward directivity pulse and without structural variability (S2/wop/wo-sv)	155
Figure 5.28. MDR variation of three cases related to Site 3 from the reference case, which is Site 3 using generic site amplification and without structural variability (S3/G/wo-sv)	156
Figure 5.29. MDR error of Site 2 and 3 from Site 1 for PGA=0.4 g	157
Figure B.1. Residual plots related to predictive models of Figure 4.3 with respect to magnitude, distance (km) and duration (s) (Site 1 generic site amplification).	204
Figure B.2. Residual plots related to predictive models of Figure 4.4 with respect to magnitude, distance (km) and duration (s) (Site 1 theoretical site amplification). ..	205
Figure B.3. Residual plots related to predictive models of Figure 4.5 with respect to magnitude, distance (km) and duration (s) (Site 2 without near-field forward directivity).	206
Figure B.4. Residual plots related to predictive models of Figure 4.6 with respect to magnitude, distance (km) and duration (s) (Site 2 with near-field forward directivity).	207
Figure B.5. Residual plots related to predictive models of Figure 4.7 with respect to magnitude, distance (km) and duration (s) (Site 3 using generic site amplification).	208
Figure B.6. Residual plots related to predictive models of Figure 4.8 with respect to magnitude, distance (km) and duration (s) (Site 3 using theoretical site amplification).	209
Figure C.1. Maximum displacement demand versus effective duration scatters for six PGA bins regarding Site 1 using generic site amplification and RF1A.....	212
Figure C.2. Maximum displacement demand versus effective duration scatters for six PGA bins regarding Site 1 using generic site amplification and RF2B	213

Figure C.3. Maximum displacement demand versus effective duration scatters for six PGA bins regarding Site 1 using generic site amplification and RF2C.....	214
Figure C.4. Maximum displacement demand versus effective duration scatters for six PGA bins regarding Site 1 using generic site amplification and MU1A.....	215
Figure C.5. Maximum displacement demand versus effective duration scatters for six PGA bins regarding Site 1 using generic site amplification and MU2B	216
Figure C.6. Maximum displacement demand versus effective duration scatters for six PGA bins regarding Site 1 using generic site amplification and MU3C	217
Figure C.7. Maximum displacement demand versus effective duration scatters for six PGA bins regarding Site 1 using theoretical site amplification and RF1A	218
Figure C.8. Maximum displacement demand versus effective duration scatters for six PGA bins regarding Site 1 using theoretical site amplification and RF2B.....	219
Figure C.9. Maximum displacement demand versus effective duration scatters for six PGA bins regarding Site 1 using theoretical site amplification and RF2C.....	220
Figure C.10. Maximum displacement demand versus effective duration scatters for six PGA bins regarding Site 1 using theoretical site amplification and MU1A	221
Figure C.11. Maximum displacement demand versus effective duration scatters for six PGA bins regarding Site 1 using theoretical site amplification and MU2B.....	222
Figure C.12. Maximum displacement demand versus effective duration scatters for six PGA bins regarding Site 1 using theoretical site amplification and MU3C.....	223
Figure C.13. Maximum displacement demand versus effective duration scatters for eight PGA bins regarding Site 2 without near-field forward directivity pulse and RF1A.....	224
Figure C.14. Maximum displacement demand versus effective duration scatters for eight PGA bins regarding Site 2 without near-field forward directivity pulse and RF2B	225

Figure C.15. Maximum displacement demand versus effective duration scatters for eight PGA bins regarding Site 2 without near-field forward directivity pulse and RF2C	226
Figure C.16. Maximum displacement demand versus effective duration scatters for eight PGA bins regarding Site 2 without near-field forward directivity pulse and MU1A.....	227
Figure C.17. Maximum displacement demand versus effective duration scatters for eight PGA bins regarding Site 2 without near-field forward directivity pulse and MU2B.....	228
Figure C.18. Maximum displacement demand versus effective duration scatters for eight PGA bins regarding Site 2 without near-field forward directivity pulse and MU3C.....	229
Figure C.19. Maximum displacement demand versus effective duration scatters for eight PGA bins regarding Site 2 with near-field forward directivity pulse and RF1A	230
Figure C.20. Maximum displacement demand versus effective duration scatters for eight PGA bins regarding Site 2 with near-field forward directivity pulse and RF2B	231
Figure C.21. Maximum displacement demand versus effective duration scatters for eight PGA bins regarding Site 2 with near-field forward directivity pulse and RF2C	232
Figure C.22. Maximum displacement demand versus effective duration scatters for eight PGA bins regarding Site 2 with near-field forward directivity pulse and MU1A	233
Figure C.23. Maximum displacement demand versus effective duration scatters for eight PGA bins regarding Site 2 with near-field forward directivity pulse and MU2B	234

Figure C.24. Maximum displacement demand versus effective duration scatters for eight PGA bins regarding Site 2 with near-field forward directivity pulse and MU3C	235
Figure C.25. Maximum displacement demand versus effective duration scatters for eight PGA bins regarding Site 3 using generic site amplification and RF1A.....	236
Figure C.26. Maximum displacement demand versus effective duration scatters for eight PGA bins regarding Site 3 using generic site amplification and RF2B	237
Figure C.27. Maximum displacement demand versus effective duration scatters for eight PGA bins regarding Site 3 using generic site amplification and RF2C.....	238
Figure C.28. Maximum displacement demand versus effective duration scatters for eight PGA bins regarding Site 3 using generic site amplification and MU1A	239
Figure C.29. Maximum displacement demand versus effective duration scatters for eight PGA bins regarding Site 3 using generic site amplification and MU2B	240
Figure C.30. Maximum displacement demand versus effective duration scatters for eight PGA bins regarding Site 3 using generic site amplification and MU3C	241
Figure C.31. Maximum displacement demand versus effective duration scatters for eight PGA bins regarding Site 3 using theoretical site amplification and RF1A.....	242
Figure C.32. Maximum displacement demand versus effective duration scatters for eight PGA bins regarding Site 3 using theoretical site amplification and RF2B.....	243
Figure C.33. Maximum displacement demand versus effective duration scatters for eight PGA bins regarding Site 3 using theoretical site amplification and RF2C.....	244
Figure C.34. Maximum displacement demand versus effective duration scatters for eight PGA bins regarding Site 3 using theoretical site amplification and MU1A...	245
Figure C.35. Maximum displacement demand versus effective duration scatters for eight PGA bins regarding Site 3 using theoretical site amplification and MU2B ...	246
Figure C.36. Maximum displacement demand versus effective duration scatters for eight PGA bins regarding Site 3 using theoretical site amplification and MU3C ...	247

LIST OF TABLES

TABLES

Table 3.1. Location and site classes of the selected sites	31
Table 3.2. Seismic parameters of the seismic zones used in this study (Adopted from Deniz, 2006)	32
Table 3.3. Seismic parameters which are used in this study as inputs (Adopted from Askan et al., 2013).....	36
Table 3.4. Input parameters for Mavroeidis and Papageorgiou (2003) analytical pulse model.....	49
Table 3.5. RMSE values for three sites with different modeling methodologies and hazard levels.....	74
Table 4.1. Hysteretic model parameters of the considered ESDOF models	83
Table 4.2. R^2 percentages of the residuals against moment magnitude	99
Table 4.3. R^2 percentages of the residuals against the closest distance to rupture.....	99
Table 4.4. R^2 percentages of the residuals against effective duration.....	101
Table 4.5. R^2 percentages and correlation type of demand vs. effective duration trend lines for Site 1 using generic site amplification	103
Table 4.6. R^2 percentages and correlation type of demand vs. effective duration trend lines for Site 1 using theoretical site amplification	103
Table 4.7. R^2 percentages and correlation type of demand vs. effective duration trend lines for Site 2 without near-field forward directivity.....	104

Table 4.8. R ² percentages and correlation type of demand vs. effective duration trend lines for Site 2 with near-field forward directivity.....	104
Table 4.9. R ² percentages and correlation type of demand vs. effective duration trend lines for Site 3 using generic site amplification.....	105
Table 4.10. R ² percentages and correlation type of demand vs. effective duration trend lines for Site 3 using theoretical site amplification.....	105
Table 4.11. Two ground motions as examples which are shown inside elliptic in Figure 4.16 regarding building sub-class RF2C	107
Table 4.12. Two ground motions as examples which are shown inside elliptic in Figure 4.16 regarding building sub-class MU2B.....	108
Table 4.13. Two ground motions as examples which are shown inside elliptic in Figure 4.16 regarding building sub-class MU3C.....	108
Table 4.14. Two ground motions as examples which are shown inside elliptic in Figure 4.16 regarding building sub-class RF2C	111
Table 4.15. Two ground motions as examples which are shown inside elliptic in Figure 4.16 regarding building sub-class MU2B.....	111
Table 4.16. Two ground motions as examples which are shown inside elliptic in Figure 4.16 regarding building sub-class MU3C.....	112
Table 4.17. Logarithmic uncertainty ($\beta_{D/IM}$) regarding regression models, without structural variability (Section 4.3).....	123
Table 4.18. Logarithmic uncertainty ($\beta_{D/IM}$) regarding regression models, with structural variability	123
Table 5.1. Mean values of the displacement limit states for the considered ESDOF models (Askan et al., 2015).....	129
Table 5.2. CDR values in this study (Adapted from Gurpinar et al., 1978)	154
Table A.1. Selected ground motions in this dissertation and their main characteristics	192



CHAPTER 1

INTRODUCTION

1.1 General

Earthquakes cause structural, economical and human losses every year all over the world. Most of these losses such as fatalities are irreversible so it becomes crucial to mitigate earthquake loss in seismically active regions. A major percentage of land in Turkey is located in earthquake prone regions. The 1939 and 1992 Erzincan earthquakes, 1999 Kocaeli and Düzce earthquakes and 2011 Van earthquake are some examples of major earthquakes in Turkey during the last century, which caused major destruction and a vast number of fatalities. Thus, the significance of proper seismic design for new structures as well as seismic risk assessment of existing structures, with the ultimate purpose of retrofitting and rehabilitation, becomes clear. Accordingly, it becomes essential to estimate the potential seismic demands on structures for reliable seismic design and risk assessment.

In order to identify the seismic demands on a structure in detail, actual ground motions recorded in recent earthquakes are commonly employed. Use of ground motions with regional characteristics is essential. However, in some regions, due to lack of recorded ground motions in the study region, engineers and researchers employ ground motion records from other regions. In some cases, this practice might cause bias due to seismotectonic differences among regions. Thus, use of simulated ground motions has recently become popular.

Seismic hazard assessment is another common tool to estimate potential seismicity. Traditionally, Deterministic Seismic Hazard Assessment (DSHA) is applied for identifying seismic activity. This methodology consists of limited earthquake scenarios, which may not be indicative of possible future earthquakes. Alternatively, probabilistic techniques insert the whole possible ground motion scenarios into

seismic hazard assessment. Therefore, Probabilistic Seismic Hazard Analysis (PSHA) has been preferred recently. The fundamental step in PSHA to estimate the ground motion amplitudes is the use of Ground Motion Prediction Equations (GMPEs). GMPEs are derived by fitting a regression model to existing regional or global ground motion databases. GMPEs are proved to be more successful in regions with sufficient past ground motion data. These equations produce a single spectral ordinate for a ground motion scenario hence they do not yield full waveform series while also neglecting seismic wave propagation characteristics.

As mentioned previously, ground motion simulation methodologies provide alternative approaches (and time series) to estimate seismic hazard of regions with sparse data. Besides, these techniques account for complex regional seismicity parameters to characterize full seismic wave propagation. Ground motion simulation methods are divided into three main groups: deterministic, stochastic and hybrid approaches. Deterministic approaches model the wave propagation in an accurate manner while yielding relatively lower frequency ground motions (<1 Hz). They require well-resolved velocity models along with considerable computational effort. Stochastic methods consider ground motion randomness in the calculations. They are more practical and they do not require as detailed velocity profiles as the deterministic approaches. Stochastic methods mostly yield accurate high frequency ground motions (>1 Hz). Hybrid methods combine motions from deterministic and stochastic methods to overcome the shortcomings of both.

The effect of simulated ground motions on structural seismic analysis needs further investigation. The simulated ground motions are implemented by researchers in seismic loss studies mostly within deterministic frameworks. The combination of probabilistic techniques in seismic hazard assessment and ground motion simulation is a novel subject. The aforementioned applications could benefit from the advantages of both probabilistic seismic hazard analysis and ground motion simulation methodology.

1.2 Literature Review

Ground motion characterization of seismically active regions is an essential and significant part of seismic damage and loss assessment. Probabilistic seismic hazard analysis, a common approach for modeling potential seismicity of a region, was first

introduced by Cornell (1968) and extended later by numerous researchers (e.g.: McGuire and Arabasz, 1990; Kramer, 1996; Thenhaus and Campbell, 2003; McGuire, 2004). The concept was widely used in seismic loss estimation studies (e.g.: Cao et al., 1999; Luco et al., 2007; Eads et al., 2013; Farsangi et al., 2014). It was stated in these studies that a single deterministic scenario is not able to capture the characteristics of future events thoroughly. Therefore a probabilistic framework should be developed to estimate the possible future earthquake scenarios.

Although PSHA is a powerful tool for estimating potential seismicity in a region, it is known to have a few shortcomings: Naeim and Lew (1995) referred to the unrealistic energy content of uniform hazard spectrum (UHS) as PSHA considers a wide range of aleatory variability. Later on Baker (2011) argued that UHS from classical PSHA is not suitable for ground motion selection and defined Conditional Mean Spectrum (CMS), which is generally observed to lie below UHS.

According to Bommer and Crowley (2006), PSHA also neglects intra-event variability. These authors proposed the use of stochastically generated earthquake catalogs with Monte Carlo Simulation (MCS), which were later employed by Crowley and Bommer (2006) for earthquake loss estimation. Assatourians and Atkinson (2013) defined a PSHA toolbox called EqHaz, which also employs the MCS approach. Musson (2000) referred to the most important advantages of MCS-based hazard functions as powerful handling of uncertainty and simplicity of deaggregation. Assatourians and Atkinson (2013) also pointed to flexibility and simplicity of Monte Carlo simulation approach to be implemented in PSHA calculations.

GMPEs (called attenuation models formerly) are the most common tools for estimating Ground Motion Intensity Parameters (GMIPs) in PSHA studies. By the help of GMPEs, it becomes possible to predict GMIPs such as spectral acceleration (SA), as a function of selected seismicity parameters like magnitude, source to site distance, site class and focal mechanism. The parametric curves of GMPEs are obtained by regression analyses. GMPEs require a large ground motion dataset for regression models to produce reliable results. The most popular local GMPEs for Turkey are Kalkan and Gulkan (2005), Akkar and Bommer (2010) and Akkar and Cagnan (2010). The most widespread GMPEs worldwide are Next Generation

Attenuation (NGA) models: They consist of five predictive equation sets, which belong to Boore and Atkinson (2008), Campbell and Bozorgnia (2008), Abrahamson and Silva (2008), Chiou and Youngs (2008) and Idriss (2008).

Wen and Wu (2001) followed the above-mentioned MCS approach to generate earthquake catalog for western, central and eastern United States. The difference was that Wen and Wu (2001) computed ground motion intensity parameters through simulated time histories instead of ground motion prediction equations. This methodology was later shown to produce agreeable estimates of linear and nonlinear structural demands by Gu and Wen (2007). Hence, it was used for the derivation of fragility functions for selected building structures (Ellingwood et al., 2007). In addition to Wen and Wu (2001), several researchers studied MCS-based seismic hazard assessment using simulated ground motions as well (e.g.: Shapira and Eck, 1993; Collins et al., 1996; Datta and Ghosh, 2008, Hashash and Moon, 2011; Papoulia et al., 2015).

Using simulated ground motions rather than ground motion prediction equations to estimate GMIP facilitates to take into account the complex source effects (such as forward directivity), path effects (such as duration) and detailed local site effects in seismic hazard and risk assessments. Besides, GMPEs are sometimes not capable of producing satisfactory results in regions with sparse data (e.g.: McGuire, 2004; Akansel et al., 2014; Raschke, 2014). In particular, the effective role of site response in seismic hazard assessment was highlighted in previous studies (e.g.: Cramer, 2006; Hashash and Moon, 2011). Yet, most ground motion prediction models consider rough site categories as rock and soil (e.g.: Ambraseys et al., 2005; Akkar and Bommer, 2010). As a result, use of simulated ground motions instead of ground motion prediction equations in probabilistic seismic hazard analyses becomes a valid option. Accordingly, ground motion simulation was also applied to estimate seismic loss by several researchers previously (e.g.: Ellingwood et al., 2007; Ansal et al., 2009; Ugurhan et al., 2011).

Seismic damage assessment of structures is one of the most important applications and outcomes of seismic hazard analysis. Calvi et al. (2006) summarized the damage assessment methodologies over the past 30 years. They divided the related approaches into two general categories: empirical and analytical. Empirical methods

are based on post-earthquake observations expressed in the form of discrete damage probability matrices (DPM) and continuous fragility functions (Whitman, 1973).

Analytical methods, however, define a physical model for any structural system and estimate the damage state of the structure by conducting nonlinear analysis. Damage probabilities derived from analytical simulations are generally represented in the form of fragility curves. Fragility functions represent the probability of exceeding a predefined limit state as a function of GMIP (e.g.: Porter, 2003; Wen et al., 2004). Considering the seismic fragility of Turkish structural systems, Erberik (2008a) derived fragility curves of typical reinforced concrete (RC) buildings in Turkey by using the structural data from damaged building databases that was developed right after the two catastrophic earthquakes in Marmara region in 1999. Fragility functions for typical Turkish masonry buildings were developed by Erberik (2008b) by considering the damaged building database after the 1995 Dinar earthquake and field database obtained during the Earthquake Masterplan Studies in different provinces of Istanbul. Gencturk et al. (2008) studied the fragility functions of wood frame buildings. Fragility functions of Turkish typical reinforced concrete buildings were also developed by Ay and Erberik (2008) by using different generation techniques and local damage conditions.

Some researchers model the actual structures by using multi degree of freedom (MDOF) systems (e.g.: Erberik and Elnashai, 2004; Ramamoorthy et al., 2006; Ramamoorthy et al., 2008; Ay and Erberik, 2008; Celik and Ellingwood, 2010; Bai et al., 2011). Some other researchers however idealize the whole structure with equivalent single degree of freedom (ESDOF) systems (e.g.: Akkar et al., 2005; Erberik, 2008a; Ozmen et al., 2010; Ugurhan et al., 2011). MDOFs represent the structure more accurately but they require higher computational efforts for time history analyses.

Nonlinear time history analysis of structural models is an essential part of seismic damage assessment. Seismic demands of the structural model (e.g.: maximum displacement) are derived from analysis results. Fragility functions are then obtained using structural demand versus GMIP statistics. Fitting a statistical distribution on structural demands given any level of GMIP, is a common approach to compute exceedance probabilities (e.g.: Erberik, 2008a; Ay and Erberik, 2008; Silva et al.,

2013; Pejovic and Jankovic, 2015). Alternatively, in some studies regressing analyses on demand-GMIP scatters are performed in order to compute seismic fragilities (e.g.: Ramamoorthy et al., 2006; Ellingwood et al., 2007; Ramamoorthy et al., 2008; Bai et al, 2011). It is possible to investigate the effect of different seismic parameters on structural demand through predictive regression models. Besides, this approach makes seismic fragility calculations more practical.

The importance of displacement demand in damage evaluation was highlighted by Calvi (1999), leading to the concept of displacement-based earthquake loss assessment (DBELA). Crowley et al. (2004) derive a formulation for displacement capacity of building classes including the height of structures. Silva et al. (2013) obtained fragility functions of typical reinforced concrete Turkish buildings using DBELA as well. A displacement-based approach was also followed by Akkar et al. (2005) to compare the field observations with analytical fragility functions of typical reinforced concrete structural systems in Turkey.

The sensitivity of fragility curves to different parameters is also an important issue. Erberik (2008a) addressed the considerable effect of degradation characteristics and limit state definitions on fragility functions of Turkish RC frame buildings. Celik and Ellingwood (2010) studied the impact of structural uncertainties on demand predictions and fragility functions. The same authors derived two sets of structural models from mean parameters and parameter uncertainties. Then, they compared the fragility curves related to two separate models. Similarly, the sensitivity of bridge fragility assessment to uncertain bridge parameters was investigated by Padgett and DesRoches (2007). Jeon et al. (2015) discussed the impact of masonry infills on fragility functions of RC frames. Crowley et al. (2005) performed intensive sensitivity analyses for seismic loss estimation of typical building structures in Marmara region, Turkey. The uncertainties, which were used in that study, are related to site classification definitions, building classifications and demand spectrum. Among the uncertainties which affect structural vulnerability, some of them are more important than the others. This issue was investigated thoroughly by Rohmer et al. (2014) for structural loss assessment in France.

Following the mentioned studies, this thesis aims to contribute to the existing literature by tackling a less-studied topic: a combination of PSHA theory with

stochastic catalogs and simulated ground motions as well as their use in fragility functions is studied herein. The following section provides the objective and scope of this dissertation in detail.

1.3 Objective and Scope

This dissertation consists of two parts. In the first part, a novel approach is employed to derive site-specific uniform hazard spectrum based on stochastic ground motion simulation. Monte Carlo simulation method is applied to determine temporal and spatial distribution of the earthquakes in the selected region. After presenting the initial results obtained from the proposed method, sensitivity analyses are performed with respect to near-field forward directivity and site amplification models. The proposed UHS are then used to select sets of spectrum-complying simulated ground motions. The combination of probabilistic seismic hazard assessment and ground motion simulation in this study is a new approach. The proposed study provides an alternative method for regional seismic hazard assessment in regions with sparse earthquake recordings. In addition, through the use of simulated motions in this study, the shortcomings of GMPEs are eliminated.

In the second part, an application of the proposed regional UHS in earthquake engineering is presented in terms of structural demands and fragility. The fragility functions are obtained through demand predictive equations, which resulted from the selected simulated ground motions in the first part. The main aim of the second part is to observe the sensitivity of fragility functions to some local seismic parameters which are related to the first part. The effects of site conditions, near-field forward directivity, site amplification models and structural variability are investigated on fragility functions. Erzincan region in Eastern Turkey is studied in this dissertation. Figure 1.1 shows the procedures applied in this dissertation in detail within a flowchart.

The outline of the thesis is as follows:

- In Chapter 2, the ground motion simulation techniques, which are used in this study are described. Stochastic point source and finite-fault models are explained in detail. The source, path and site functions, which are the principle parts of ground motion simulation, are defined. This chapter also

contains the approach to calibrate stress drop parameter of point-source simulation used in this dissertation.

- In Chapter 3, the methodology for construction of UHS is proposed based on MCS approach and stochastic ground motion simulation. The proposed UHS in this study are compared to those from classical PSHA. The effects of near-field forward directivity and site amplification models on the proposed seismic hazard assessment are studied in detail. Ground motion selection with respect to UHS is performed in this chapter as well. The acceleration time histories for use in structural analyses are selected from the simulated ground motions which were employed to construct the UHS.
- In Chapter 4, the selected ground motions in the previous chapter are used to perform nonlinear time history analysis of structural models. The typical structural systems in Erzincan are modeled using equivalent single degree of freedom (ESDOF) systems. Structural response statistics resulted from the time history analyses are shown in this chapter. Predictive equations are also developed for structural demands as functions of ground motion intensity parameters.
- In Chapter 5, the demand prediction equations in Chapter 4 are applied to calculate the fragility functions of each building class that is represented by the corresponding ESDOF model. The effects of site conditions, near-field forward directivity, site amplification models and structural variability are investigated on fragility functions. This chapter shows how simulated ground motions incorporating the regional seismotectonics influence structural damage assessment in the region.
- Chapter 6 presents a brief summary followed by the conclusions, contributions and limitation of this study. Recommendations for future studies are also presented.

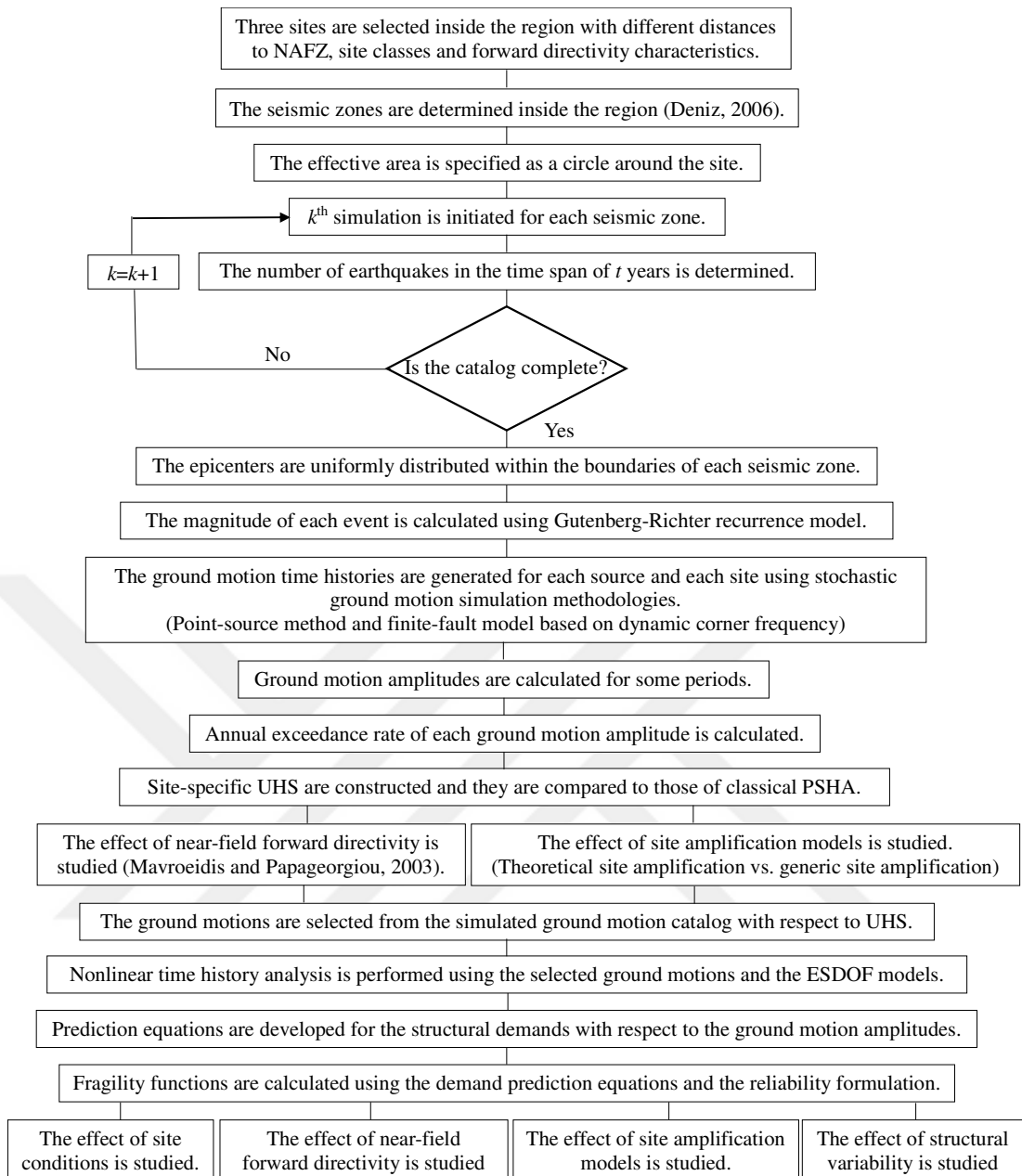


Figure 1.1. Flowchart for step-by-step procedures in this dissertation



CHAPTER 2

GROUND MOTION SIMULATION METHODOLOGY

2.1 Introduction

In this chapter, ground motion simulation techniques which are used in this thesis are described. Stochastic point-source model is applied for simulating the ground motions regarding areal seismic sources. Stochastic finite-fault model based on dynamic corner frequency is used for modeling ground motions radiating from extended faults. Both stochastic point-source and finite-fault models are explained in detail in Sections 2.2 and 2.3, respectively.

The input simulation parameters for the study region are adopted from the literature. Hence calibration of simulation parameters with respect to observed data is beyond the scope of this study. Stress drop of point-source model is the only parameter which is estimated in this chapter through sensitivity analyses between simulated and observed data.

2.2 Stochastic Point-Source Model

In general, there are three categories for ground motion simulation methods: deterministic, stochastic and hybrid approaches. Deterministic methods mostly involve numerical solutions of wave propagation equation in heterogeneous media (e.g.: Frankel, 1993; Olsen et al., 1996). These techniques model the physical process accurately; however they require well-resolved velocity models and considerable computational effort to simulate frequencies of engineering interest (lower than 1 Hertz).

Stochastic approaches account for the inherent randomness in ground motions. They are practical but do not involve models of the physical processes as refined as in the

deterministic approaches (e.g.: Boore, 1983; Beresnev and Atkinson, 1997; Boore, 2003). Yet, stochastic methods have been employed effectively in particular for higher frequencies that are of engineering interest (higher than 1 Hertz) (e.g.: Roumelioti et al., 2004; Yalcinkaya, 2005; Shoja-Taheri and Ghofrani, 2007; Ugurhan and Askan, 2010; Rodriguez-Perez et al., 2012; Ugurhan et al., 2012; Ghofrani et al., 2013). For regions without detailed source descriptions and well-resolved velocity models, stochastic methods are particularly preferred (e.g.: Zafarani et al., 2009; Chopra et al., 2012; Askan et al., 2013).

Hybrid methods are developed more recently to overcome shortcomings related to both deterministic and stochastic techniques (e.g.: Graves and Pitarka, 2010; Mena et al., 2010). These techniques mainly combine motions derived from deterministic and stochastic methods for the low and high frequencies, respectively and generate reliable broadband synthetics.

Stochastic method, which deals with high-frequency portion of ground motions, is implemented confidently in this study as it effectively simulates the frequency band for low-rise and mid-rise residential buildings with fundamental periods mostly shorter than one second. Stochastic point-source model of Boore (2003) is used for areal zones since those seismic sources are considered as a single point. This model is mostly preferred when dimensions of the source are negligible with respect to distance to site (Boore, 2009). This point is taken into account in this study for areal sources that are far away from the observation sites and for events with relatively small magnitudes ($M_w \leq 5.8$).

The stochastic point-source methodology is based on a deterministic ground motion amplitude spectrum combined with a random phase spectrum which is then converted to time domain with a specified duration (Hanks and McGuire, 1981). The main goal of stochastic simulation is to generate a shear-wave time series whose amplitude spectrum is the deterministic S-wave amplitude spectrum stated as follows:

$$Y(M_0, R, f) = E(M_0, f).P(R, f).G(f).I(f) \quad (2.1)$$

where M_0 , R and f are seismic moment, source to site distance and frequency, respectively. Seismic moment is related to moment magnitude (M_w) via the following empirical relationship by Hanks and Kanamori (1979):

$$M_w = \frac{2}{3} \log M_0 - 10.7 \quad (2.2)$$

In Equation 2.1, E , P and G are frequency-dependent source, path and site functions, respectively. These functions are described in detail in the following sections. I is the type of ground motion which is calculated as follows:

$$I(f) = (2\pi fi)^n \quad (2.3)$$

where $n = 0, 1, 2$ for ground displacement, velocity and acceleration, respectively and $i = \sqrt{-1}$.

Figure 2.1 is a schematic representation of ground motion decomposition into source, path and site factors.

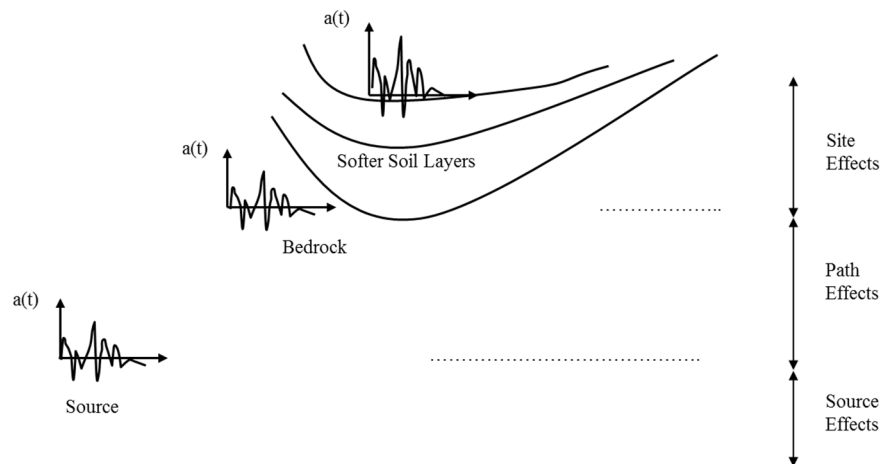


Figure 2.1. Schematic representation of source, path and site factors in surface ground motion amplitudes

2.2.1 Simulation of Acceleration Time History

Hanks and McGuire (1981) fundamentally stated that high-frequency shear-wave motion is a band limited, finite duration white Gaussian noise. The generated random noise is then windowed and transformed into Fourier amplitude spectrum (FAS). FAS of white noise is later normalized to square root of mean square amplitude spectrum. This normalized spectrum is multiplied by theoretical deterministic (target) amplitude spectrum (Equation 2.1). The product is transformed into time series. Figure 2.2 shows the main steps in simulation of stochastic time series.

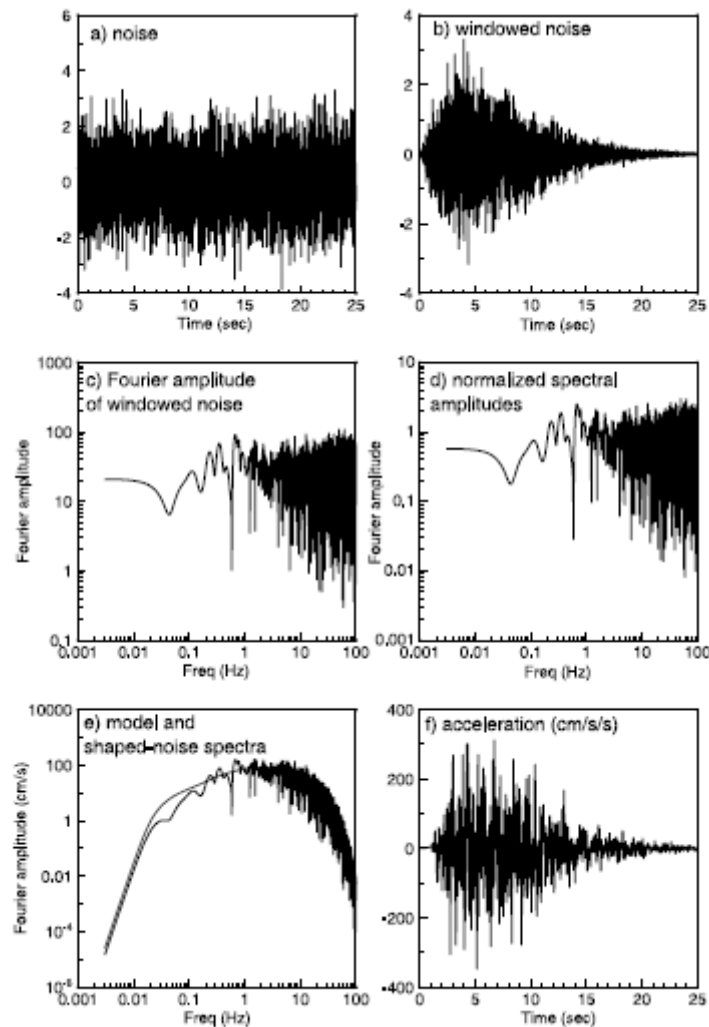


Figure 2.2. Flowchart for stochastic time series simulation (Boore, 2003)

Windowing function may be either box or exponential shape. Saragoni and Hart (1974) developed an exponential windowing function as follows:

$$w(t, \varepsilon, \eta, t_\eta) = a(t/t_\eta)^b \exp(-c(t/t_\eta)) \quad (2.4)$$

where parameters b , c , a and t_η are obtained from Equations 2.5, 2.6, 2.7 and 2.8 respectively:

$$b = -(\varepsilon \ln \eta) / [1 + \varepsilon(\ln \varepsilon - 1)] \quad (2.5)$$

$$c = b / \varepsilon \quad (2.6)$$

$$a = (\exp(1) / \varepsilon)^b \quad (2.7)$$

$$t_\eta = f_{T_{gm}} \times T_{gm} \quad (2.8)$$

Based on the original observations of Saragoni and Hart (1974), the parameter values are set as follows: $\varepsilon = 0.2$, $\eta = 0.05$ and $f_{T_{gm}} = 2.0$.

2.2.2 Random Vibration Theory

Random vibration theory is a practical and quick way of predicting peak responses without solving the entire time history. The ratio of peak response (y_{max}) and root-mean-square response (y_{rms}) is estimated through this technique. The aforementioned ratio is given by Cartwright and Longuet-Higgins (1956) as follows:

$$\frac{y_{max}}{y_{rms}} = 2 \int_0^{\infty} \{1 - [1 - \xi \exp(-z^2)]^{N_e}\} dz \quad (2.9)$$

where $\xi = N_z / N_e$. N_z and N_e are number of zero crossings and extrema, respectively. Equation 2.9 is solved for larger N as follows:

$$\frac{y_{max}}{y_{rms}} = [2 \ln(N_z)]^{1/2} + \frac{0.5772}{[2 \ln(N_z)]^{1/2}} \quad (2.10)$$

Number of zero crossings and extrema is related to frequencies of zero crossings (\tilde{f}_z) and extrema (\tilde{f}_e) as well as duration (T) via the following equation:

$$N_{z,e} = 2\tilde{f}_{z,e} T \quad (2.11)$$

where

$$\tilde{f}_z = \frac{1}{2\pi} (m_2 / m_0)^{1/2} \quad (2.12)$$

$$\tilde{f}_e = \frac{1}{2\pi} (m_4 / m_2)^{1/2} \quad (2.13)$$

where m_k is moment of the squared amplitude spectrum. This is the most critical parameter in random vibration theory.

$$m_k = 2 \int_0^{\infty} (2\pi f)^k |Y(f)|^2 df \quad (2.14)$$

where Y is deterministic amplitude spectrum which is defined in Equation 2.1.

Even though random vibration theory needs further investigations when oscillator period is much longer than ground motion duration and when damping is small, it yields applicable response spectra. Therefore this technique is preferred in this dissertation for stochastic point-source simulations due to its efficiency and speed.

2.2.3 The Source Function

Single corner frequency ω -squared model of Aki (1967) is the most widespread method to identify the source spectrum. Aki (1967) derived a relationship (scaling law) between seismic moment (M_0) and corner frequency (f_0) as shown in Figure 2.3 expressed as follows:

$$M_0 f_0^3 = \text{Constant} \quad (2.15)$$

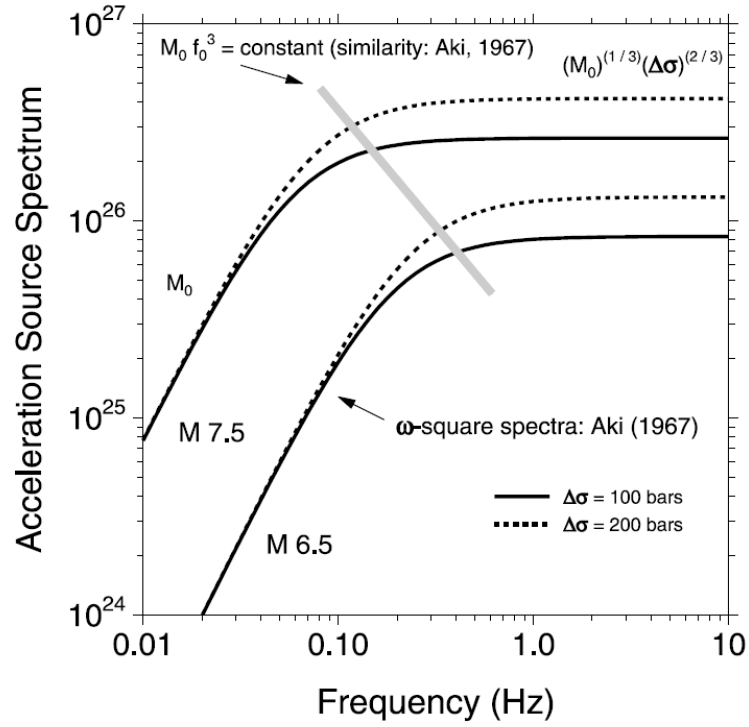


Figure 2.3. Single corner frequency ω -squared source spectrum proposed by Aki (1967)

Brune (1970) and Brune (1971) derived a relationship between corner frequency and stress drop parameter ($\Delta\sigma$). Therefore corner frequency is formulated accordingly:

$$f_0 = 4.9 \times 10^6 \beta_s (\Delta\sigma / M_0)^{1/3} \quad (2.16)$$

where β_s is shear-wave velocity in vicinity of the source.

The source spectrum is directly related to size of earthquake and it is expressed as follows:

$$E(M_0, f) = CM_0 S(M_0, f) \quad (2.17)$$

where C is a constant which is given as follows:

$$C = \langle R\Theta\Phi \rangle VF / (4\pi\rho_s\beta_s^3 R_0) \quad (2.18)$$

where $\langle R\Theta\Phi \rangle$ is radiation pattern, V is partition of shear-wave into horizontal components ($=1/\sqrt{2}$), F is free surface effect ($=2$), R_0 is reference distance ($=1$), ρ_s and β_s are density and shear-wave velocity in the vicinity of source, respectively.

$S(M_0, f)$ is the source displacement spectrum defined as follows:

$$S(M_0, f) = S_a(M_0, f) \times S_b(M_0, f) \quad (2.19)$$

where S_a and S_b are seismic moment-based and frequency-based shape spectra. For ω -squared source model, the following shape function of Frankel et al. (1996) is preferred:

$$\begin{aligned} S_a(M_0, f) &= \frac{1}{1 + (f/f_a)^2} \\ S_b(M_0, f) &= 1 \end{aligned} \quad (2.20)$$

where f_a is corner frequency. This corner frequency parameter is defined by Equation 2.16.

2.2.4 The Path Function

Seismic waves radiating from sources propagate through the crust which can be expressed in the frequency domain with the path function. Path effect consists of intrinsic attenuation, geometrical spreading and duration function. The mathematical formulation of path function is as follows:

$$P(R, f) = Z(R) \exp(-\pi f R / Q(f) \beta_s) \quad (2.21)$$

$-\pi f R / Q(f) \beta_s$ is intrinsic or anelastic attenuation where $Q(f)$ is frequency-dependent quality factor and R is source to site distance. $Z(R)$ is geometrical spreading which is a stepwise function of distance defined as follows:

$$Z(R) = \begin{cases} \frac{R_0}{R} & R \leq R_1 \\ Z(R_1) \left(\frac{R_1}{R}\right)^{p_1} & R_1 < R \leq R_2 \\ \vdots & \\ Z(R_n) \left(\frac{R_n}{R}\right)^{p_n} & R_n \leq R \end{cases} \quad (2.22)$$

R is generally the closest distance to rupture but it is equivalent to hypocentral distance when the dimensions of rupture are small with respect to source-to-site distance.

Frequency-dependent quality factor ($Q(f)$) is derived through averaging of weak-motion observations. Aki (1980) put forward the general shape of Q as a piecewise trilinear segments (Figure 2.4). Two outer lines are characterized by intercepts (Qr_1 and Qr_2) and slopes (s_1 and s_2). These two lines are simply connected by a middle line at joining frequencies (ft_1 and ft_2).

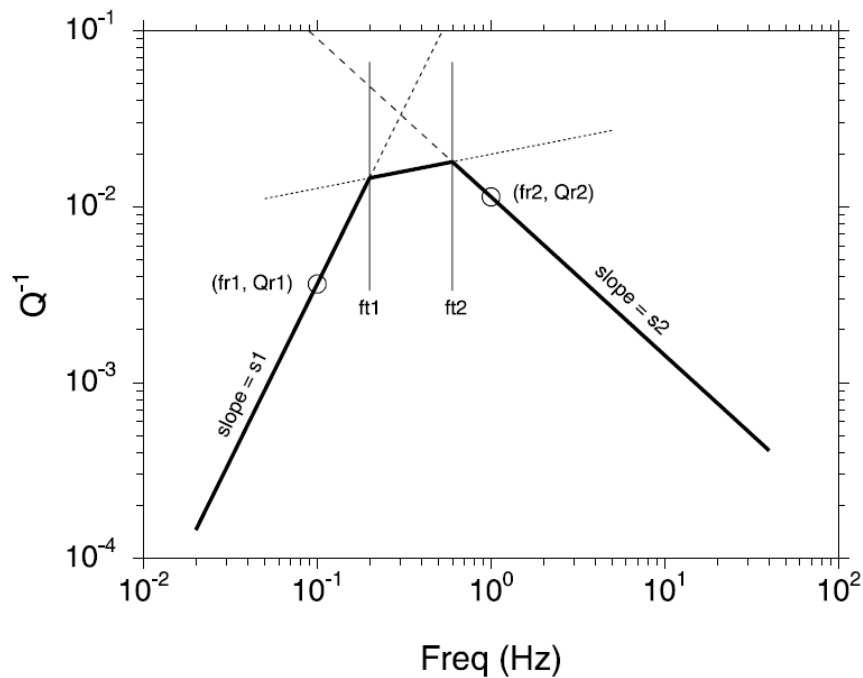


Figure 2.4. General shape of Q function in log-log space proposed by Aki (1980)

Geometrical spreading and quality factor are mostly obtained from observed data simultaneously. Because combined effect of these two parameters is inserted into waveform calculations. Q is generally expressed as a single function for s_2 branch in Figure 2.4 due to data insufficiency in the long-period range. Equation 2.23 demonstrates general functional form of Q :

$$Q(f) = Q_{r2}f^{s_2} \quad (2.23)$$

The third path parameter is the duration function: Duration model contains contributions from both source and path. Source-dependent duration is generally the reciprocal of corner frequency according to Frankel et al. (1996) model. Atkinson and Boore (1995) proposed the path-dependent part as stepwise linear functions of distance. Path duration may be expressed as a single straight line as function of distance according to Herrmann (1985).

2.2.5 The Site Function

The site function is the product of amplification function, $A(f)$, and diminution function, $D(f)$, in the frequency domain:

$$G(f) = A(f).D(f) \quad (2.24)$$

Site amplification factors are mainly defined as the frequency-dependent ratios of surface motion to bedrock motion. There are various methods to model amplification function: Empirical, theoretical site-specific and theoretical generic methods. Empirical methods are useful particularly when there is plenty of well-quality accelerometer data. One of the common empirical methodologies is Horizontal to Vertical Spectral Ratio (HVSr) (Nogoshi and Igarashi, 1971; Nakamura, 1989). This approach is derived from the assumption that vertical components are less amplified than horizontal components. Theoretical site amplification considers detailed soil conditions at a site of interest in order to determine amplification function. Generic site amplifications are also commonly used and they are based on quarter-wavelength method as proposed by Boore and Joyner (1997). Both generic and theoretical site amplifications along with effect of site response in simulated ground motions is described in Chapter 3.

Site diminution is a path-independent attenuation function based on high-frequency loss of seismic energy due to site features. Anderson and Hough (1984) proposed an exponential model for the diminution function known as the kappa model as follows:

$$D(f) = \exp(-\pi\kappa_0 f) \quad (2.25)$$

where κ_0 is high frequency spectral decay (kappa) factor obtained through empirical linear models of the amplitude decay. Figure 2.5 shows total site effect (combination of amplification and diminution) for generic rock site and different κ_0 values. It is obvious that high-frequency amplitude is reduced as κ_0 increases for softer soils.

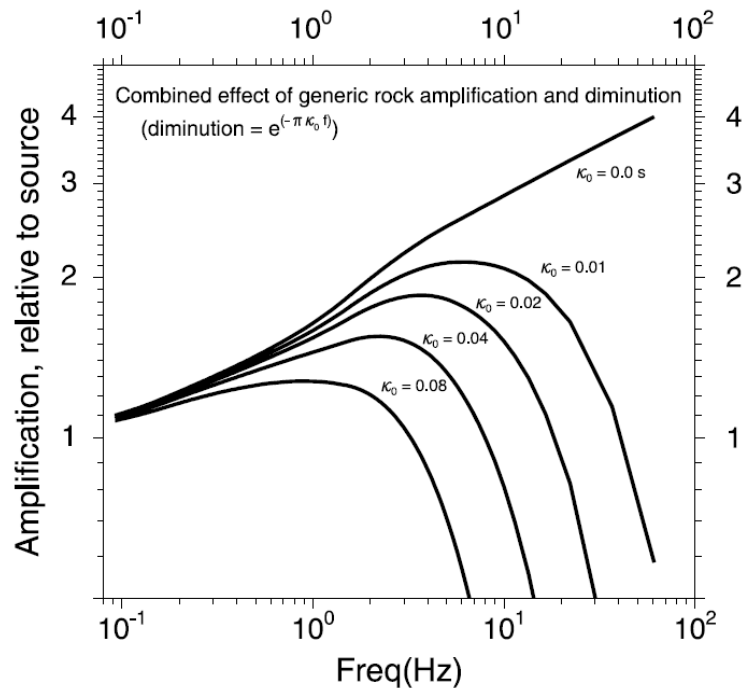


Figure 2.5. Combination of generic site amplification and different diminution factors (Adopted from Boore and Joyner, 1997)

Finally, the entire set of calculations related to stochastic point-source model are performed using SMSIM program. This code is developed by Boore (2003) and is freely available via http://www.daveboore.com/pubs_online.html.

2.3 Stochastic Finite-Fault Model

Point-source model is not very effective for simulations of ground motions from large earthquakes at close distances. Therefore finite-fault model is preferred for bigger events occurring on larger fault dimensions. The significance of finite-fault effects on ground motions is highlighted by several researchers (e.g.: Hartzell, 1978; Joyner and Boore, 1986; Somerville et al, 1991; Beresnev and Atkinson, 1998a). For modeling the rupture propagation on large faults, Hartzell (1978) puts forward the idea of expressing the total ground motion in terms of contributions from smaller sources. Hence finite fault model divides the entire fault into subfaults where each subfault is modeled as a point source. The ground motion radiating from each subfault is calculated using the stochastic point-source model which was discussed in the previous section. The resulting ground motions are then summed up considering a proper time delay as follows:

$$a(t) = \sum_{i=1}^{n_l} \sum_{j=1}^{n_w} a_{ij}(t + \Delta t_{ij}) \quad (2.26)$$

where $a(t)$ is ground motion amplitude of the entire fault, a_{ij} is ground motion amplitude of ij^{th} subfault, Δt_{ij} is time delay of ij^{th} subfault, n_l and n_w are number of subfaults along length and width of extended fault, respectively. Figure 2.6 illustrates rupture propagation on a finite-fault source model.

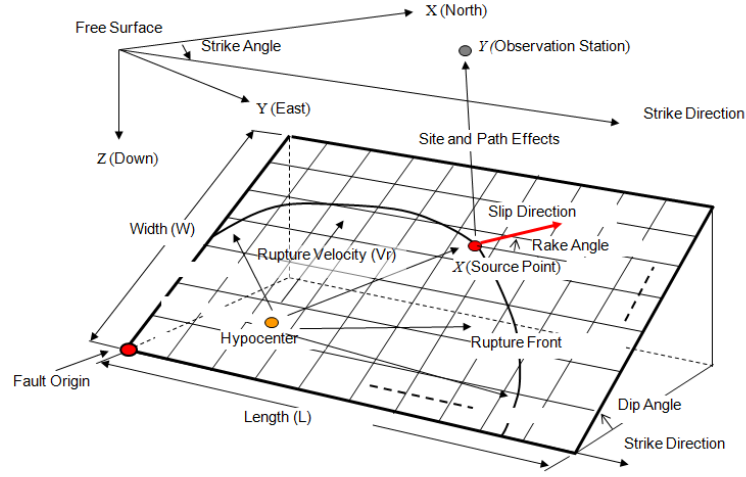


Figure 2.6. Rupture propagation on a finite-fault source model and subfaults
(Adopted from Hisada, 2008)

Ground motion amplitude related to each subfault is obtained from the following equation:

$$A_{ij}(f) = \left\{ CM_{0ij} (2\pi f)^2 / [1 + (f_{0ij})^2] \right\} \left\{ \exp(-\pi f \kappa) \exp(-\pi f R_{ij} / Q(f) \beta_s) A(f) Z(R_{ij}) \right\} \quad (2.27)$$

where M_{0ij} , R_{ij} and f_{0ij} are seismic moment, distance to site and corner frequency related to ij^{th} subfault. All the other parameters are as introduced in the previous section. Seismic moment of each subfault is obtained from seismic moment of entire fault divided by the number of subfaults (N) if the subfaults are identical ($M_{0ij} = M_0 / N$). Otherwise, seismic moment is distributed among subfaults with respect to their relative slip weights as follows:

$$M_{0ij} = \frac{M_0 S_{ij}}{\sum_{l=1}^{nl} \sum_{k=1}^{nk} S_{kl}} \quad (2.28)$$

where S_{ij} is relative slip weight of the ij^{th} subfault. Corner frequency of each subfault is obtained from Equation 2.16 while M_{0ij} is considered as seismic moment of the ij^{th} subfault.

Ground motion amplitude of entire fault is shown to be dependent on number of subfaults in this classical finite-fault model (Joyner and Boore, 1986; Beresnev and Atkinson, 1998b; Motazedian and Atkinson, 2005). Motazedian and Atkinson (2005) investigated this issue for an arbitrary fault with a moment magnitude of M_w 7 and an area of 800 km^2 . The authors of that study calculated square of Fourier amplitude spectrum, which is representative of received energy, for different subfault sizes (or number of subfaults). Figure 2.7 shows the variation of received energy for subfault lengths of 1, 2, 6 and 10 km.

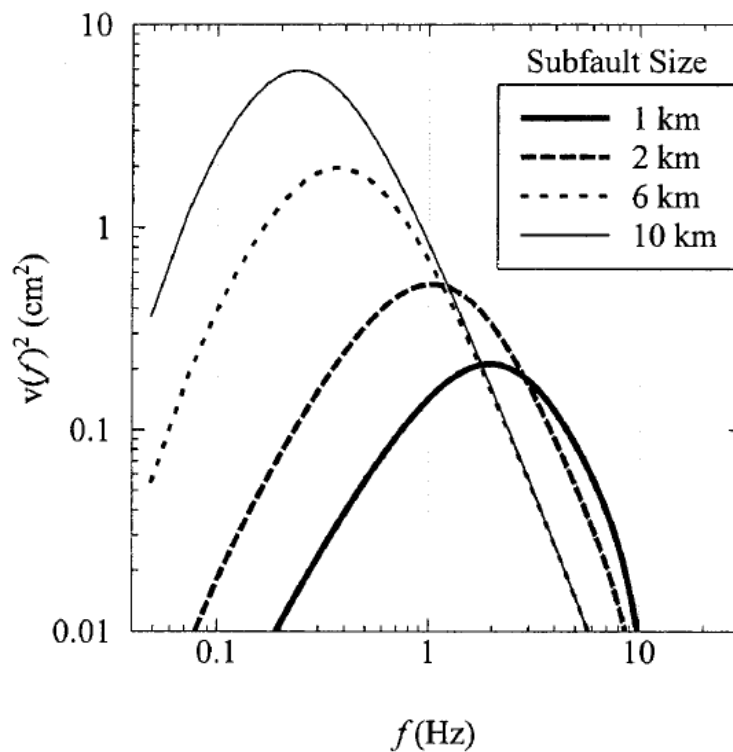


Figure 2.7. Dependency of radiated seismic energy on subfault size in finite-fault model (Adopted from Motazedian and Atkinson, 2005)

It is obvious from Figure 2.7 that when number of subfaults is increased (i.e. subfault size is decreased), the energy content is decreased for lower frequencies and it is increased for higher frequencies. Total energy for subfault size of 1 km (i.e. 800

numbers of subfaults) is higher than the one with subfault size of 10 km (i.e. 8 numbers of subfaults). Motazedian and Atkinson (2005) then provide a solution for this problem by introducing the concept of dynamic corner frequency in which corner frequency is dependent upon time. The basic idea is that the corner frequency is inversely proportional to rupture area and rupture area increases with time according to finite-fault model. Hence Equation 2.16 is modified to involve the effect of ruptured area up to time t as follows:

$$f_{0ij}(t) = N_R(t)^{-1/3} \cdot 4.9 \times 10^6 \beta_s (\Delta\sigma / M_0 / N)^{1/3} \quad (2.29)$$

where $N_R(t)$ is cumulative number of ruptured subfaults at time t . The concept of dynamic corner frequency causes corner frequency to move towards lower frequencies with time. This trend leads to a reduction of high-frequency energy content. Hence a scaling factor is required to conserve high-frequency ground motion amplitudes. Motazedian and Atkinson (2005) introduce scaling factor (H_{ij}) considering that total radiated energy is N times the radiated energy of each subfault:

$$H_{ij} = (N \sum \{f^2 / [1 + (f/f_0)^2]\} / \sum \{f^2 / [1 + (f/f_{0ij})^2]\})^{1/2} \quad (2.30)$$

It is significant to be cautious about maximum active pulsing area in this finite-fault model using dynamic corner frequency concept. As time passes, number of ruptured subfaults increases until it becomes constant after a specified time. In other words, all the subfaults are not active during rupture. Maximum active pulsing area is expressed as a percentage of total fault area and it governs low-frequency part of ground motion. This parameter is based on ‘‘Self-healing’’ model of Heaton (1990) although there are some differences: The main difference is that ‘‘Self-healing’’ model points to very short duration at any location of fault with respect to total rupture duration. Pulse duration is not increasing during rupture in ‘‘Self-healing’’ model in contrary with the dynamic corner frequency model in which the corner frequency decreases as rupture propagates.

To test the dynamic corner frequency concept, Motazedian and Atkinson (2005) performed the previous simulations and obtained the energy spectra in Figure 2.8.

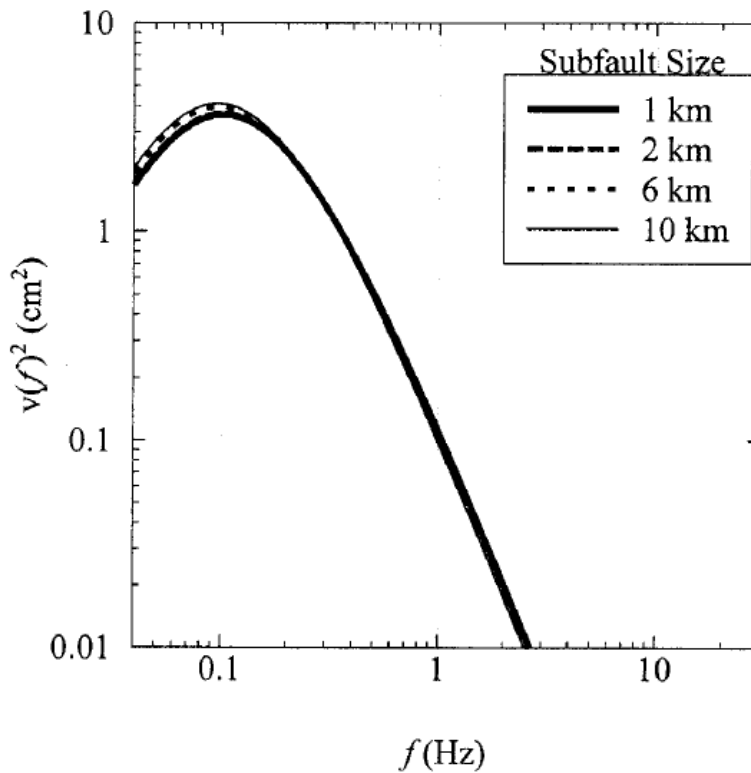


Figure 2.8. Independency of radiated seismic energy of subfault size in finite-fault model based on dynamic corner frequency
(Adopted from Motazedian and Atkinson, 2005)

Figure 2.8 shows that total seismic energy content is the same for different subfault sizes (i.e. number of subfaults). Hence dynamic corner frequency formulation is more physical than the traditional finite-fault models. EXSIM_beta computer program is used in this thesis to model stochastic finite-fault method based on dynamic corner frequency. This code is developed by Motazedian and Atkinson (2005) and is freely available via <http://http-server.carleton.ca/~dariush/>.

As mentioned before, calibration of simulation parameters with respect to observed data is beyond the scope of this study. Stress drop value for point-source simulations is the only parameter which is estimated in this chapter. Next section presents the sensitivity analyses between simulated and observed data to calibrate the values of stress drop for point source simulations as compared to finite-fault simulations.

2.4 Calibration of Stress Drop for Point Sources

Atkinson et al (2009) states that the stress drop parameter that controls the strength of the high-frequency radiation does not actually have the same meaning in EXSIM and SMSIM. In SMSIM, it is directly related to the Brune source model for a given stress parameter where the stress drop, corner frequency and seismic moment altogether control the spectral amplitudes. However, in EXSIM, it has this meaning only for a particular subfault (Atkinson et al., 2009). Hence, as discussed by Moghaddam et al. (2010), stress drop must be larger for point source simulations in order to be consistent with the corresponding amplitudes of finite-fault simulations.

To investigate this point, some comparisons are made in this study between finite-fault and point source models using different values of stress drop for point source simulations. 13 March 1992 Erzincan earthquake recordings are used in the comparisons. To quantify the differences, a misfit term is defined as follows:

$$E(f) = \frac{1}{n} \sum_{i=1}^n \log \left(\frac{A_i(f)_{FF}}{A_i(f)_{PS}} \right) \quad (2.31)$$

where n is number of stations which is three in this case study (stations ERC, TER and REF) since the 1992 Erzincan main shock was recorded only by these stations within 200 km epicentral distance. $A_i(f)$ is the amplitude of response spectrum (PSA) or Fourier amplitude spectrum (FAS) related to finite-fault (FF) and point source (PS) models. Then, a sensitivity index in the frequency domain is computed for each station as follows:

$$SI = \frac{1}{n} \sum_{i=1}^n \log \left(\frac{A_i(f)_{FF}}{A_i(f)_{PS}} \right) \quad (2.32)$$

where n is number of discrete frequencies and the other terms are as defined previously.

Ground motion time histories of the 1992 Erzincan earthquake are initially simulated using finite-fault model. The corresponding ground motions are also modeled using point source method with five different values of stress drop which are 1, 1.25, 1.5, 1.75 and 2 times the stress drop of finite-fault model. All of the other simulation parameters are kept constant. Figure 2.9 shows misfit and sensitivity indices for PSA

and FAS from point source simulations with different stress drop ratios with respect to finite-fault models.

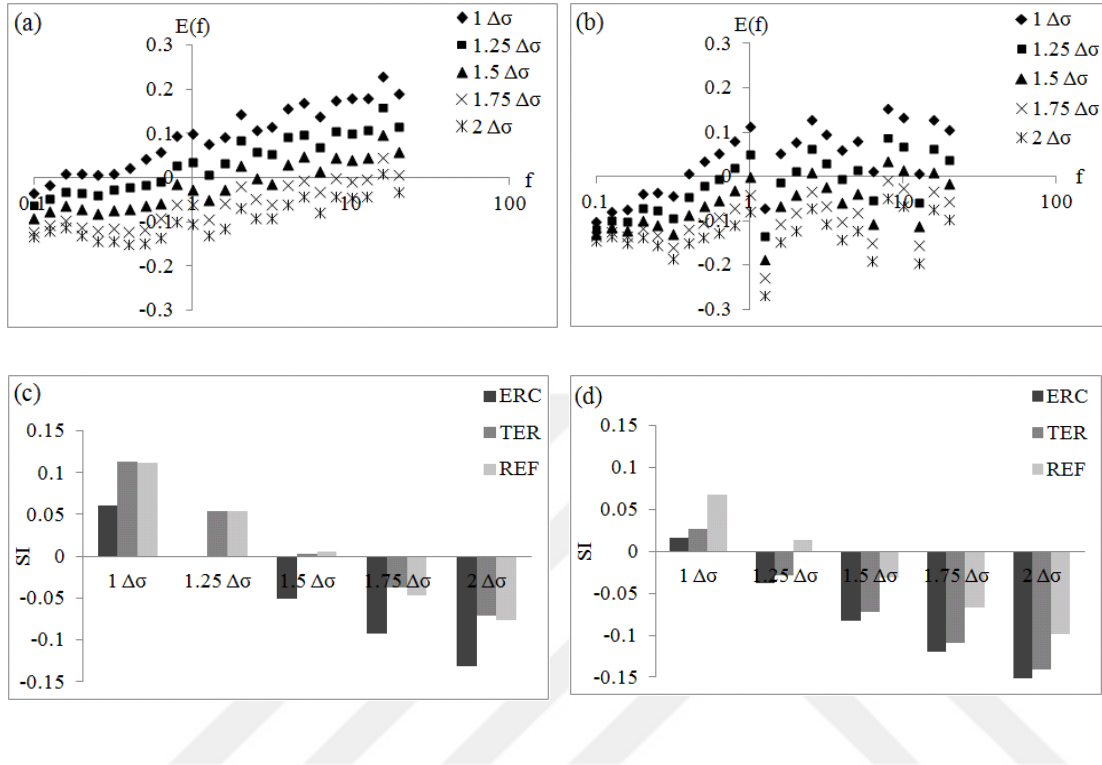


Figure 2.9. Misfit ($E(f)$) related to a) PSa b) FAS, and sensitivity index (SI) related to c) PSa d) FAS for point source simulations with different stress drop values with respect to finite-fault model

Finally, based on the observations in Figure 2.9, throughout this thesis the stress drop of SMSIM is assumed to be 1.5 times the corresponding value for extended fault. This value also complies with previous discussions of Atkinson et al. (2009) and Moghaddam et al. (2010).

Next chapter involves the incorporation of the simulation methods mentioned herein into seismic hazard analyses.

CHAPTER 3

CONSTRUCTION OF SITE-SPECIFIC UNIFORM HAZARD SPECTRUM AND GROUND MOTION SELECTION

3.1 Introduction

In this chapter, Uniform Hazard Spectrum (UHS) of Erzincan region in Eastern Turkey is constructed using simulated ground motions. Simulation methodologies described in Chapter 2, are used to calculate the corresponding ground motion amplitudes. The study area and the methodology for derivation of UHS are demonstrated in Section 3.2. The proposed methodology is indeed an alternative approach for seismic hazard assessment of regions with sparse data. The proposed seismic hazard curves are compared with those of the classical approach to observe the discrepancies. The main causes of these discrepancies are described along with simulated ground motion scatters versus their variance from GMPE. The effects of near-field forward directivity and alternative site amplification functions on the proposed UHS are then investigated in Section 3.3.

Next, the ground motion time histories are selected in Section 3.4 according to the derived UHS from the synthetic ground motion catalog used for seismic hazard calculations. The main benefits of the uniform hazard ground motions are described as well. The effects of the proposed regional UHS and the corresponding ground motions on seismic response of structures are later studied in Chapters 4 and 5 through nonlinear time history analyses.

3.2 Derivation of Uniform Hazard Spectrum Based on Simulated Ground Motions

3.2.1 Study Area

Erzincan region in Eastern Turkey is selected as the case study area in this dissertation. The region is in the relatively less-studied and sparsely-monitored Eastern part of the North Anatolian Fault zone (NAFZ). Erzincan city is located in a tectonically very complex regime, in the conjunction of three active faults, namely North Anatolian Fault Zone, North East Anatolian Fault Zone (NEAFZ) and East Anatolian Fault Zone (EAFZ) (Figure 3.1). NAFZ displays right-lateral strike-slip faulting whereas EAFZ and NEAFZ have left-lateral strike-slip faulting in the area (Askan et al., 2013).

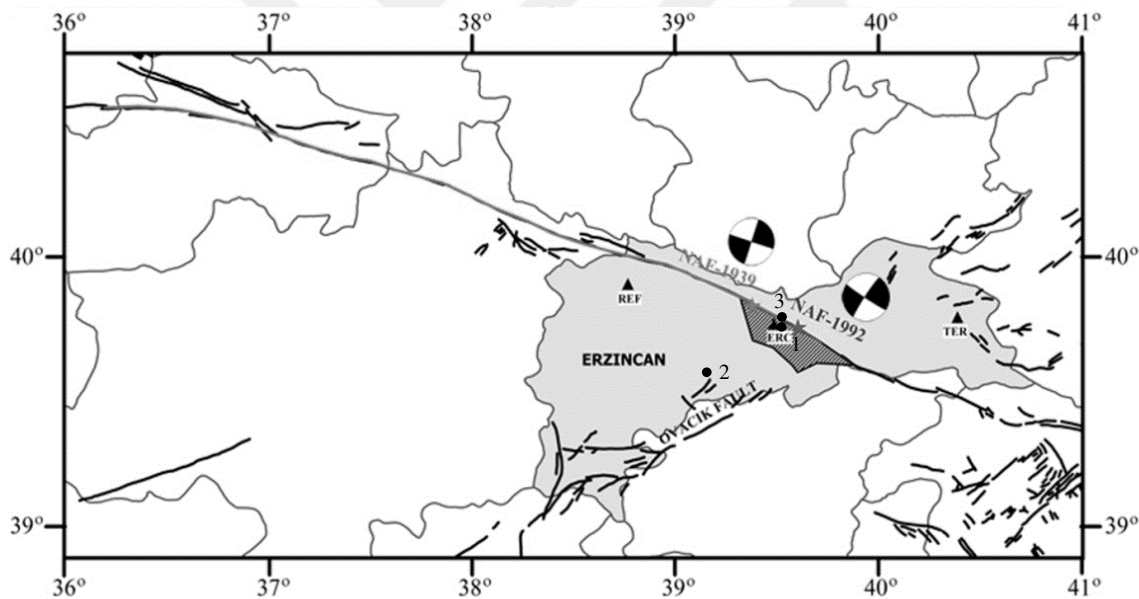


Figure 3.1. Regional map showing the epicenters, rupture zones and the mechanisms of the 1939 and 1992 earthquakes (epicenters are indicated with stars) and strong ground motion stations that recorded 1992 Erzincan earthquake are indicated with triangles (Adopted from Askan et al., 2013). The sites, which are used in this study, are indicated with solid circles with site numbers beside them.

This region is particularly selected since until very recently there were only a few strong motion stations around Erzincan. Indeed, the destructive 1992 Erzincan (Mw=6.6) mainshock was recorded only by 3 stations within 200 km epicentral distance. It is thus difficult to select a suitable GMPE based on a comparison between the limited past dataset and predictive models. As a result, the region is a good candidate for the proposed approach where ground motion simulations are employed instead of GMPEs.

Three sites are selected in this region. Site 1 is Erzincan city center, which is very close to NAFZ¹ and is located on soft soil. Site 2 is near Ovacik in southwest of Erzincan city, which is exposed to forward directivity effects more than the other two sites. Site 3 is inside Erzincan city near Cumhuriyet neighborhood, which is close to NAFZ and is located on stiff soil. The sites are selected according to their different distances from NAFZ, different soil conditions and different rupture directivity characteristics. Table 3.1 represents coordinates of the selected sites together with the site classes according to the NEHRP classification.

Table 3.1. Location and site classes of the selected sites

Site ID	Coordinates	Site class
Site 1	39.7464 °N 39.4914 °E	NEHRP D
Site 2	39.6200 °N 39.2000 °E	NEHRP D
Site 3	39.7566 °N 39.4925 °E	NEHRP C

In this study, the seismic zones inside the effective areas around the selected sites, are considered. The effective area is defined as a circle with a radius of 150 km around the site of interest. The coordinates and other physical properties of the seismic zones are derived from Deniz (2006). There are nine seismic zones

¹ The term “close to NAFZ” in this study means: “large number of fault ruptures inside NAFZ with short distance to site”.

consisting of five fault zones and four areal seismic zones in the region of interest. Table 3.2 and Figure 3.2 respectively show the seismic properties and locations of these seismic zones.

Table 3.2. Seismic parameters of the seismic zones used in this study
(Adopted from Deniz, 2006)

No	Name	M_{\max}	M_{\min}	Average Depth (km)	λ	β
1	North Anatolian Fault Zone-Segment D	8	4.5	25.04	1.07	1.347
2	East Anatolian Fault Zone	7.5	4.5	24.29	2.161	2.14
3	North East Anatolian Fault Zone	7.8	4.5	22.15	1.141	2.162
4	Central Anatolian Fault Zone	7.1	4.5	20.1	0.56	2.74
5	Yazyurdu-Goksun Fault Zone	7	4.5	20.27	1.008	3.431
6	Bachground Inner 3	5.4	4.5	6.67	0.075	2.197
7	Bachground Inner 4	5.4	4.5	22.22	0.636	2.625
8	Background north	5.8	4.5	18.51	0.738	3.27
9	Bachground Inner 5	5.6	4.5	36.62	1.996	2.395

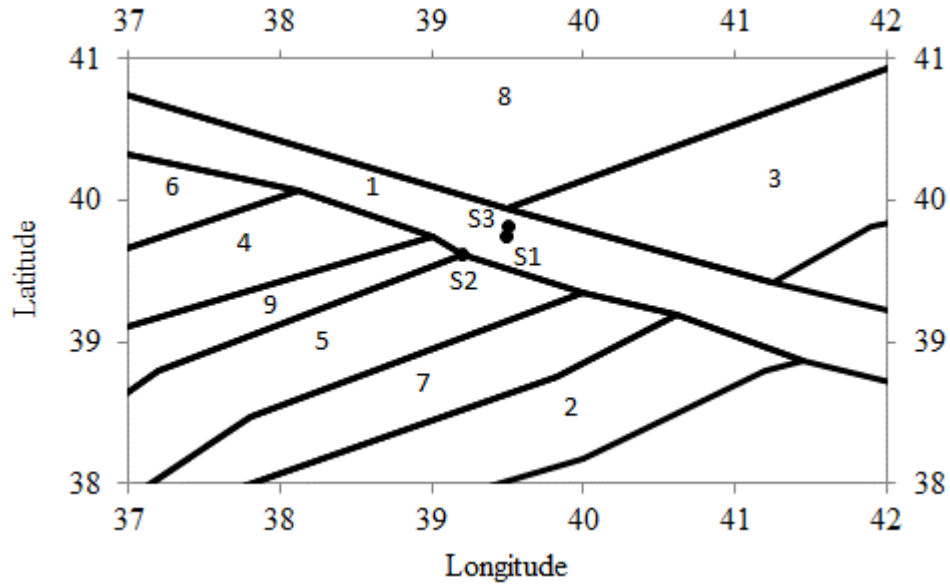


Figure 3.2. Locations of seismic zones which are defined in Table 3.2. The three sites (S1, S2 and S3) in this study are shown with solid circles.

In Table 3.2, λ is activity rate of each seismic zone which is defined as annual rate of earthquakes with magnitudes larger than or equal to minimum magnitude (M_{min}). This λ parameter is modified in this study according to the area percentage of each seismic zone inside the effective area. β is Gutenberg-Richter recurrence parameter of each seismic zone.

3.2.2 Methodology

In this thesis, a novel approach is proposed for generating UHS using a stochastically-generated catalog and simulated ground motions. This approach allows to generate a complete catalog and to simulate ground motions of regional character. In this section, initially, the proposed methodology will be described in detail followed by an application in Erzincan to generate the regional UHS. Next, in Section 3.2.3, results will be compared to those of classical PSHA.

As the first step of the methodology, the events are distributed within certain time spans using Monte Carlo simulation method. This approach is defined as a controlled selection of a random number from a probability distribution. The number of

earthquakes within a specified time span related to each seismic zone is obtained assuming Poisson distribution (Wu and Wen, 2000):

$$\sum_{x=0}^{n_k-1} \frac{(tv_k)^x}{x!} \exp(-tv_k) < u_k \leq \sum_{x=0}^{n_k} \frac{(tv_k)^x}{x!} \exp(-tv_k) \quad (3.1)$$

where v_k is the activity rate of k^{th} seismic zone, n_k is the number of earthquakes inside k^{th} seismic zone, t is the time span which is taken as 10 years herein and u_k is a random number between 0 and 1 with uniform distribution. These simulations are repeated until a complete catalog is acquired. In this study, 1000 simulations are used so the catalog period is 10000 years. Previously, Wu and Wen (2000) discussed 9000 simulation years to be adequate for a similar application. After identifying the total number of events, magnitude of each event is calculated through Gutenberg-Richter recurrence model:

$$\log(N) = a - bM \quad (3.2)$$

where N is the number of earthquakes with magnitude larger than M ; a and b are recurrence parameters corresponding to each seismic zone. b is proportional to β parameter in Table 3.2 ($b = \beta / \ln(10)$).

The epicenters of events are distributed randomly inside each seismic zone. For this purpose, two random numbers for latitude and longitude are generated inside the borders of each seismic zone. A random number within the seismogenic depth is generated for the depth parameter related to small events. On the other hand, for large events ($M_w \geq 6$) surface rupture is considered. Figure 3.3 shows distribution of epicenters inside effective area for a catalog period of 3000 years related to Site 1.

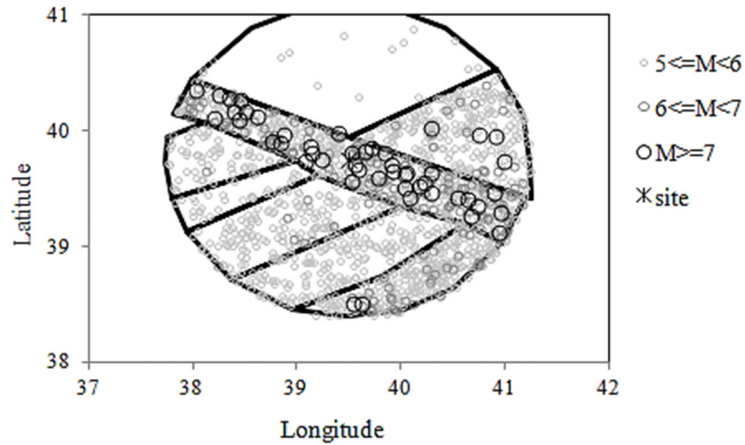


Figure 3.3. Distribution of events in 3000-year stochastic earthquake catalog related to Site 1

Next, ground motion time histories due to seismic waves propagating from each source to the site of interest, are simulated. The ground motions of events that occur on fault zones are modeled using stochastic finite-fault model based on dynamic corner frequency proposed by Motazedian and Atkinson (2005). For areal seismic zones, stochastic point-source method is used following the approach outlined in Boore (2003). The formulations related to both models were described extensively in Chapter 2. Point-source model is mostly preferred when dimensions of the source are negligible with respect to distance to site (Boore, 2009). This point is taken into account in this study for areal seismic zones that are far away from the sites with relatively smaller magnitudes ($M_w \leq 5.8$). SMSIM computer program is used to model point-source ground motion simulations.

In this study, through the simulations, local seismicity parameters are taken into account in hazard calculations, which is not the case in classical PSHA. Model for geometric spreading, quality factor, high frequency decay factor and ground motion duration are taken from Askan et al. (2013). The authors validated the aforementioned parameters by simulating records of the 13 March Erzincan 1992 ($M_w = 6.6$) earthquake. Table 3.3 defines local seismicity parameters which are used as inputs to the simulations in this study.

Table 3.3. Seismic parameters which are used in this study as inputs
(Adopted from Askan et al., 2013)

Parameter	Value
Crustal shear wave velocity	3700 m/s
Rupture velocity	3000 m/s
Crustal density	2800 kg/m ³
Pulsing area percentage	50
Quality factor	$Q = 122f^{0.68}$
Geometrical spreading	$R^{-1.1} \quad R \leq 25 \text{ km}$ $R^{-0.5} \quad R > 25 \text{ km}$
Duration model	$T = T_0 + 0.05R$
Windowing function	Saragoni-Hart
Kappa factor	Regional kappa model ($\kappa_0=0.066$)

In addition to those given in Table 3.3, following models and parameters are employed in the simulations: Generic soil site amplification based on local Vs30 values measured in the region is used in this section (Boore and Joyner, 1997). This approach is explained extensively in Section 3.3.2 and challenged later in this Chapter. Regarding the source parameters, rupture dimensions are estimated from empirical relationships defined by Wells and Coppersmith (1994). Stress drop is estimated from empirical relations in Mohammadioun and Serva (2001) that relate its value to rupture dimensions as follows:

$$\Delta\sigma = 8.9 \times W^{0.8} \quad (3.3)$$

where W is rupture width. It must be noted that Equation 3.3 is valid for stress drops less than 100 bars. Stress drop becomes constant after $\Delta\sigma=100$ bars according to Mohammadioun and Serva (2001). Stress drop of point-source model is assumed as 1.5 times the corresponding value of finite-fault model according to the analyses presented in Section 2.4.

Finally, EXSIM computer program is used to model extended faults (Motazedian and Atkinson, 2005). This program has some limitations especially while modeling ground motion duration and phases. However it is currently the most effective approach for stochastic ground motion simulation and it has been used widely by researchers worldwide (e.g: Ugurhan and Askan, 2010; Nicknam et al., 2010; Demartinos and Faccioli, 2012; Chopra et al., 2012; Ugurhan et al., 2012; Ghofrani et al., 2013).

The stochastically-generated ground motion catalog is one of the important achievements in this study. In addition to being temporally and spatially complete, this catalog is based on regional seismic wave propagation characteristics. The developed ground motion catalog is useful for several research areas in addition to the proposed approach in this study. The most important applications of this catalog might be derivation of regional ground motion prediction equations and ground motion selection for structural time history analyses.

As the final step, response spectra of each simulated ground motion are calculated for a period range. Then ground motion amplitudes related to each period are sorted from largest to smallest, the first value has annual exceedance rate of $1/n$, the second value has annual exceedance rate of $2/n$ and so on, where n is catalog period in terms of years. The ground motion amplitudes related to the same annual exceedance rate for the entire period range yields site-specific UHS. The same approach for calculation of annual exceedance rate was also effectively employed by Assatourians and Atkinson (2013).

3.2.3 Initial Results of the Proposed Methodology and Comparisons with Results from Classical PSHA

Figures 3.4, 3.5 and 3.6 show hazard curves in terms of PGA and PSA (at selected period values of $T=0.1, 0.2, 0.5, 0.7, 1.0, 1.5$ and 2.0 seconds) as well as uniform hazard spectra of 2%, 10% and 50% exceedance probability in 50 years for Site 1, Site 2, and Site 3, respectively. The corresponding results from the proposed study are compared with results of classical PSHA. The GMPE by Akkar and Bommer (2010) is used for classical PSHA application herein because it is among the most suitable models derived using the Turkish ground motion database (Kale and Akkar, 2013).



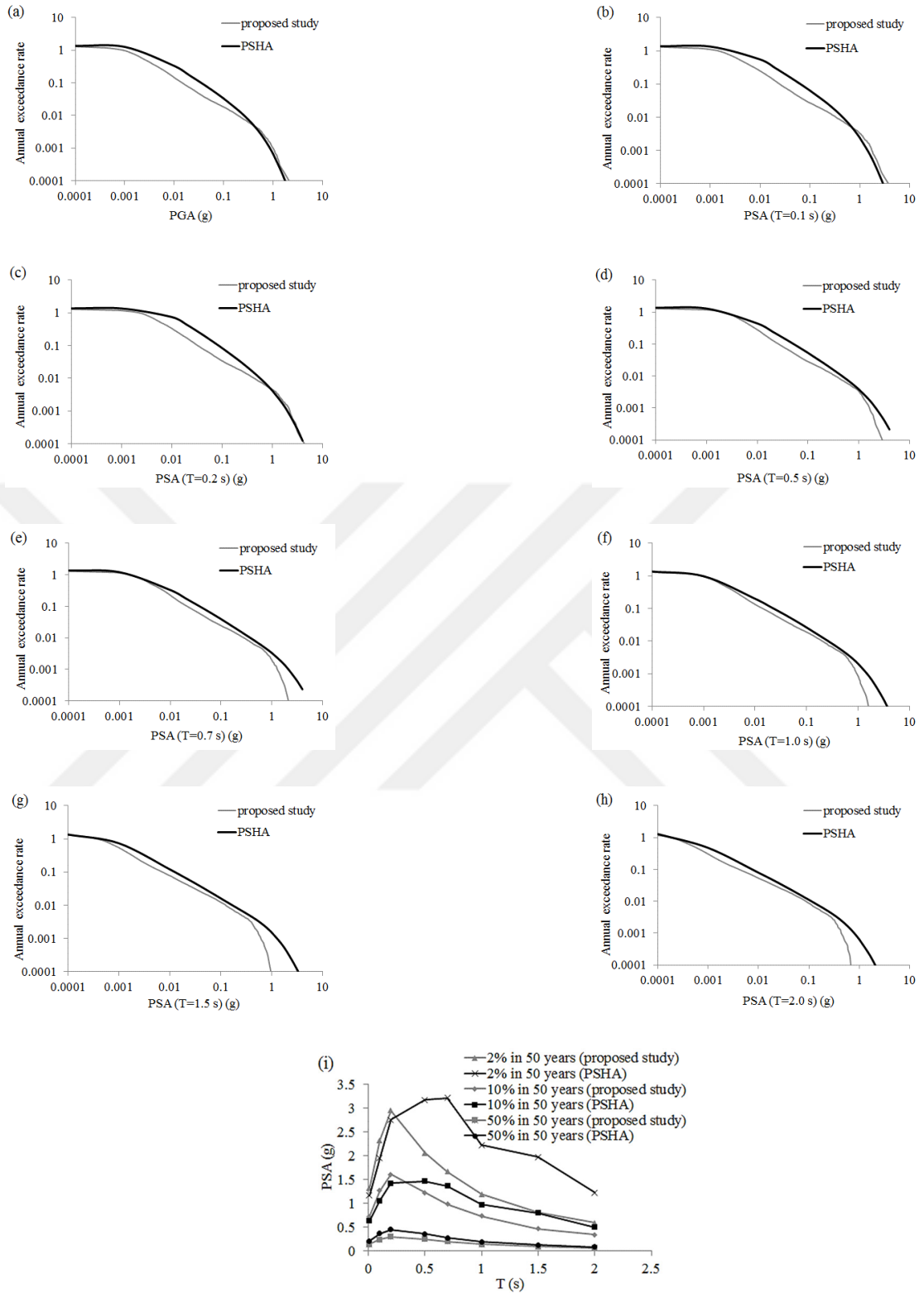


Figure 3.4. Hazard curves for a) PGA b) PSA (T=0.1 s) c) PSA (T=0.2 s) d) PSA (T=0.5 s) e) PSA (T=0.7 s) f) PSA (T=1.0 s) g) PSA (T=1.5 s) h) PSA (T=2.0 s) and i) UHS of proposed study and classical PSHA for Site 1

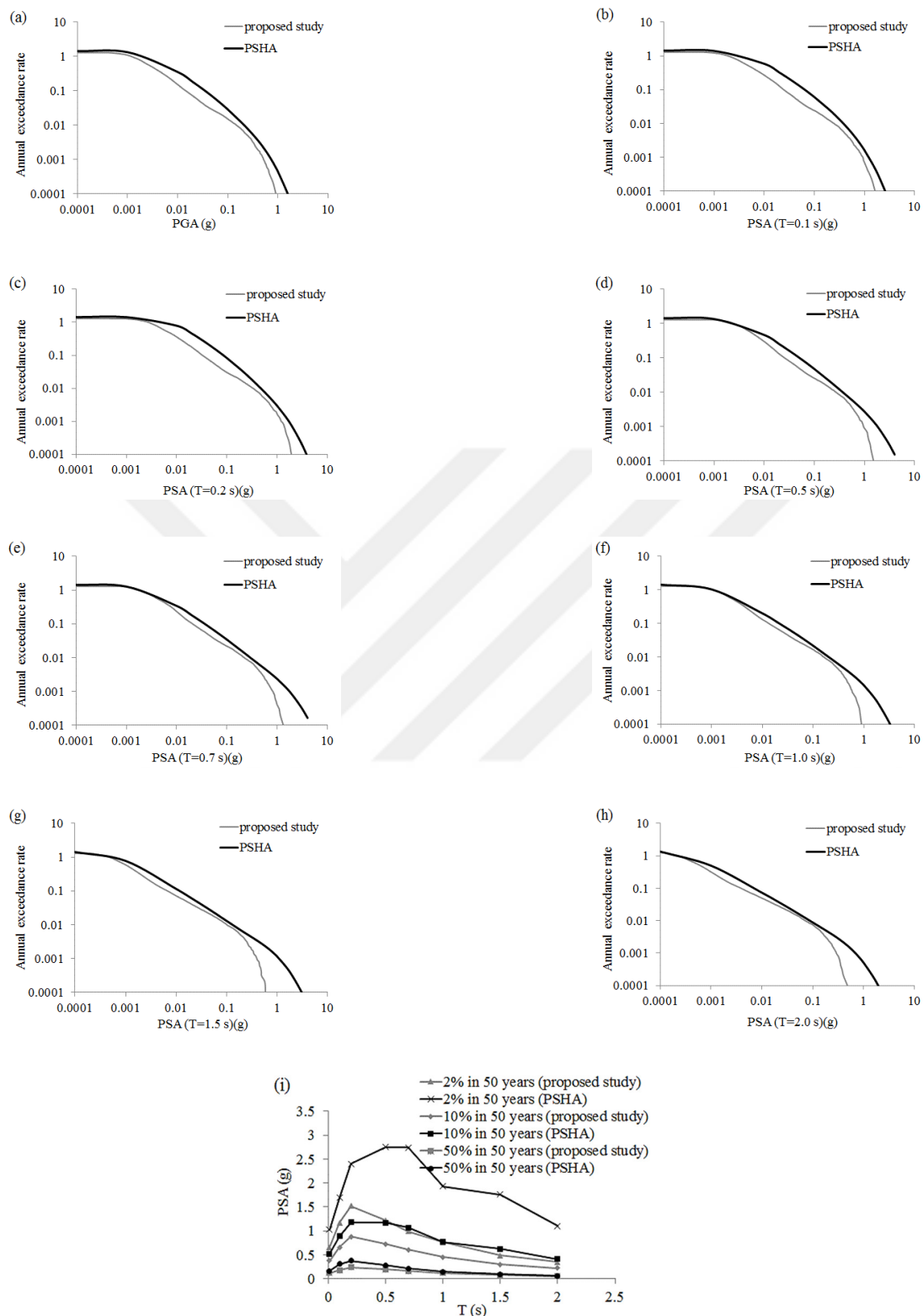


Figure 3.5. Hazard curves for a) PGA b) PSA (T=0.1 s) c) PSA (T=0.2 s) d) PSA (T=0.5 s) e) PSA (T=0.7 s) f) PSA (T=1.0 s) g) PSA (T=1.5 s) h) PSA (T=2.0 s) and i) UHS of proposed study and classical PSHA for Site 2

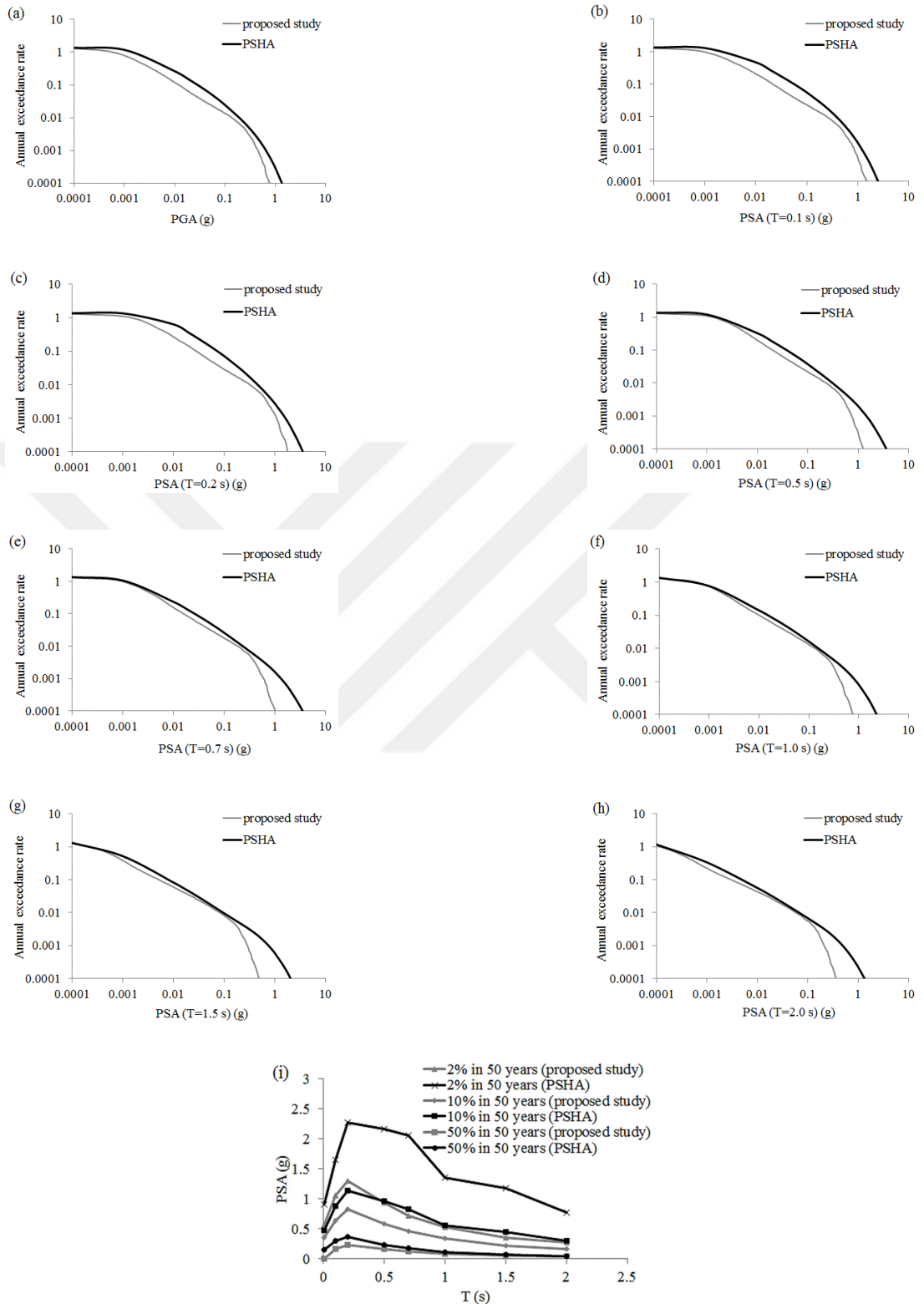


Figure 3.6. Hazard curves for a) PGA b) PSA (T=0.1 s) c) PSA (T=0.2 s) d) PSA (T=0.5 s) e) PSA (T=0.7 s) f) PSA (T=1.0 s) g) PSA (T=1.5 s) h) PSA (T=2.0 s) and i) UHS of proposed study and classical PSHA for Site 3

In Figure 3.4, the ground motion amplitudes obtained from the proposed study are observed to be slightly larger than PSHA for lower annual exceedance rates (2% and 10% in 50 years) and lower periods (lower than 0.5 s). However classical PSHA produces larger ground motion amplitudes for higher annual exceedance rates (higher than 10% in 50 years) within the whole period range. As period increases, hazard curves from the proposed method and PSHA converge to each other for higher annual exceedance rates while they diverge from each other for lower annual exceedance rates.

It is observed from Figure 3.5 that at Site 2, classical PSHA yields larger PSA values compared to those from the proposed method for the entire period range and the whole hazard levels contrary to Site 1 which had an exception for low periods and low annual exceedance rates. There seems a remarkable difference between two approaches especially for the 2475-year return period in the longer period range. As period increases, the differences between two approaches become more evident for low annual exceedance rates while the difference is not as obvious for high annual exceedance rates.

The results related to Site 3 in Figure 3.6 are similar to Site 2, as PSHA produces considerably higher ground motion amplitudes than proposed study especially for 2% in 50 years. Similarly, hazard curves of two methods become consistent for higher annual exceedance rates and become far apart for the lower annual exceedance rates, as period increases.

As it was mentioned previously, Site 1 differs from Site 2 and Site 3 in that low-frequency ground motion amplitudes of the proposed study are slightly larger than the corresponding values of classical PSHA for lower annual exceedance rates. This observation is resulted from saturation of high-frequency ground motion at short distance related to GMPEs. As a definition of saturation, the increase of high-frequency spectral ordinates with magnitude, at short distance is less than that at long distance. In addition to its close distance to NAFZ, Site 1 is located on soft soil hence it is associated with major events which cannot be predicted by GMPEs effectively. Another reason of this discrepancy is the amplified simulated high-frequency ground motion at close distance which is highlighted by Assatourians and Atkinson (2007).

Assatourians and Atkinson (2007) refer to the existence of high-frequency near-field pulses as an inherent property in finite-fault simulation approach.

Overall, traditional PSHA yields larger ground motion amplitudes than the proposed methodology due to large aleatory variability of GMPE (sigma) as well as the wide range of standard deviations involved in PSHA (-3 to +3 standard deviations). This wide range of aleatory variability (both sigma and standard deviations) leads to overestimated spectral ordinates of classical UHS which is also addressed by several researchers (e.g.: Naeim and Lew, 1995; Baker, 2011). The main reason for considering this wide range of aleatory variability is the current simplifying assumptions in GMPE. One of the simplifying assumptions is that GMPEs produce a single spectral ordinate for an earthquake scenario without considering seismic wave propagation characteristics. Another simplifying assumption is related to simple and general seismological parameters involved in GMPE (such as magnitude and distance). According to the above discussions, ground motion simulation is believed to compute ground motion amplitudes in a physical manner without any need to insert large aleatory variability in seismic hazard calculations.

In order to observe the variance of simulated ground motions from the corresponding median values for Site 1, Site 2 and Site 3, the number of standard deviations (ϵ) versus simulated GMIPs are plotted in Figures 3.7, 3.8 and 3.9, respectively. The median PSAs are obtained from predictive equations of Akkar and Bommer (2010).

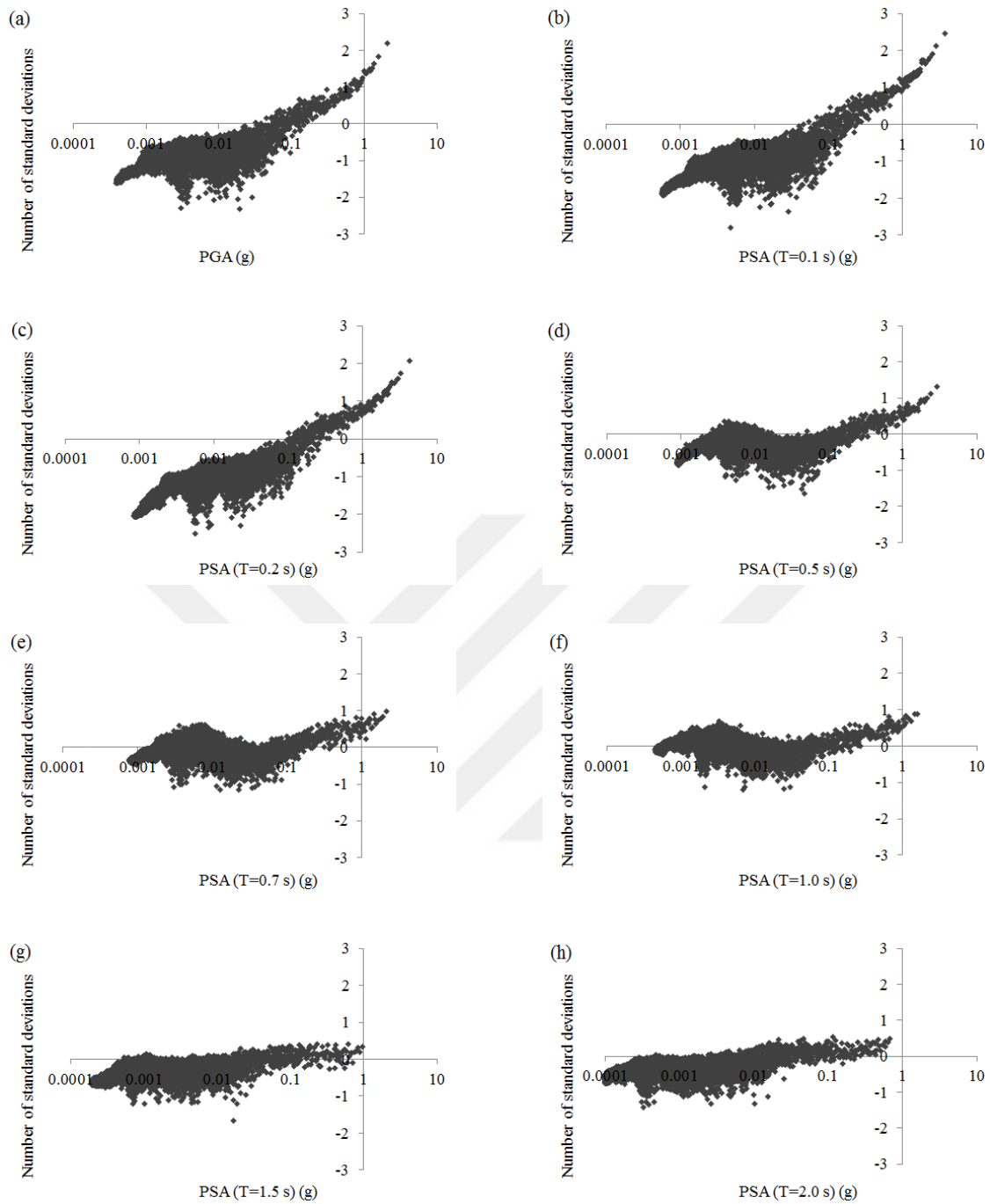


Figure 3.7. Number of standard deviation of simulated GMIPs from the corresponding median values (Akkar and Bommer, 2010) versus simulated GMIPs for a) PGA b) PSA (T=0.1 s) c) PSA (T=0.2 s) d) PSA (T=0.5 s) e) PSA (T=0.7 s) f) PSA (T=1.0 s) g) PSA (T=1.5 s) and h) PSA (T=2.0 s) for Site 1

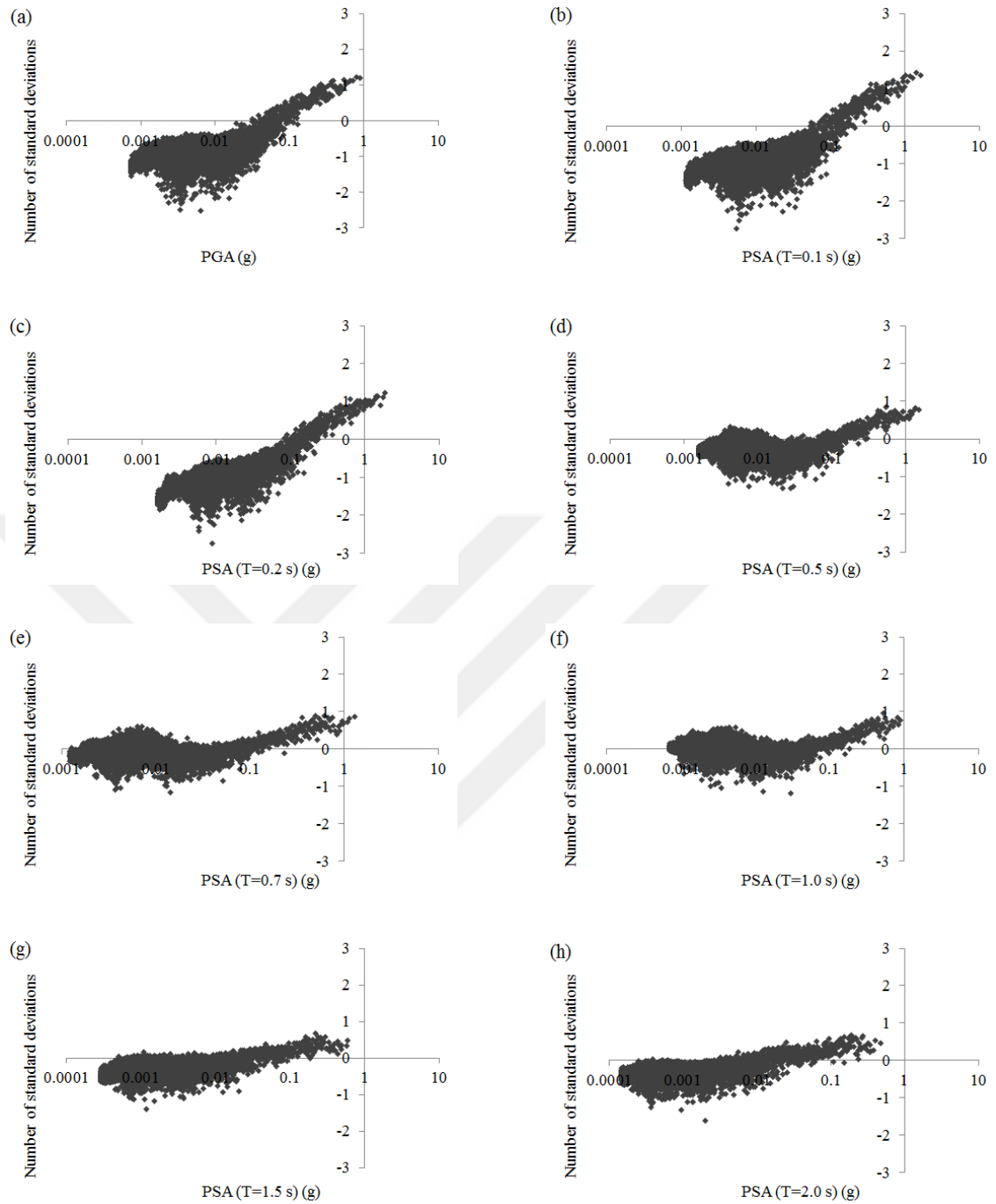


Figure 3.8. Number of standard deviation of simulated GMIPs from the corresponding median values (Akkar and Bommer, 2010) versus simulated GMIPs for a) PGA b) PSA (T=0.1 s) c) PSA (T=0.2 s) d) PSA (T=0.5 s) e) PSA (T=0.7 s) f) PSA (T=1.0 s) g) PSA (T=1.5 s) and h) PSA (T=2.0 s) for Site 2

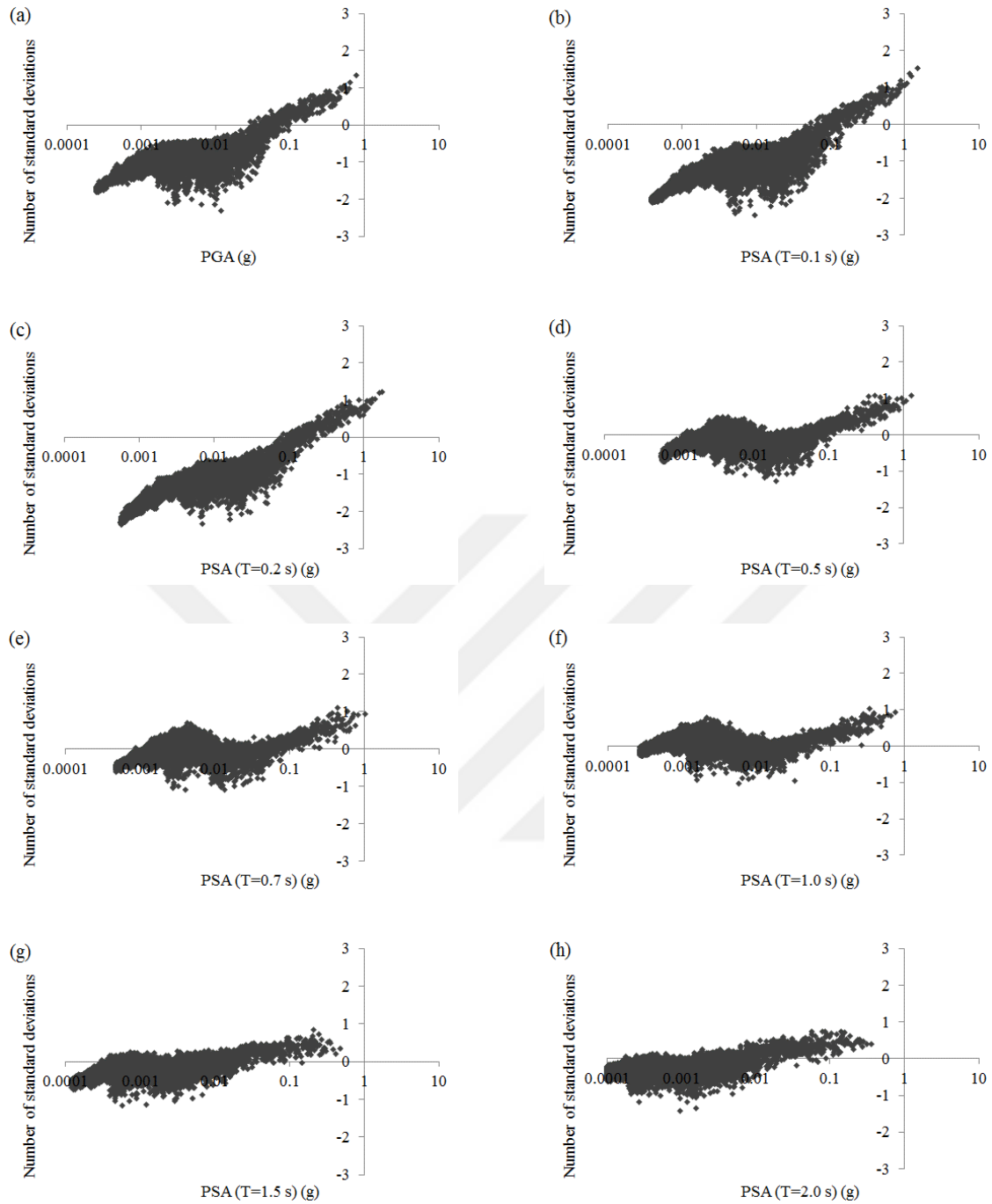


Figure 3.9. Number of standard deviation of simulated GMIPs from the corresponding median values (Akkar and Bommer, 2010) versus simulated GMIPs for a) PGA b) PSA (T=0.1 s) c) PSA (T=0.2 s) d) PSA (T=0.5 s) e) PSA (T=0.7 s) f) PSA (T=1.0 s) g) PSA (T=1.5 s) and h) PSA (T=2.0 s) for Site 3

Figure 3.7 augments the above discussions related to Figure 3.4. It is inferred from Figure 3.7 that synthetic ground motions yield larger spectral amplitudes for larger GMIPs (generally larger than 0.1 g). These higher values refer to major events so the ground motion prediction equations may not predict them efficiently because of the well-known inherent data scarcity from large events. However, this discrepancy seems to be insignificant for larger periods where positive ϵ 's are also observed for smaller PSAs. In other words, the high-frequency ground motions predicted by GMPE saturate at short distance. This observation confirms the previous discussions to some extent. For smaller periods and larger PSA values, ϵ 's of Figure 3.7 are larger than or equal to dominant ϵ of PSHA. For larger periods, however, simulated PSAs for low hazard rates decrease so that ϵ 's of Figure 3.7 become less than the dominant ϵ of PSHA.

Figures 3.8 and 3.9 are similar to Figure 3.7 in terms of the decreasing and increasing trends of ϵ 's with period corresponding to larger and smaller ground motion amplitudes, respectively which clarifies the previous observations regarding hazard curves. The only visible discrepancy is that the number of standard deviations for lower periods and larger amplitudes regarding Site 2 and Site 3 ($\epsilon_{\max}=1.5$) is less than the corresponding value of Site 1 ($\epsilon_{\max}=2.5$).

The observations of Figures 3.4, 3.5 and 3.6 are supplemented by Figures 3.7, 3.8 and 3.9: As period increases, ϵ for all of the three sites increases for lower GMIPs and decreases for higher GMIPs, lying in a plateau around $\epsilon=0$ in the long-period region. As it was mentioned previously, as period increases, the hazard curves from the proposed study become closer to those of classical PSHA for higher annual exceedance rates. On the other hand, the hazard curves from the proposed study become apart from those of classical PSHA for lower annual exceedance rates, as period increases.

The simulated GMIPs related to low hazard rates decrease with period as compared to medians of GMPE due to the following as mentioned previously: saturation of GMPEs, inefficiency of GMPEs regarding major events and amplified high-frequency simulated motions. However, the simulated GMIPs related to high hazard rates increase with period due to the stress drop parameter. These GMIPs are related

to high hazard rates which are associated with minor events resulting in quite small stress drops. This is mainly due to the fact that the stress drop parameter deals with high-frequency portion of simulated ground motions (Aki, 1967).

3.3 Sensitivity of the Proposed UHS

In this section, the effects of near-field forward directivity and alternative site amplification models are inspected on the proposed hazard functions and UHS. The resulted hazard curves and UHS after considering near-field forward directivity and theoretical site amplification factors instead of generic amplification factors are compared with the initial results of Section 3.2.3.

3.3.1 Sensitivity of the Proposed UHS to Near-Field Forward Directivity

In this section, the effect of forward directivity model on hazard functions is investigated for Site 2. Site 2 is selected in this section since it is anticipated to be exposed to potential rupture directivity effects of NAFZ more than two other sites (Figure 3.2). The analytical formulation of Mavroeidis and Papageorgiou (2003) is used to characterize pulse like motion related to near-field scenarios. EXSIM program already has this model implemented as described by Motazedian and Atkinson (2005). Hazard scenarios that are affected by directivity pulses involve rupture distances less than 15 kilometers with epicenters located to the right of Site 2 since NAFZ is a right-lateral strike slip fault zone.

Mavroeidis and Papageorgiou (2003) proposed the following mathematical expression for the acceleration time history of the long-period pulse:

$$a(t) = \begin{cases} -\frac{A\pi f_p}{\gamma} \left[\begin{array}{l} \sin\left(\frac{2\pi f_p}{\gamma}(t-t_0)\right) \times \cos(2\pi f_p(t-t_0)+\nu) \\ + \gamma \sin(2\pi f_p(t-t_0)+\nu) \times [1 + \cos\left(\frac{2\pi f_p}{\gamma}(t-t_0)\right)] \end{array} \right] & t_0 - \frac{\gamma}{2f_p} \leq t \leq t_0 + \frac{\gamma}{2f_p} \\ 0 & \text{otherwise} \end{cases} \quad (3.4)$$

where A , f_p , γ , ν and t_0 are pulse amplitude, pulse frequency, oscillatory character, phase angle and time shift to specify time history peak, respectively. These are the basic input parameters for modeling near-field pulse which are determined by

fitting previously-recorded pulse like ground motions to analytical function in Equation 3.4. Mainshock record at ERC station during the 13 March 1992 Erzincan earthquake displays pulsive behavior mostly in the North-South component (Askan et al., 2013) hence it is used for the calibration of parameters herein.

The parameter t_0 is estimated such that peak of pulse and actual time history occur at the same time. Pulse amplitude, A , is determined in order to make the peak ground velocity (PGV) and peak pseudo-velocity spectrum (PSv) values of analytical pulse consistent with the corresponding values of recorded ground motion. Pulse period, $T_p = 1/f_p$, is calibrated so that peak of PSv from analytical pulse and recorded ground motions occur at the same frequency. Finally, analytical and recorded velocity and displacement time histories are attempted to be fitted in order to estimate γ and ν parameters. It should be noted that the parameters are determined through a simultaneous trial and error process. The calibration method is described extensively in Mavroeidis and Papageorgiou (2003). The final optimized parameters are demonstrated in Table 3.4. Figure 3.10 shows analytical PSv, velocity and displacement time histories using Equation 3.4 and the input parameters listed in Table 3.4 in comparison with the observed motion.

Table 3.4. Input parameters for Mavroeidis and Papageorgiou (2003) analytical pulse model

Parameter	Value
A	80 cm/s
T_p	2 seconds
γ	2.3
ν	180 degrees

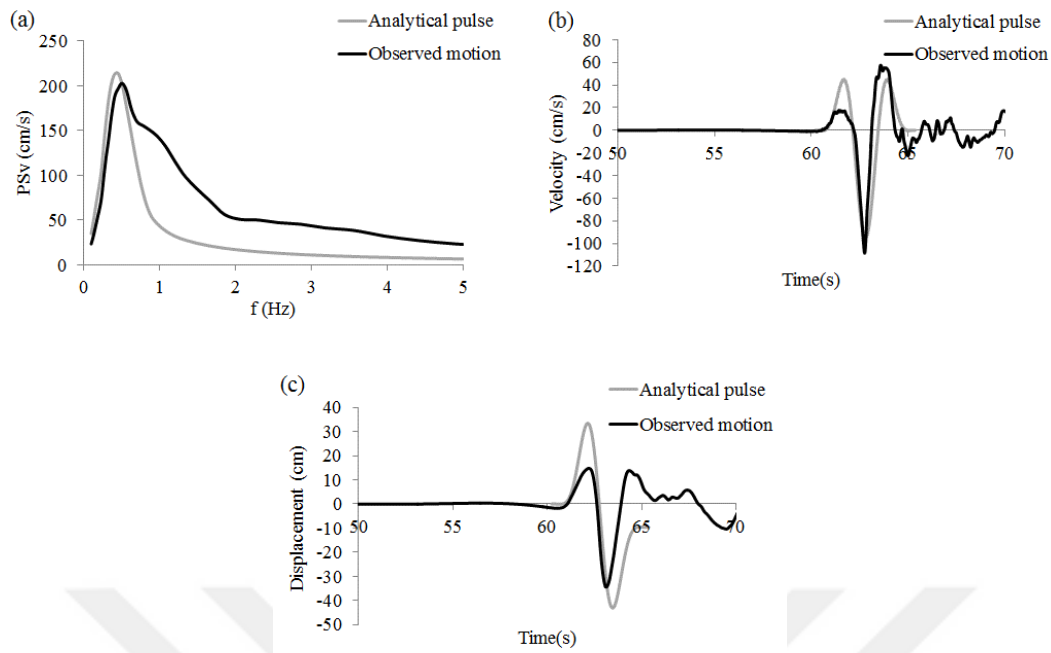


Figure 3.10. Calibration of parameters in Table 3.4 with respect to 13 March 1992 earthquake (ERC recording) in terms of a) PSv, b) Velocity time series and c) Displacement time series

Figure 3.11 exhibits Fourier amplitude spectrum (FAS) and Pseudo-acceleration spectrum (PSa) of observed and simulated ground motions with and without forward directivity. It is clearly observed that simulated ground motion agrees better with the observed one for low-frequency region, after implementing directivity parameters.

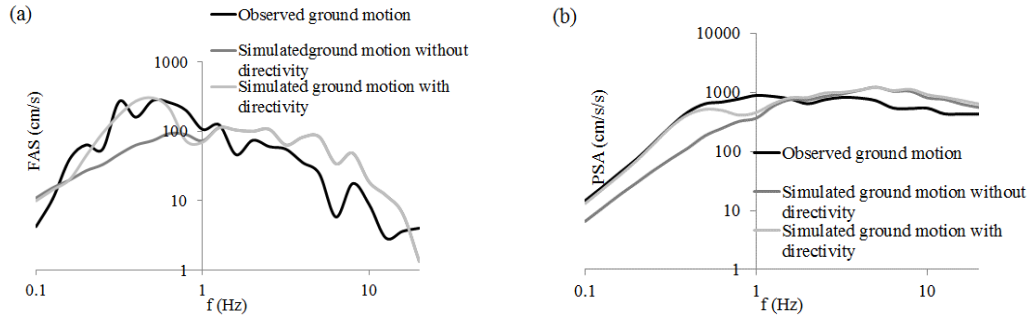


Figure 3.11. Observed and simulated ground motions of 13 March 1992 earthquake (ERC recording) with and without considering forward directivity in terms of a) FAS and b) PSA considering parameters of Table 3.4

It is inferred from Figures 3.10 and 3.11 that, the calibrated pulse parameters in Table 3.4 might be used with certainty in ground motion simulations of Erzincan region. Among the parameters stated in Table 3.4, A and T_p are modified for different scenarios. It is not possible to estimate these two parameters using the aforementioned trial and error procedures for each scenario due to lack of past data in the region. However, as it is highlighted by several authors, pulse period is observed to be dependent on magnitude (Somerville, 1998; Mavroeidis and Papageorgiou, 2003; Shahi and Baker, 2011). Similarly, Mavroeidis and Papageorgiou (2003) expressed a predictive model for pulse period as follows:

$$\log T_p = -2.9 + 0.5M_w \quad (3.5)$$

This relationship is already implemented in EXSIM program. Besides, Mavroeidis and Papageorgiou (2003) pointed to a strong relationship between A and PGV. Hence ground motion prediction models for near-field ground motions can be applied to predict PGV and as a result to predict A .

Somerville (1998) developed the following empirical relationship for PGV using a subset of near-fault recordings on soil sites from earthquakes with moment magnitude (M_w) range of 6.5 and 7 and closest distance (R) range of 3 to 10 kilometers:

$$\log \text{PGV} = -1.0 + 0.5M_w - 0.5 \log R \quad (3.6)$$

Equation 3.6 gives median PGV as 76.59 cm/s for ERC record of the 13 March 1992 Erzincan earthquake. Although median PGV from this model agrees well with A parameter, the model has the limitation of magnitude, distance and site class range.

The other empirical model is defined by Alavi and Krawinkler (2000) which included a little bit wider range of magnitude and distance compared to the previous model. On the other hand, the model underestimates pulse amplitude of the above-mentioned scenario ($\text{PGV}_{\text{median}}=69.29$ cm/s). The functional form of this predictive model is as follows:

$$\log \text{PGV} = -2.22 + 0.69M_w - 0.58 \log R \quad (3.7)$$

Recently, Rupakhety et al. (2012) constructed a more complicated model for PGV with the following mathematical formulation:

$$\begin{aligned} \log \text{PGV} &= -5.17 + 1.98M_w - 0.14M_w^2 - 0.11 \log(R^2 + 0.75^2) \quad M_w \leq 7 \\ \log \text{PGV} &= -5.17 + 1.98(M_w = 7) - 0.14(M_w = 7)^2 - 0.11 \log(R^2 + 0.75^2) \quad M_w > 7 \end{aligned} \quad (3.8)$$

where R is Joyner-Boore distance or epicentral distance. This model produces a considerably low PGV compared to calibrated pulse amplitude ($\text{PGV}_{\text{median}}=44.07$ cm/s).

In their study, Bray and Rodriguez-Marek (2004) proposed two separate predictive models for rock and soil. These models are applicable to moment magnitude range of 6 to 8 and closest distance range of 0 to 15 km. The authors studied a large database for regression analysis. The following formula represents the model for soil conditions:

$$\text{LnPGV} = 4.58 + 0.34M_w - 0.58 \text{Ln}(R^2 + 7^2) \quad (3.9)$$

This model yields an agreeable estimation of median PGV as 71 cm/s at ERC station. Thus, in this study, we estimate PGV from the predictive model of Bray and Rodriguez-Marek (2004) due to the large database involved, large range of moment magnitude and distance in addition to the agreeable estimation of PGV for the ERC

recording of the 13 March 1992 Erzincan earthquake. Figure 3.12 compares hazard curves and uniform hazard spectra (UHS) at Site 2 with and without considering a forward directivity model.



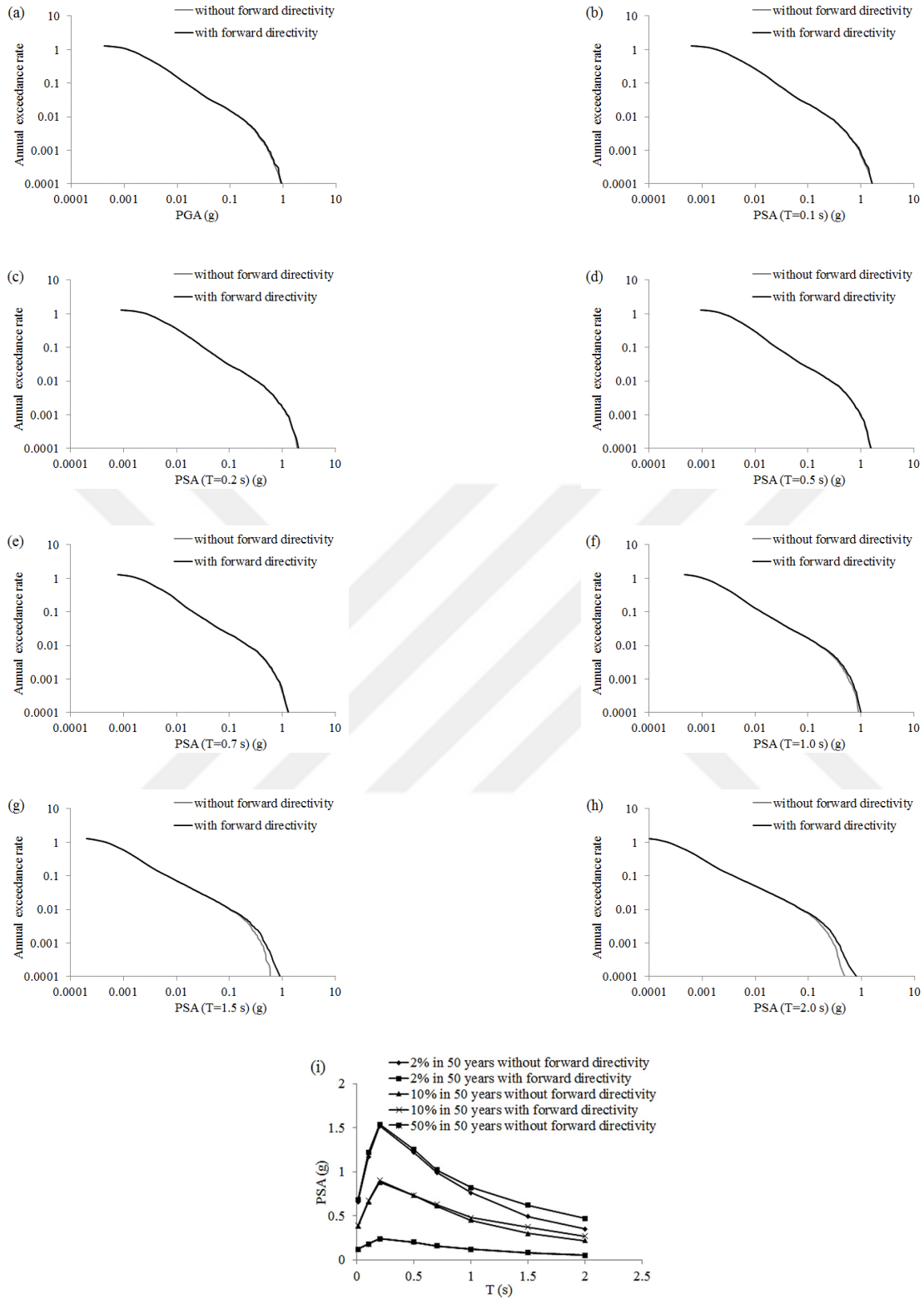


Figure 3.12. Hazard curves for a) PGA b) PSA (T=0.1 s) c) PSA (T=0.2 s) d) PSA (T=0.5 s) e) PSA (T=0.7 s) f) PSA (T=1.0 s) g) PSA (T=1.5 s) h) PSA (T=2.0 s) and i) UHS of proposed study with and without near-field forward directivity for Site 2

It is obvious from Figure 3.12 that near-field pulses tend to increase long-period PSA values for 2% and 10% exceedance probability in 50 years. The results from two approaches display differences that start from 1 second period and increase monotonically with period. The difference is larger for hazard spectra with 2475-year return period compared to that with 475-year one. The increase in spectral amplitudes at T=2 seconds for 2% in 50 years hazard level due to forward directivity is 32% which is consistent with 30% amplification for T=3 seconds and 1500 years given by Abrahamson (2000). In addition, this percentage agrees well with amplification ratios calculated by Shahi and Baker (2011) which varies between 1.1 and 1.4.

Response spectrum is known to be inadequate to characterize directivity (e.g.: Somerville, 1998). Ground motion duration is also affected by pulse like behavior. Besides, duration plays an important role in identifying structural response due to nonlinear degradation (e.g.: Bolt, 1973; Novikova and Trifunac, 1994). Empirical relations were developed to predict duration based on seismic parameters such as magnitude, distance and site class (e.g.: Novikova and Trifunac, 1994; Bommer and Martinez-Pereira, 1999; Kempton and Stewart, 2006). These studies presented the possibility of considering duration in PSHA but none of them calculated duration directly from ground motion time history.

In this study, significant duration is calculated via Arias intensity from the simulated time histories (Arias, 1970):

$$I_A = (\pi/2g) \int_0^{t_d} a^2(t) dt \quad (3.10)$$

where $a(t)$ is acceleration times series, t_d is total ground motion duration. Effective duration is defined for the whole scenarios as time span between 5% and 95% of maximum Arias intensity. Then the scenarios are divided into two categories: ground motions with effective duration less than 10 seconds (i.e. short duration) and above (i.e. long duration). The hazard curves are deaggregated for 2% and 10% exceedance probability in 50 years according to these two groups. Contribution ratios

of ground motions with long duration with respect to these two hazard levels are illustrated in Figure 3.13 with and without taking rupture directivity into account.

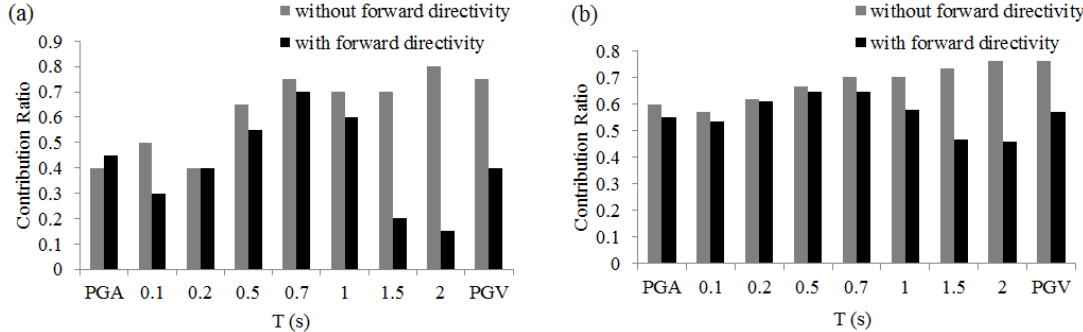


Figure 3.13. Contribution of long duration ground motions in a) 2% in 50 years and b) 10% in 50 years hazard levels for Site 2 with and without considering forward directivity

Figure 3.13 shows that ground motions with long duration are dominant for long-period spectral ordinates without near-field effects. Contribution of long duration is approximately 80% for long-period PSAs and both hazard levels; whereas for short-period ground motion amplitudes, this percentage reduces to about 40% and 60% for 2475 and 475-year, respectively. There is also a monotonic and gradual growth in contribution ratio with increasing periods for 475-year return period.

Forward directivity model leads to a lower contribution ratio of long duration ground motion for periods larger than $T=1$ seconds. There is even less than 20% contribution for 2475 and 40% for 475 return periods in the long-period range. The reason is that forward directivity analytical pulse causes ground motion to release the majority of energy in a short duration. Ground motions with short duration contribute less to 475 return period, since this probability level is less affected by rupture directivity. The same conclusion was derived in terms of UHS in Figure 3.12. However considering the entire period range and both return periods, taking near-fault forward directivity effects into account in simulations lead to shorter ground motion durations. PGV hazard function as well exhibits less contribution of long duration after considering

forward directivity pulse but this contribution ratio is larger than that of long-period spectral acceleration.

3.3.2 Sensitivity of the Proposed UHS to Site Amplification Functions

3.3.2.1 Generic Site Amplification

In the previous sections, generic site amplification factors based on local V_{s30} measurements were used to model site response. This methodology was proposed by Boore and Joyner (1997) applying quarter-wavelength approximation (Joyner et al., 1981). The authors collected data from borehole surveys on rock sites then they calculated frequency-dependent amplification function as follows:

$$A(f(z)) = \sqrt{\rho_s \beta_s / \bar{\rho}(z) \bar{\beta}(z)} \quad (3.11)$$

where ρ_s , β_s are density and shear wave velocity related to source. $\bar{\rho}(z)$ and $\bar{\beta}(z)$ are average density and shear wave velocity related to depth of z . $f(z)$ is the frequency related to depth of z expressed as follows:

$$f(z) = 1/[4 \times S_{tt}(z)] \quad (3.12)$$

where $S_{tt}(z)$ is S-wave time travel to depth of z . Site amplifications from Equation 3.11 were modified using V_{s30} values and predictive equations in order to obtain the corresponding factors for other site classes. It must be noted that this technique does not produce dominant peaks and troughs in amplification function due to disregarding detailed seismic wave propagation within geotechnical layers. Although it provides an agreeable estimate of average amplification response, it may underestimate the response of models with significant velocity gradients (Boore, 2013).

3.3.2.2 Theoretical Site Amplification

One-dimensional (1D) site response analysis is commonly performed at soil sites with known soil profiles to yield amplification factors in terms of theoretical transfer functions. 1D soil layers on an elastic half-space are illustrated in Figure 3.14. The 1D assumption is that, soil layers are horizontally infinite and seismic waves are assumed to move toward only vertical direction.

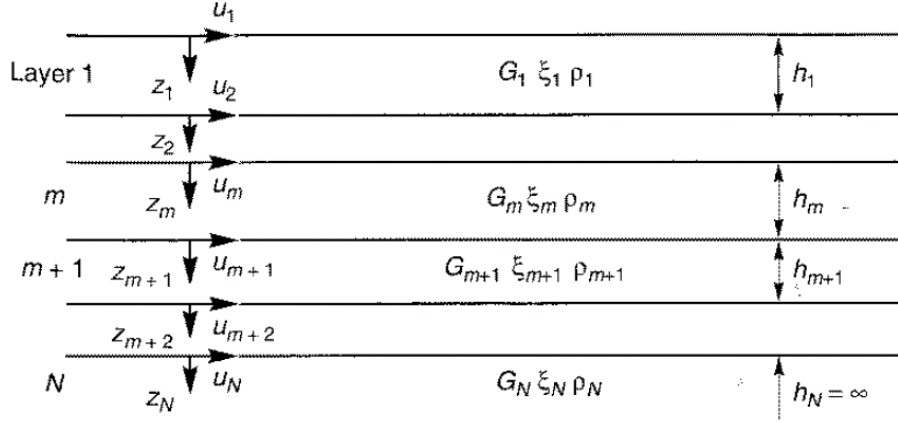


Figure 3.14. 1D soil deposit layers on elastic half-space
(Adopted from Kramer, 1996)

The horizontal displacement of each layer due to vertical S-wave propagation is expressed as follows (Kramer, 1996):

$$u(z, t) = Ae^{i(\omega t + k^* z)} + Be^{i(\omega t - k^* z)} \quad (3.13)$$

where A and B are wave amplitudes toward $-z$ and $+z$ directions, respectively. Due to compatibility of displacement and continuity of shear stress, these parameters at the bottom of each layer must be equal to the corresponding values at the top of the layer below. As a result, amplitudes for layer m become available as a function of amplitudes at the first layer:

$$A_m = a_m(\omega)A_1 \quad (3.14a)$$

$$B_m = b_m(\omega)B_1 \quad (3.14b)$$

The transfer function which is the ratio of displacement between two arbitrary layers of i and j, is obtained from the following:

$$F_{ij}(\omega) = \frac{|u_i|}{|u_j|} = \frac{a_i(\omega) + b_i(\omega)}{a_j(\omega) + b_j(\omega)} \quad (3.15)$$

The whole procedures to calculate transfer function are described thoroughly by Kramer (1996). In this section, SHAKE software (Schnabel et al., 1972) is used to compute frequency-dependent site amplification factors using local soil conditions. Velocity profiles and the geotechnical input parameters of soil layers are obtained via detailed field observations at nine sites in Erzincan within Project TUJJB-UDP-01-12 (Askan et al., 2015). Two different bedrock motions are used as input ground motions in the program with PGAs of 0.002g and 0.4g. These motions are called as small and large input motions, respectively from this point onward. These ground motions are acquired from Turkish National Strong Motion Network (<http://daphne.deprem.gov.tr>).

Among the sites with available velocity profiles, closest nodes to Site 1 and 3 are selected and ground response is computed by making use of the small and large input motions at bedrock level. Figure 3.15 represents the anticipated 1D velocity profiles at Site 1 and 3, which are used in this study. Figure 3.16 shows theoretical amplification functions and the generic ones at Site 1 and 3. To present the full site response, the high-frequency kappa factor is also applied on the amplification factors as shown in Figure 3.16.

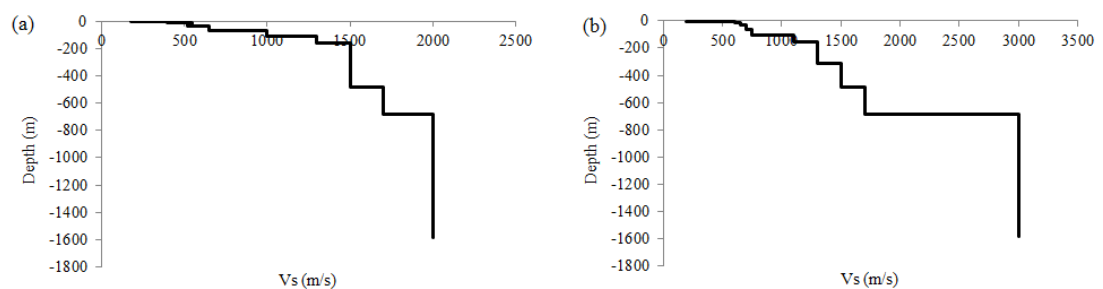


Figure 3.15. 1D Shear wave velocity profile of a) Site 1 and b) Site 3
(Adopted from Askan et al., 2015)

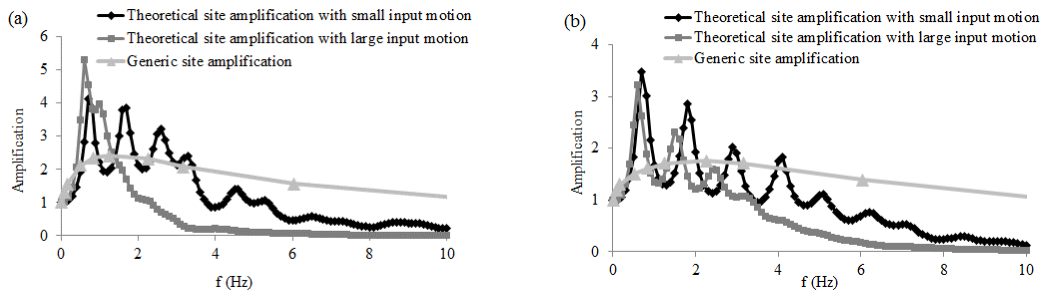


Figure 3.16. Theoretical and generic attenuated site amplification factor as a function of frequency for a) Site 1 and b) Site 3

As expected, generic amplification function corresponds to the average and smoothed form of the theoretical transfer function corresponding to small input motion. Yet, the transfer function displays a completely different trend when the large rock motion is employed as input. It exhibits deamplification for larger frequencies which is addressed as soil nonlinearity in literature (e.g.: Beresnev et al., 1998; Khaheshi Banan et al., 2012). This phenomenon was included in recent NGA attenuation models as well (e.g.: Abrahamson and Silva, 2008). The definition of soil nonlinearity is that, soil amplification becomes less significant for larger ground motion amplitudes and smaller periods.

It is also observed in Figure 3.16 that, site deamplification regarding Site 3 begins at frequencies larger than those at Site 1 since Site 3 is stiffer. Two approaches are followed in this section for calculating hazard spectra to see the effects of including soil nonlinearity in hazard calculations. First, theoretical site response with small bedrock motion is accounted for the whole scenarios (i.e., soil nonlinearity is ignored). Then, theoretical site response of large and small bedrock motions are implemented for scenarios with median PGA larger and smaller than 0.1 g, respectively (i.e., soil nonlinearity is regarded, if present).

3.3.2.3 Results of Hazard Analyses with Theoretical Site Amplification Factors and Comparisons against Results with Generic Amplification Factors

In this section, UHS of Site 1 and 3 are recalculated via theoretical site amplification factors. Figures 3.17 to 3.20 show hazard curves as well as UHS using theoretical site amplification factors with and without soil nonlinearity effects at Site 1 and Site 3. The results obtained in this section are compared with the initial results of Section 3.2.3.



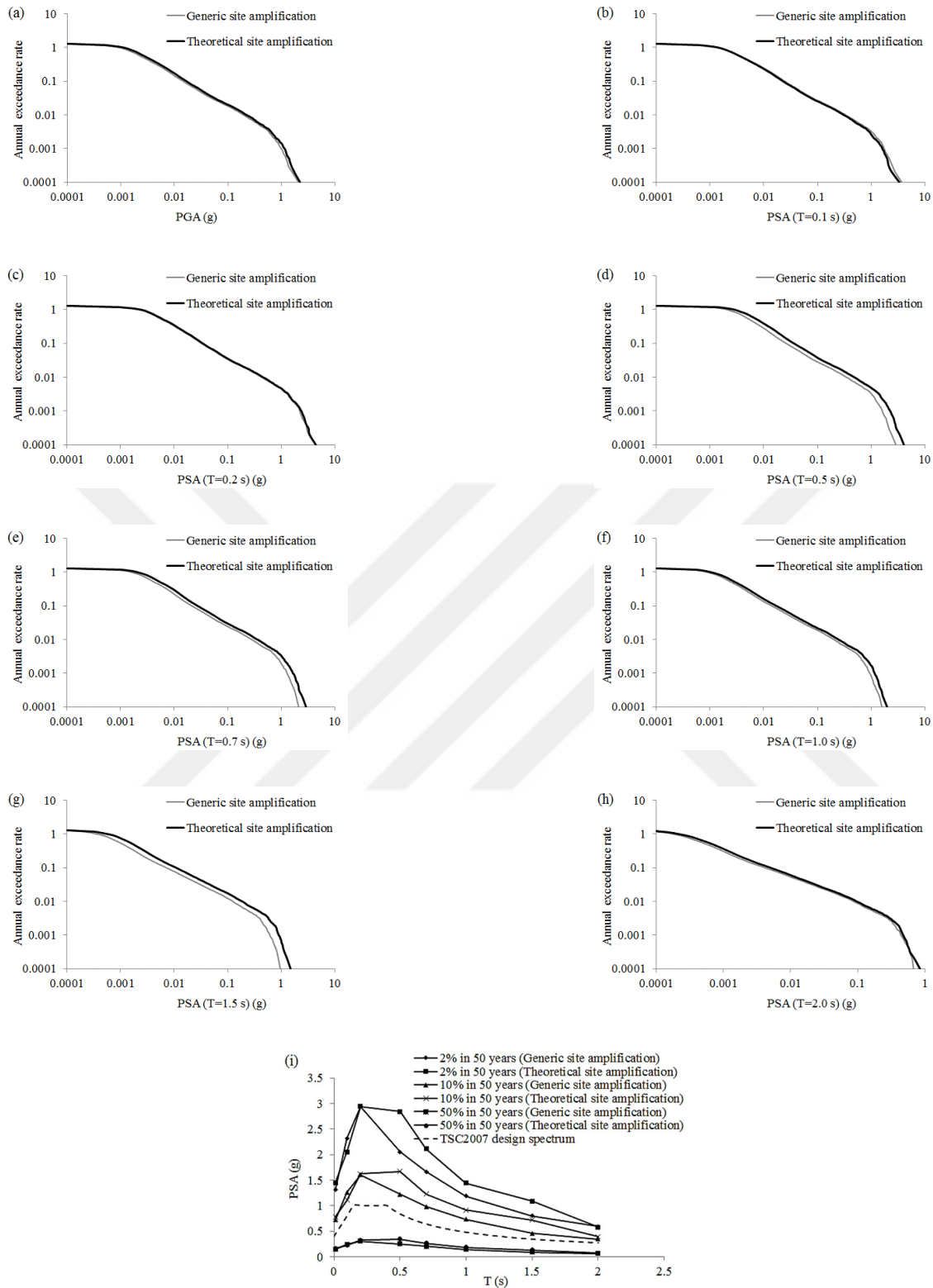


Figure 3.17. Hazard curves for a) PGA b) PSA ($T=0.1$ s) c) PSA ($T=0.2$ s) d) PSA ($T=0.5$ s) e) PSA ($T=0.7$ s) f) PSA ($T=1.0$ s) g) PSA ($T=1.5$ s) h) PSA ($T=2.0$ s) and i) UHS of the proposed study without soil nonlinearity for Site 1

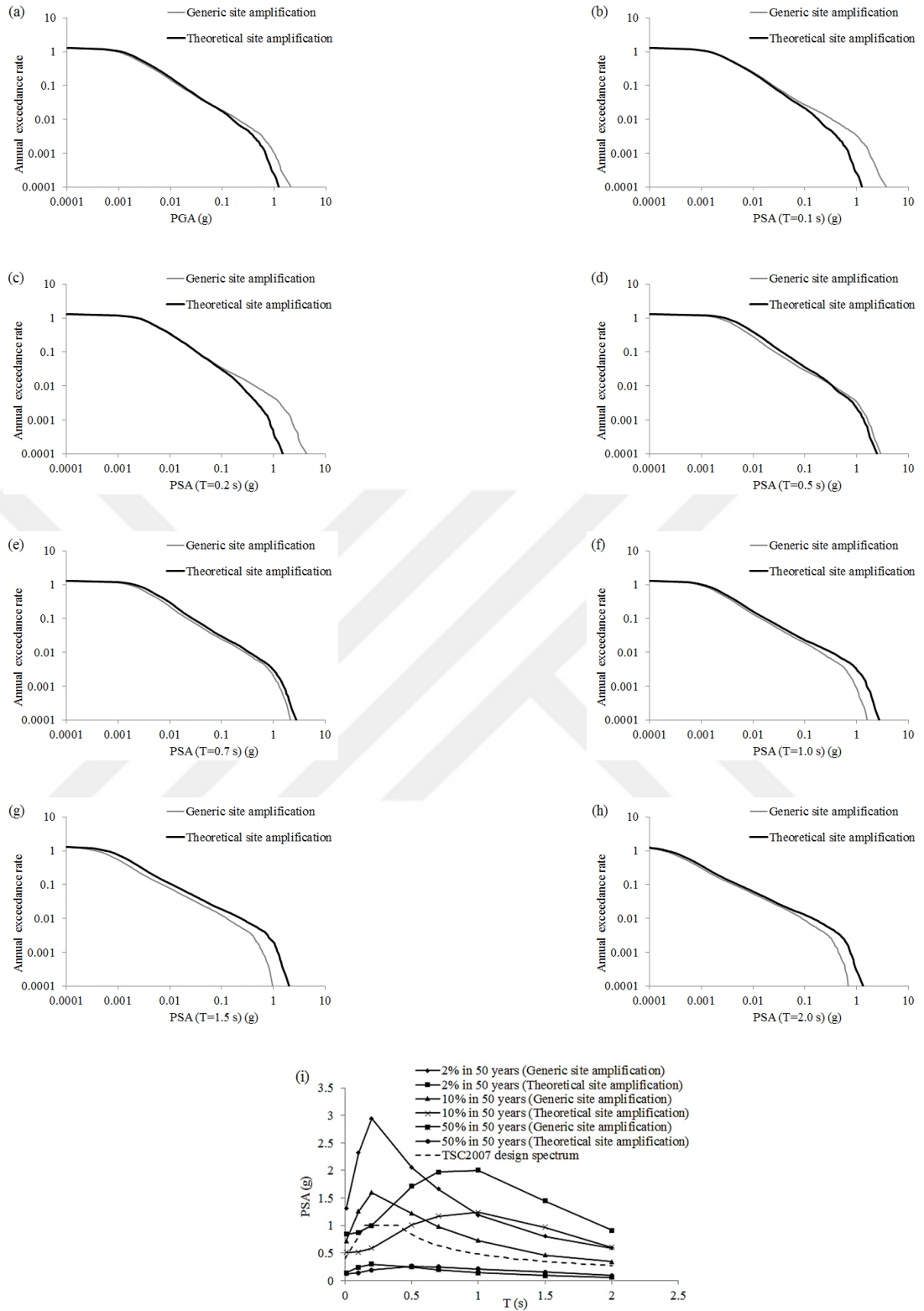


Figure 3.18. Hazard curves for a) PGA b) PSA (T=0.1 s) c) PSA (T=0.2 s) d) PSA (T=0.5 s) e) PSA (T=0.7 s) f) PSA (T=1.0 s) g) PSA (T=1.5 s) h) PSA (T=2.0 s) and i) UHS of the proposed study with soil nonlinearity for Site 1

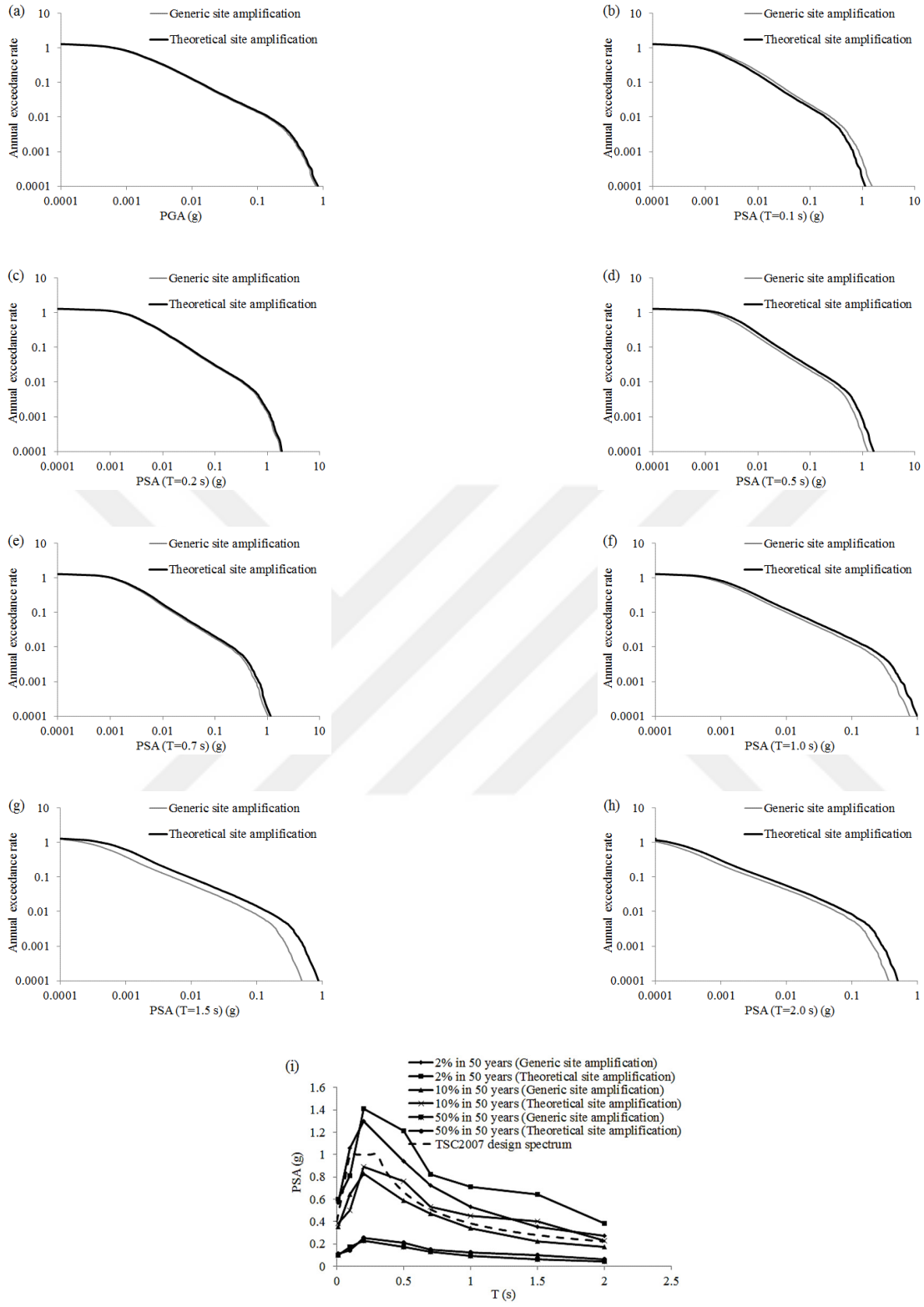


Figure 3.19. Hazard curves for a) PGA b) PSA (T=0.1 s) c) PSA (T=0.2 s) d) PSA (T=0.5 s) e) PSA (T=0.7 s) f) PSA (T=1.0 s) g) PSA (T=1.5 s) h) PSA (T=2.0 s) and i) UHS of the proposed study without soil nonlinearity for Site 3

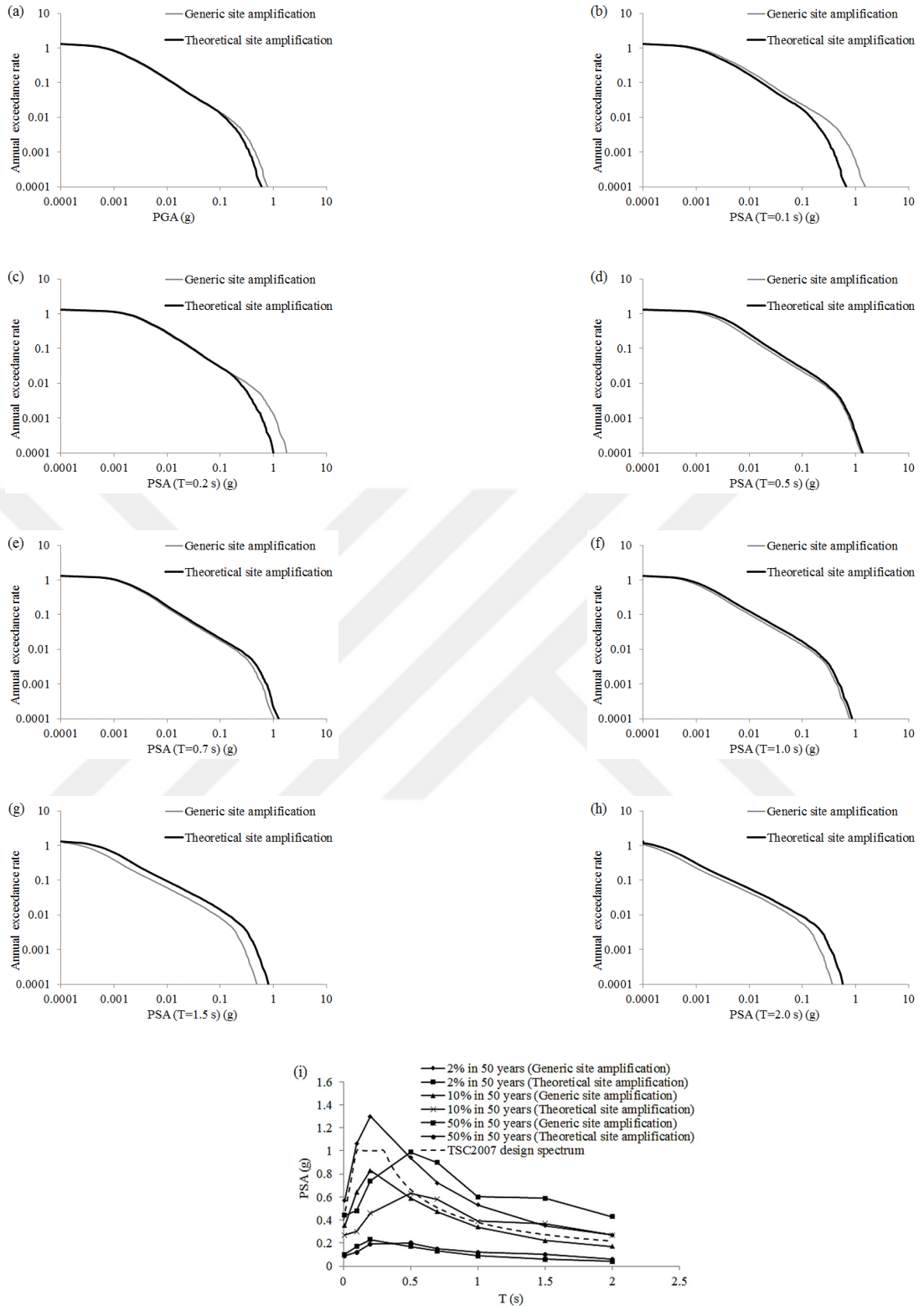


Figure 3.20. Hazard curves for a) PGA b) PSA (T=0.1 s) c) PSA (T=0.2 s) d) PSA (T=0.5 s) e) PSA (T=0.7 s) f) PSA (T=1.0 s) g) PSA (T=1.5 s) h) PSA (T=2.0 s) and i) UHS of the proposed study with soil nonlinearity for Site 3

Theoretical transfer function leads to larger ground motion amplitudes than generic response for larger periods (between 0.2 and 2 seconds) at Site 1 while disregarding soil nonlinearity. The difference between two methods becomes larger for periods around 0.5 and 1.5 seconds since there are obvious peaks in theoretical amplification function around these periods. Generic and theoretical amplifications yield the same results for $T=2$ seconds and slightly different results for $T=0.1$ seconds. These observations are also valid for 2%, 10% and 50% in 50 years exceedance probability levels. Design spectrum of Turkish Seismic Code (TSC, 2007) corresponding to the same site conditions is also illustrated along with UHS in Figures 3.17-3.20. It is observed that the shape of UHS considering the theoretical response is more similar to design spectrum which also corresponds to 10% exceedance probability in 50 years. It is noted that the UHS related to 10% probability of exceedance in 50 years is approximately 50% larger than design spectrum.

Theoretical response considering nonlinearity significantly underestimates the hazard for periods less than 0.6 seconds while it overestimates the hazard for periods above related Site 1. The vast underestimation for smaller periods is the result of deamplification due to soil nonlinearity which was discussed previously. The shape of UHS from this approach differs completely from the code-based spectrum due to this vast underestimation of low-period spectral ordinates. The underestimation of theoretical site model for small periods seems to be more obvious for lower hazard probabilities. This finding augments the concept of soil nonlinearity which is more significant for larger ground motion amplitudes.

The general behavior of the curves at Site 3 is similar to those of Site 1. Theoretical response with small input motion yields amplified GMIPs for periods of 0.2 to 2 seconds which is more obvious for $T=0.5$ and 1.5 seconds. Besides, theoretical site response gives larger spectral ordinates at $T=0.2$ and 2 seconds. Design spectrum and UHS related to 475 years for Site 3 are not as similar as the ones for Site 1 in terms of shape due to the impedance differences between the soil layers at Site 3, but the spectral amplitudes are more consistent for this site. Design spectrum produces larger spectral ordinates than both UHS related to 475 years for periods less than 0.5 seconds and it lies between the two curves for periods longer than 0.5 seconds.

Again the general trend for two sites is similar while considering soil nonlinearity. The underestimation of the theoretical response with respect to generic response for Site 3 is smaller and it terminates at a smaller period than that observed at Site 1. The main reason is that soil nonlinearity for Site 3 is not as dominant. Design spectrum overestimates both 10% in 50 years UHS for periods less than 0.5 seconds and lies between two curves for periods more than 0.5 seconds. Site 3 yields more complex spectra than Site 1 while implementing theoretical site amplification due to the impedance differences between the soil layers at Site 3.

As it was mentioned previously, while disregarding soil nonlinearity, TSC-based design spectrum provides lower spectral ordinates than the corresponding UHS of Site 1 (soft soil). However the code-based design spectral ordinates are more comparable to the corresponding UHS of Site 3 (stiff soil) than that of Site 1. This observation highlights the significance of site amplification function in seismic hazard assessments and seismic design approaches. The spectral ordinates of TSC-based design spectrum remain constant for different site classes which require further modifications. In addition to spectral ordinates, the previous observations put forward the significance of site amplification regarding the shape of spectrum.

This section demonstrates the effect of local site conditions and different amplification models on seismic hazard calculations. The proposed study in this dissertation facilitates implementation of detailed site response inside probabilistic hazard studies. It is difficult, however, to account for such site response models via traditional PSHA as the site parameters are usually coarsely included in ground motion prediction models.

3.4 Ground Motion Selection According to the Proposed UHS

3.4.1 Methodology

In this section, ground motions are selected with respect to the UHS derived in the previous sections. The main objective of the selection and scaling methodologies is to provide suitable ground motions as input for structural time history analysis (e.g.: Ay, 2012). It is important to choose a proper methodology for ground motion selection since it affects structural response. Haselton (2009) divided the selection and scaling methodologies into five groups as follows:

- I. Selecting with respect to magnitude and distance and scaling to target $S_a(T_1)$.
- II. Selecting and scaling with respect to UHS.
- III. Selecting and scaling with respect to CMS.
- IV. Selecting and scaling using proxy for UHS.
- V. Selecting and scaling using inelastic response.

Haselton (2009) investigated all of these approaches in terms of structural response analysis and concluded that the methods which consider spectral matching (group II and III) are advantageous over the other groups. The main reason is that the structure becomes more flexible during time history analysis thus the effective period of structure moves toward longer periods (elongation). This point highlights the significance of spectral shape in ground motion selection. Spectral matching techniques are addressed in several building design codes (i.e. UBC, 1997; ASCE, 2005). The efficiency of spectral matching approach is also confirmed by several other researchers (e.g.: Bommer and Acevedo, 2004; Kottke and Rathje, 2008; Jayaram et al., 2011).

Earlier, Shome et al. (1998) pointed to disadvantage of selection based on magnitude and distance bins (group I). Because seismic risk is related to a combination of different earthquakes rather than the ground motions with a specified magnitude and distance range. The authors then referred to the advantage of S_a as a tool for ground motion selection. Similarly, according to Wu and Wen (2000), ground motion selection with respect to magnitude and distance bins requires deaggregation which is more suitable for a specific structure rather than a building stock.

Ground motion scaling is mostly used to adjust spectral ordinates of the selected recordings according to the target spectrum. The most important disadvantage of scaling is that it artificially suppresses ground motion randomness (e.g.: Jayaram et al., 2011; Ay and Akkar, 2012). Besides, scaling changes spectral ordinate artificially whereas ground motion duration remains constant so it leads to bias (Wu and Wen, 2000; Bommer and Acevedo, 2004). According to Bommer and Acevedo (2004), if the median of selected ground motions are close enough to the target spectrum while selecting via spectral matching approach, there is no need for ground motion scaling. In this thesis, spectral matching technique is preferred to select the ground motions. For this purpose, in this section, sum of squared error (SSE) is calculated for the entire set of simulated ground motion time histories which were generated in

Sections 3.2 and 3.3. Then the ground motions with the smallest SSEs are selected. This approach is effectively implemented in previous similar research (i.g.: Somerville et al., 1998; Jayaram et al., 2011). The SSE is defined as follows:

$$SSE = \sum_{j=1}^p (\ln S_a(T_j) - \ln S_a^{\text{tar}}(T_j))^2 \quad (3.16)$$

where p is number of period values employed, $\ln S_a(T_j)$ is logarithm of spectral acceleration of ground motion at j^{th} period, $\ln S_a^{\text{tar}}(T_j)$ is logarithm of spectral acceleration of target spectrum at j^{th} period. Target spectrum is the UHS from the previous sections for three sites with different directivity and site characterization cases. Four different hazard levels corresponding to 2%, 10%, 20% and 50% exceedance probabilities in 50 years are taken into account. Twenty ground motions are selected for each hazard level.

Due to the large variety of simulated ground motions in this study, it is relatively straightforward to find ground motions whose median is close enough to UHS. This variety of ground motions is one of the significant advantages of the proposed approach. This point is proved by computing root mean square error (RMSE) between median spectrum and target spectrum:

$$RMSE = \sqrt{\frac{1}{p} \sum_{j=1}^p (\ln S_a^{\text{med}}(T_j) - \ln S_a^{\text{tar}}(T_j))^2} \quad (3.17)$$

where $\ln S_a^{\text{med}}(T_j)$ is logarithm of spectral acceleration of median spectrum at j^{th} period.

Kottke and Rathje (2008) explain that 20 selected ground motions with $RMSE \leq 0.05$ provide a proper match to target spectrum and agreeable structural response estimation. In this case, scaling may be skipped therefore the inherent variability of ground motion is preserved. The results related to ground motion selection and their match with respect to UHS are shown and discussed in the next section.

3.4.2 Selected Ground Motions

Figures 3.21 to 3.26 exhibit selected recordings individually for three sites with different modeling techniques and for four hazard levels. Also shown are the median

of selected recordings and target uniform hazard spectra for each case. Table 3.5 shows RMSE for different cases.

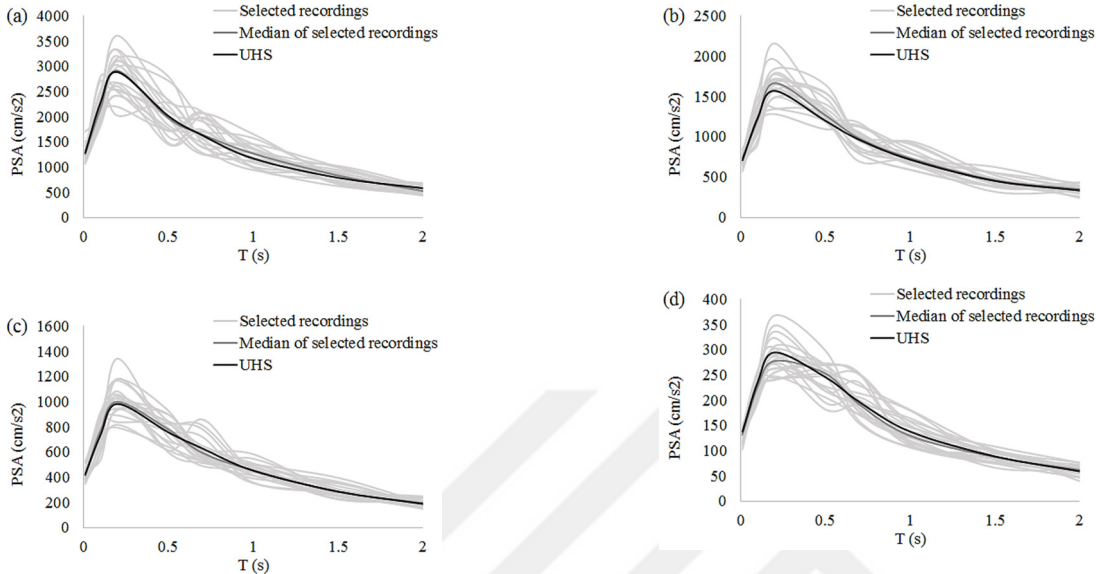


Figure 3.21. Selected recordings, median of selected recordings and UHS related to Site 1 with generic site amplification for return periods of a) 2475 years b) 475 years c) 225 years and d) 75 years

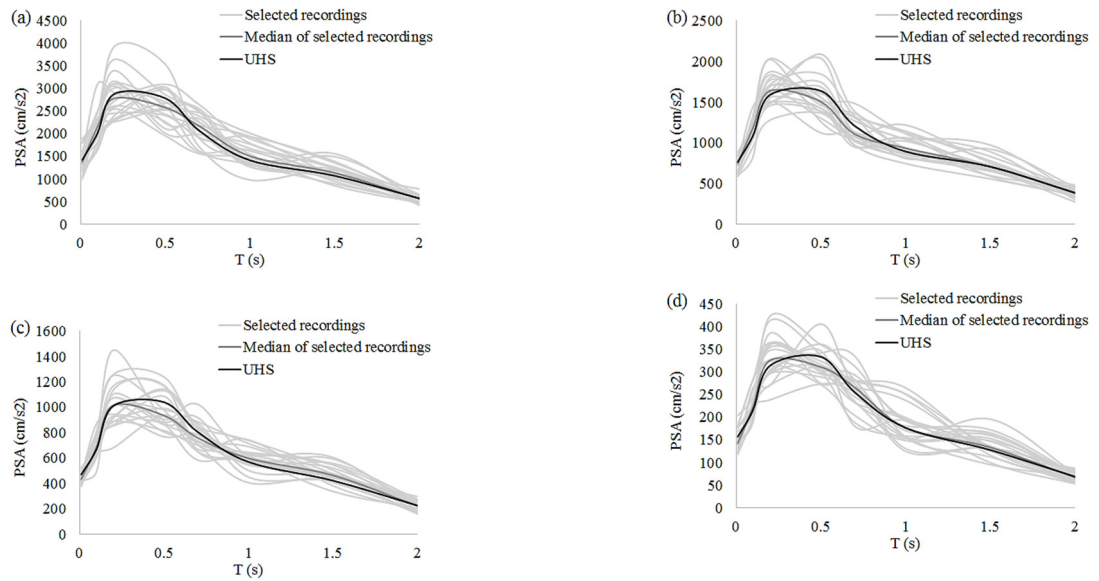


Figure 3.22. Selected recordings, median of selected recordings and UHS related to Site 1 with theoretical site amplification for return periods of a) 2475 years b) 475 years c) 225 years and d) 75 years

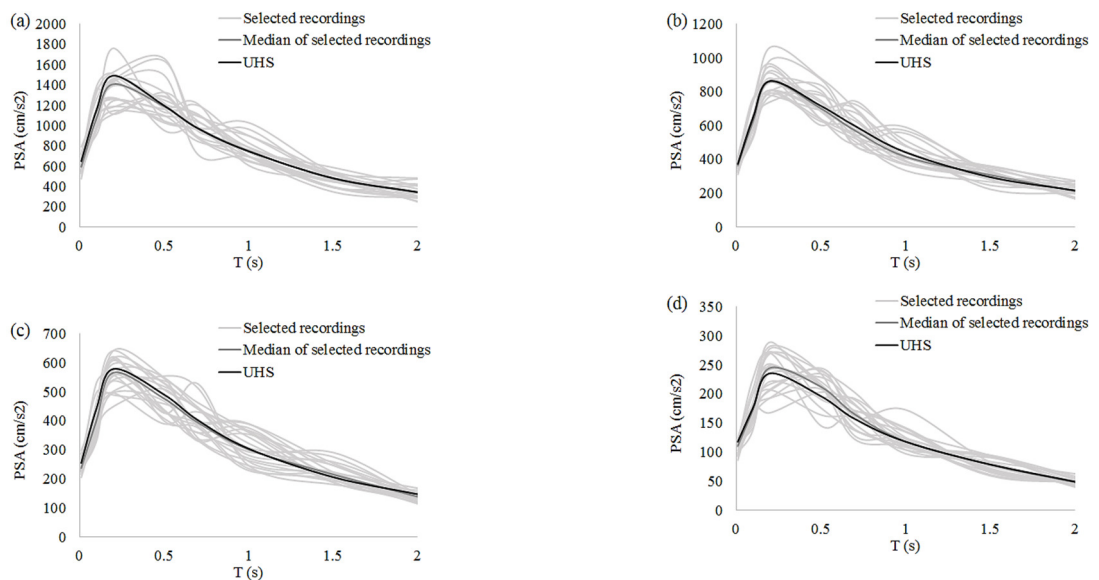


Figure 3.23. Selected recordings, median of selected recordings and UHS related to Site 2 without near-field effect for return periods of a) 2475 years b) 475 years c) 225 years and d) 75 years

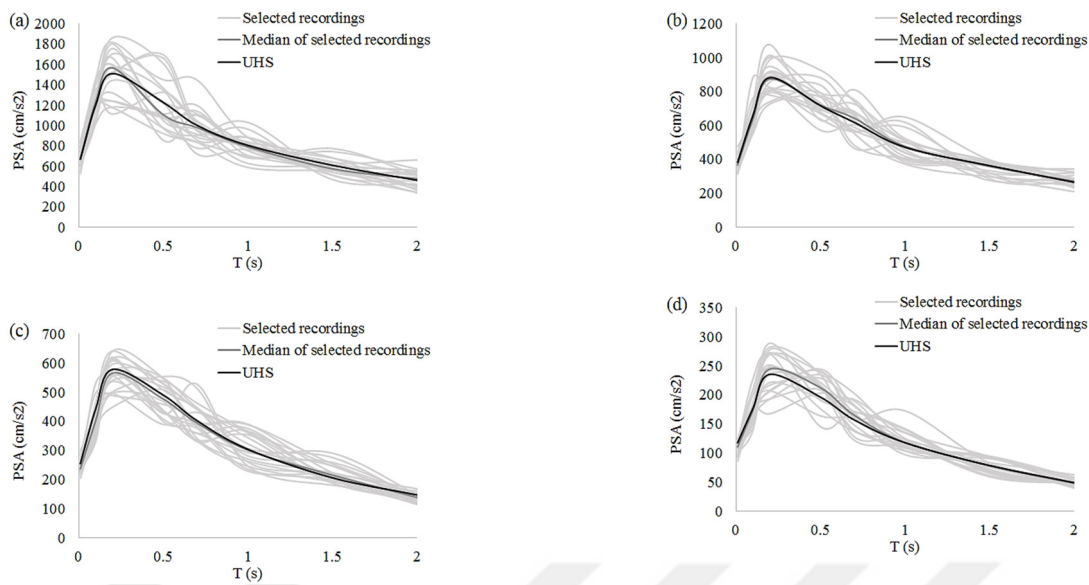


Figure 3.24. Selected recordings, median of selected recordings and UHS related to Site 2 with near-field effect for return periods of a) 2475 years b) 475 years c) 225 years and d) 75 years

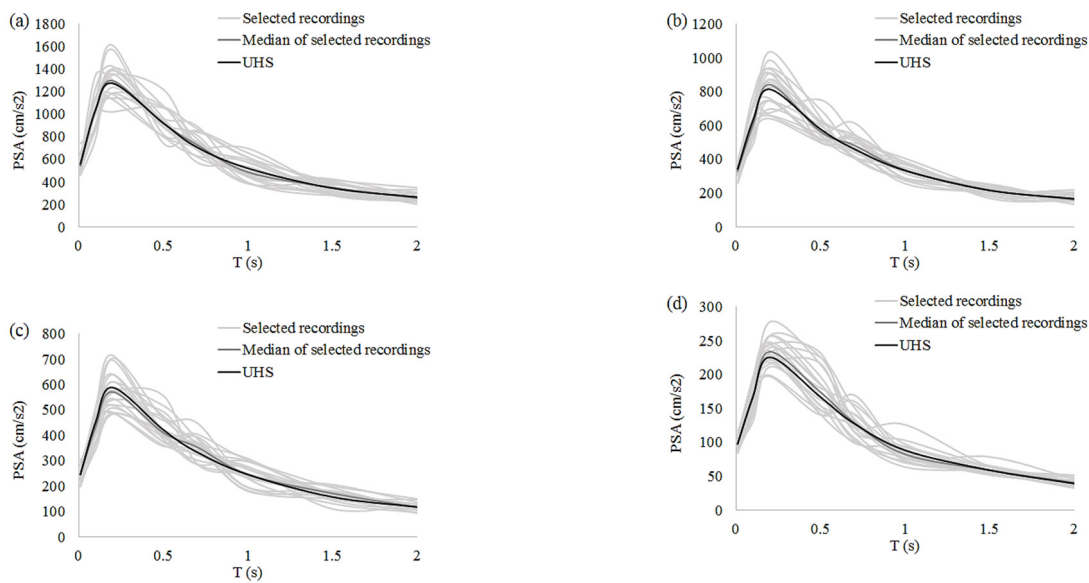


Figure 3.25. Selected recordings, median of selected recordings and UHS related to Site 3 with generic site amplification for return periods of a) 2475 years b) 475 years c) 225 years and d) 75 years

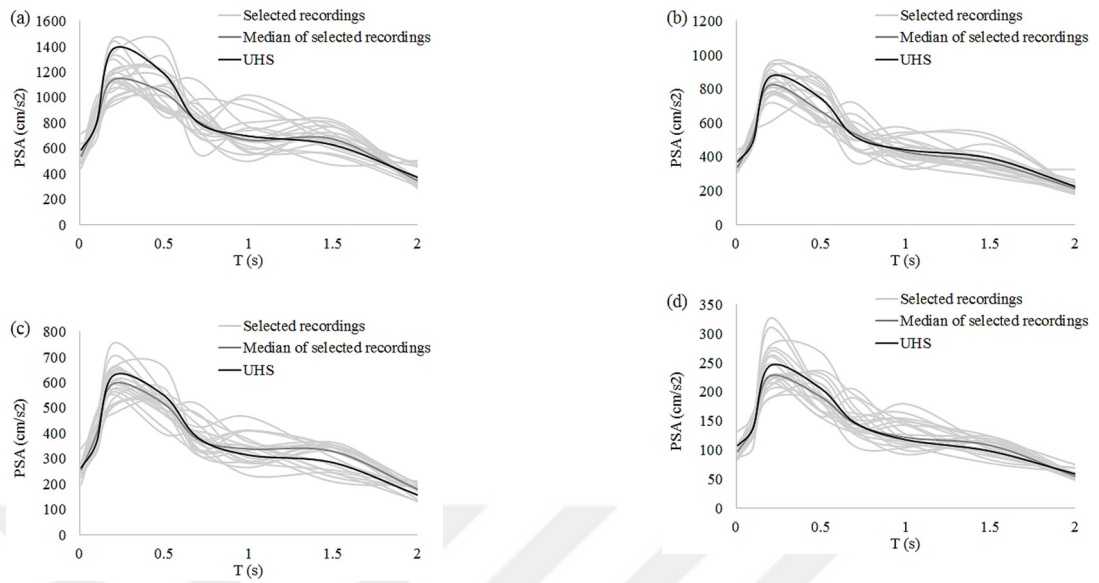


Figure 3.26. Selected recordings, median of selected recordings and UHS related to Site 3 with theoretical site amplification for return periods of a) 2475 years b) 475 years c) 225 years and d) 75 years

Table 3.5. RMSE values for three sites with different modeling methodologies and hazard levels

Site	Case	Return period (years)	RMSE (Eq. 3.25)
1	Generic site amplification	2475	0.050
1	Generic site amplification	475	0.039
1	Generic site amplification	225	0.034
1	Generic site amplification	75	0.042
1	Theoretical site amplification	2475	0.050
1	Theoretical site amplification	475	0.056
1	Theoretical site amplification	225	0.065
1	Theoretical site amplification	75	0.050
2	Without near-field effect	2475	0.045
2	Without near-field effect	475	0.036
2	Without near-field effect	225	0.050
2	Without near-field effect	75	0.044
2	With near-field effect	2475	0.048
2	With near-field effect	475	0.026
2	With near-field effect	225	0.050
2	With near-field effect	75	0.044
3	Generic site amplification	2475	0.033
3	Generic site amplification	475	0.033
3	Generic site amplification	225	0.043
3	Generic site amplification	75	0.034
3	Theoretical site amplification	2475	0.096
3	Theoretical site amplification	475	0.067
3	Theoretical site amplification	225	0.086
3	Theoretical site amplification	75	0.067

It is observed from Figures 3.23 and 3.24 that there is an agreeable match between the median and target spectrum for Site 2. Figures 3.21 and 3.25 also show a consistent match between the two spectra for Site 1 and Site 3 using generic site

amplification factors. Table 3.5 confirms the above observations. RMSEs are smaller than or equal to 0.05 for Site 2, Site 1 and Site 3 using generic site amplification factors. They are a bit larger than 0.05 for Site 1 with theoretical site amplification factors. RMSEs are observed to be quite larger than 0.05 for Site 3 with theoretical site amplification factors. The reason for this finding is that theoretical site amplification factors leads to a jagged spectrum due to peaks and troughs in amplification function. This point was discussed thoroughly in Section 3.3. The jagged behavior in UHS is more visible for Site 3 due to the complex velocity profile at this site compared to Site 1 (Figure 3.15). Hence RMSE values are much larger than 0.05 for Site 3 using theoretical site amplification. Selected recordings also exhibit larger scatter for this case than other cases (Figure 3.26).

It is observed that the median of recordings are close enough to UHS ($RMSE \leq 0.05$) for most of the cases. Hence it is assumed that the selected recordings in this section are adequate for the structural analysis presented in Chapter 4. The main characteristics of the selected ground motions in this section are listed in detail in Appendix A. The ground motions in this section are selected from the simulated ground motion catalog which is used earlier in this chapter for the proposed seismic hazard approach. Accordingly, the selected ground motions correspond to the same hazard level and include the regional seismicity characteristics. Hence this study provides uniform hazard ground motions for eastern Turkey which would be useful for engineers and researchers as well.

3.5 Main Findings of Chapter 3

In this chapter, site-specific uniform hazard spectrum based on synthetic ground motions is proposed. Following observations are made:

- The proposed UHS yields generally smaller ground motion amplitudes than classical PSHA. The main reason is that, classical PSHA considers a wide range of aleatory variability in seismic hazard calculations.
- Adding near-field forward directivity effects to the simulations of Site 2 leads to larger ground motion amplitudes for 2475 and 475 return periods and for periods longer than 1 seconds.
- Use of theoretical transfer functions without soil nonlinearity produces larger ground motion amplitudes for periods between 0.2 and 2 seconds as compared to generic site amplification for Site 1 and Site 3.

- Use of theoretical transfer functions with soil nonlinearity produces considerably smaller ground motion amplitudes for lower periods (less than about 0.6 seconds) as compared to generic site amplification for Site 1.
- The decrease in low-period ground motion amplitudes due to theoretical site amplification with soil nonlinearity at Site 3 is not as significant as that of Site 1 and it terminates at lower periods than Site 1.

Next, the simulated ground motions are selected with respect to the proposed UHS for a specified hazard level.

- The ground motions are selected from the simulated ground motion catalog which is generated stochastically to derive site-specific UHS in this study.
- 20 ground motions with the smallest SSEs from the proposed UHS are selected regarding each hazard level.
- The median of selected ground motions provides an agreeable fit to the proposed UHS (RMSEs are less than 0.05 for most of the cases).

Main advantages of using simulations in this study so far are as follows:

- Ground motion simulation is believed to yield ground motion amplitudes in a physical manner due to considering complex seismological parameters and seismic wave characteristics.
- Near-field forward directivity and detailed local site condition are implemented into seismic hazard assessment in a straightforward manner.
- There are variety of simulated ground motions in this study which result in a straightforward ground motion selection with agreeable match to UHS. On the contrary, it is generally difficult to find recorded ground motions with common characteristics which match the target spectrum.
- The selected synthetic ground motions are appropriate for regional applications whereas real ground motions are often adopted from different areas in regions with sparse past data.
- Scaling is not required in this study hence inherent variability of ground motions is preserved.

Finally, the selected ground motions will be employed in Chapter 4 for nonlinear time history analyses of equivalent single degree of freedom systems which represent typical residential buildings in the region. The seismic demand statistics resulted from ESDOF analyses are used in Chapter 5 to study the sensitivity of fragility

functions to regional seismicity parameters. The effect of the selected simulated ground motions on structural seismic demand and fragility is investigated in Chapter 4 and 5.





CHAPTER 4

PREDICTION OF SEISMIC DEMAND BASED ON EQUIVALENT SINGLE DEGREE OF FREEDOM ANALYSES

4.1 Introduction

In Chapter 3, a regional UHS was proposed for Erzincan region based on simulated ground motions and stochastically-generated earthquake catalog. Monte Carlo simulation method was applied to determine temporal and spatial distribution of events in stochastic ground motion catalog. Stochastic point-source method and finite-fault model based on dynamic corner frequency which were described extensively in Chapter 2, were implemented to simulate the ground motions. After derivation of UHS, the ground motions which had minimum deviation from the UHS regarding 4 hazard levels, were selected from the simulated ground motion database.

In this chapter, simulated ground motions, which were selected in Chapter 3, are used for nonlinear time history analyses of typical residential structures in Erzincan. The most common buildings in Erzincan are idealized as equivalent single degree of freedom (ESDOF) systems. Each ESDOF model represents a building stock with common characteristics such as structural type, number of stories, hysteretic model parameters and etc. In Section 4.3, response statistics of ESDOFs with mean values of structural parameters are investigated (structural variability is disregarded). In Section 4.4, the impact of ground motion effective duration on structural demands are studied. The effect of seismic parameters other than effective duration on structural demands are inspected in Section 4.5. In Section 4.6, response statistics of ESDOFs with probabilistic distribution of structural parameters are investigated (structural variability is regarded).

The main goal of this chapter is to provide seismic demand prediction models based on ground motion intensity parameter for calculation of fragility functions in Chapter 5. The demand variations with respect to GMIP resulting from the selected ground motions in this study requires regression analyses to yield fragility functions. In other words, this chapter is essential to derive fragility functions in Chapter 5. Residual analyses with respect to several parameters are performed to check the sufficiency and efficiency of the regression models. These predictive models and demand scatters enable one to witness the effect of some ground motion parameters on structural demands. The most important parameter which is investigated in this chapter is the ground motion effective duration. The effect of structural variability on the demand prediction models is also observed in this chapter.

4.2 Methodology

In regional seismic risk studies, it is technically impossible to analyze the whole structures in the building stock in detail. In such cases, practical and simple approaches such as ESDOFs are preferred by researchers (e.g.: Jeong and Elnashai, 2007; Erberik, 2008a; Ozmen et al., 2010; Ugurhan et al., 2011). In this study, six ESDOF models to represent the corresponding typical classes of building structures are taken into account, which consist of low- and mid-rise reinforced concrete (RC) frames as well as masonry structures with one, two and three stories. These ESDOFs represent the most common building structures in the study region. The ESDOF classes used in this study are determined via detailed field observations in Erzincan within Project TUJJB-UDP-01-12 (Askan et al., 2015).

The abbreviations of the building classes are RF1A, RF2B, RF2C, MU1A, MU2B and MU3C. The letters “RF” and “MU” in these codes stand for the building construction type, i.e. RC frame structure or unreinforced masonry structure, respectively. Numbers “1” and “2” in abbreviations of the RF classes denote low-rise and mid-rise structures, respectively. The number of stories for low-rise range between 1 and 3 whereas it ranges between 4 and 8 in the case of mid-rise. For MU classes, numbers “1”, “2” and “3” directly stand for the number of stories. Finally, the letters “A”, “B” and “C” represent high, moderate and low levels of conformity of the considered building class to the modern principles of seismic design and earthquake engineering, respectively. If a structure has been designed and constructed according to these principles, it is expected that it will exhibit a ductile

behavior with no or slight degradation. On the other hand, if a structure violates most of the seismic design principles, then it has a high potential to experience severe damage or even get collapse in a brittle mode with significant degradation. Hence the six ESDOF models in this study are assumed to cover a wide range of existing building structures in the study region with different construction types, number of stories and structural response characteristics.

There exist several major structural parameters to define an ESDOF model. The ones, which are independent of the selected hysteretic model for inelastic response, are period (T), strength ratio (η) and ductility factor (μ). Other structural parameters are generally related with the hysteretic model employed. The model that is considered in this study is the peak oriented hysteretic model of Ibarra et al. (2005), also known as the modified Ibarra-Medina-Krawinkler hysteretic model. It is a piecewise linear model with capping and residual strength parameters on the skeleton curve that enables to simulate the global force and displacement capacities of the considered structure. It also includes stiffness degradation and strength deterioration, which are important for the degrading cyclic response of deficient existing structures under dynamic loading. The backbone curve of this model is shown in Figure 4.1.

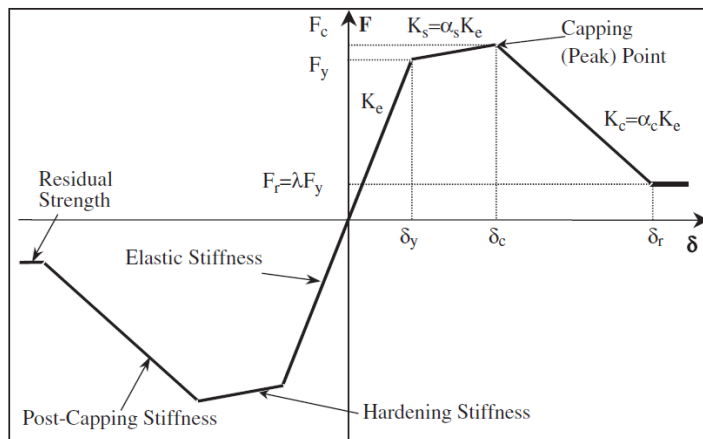


Figure 4.1. The backbone curve of peak-oriented hysteretic model (Ibarra et al., 2005)

In Figure 4.1, F_y , F_c and F_r are the yield, capping and residual strength parameters, respectively. Strength ratio is calculated by using F_y as below:

$$\eta = \frac{F_y}{W} \quad (4.1)$$

The capping strength can be obtained by introducing α_s , which can be defined as the post-yield stiffness ratio.

$$K_s = \alpha_s K_e \quad (4.2)$$

where K_e and K_s are elastic stiffness and post-yield stiffness, respectively. In a similar manner, residual strength can be obtained by introducing α_c , which can be defined as the post-capping stiffness ratio.

$$K_c = \alpha_c K_e \quad (4.3)$$

where K_c is the post-capping stiffness. Residual strength can also be defined in terms of yield strength as:

$$F_r = \lambda F_y \quad (4.4)$$

where λ is called as the strength reduction factor.

The displacement based parameters corresponding to these transition points are yield (δ_y), capping (δ_c) and residual (δ_r) displacements, respectively. Ductility factor can be defined by using yield and capping displacements as

$$\mu = \frac{\delta_c}{\delta_y} \quad (4.5)$$

It should also be noted that one of the major ESDOF parameters, period, is calculated by using the initial elastic stiffness (K_e) of the model.

Hysteretic energy dissipation parameter γ can simulate the cyclic modes of strength and stiffness degradation in the modified Ibarra-Medina-Krawinkler model. The parameter is based on cumulative hysteretic energy dissipation, for which more details can be found in Ibarra et al. (2005).

The seismic response of the ESDOF models under consideration can be defined completely in the modified Ibarra-Medina-Krawinkler model by assigning values to model parameters T , η , μ , α_s , α_c , λ and γ . Table 4.1 presents the assigned values of

these parameters for the six ESDOF models. Among these, the major structural parameters (T , η , μ) have been taken as random variables with normal distribution in order to account for the structural variability considered in fragility analysis. Each of these parameters is characterized with a mean value (MN in Table 4.1) and its standard deviation (STD in Table 4.1). The values for these statistical parameters are obtained by considering the statistical building data obtained from different studies focused on similar construction types (Kadas, 2006; Metin, 2006; Ay and Erberik, 2008; Erberik, 2008a; Karaca, 2014). The other model parameters (α_s , α_c , λ and γ) have been considered as constant and the values have been obtained by considering the calibration studies of the model for different structural systems and components (Ibarra and Krawinkler, 2005; Ibarra et al., 2005; Lignos and Krawinkler, 2011; Lignos and Krawinkler, 2012) and also engineering judgment to some extent. Further details regarding the attainment of the values of the model parameters can be obtained from the technical report of the Project TUJJB-UDP-01-12 (Askan et al., 2015).

Table 4.1. Hysteretic model parameters of the considered ESDOF models

Sub-class	T(s)		η		μ		$\alpha_s(\%)$	$\alpha_c(\%)$	λ	γ
	MN	STD	MN	STD	MN	STD				
RF1A	0.38	0.18	0.4	0.08	9	3.12	4	-20	0.2	800
RF2B	0.7	0.27	0.26	0.09	6.1	1.75	4	-25	0.2	400
RF2C	0.7	0.27	0.17	0.06	5.1	1.38	4	-30	0.2	200
MU1A	0.057	0.017	0.861	0.172	3.53	0.706	0	-20	0.2	600
MU2B	0.115	0.035	0.425	0.10625	2.62	0.655	0	-25	0.2	300
MU3C	0.173	0.052	0.142	0.0426	2.05	0.615	0	-30	0.2	150

The ESDOF systems are modeled through OPENSEES platform (<http://opensees.berkeley.edu/index.php>), in which the selected modified Ibarra-Medina-Krawinkler hysteretic model has been embedded. Nonlinear time history analysis is performed using the selected ground motions in Chapter 3. Maximum displacement is considered as the main structural demand parameter. As it was mentioned previously, ground motion time histories are selected with respect to return periods of 2475, 475, 225 and 75 years. The ground motions corresponding to 2475-year return period related to Site 1 generally cause unphysically large structural demands because of vicinity to NAFZ and soft soil conditions. Hence this hazard level is disregarded for Site 1.

Predictive equations are developed for structural seismic demand as a function of earthquake intensity. In this study, regression analysis is preferred over lognormal distribution fit because the selected ground motions for different hazard levels lead to cloud demand scatters (e.g.: Celik and Ellingwood, 2010). Besides, by using the predictive models, it is more practical to generate fragility curves in Chapter 5 through reliability formulation. The predictive model has the functional form in Equation 4.6, as most of the researchers consider this functional form (e.g.: Krawinkler et al., 2003; Wen et al., 2004; Ramamoorthy et al., 2006; Ellingwood et al., 2007; Ramamoorthy et al., 2008; Bai et al., 2011).

$$\ln(D) = \theta_0 + \theta_1 \ln(IM) + \sigma\varepsilon \quad (4.6)$$

In Equation 4.6, D and IM stand for structural demand and ground motion intensity measure, respectively. In this study, peak ground acceleration (PGA) is selected as ground motion intensity parameter. The ε term in Equation 4.6 is a random variable with zero mean and unit standard deviation and σ is standard deviation of model errors.

In some cases, $\ln(D)-\ln(IM)$ scatters do not follow a linear trend. Hence Equation 4.6 is not adequate for these cases since it underestimates or overestimates the observed data. For such cases, some researchers propose to use bilinear trend lines similar to Equation 4.7 (e.g.: Ramamoorthy et al., 2006; Ramamoorthy et al., 2008; Bai et al., 2011). Figure 4.2 illustrates the schematic form of the proposed bilinear formulation. In Figure 4.2, $\ln(IM_i)$ is the ground motion intensity parameter related to the

intersection point which is acquired via trial and error process to yield the largest R^2 of regression model.

$$\begin{aligned} \ln(D) &= \theta_0 + \theta_1 \ln(IM) + \sigma_1 \varepsilon_1 & \text{IM} \leq \text{IM}_i \\ \ln(D) &= [\theta_0 + \theta_1 \ln(\text{IM}_i)] + \theta_2 [\ln(IM) - \ln(\text{IM}_i)] + \sigma_2 \varepsilon_2 & \text{IM} > \text{IM}_i \end{aligned} \quad (4.7)$$

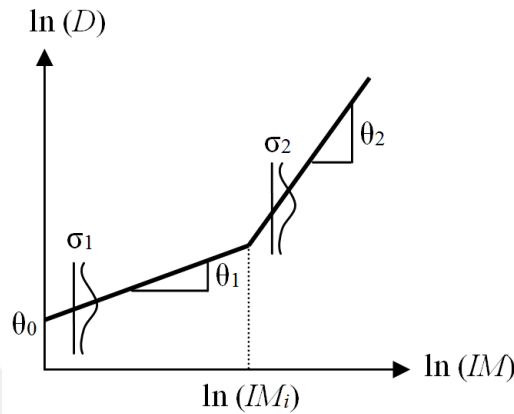


Figure 4.2. Schematic illustration of bilinear demand formulation
(Adapted from Bai et al., 2011)

4.3 ESDOF Response Statistics without Structural Variability

In this section, mean values (i.e. MN) of T , η and μ in Table 4.1 are used, thus the structural variability (i.e. STD) is disregarded. Standard least square regression methodology is applied to estimate parameters θ_0 , θ_1 , θ_2 , σ_1 and σ_2 in Equations 4.6 and 4.7. Displacement demand predictive models are exhibited along with demand versus PGA scatters. Then residual analyses on predictive models are performed with respect to PGA, magnitude and distance.

4.3.1 Demand Predictive Equations

Figures 4.3-4.8 show displacement demand variations with respect to PGA as well as the predictive equations for three sites with different site amplification and forward directivity models. Theoretical site amplification without soil nonlinearity is considered in this chapter since soil nonlinearity underestimates UHS considerably.

As it was mentioned previously, bilinear predictive models are preferred for some ESDOFs. For such cases, original linear model is also shown in grey to exhibit the difference in trends.

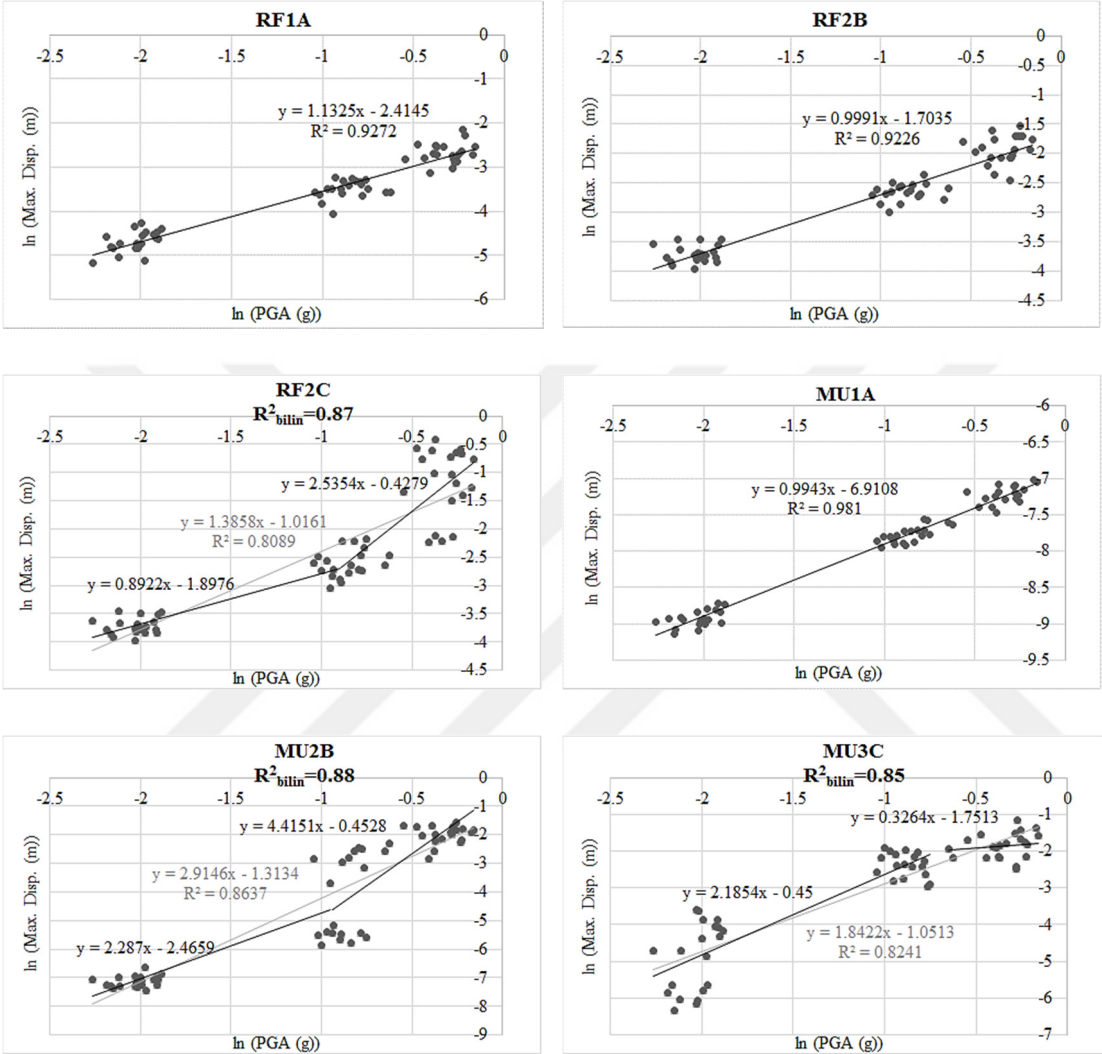


Figure 4.3. Variation of maximum displacement demand with respect to PGA and the predictive regression models for Site 1 using generic site amplification

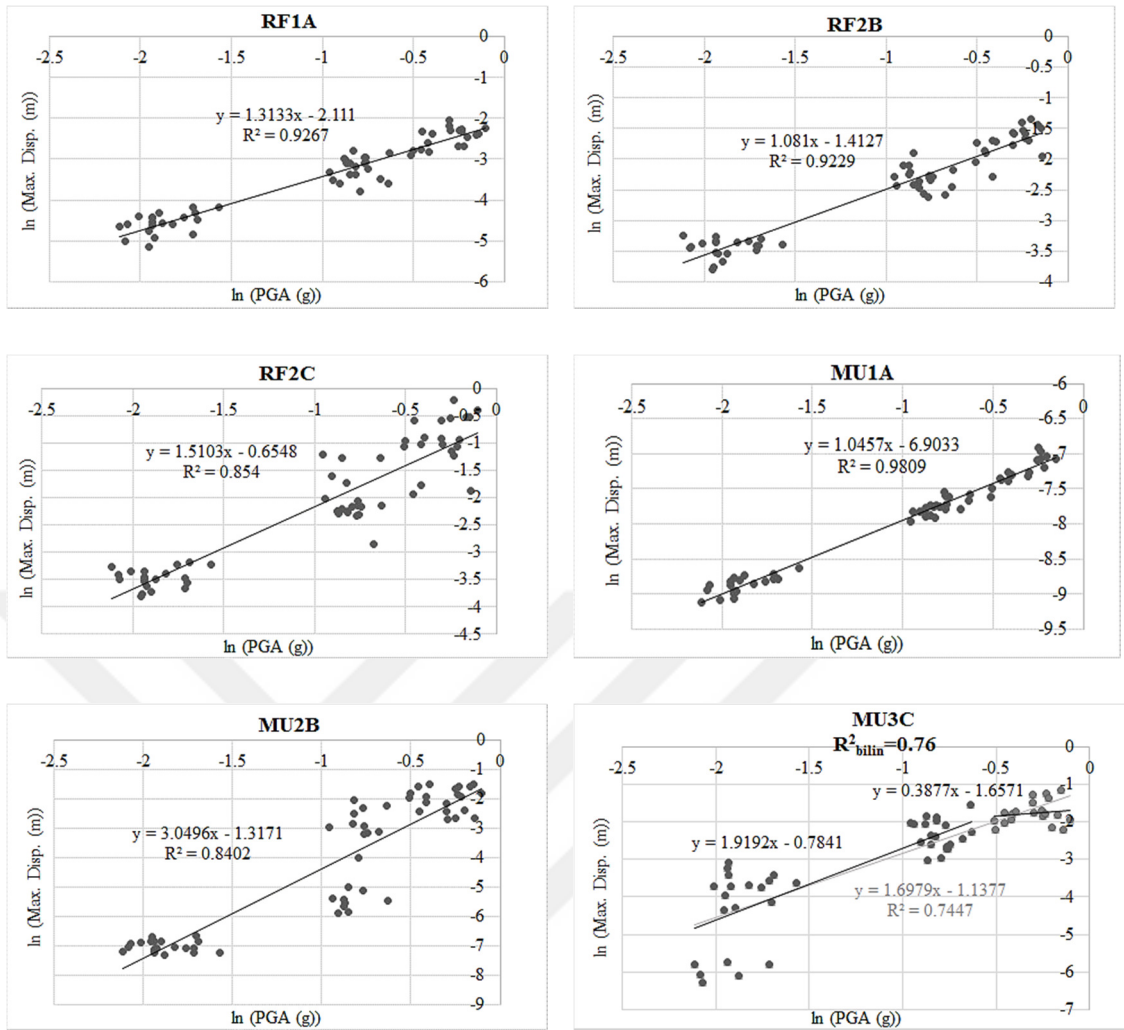


Figure 4.4. Variation of maximum displacement demand with respect to PGA and the predictive regression models for Site 1 using theoretical site amplification

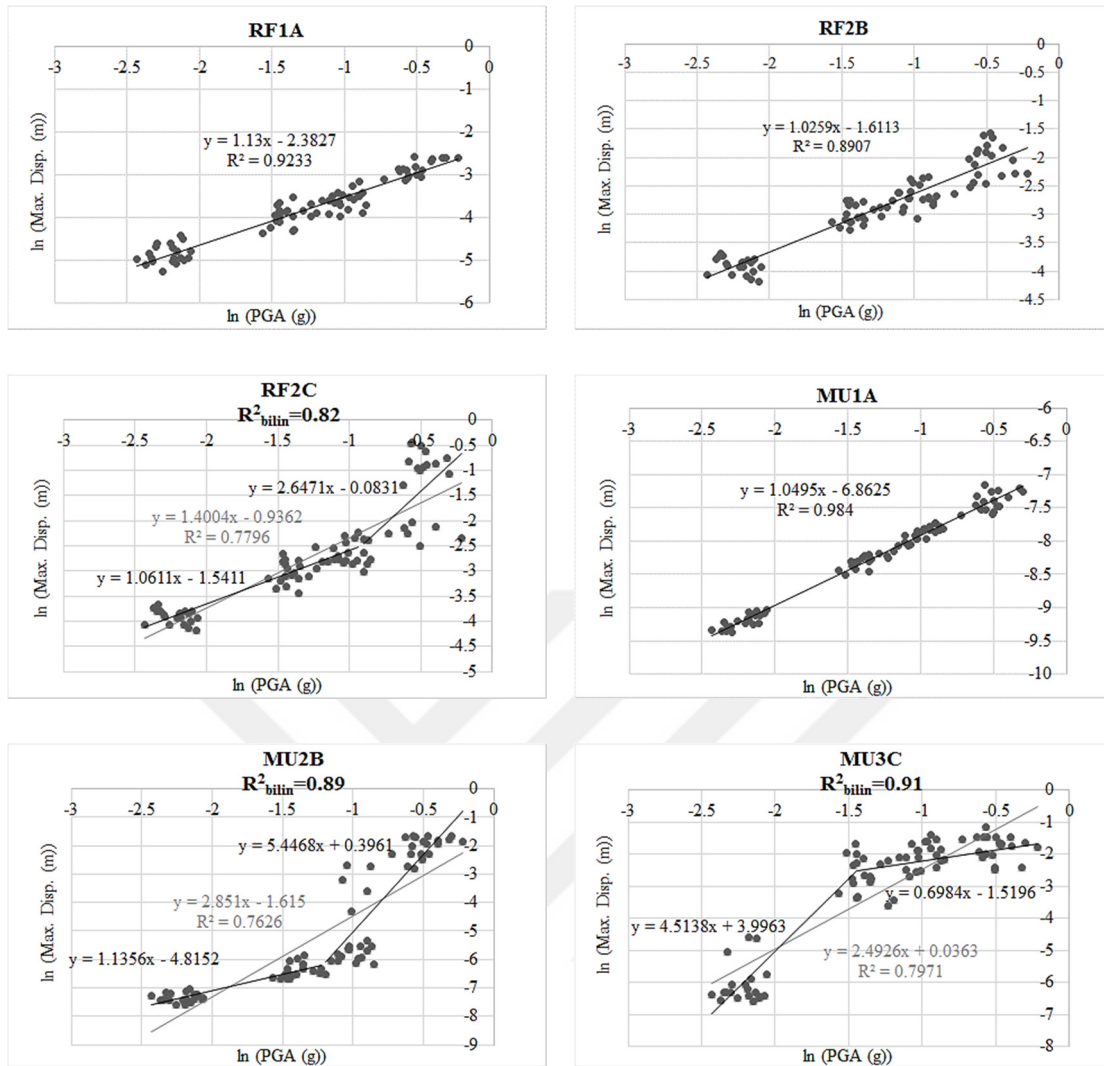


Figure 4.5. Variation of maximum displacement demand with respect to PGA and the predictive regression models for Site 2 without near-field forward directivity effect

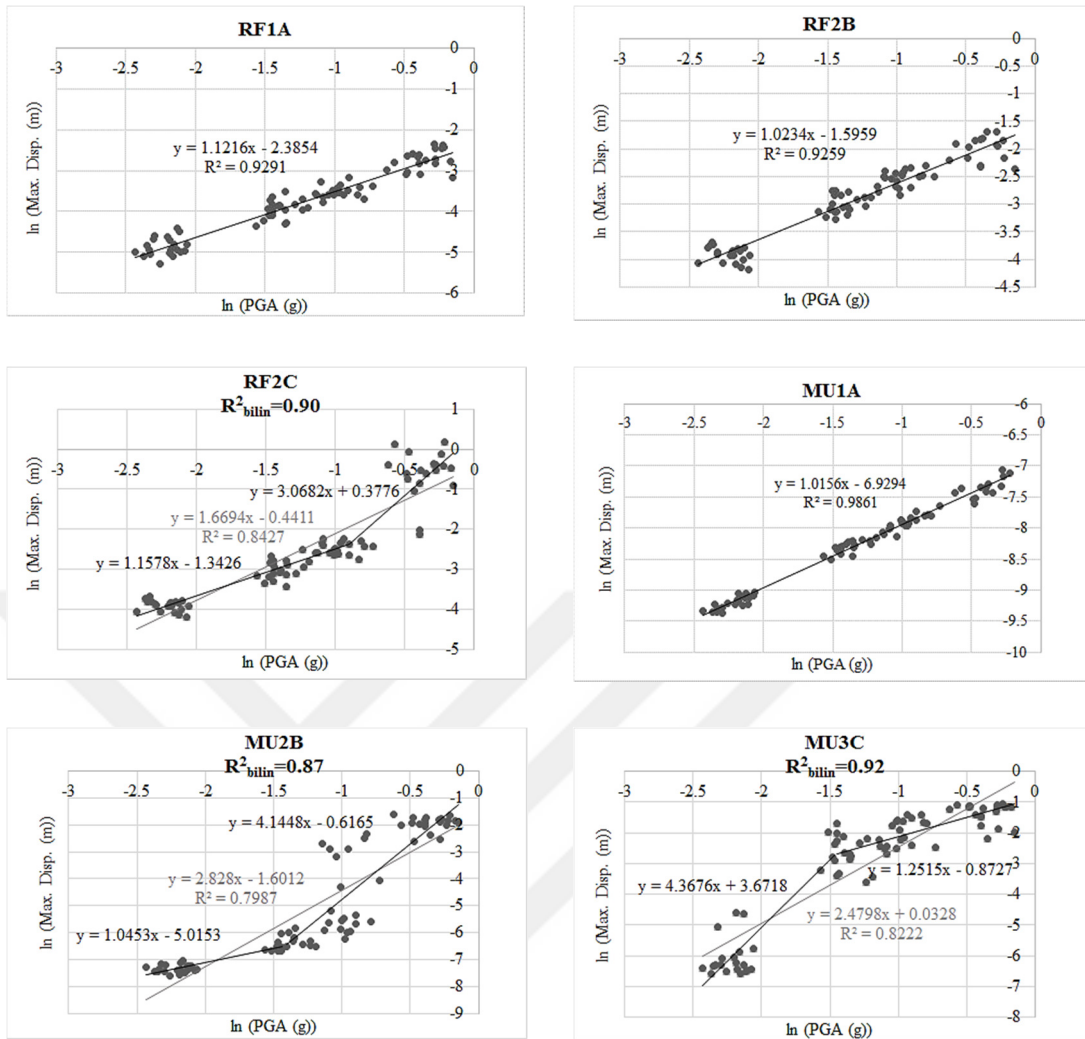


Figure 4.6. Variation of maximum displacement demand with respect to PGA and the predictive regression models for Site 2 with near-field forward directivity effect

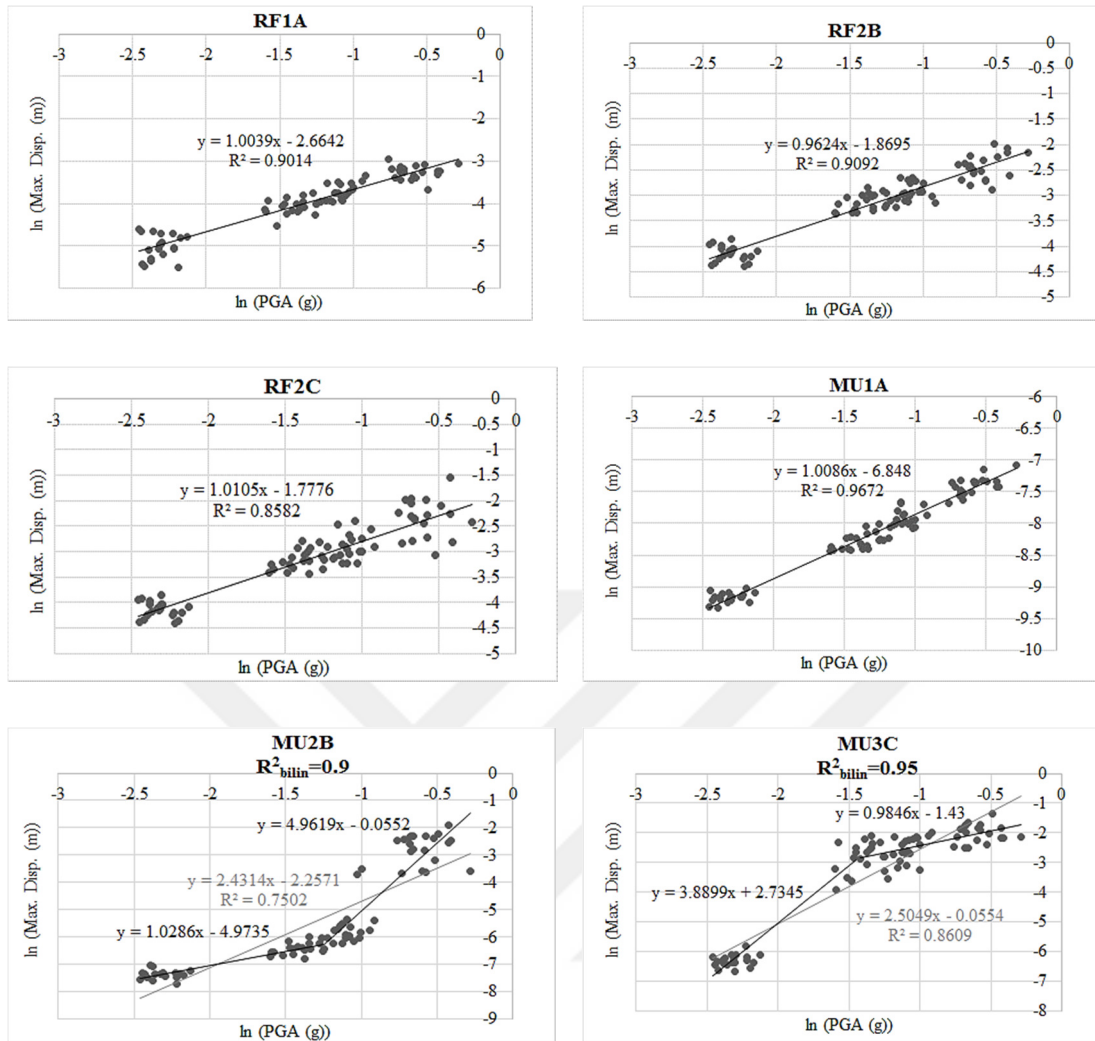


Figure 4.7. Variation of maximum displacement demand with respect to PGA and the predictive regression models for Site 3 using generic site amplification

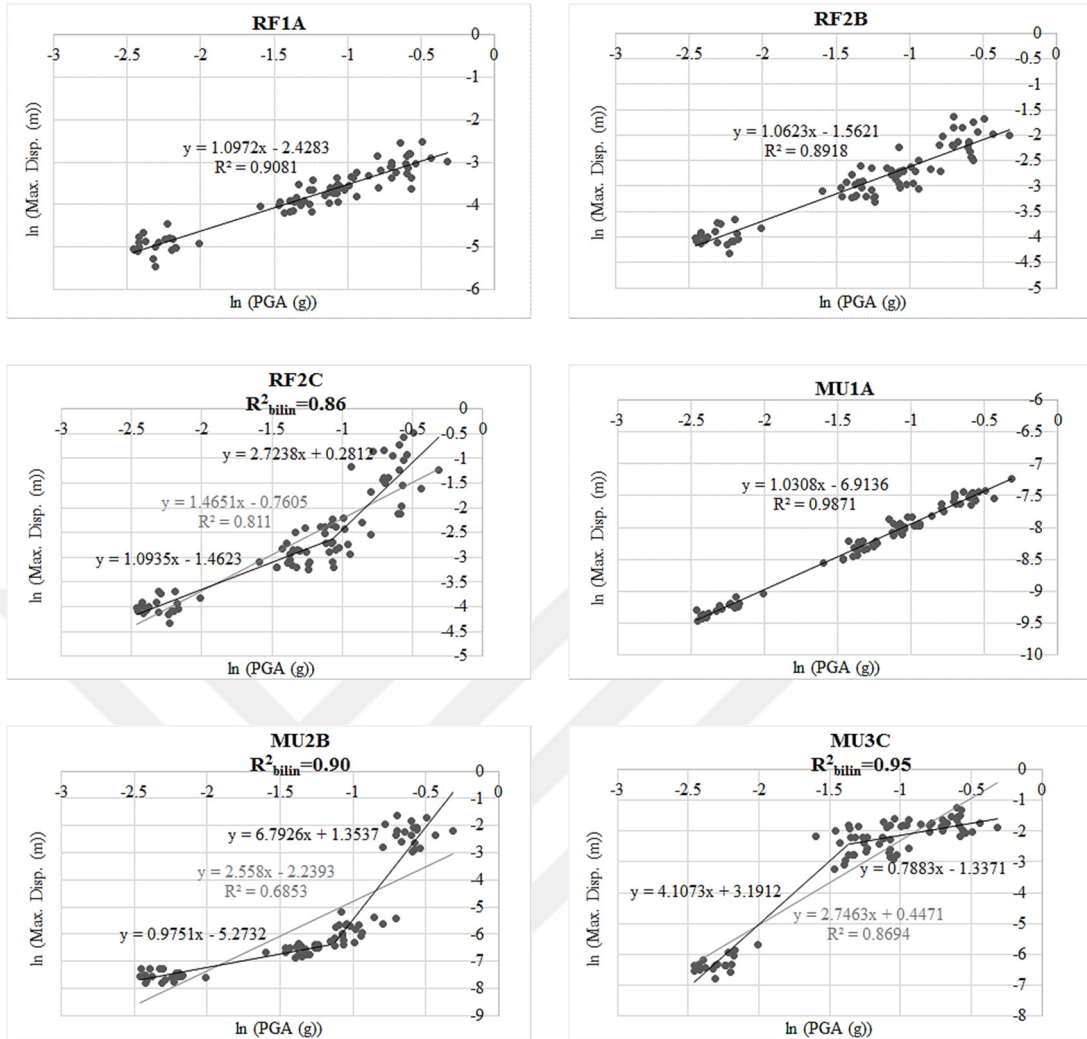


Figure 4.8. Variation of maximum displacement demand with respect to PGA and the predictive regression models for Site 3 using theoretical site amplification

It is observed from Figures 4.3-4.8 that, in most of the cases, RF2C, MU2B and MU3C require bilinear predictive models. These ESDOF models demonstrate the highest deterioration among the whole models (They have the smallest γ 's). R^2_{bilin} is the corresponding R^2 value for the whole bilinear model. It should be noted that the intersection point of two lines regarding bilinear models is selected by trial and error procedures to give the largest R^2_{bilin} . This R^2_{bilin} parameter is increased especially for Site 2 and Site 3 after modifying the predictive linear models into bilinear form since Site 1 is the most critical site (short distance to NAFZ and soft soil).

The second slope is greater than the first one for RF2C and MU2B models. Therefore, as PGA increases, demand is increasing more rapidly for large ground motion amplitudes than small ones. The second slope is smaller than the first one for MU3C. Regarding this model, as PGA increases, demand is increasing more slowly for large ground motion amplitudes than small ones. In other words, low hazard rates (with 2475 or 475 return periods) are more critical for MU2B and RF2C. However, high and intermediate hazard rates (with 225 or 75 return period) are more critical for MU3C, which is the most vulnerable building class among all.

4.3.2 Residual Analyses on Predictive Models with respect to magnitude and distance

It is important to assess the residual scatters with respect to the independent variable in the model and the other effective parameters that do not exist in the model but are thought to be important. Residual plots for predictive models are shown in Figures 4.9-4.14. In these figures, horizontal axis shows the independent variable which is $\ln(\text{PGA})$ in this study and the vertical axis represents the residuals as follows:

$$\text{Residuals} = \ln(\text{observed demand}) - \ln(\text{predicted demand}) \quad (4.8)$$

where “observed demand” represents the displacement demands resulted from nonlinear time history analyses and “predicted demand” represents the displacement demands obtained from the predictive demand models of Figures 4.3-4.8. If there is no observable trend line for residual versus $\ln(\text{PGA})$ scatters, then linear and bilinear models of Equations 4.6 and 4.7 are believed to be adequate in terms of PGA.

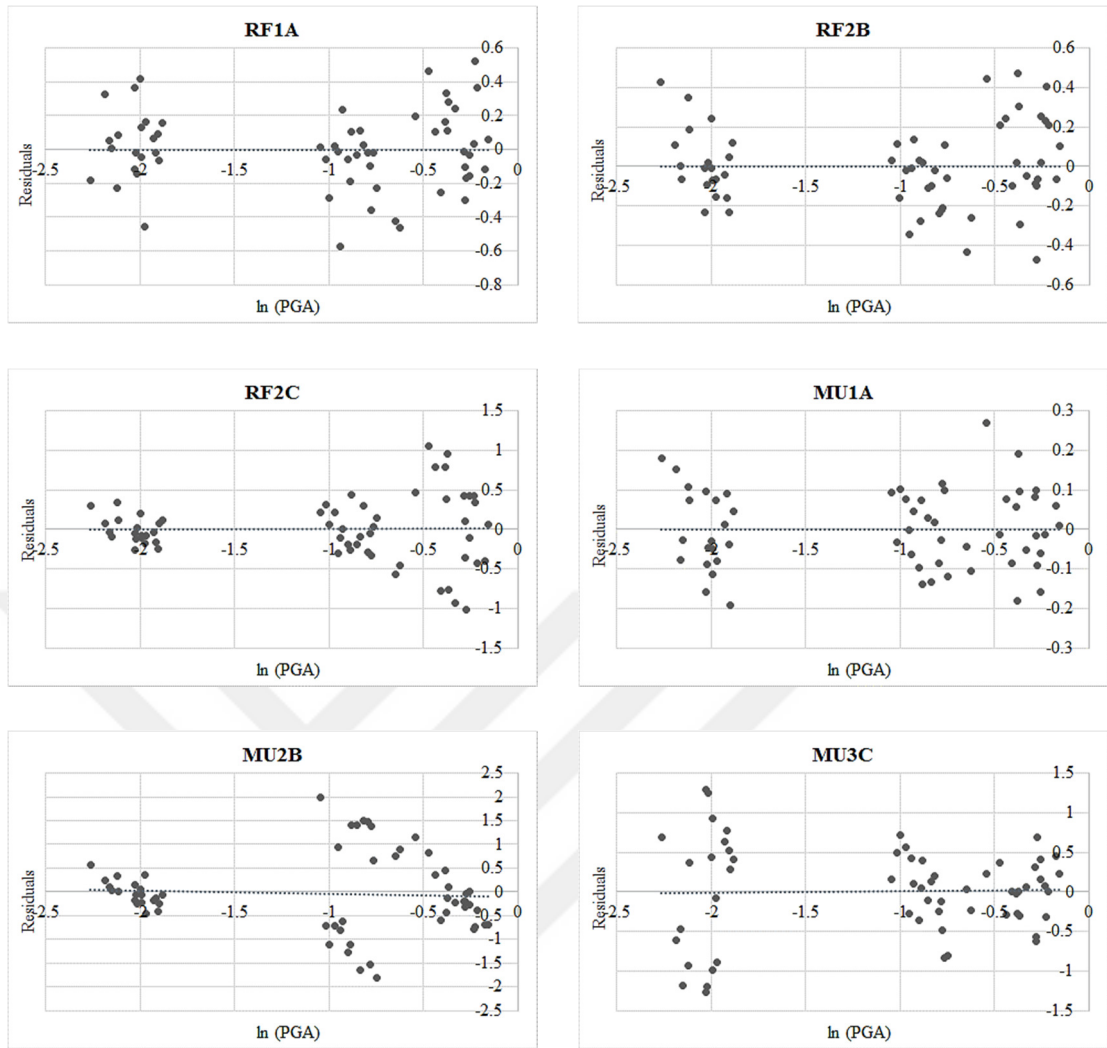


Figure 4.9. Residual plots and the corresponding trend lines related to predictive models of Figure 4.3 (Site 1 using generic site amplification)

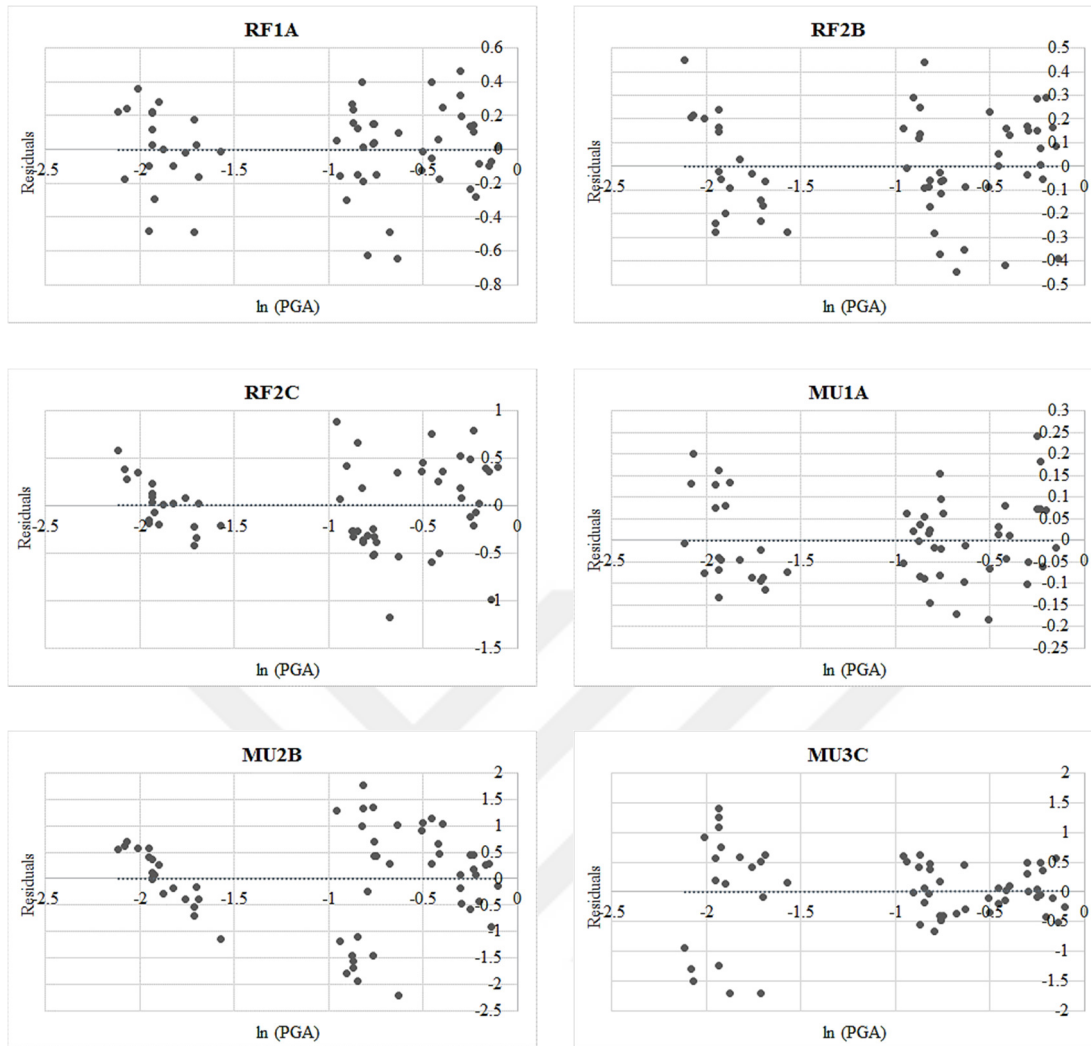


Figure 4.10. Residual plots and the corresponding trend lines related to predictive models of Figure 4.4 (Site 1 using theoretical site amplification)

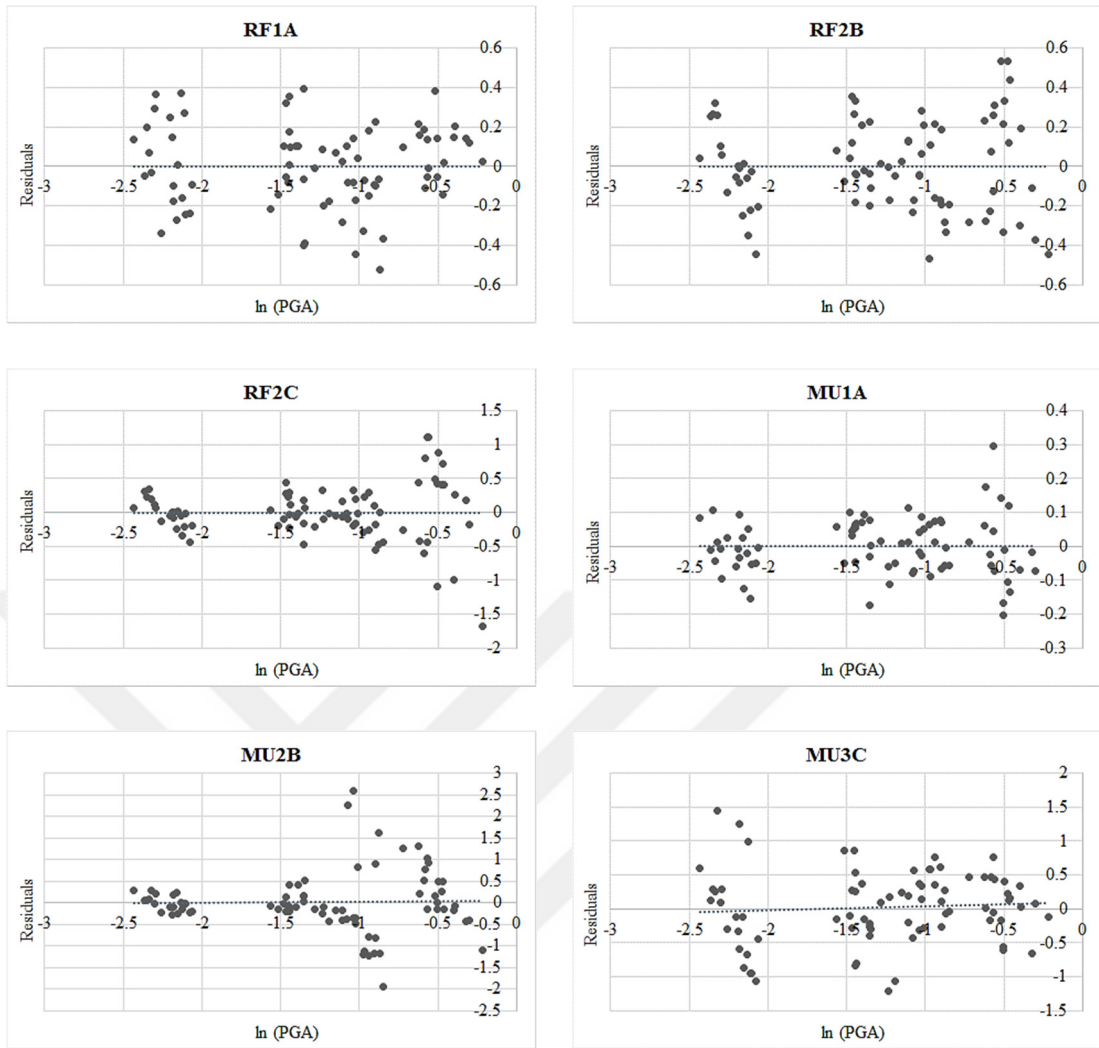


Figure 4.11. Residual plots and the corresponding trend lines related to predictive models of Figure 4.5 (Site 2 without near-field forward directivity)

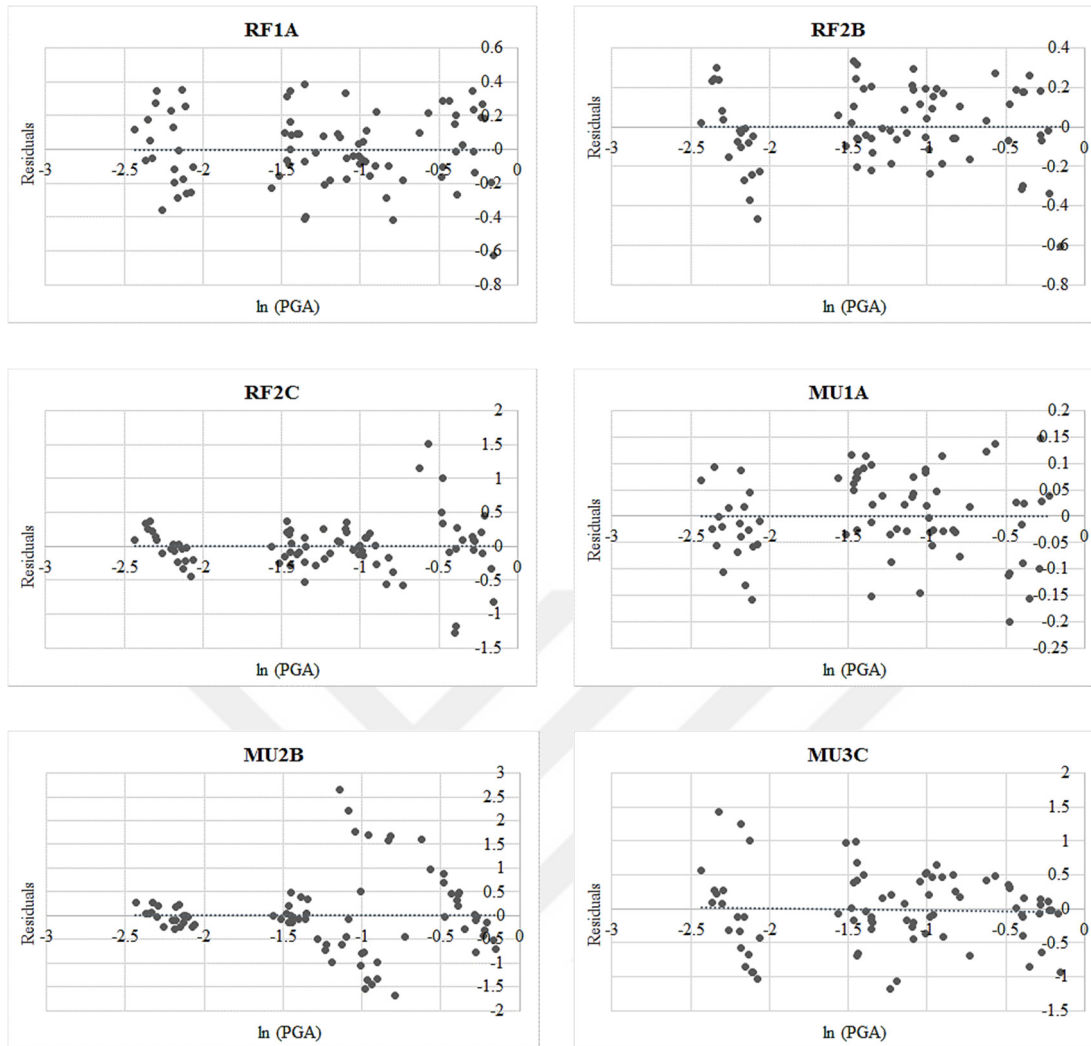


Figure 4.12. Residual plots and the corresponding trend lines related to predictive models of Figure 4.6 (Site 2 with near-field forward directivity)

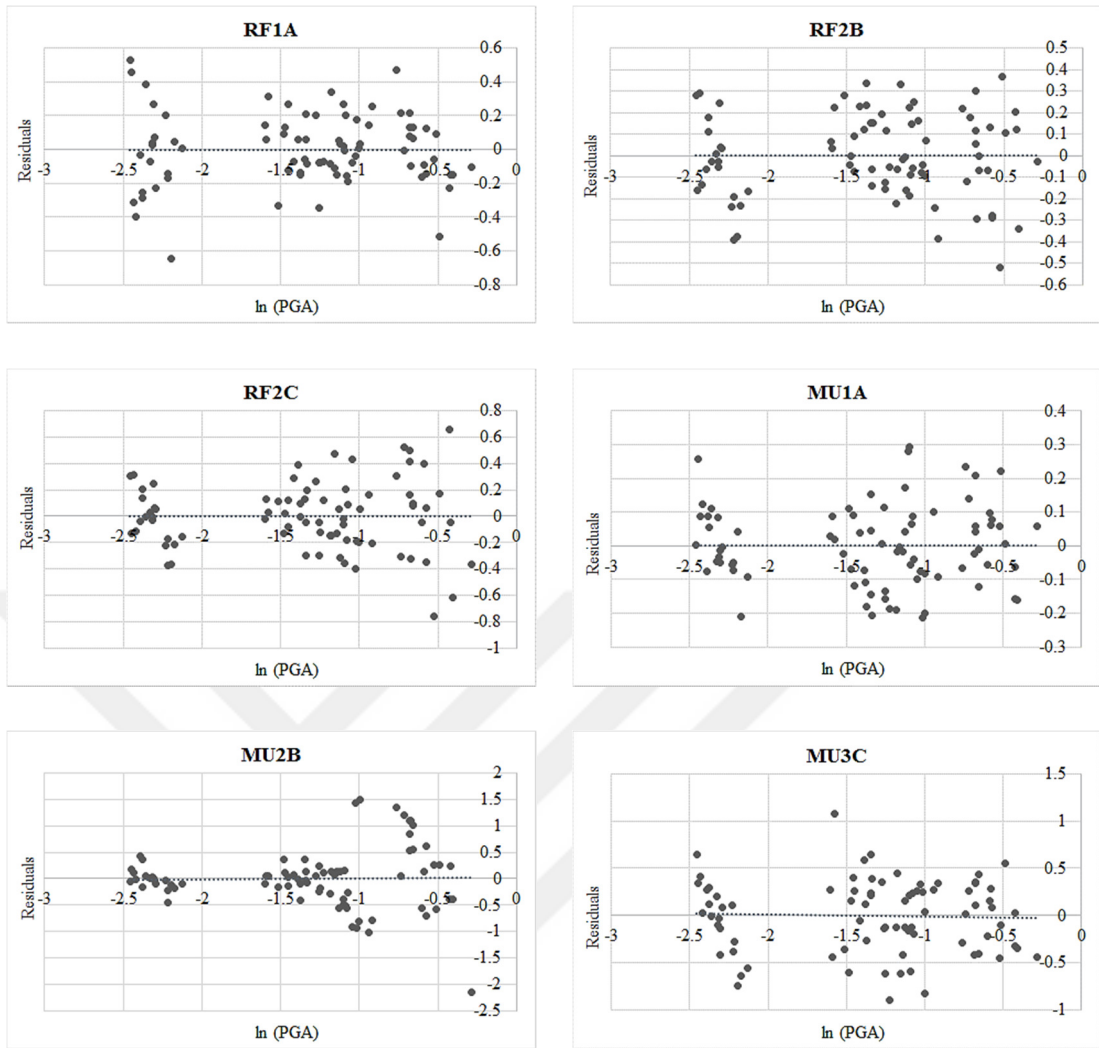


Figure 4.13. Residual plots and the corresponding trend lines related to predictive models of Figure 4.7 (Site 3 using generic site amplification)

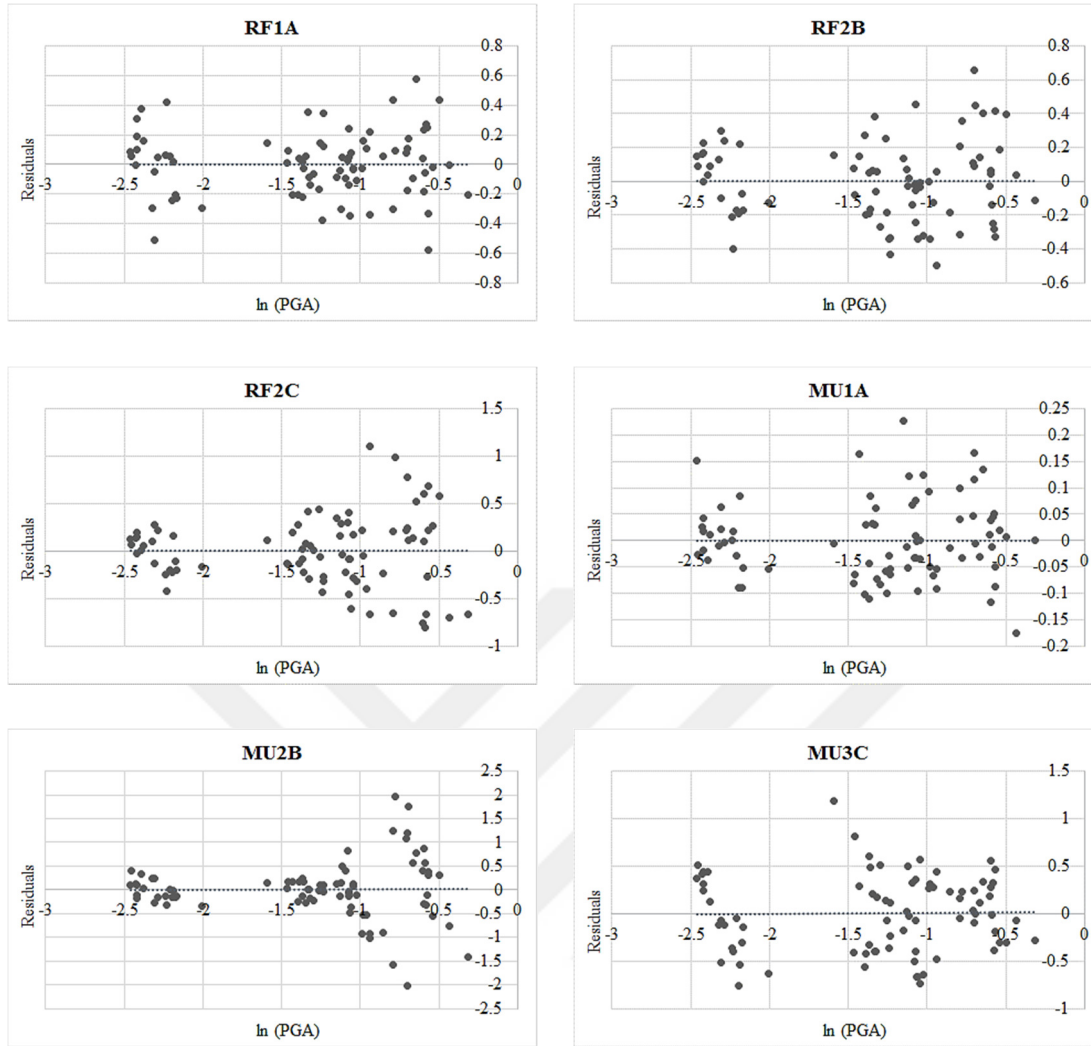


Figure 4.14. Residual plots and the corresponding trend lines related to predictive models of Figure 4.8 (Site 3 using theoretical site amplification)

According to Figures 4.9-4.14, the residuals spread randomly around zero without any systematic bias. Therefore, linear and bilinear predictive demand equations which are defined in Figures 4.3-4.8, are concluded to be sufficient in terms of PGA. Zero mean of the residuals is also perceived from Figures 4.9-4.14, which is an important requirement of regression analysis.

The effect of parameters other than PGA (which are not present in the model) on demand predictive models may also be investigated through residual analysis. Residual scatters with respect to moment magnitude (M_w) and closest distance to

rupture (R_{rup}) are shown in Appendix B for the sake of brevity. If the trend lines of residual scatters have quite large R^2 values, then the parameter under study affects the demand predictions. Tables 4.2 and 4.3 demonstrate R^2 percentages of the trend lines related to residual scatters with respect to M_w and R_{rup} .

Table 4.2. R^2 percentages of the residuals against moment magnitude

	RF1A	RF2B	RF2C	MU1A	MU2B	MU3C
Site 1 using generic site amplification	0.45	0.52	0.22	0.02	0.28	0.09
Site 1 using theoretical site amplification	0.57	7.97	9.47	2.55	4.91	4.48
Site 2 without near-field forward directivity	2.67	2.64	1.71	4.31	0.52	9.12
Site 2 with near-field forward directivity	0.6	7.15	1.82	5.22	0.3	7.86
Site 3 using generic site amplification	2.72	0.1	0.77	0.84	0.06	4.56
Site 3 using theoretical site amplification	0.41	4.2	0	3	0.05	4.71

Table 4.3. R^2 percentages of the residuals against the closest distance to rupture

	RF1A	RF2B	RF2C	MU1A	MU2B	MU3C
Site 1 using generic site amplification	0.27	0.29	0.26	0.76	0.06	1.14
Site 1 using theoretical site amplification	0.17	0.35	0.21	6.53	0	3.47
Site 2 without near-field forward directivity	1.33	0.81	0.1	0.03	1.47	0.59
Site 2 with near-field forward directivity	0.62	1.39	0.08	0.37	1.98	3.17
Site 3 using generic site amplification	0.99	0.43	0.42	0.69	0.83	1.62
Site 3 using theoretical site amplification	0.02	2.12	0.78	2.59	1.38	0.05

It is perceived from Tables 4.2 and 4.3 that the residuals are more dependent on magnitude than distance. Statistical overview of residual analyses indicates that, 17% and 47% of the residual scatters versus magnitude have R^2 values larger than 5% and 2%, respectively. These percentages are reduced to 3% and 14% for R^2 's larger than 5% and 2%, respectively, regarding residuals versus distance scatters.

Generally, when residual plots display significant trend lines against the parameter not existing in the predictive model, that parameter must be added to the model. In this study, majority of the cases do not show considerable trends (most of the R^2 's are smaller than 5%). Therefore magnitude and distance parameters are not required to be added to the predictive models.

4.4 The Impact of Effective Duration on Displacement Demands

Ground motion effective duration is believed to be the second most effective parameter on structural responses other than the peak amplitudes. While magnitude and distance are as well critical, it is believed that they have some effects on PGA, which is already in the predictive model. In this section, the impact of effective duration which is defined in Chapter 3, is studied on displacement demands of ESDOFs without structural variability.

In this section, initially, the residual analyses of predictive demand models in Section 4.3, are performed with respect to effective duration. These residual analyses help one to observe whether it is essential to insert this parameter into the demand prediction equations. Next, the effect of this parameter is inspected in detail on displacement demands within PGA bins. Finally, the effect of this parameter on different displacement demands resulted from some ground motions with similar PGAs is studied.

4.4.1 Residual Analyses on Demand Predictive Models with Respect to Effective Duration

The variations of residuals of demand predictive models are studied against effective duration. The residuals versus effective duration scatters are shown in Appendix B for the sake of brevity. Table 4.4 shows R^2 percentages of trend lines regarding residual scatters versus effective duration.

Table 4.4. R^2 percentages of the residuals against effective duration

	RF1A	RF2B	RF2C	MU1A	MU2B	MU3C
Site 1 using generic site amplification	1.94	0.35	0.18	0.21	0.97	0.06
Site 1 using theoretical site amplification	0.44	1.08	7.04	1.03	13.06	4.44
Site 2 without near-field forward directivity	0	0.08	0.08	6.77	0.27	6.99
Site 2 with near-field forward directivity	0.23	2.58	0.1	4.26	1.49	5.45
Site 3 using generic site amplification	0.58	0.95	2.72	0.7	0	7.8
Site 3 using theoretical site amplification	0.2	4.56	0.02	3.57	0.05	8.68

According to Table 4.4, 19% and 36% of residual trend lines versus effective duration have R^2 values larger than 5% and 2%, respectively. Hence R^2 's are not considerably high in most of the cases (about 80 % of the cases have R^2 's smaller than 5%). This observation indicates that effective durations is not required to be inserted into the demand prediction equations. However Table 4.4 reveals the significance of effective duration for some cases. Most of the residual scatters with R^2 's larger than 5% in Table 4.4, belong to RF2C, MU2B and MU3C (i.e. the structures with severe degradation characteristics). This dependency of structural demands on effective duration for some ESDOFs necessitates further investigations

4.4.2 The Impact of Effective Duration on Displacement Demands within PGA Bins

In order to observe the effective duration impact in detail, the ground motions which are used to derive demand predictive models, are divided into PGA bins. Each bin contains ten ground motions with similar PGAs. Next, the maximum displacement demands are plotted against effective duration for each bin. Figure 4.15 shows demand-duration scatters for six PGA bins as well as trend lines regarding Site 1 using generic site amplification and building sub-class MU3C.

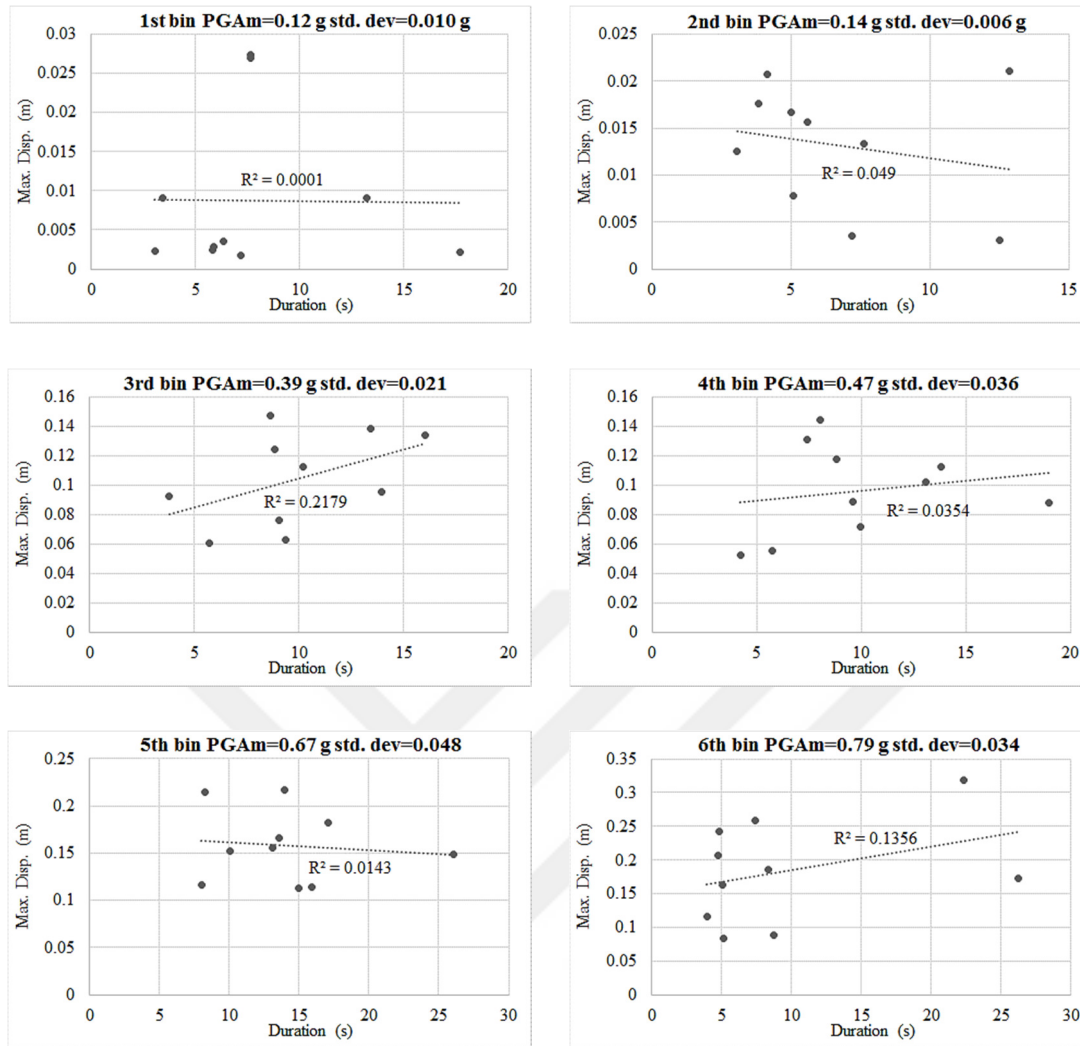


Figure 4.15. Maximum displacement demand versus effective duration scatters for six PGA bins regarding Site 1 using generic site amplification and MU3C. $PGAm$ and std. dev stand for mean and standard deviation of PGAs inside each bin, respectively.

Figure 4.15 indicates that there may be either positive correlation (positive slope of the trend line) or negative correlation (negative slope of the trend line) or no correlation (slope of the trend line is close to zero) between demand and effective duration. Tables 4.5-4.10 present R^2 's of demand tend lines versus effective duration for the whole cases. The correlation type between demand and effective duration is also shown inside parentheses with “po”, “ne” and “no” which stand for “positive”,

“negative” and “no correlation”, respectively. It is assumed herein that, $R^2 \leq 2\%$ shows no correlation between demand and duration. The demand-duration plots related to the whole cases are shown in Appendix C (three sites with different site amplification and forward directivity models as well as six ESDOFs).

Table 4.5. R^2 percentages and correlation type of demand vs. effective duration trend lines for Site 1 using generic site amplification

	RF1A	RF2B	RF2C	MU1A	MU2B	MU3C
$PGA_m=0.12$ g	7.69 (po)	0.09 (no)	0.26 (no)	3.06 (ne)	5.35 (po)	0.01 (no)
$PGA_m=0.14$ g	0.45 (no)	6.31 (ne)	9.34 (ne)	1.84 (no)	0.87 (no)	4.9 (ne)
$PGA_m=0.39$ g	12.4 (ne)	0.27 (no)	19.05 (po)	1.28 (no)	0.22 (no)	21.79 (po)
$PGA_m=0.47$ g	3.16 (po)	37.1 (ne)	26.34 (ne)	6.49 (ne)	13.12 (po)	3.54 (po)
$PGA_m=0.67$ g	2.73 (ne)	8.22 (ne)	1.39 (no)	23.27 (po)	31.86 (po)	1.43 (no)
$PGA_m=0.79$ g	8.87 (ne)	0.45 (no)	0.38 (no)	6.31 (ne)	2.51 (ne)	13.58 (po)

Table 4.6. R^2 percentages and correlation type of demand vs. effective duration trend lines for Site 1 using theoretical site amplification

	RF1A	RF2B	RF2C	MU1A	MU2B	MU3C
$PGA_m=0.14$ g	62.33 (po)	19.22 (po)	16.92 (po)	14.24 (ne)	1.85 (no)	7.46 (po)
$PGA_m=0.17$ g	0.66 (no)	4.66 (po)	7.78 (ne)	3.09 (ne)	23.62 (po)	3.31 (po)
$PGA_m=0.42$ g	0.71 (no)	0.04 (no)	4.5 (po)	40.9 (ne)	13.14 (po)	12.44 (po)
$PGA_m=0.48$ g	17.62 (po)	10.46 (ne)	6.4 (po)	2.52 (ne)	69.46 (po)	39.12 (po)
$PGA_m=0.67$ g	16.41 (ne)	33.18 (ne)	7.21 (ne)	1.5 (no)	17.37 (po)	26.19 (ne)
$PGA_m=0.82$ g	0.56 (no)	4.58 (po)	55.06 (po)	4.04 (ne)	30.92 (po)	14.09 (po)

Table 4.7. R^2 percentages and correlation type of demand vs. effective duration trend lines for Site 2 without near-field forward directivity

	RF1A	RF2B	RF2C	MU1A	MU2B	MU3C
$PGA_m=0.1$ g	3.95 (po)	18.11 (po)	12.89 (po)	39.8 (po)	12.25 (ne)	1.42 (no)
$PGA_m=0.12$ g	1.98 (no)	11.84 (po)	11.86 (po)	0.48 (no)	43.53 (ne)	1.02 (no)
$PGA_m=0.23$ g	0.51 (no)	0.62 (no)	15.57 (ne)	3.63 (po)	0.87 (no)	8.23 (po)
$PGA_m=0.27$ g	0.47 (no)	8.37 (ne)	43.62 (ne)	1.4 (no)	0.12 (no)	19.38 (po)
$PGA_m=0.35$ g	3.73 (po)	18.52 (ne)	0.57 (no)	76.22 (ne)	0.51 (no)	5.13 (po)
$PGA_m=0.42$ g	1.1 (no)	0.27 (no)	1.97 (no)	4.49 (ne)	0.59 (no)	56.59 (po)
$PGA_m=0.63$ g	8.73 (ne)	28.15 (ne)	23.14 (ne)	40.89 (po)	37.53 (ne)	9.51 (po)
$PGA_m=0.78$ g	7.7 (po)	0.02 (no)	25.31 (po)	77.59 (po)	74.73 (po)	0.07 (no)

Table 4.8. R^2 percentages and correlation type of demand vs. effective duration trend lines for Site 2 with near-field forward directivity

	RF1A	RF2B	RF2C	MU1A	MU2B	MU3C
$PGA_m=0.1$ g	3.95 (po)	1.81 (no)	12.8 (po)	39.8 (po)	12.2 (ne)	1.4 (no)
$PGA_m=0.12$ g	1.98 (no)	1.18 (no)	11.8 (po)	0.4 (no)	43.5 (ne)	1 (no)
$PGA_m=0.23$ g	0.51 (no)	0.6 (no)	15.5 (ne)	3.6 (po)	0.8 (no)	8.2 (po)
$PGA_m=0.27$ g	0.47 (no)	8.3 (ne)	43.6 (ne)	1.4 (no)	0.1 (no)	19.3 (po)
$PGA_m=0.34$ g	50.97 (po)	1 (no)	0.2 (no)	0.9 (no)	2.6 (ne)	2.6 (po)
$PGA_m=0.4$ g	37.31 (ne)	6 (po)	2.1 (po)	17.9 (ne)	7.6 (ne)	35.8 (po)
$PGA_m=0.56$ g	4.82 (ne)	4.2 (ne)	5.2 (ne)	22 (ne)	3.1 (po)	0.6 (no)
$PGA_m=0.68$ g	3.79 (ne)	0 (no)	7.5 (ne)	37.3 (po)	2.2 (ne)	0 (no)

Table 4.9. R^2 percentages and correlation type of demand vs. effective duration trend lines for Site 3 using generic site amplification

	RF1A	RF2B	RF2C	MU1A	MU2B	MU3C
$PGA_m=0.09$ g	0 (no)	0.67 (no)	0.67 (no)	0.28 (no)	1.82 (no)	5.67 (ne)
$PGA_m=0.1$ g	0.04 (no)	4.41 (po)	4.36 (po)	12.15 (po)	18.8 (po)	8.79 (ne)
$PGA_m=0.22$ g	9.86 (po)	0.26 (no)	0 (no)	2.59 (po)	1.93 (no)	6.3 (po)
$PGA_m=0.27$ g	33.02 (po)	16.74 (ne)	0.11 (no)	2.67 (po)	12.98 (po)	73.32 (po)
$PGA_m=0.32$ g	4.22 (po)	1.25 (no)	1.59 (no)	12.1 (ne)	0.02 (no)	10.29 (po)
$PGA_m=0.36$ g	13.65 (po)	13.75 (ne)	0.35 (no)	0.63 (no)	21.94 (po)	43.82 (po)
$PGA_m=0.5$ g	33.21 (ne)	0.05 (no)	2.57 (po)	9.3 (po)	13.03 (po)	0.12 (no)
$PGA_m=0.62$ g	10.76 (ne)	9.77 (po)	39.66 (po)	12.63 (ne)	3.76 (po)	9.45 (po)

Table 4.10. R^2 percentages and correlation type of demand vs. effective duration trend lines for Site 3 using theoretical site amplification

	RF1A	RF2B	RF2C	MU1A	MU2B	MU3C
$PGA_m=0.09$ g	27.23 (po)	55.96 (ne)	55.96 (ne)	3.76 (po)	12.1 (ne)	8.28 (po)
$PGA_m=0.11$ g	6.48 (po)	0.1 (no)	0.13 (no)	27.09 (po)	1.77 (no)	82.07 (po)
$PGA_m=0.24$ g	5.08 (po)	31.91 (ne)	40.49 (ne)	0.22 (no)	35.21 (po)	67.98 (po)
$PGA_m=0.28$ g	0.72 (no)	2.49 (ne)	0.13 (no)	10.99 (ne)	21.84 (ne)	42.37 (po)
$PGA_m=0.34$ g	46.91 (ne)	43.6 (ne)	24.73 (ne)	46 (ne)	21.36 (ne)	24.85 (po)
$PGA_m=0.38$ g	0.63 (no)	5.35 (ne)	0.13 (no)	19.9 (ne)	0.01 (no)	25.6 (po)
$PGA_m=0.5$ g	1.88 (no)	10.79 (ne)	13.74 (po)	0.2 (no)	3.86 (po)	28.61 (po)
$PGA_m=0.59$ g	19.04 (po)	13.94 (po)	28.23 (po)	0.99 (no)	36.33 (po)	2.06 (po)

Statistical overview of Tables 4.5-4.10 shows positive correlation between demand and effective duration for 40% of the cases. 33% and 27% of the scatters display no and negative correlation, respectively. It means that the ground motions with long duration are likely to cause more damage to structures than the ones with short duration even if their PGAs are similar.

It is also observed from Tables 4.5-4.10 that, most of the positive demand-duration correlations are related to MU3C, MU2B and RF2C (62%). Among the whole positive correlation cases, the percentages regarding MU3C, MU2B and RF2C are 29%, 17% and 16%, respectively. The reason is clearly severe degradation characteristics of these three models. Therefore ground motion effective duration is observed to have a more destructive effect on the structures with severe degradation of strength and stiffness.

The impact of effective duration on displacement demands of ESDOFs within PGA bins is also examined for each site separately. 40% of the demand-duration scatters of Site 1 have positive correlation. This percentage is 35% and 44% regarding Site 2 and Site 3, respectively. Among the demand-duration scatters of Site 1 with positive correlation, 70% of the cases are related to the structural models with severe degradation characteristics. This percentage is 50% and 61% regarding Site 2 and Site 3, respectively. These statistics highlight the significance of effective duration impact on displacement demands of ESDOFs with severe degradation characteristics at sites with short distance to NAFZ. It means that, the near-field pulses which are introduced by finite-fault ground motion simulation techniques amplify the effect of duration on structures with high deterioration.

4.4.3 The impact of Effective Duration on Displacement Demands Resulted from Some Ground Motions with Similar PGAs

The impact of effective duration on displacement demand is evident in some demand-PGA scatters. This is observed in terms of considerable difference in structural demands from ground motions with similar PGAs. Figure 4.16 exhibits some examples about this observation.

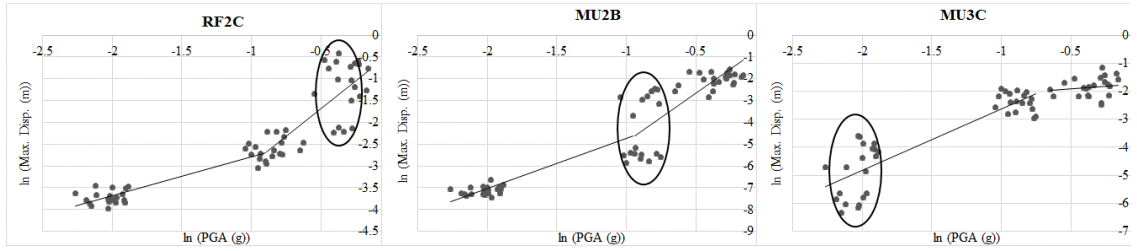


Figure 4.16. Ground motions with similar PGAs and considerably different demands which are shown inside elliptic (Site 1 using generic site amplification adapted from Figure 4.3)

Two ground motions are studied in detail for each ESDOF model used in Figure 4.16 in Tables 4.11-4.13 as examples. In all cases, one of the ground motions leads to less demand whereas the other one causes significantly more demand. The third row in Tables 4.11-4.13 is the ratio of the ground motion with more demand to the one with less demand in terms of magnitude, distance, duration and resulted displacement demand. Figures 4.17-4.19 exhibit Tables 4.11-4.13 in graphical form.

Table 4.11. Two ground motions as examples which are shown inside elliptic in Figure 4.16 regarding building sub-class RF2C

GM ID	Mag	R_{rup} (km)	PGA (g)	Effective Duration (s)	Max. Disp.(m)
S1G475_13	7.20	12.16	0.67	10.07	0.11
S1G475_07	7.88	11.93	0.68	26.07	0.54
Ratio	1.09	0.98	1.02	2.59	5.04

Table 4.12. Two ground motions as examples which are shown inside elliptic in Figure 4.16 regarding building sub-class MU2B

GM ID	Mag	R _{rup} (km)	PGA (g)	Effective Duration (s)	Max. Disp.(m)
S1G225_11	7.31	20.53	0.46	13.06	0.004
S1G225_06	7.69	17.11	0.45	18.98	0.085
Ratio	1.05	0.83	0.99	1.45	19.47

Table 4.13. Two ground motions as examples which are shown inside elliptic in Figure 4.16 regarding building sub-class MU3C

GM ID	Mag	R _{rup} (km)	PGA (g)	Effective Duration (s)	Max. Disp.(m)
S1G75_02	5.95	14.45	0.13	3.06	0.002
S1G75_20	6.72	29.88	0.13	7.66	0.03
Ratio	1.13	2.07	1.01	2.51	11.68

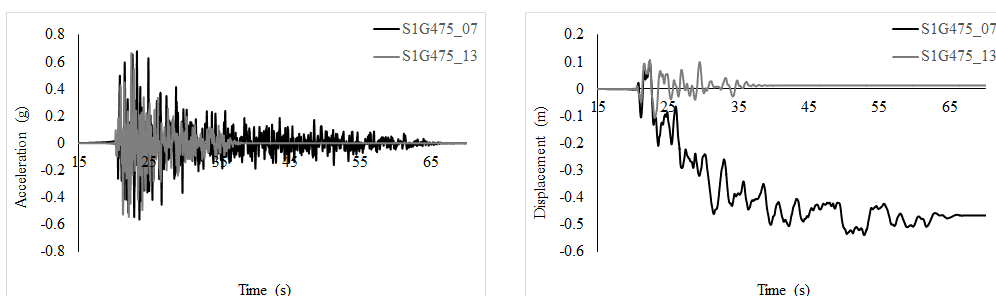


Figure 4.17. Ground acceleration and displacement demand related to Table 4.11

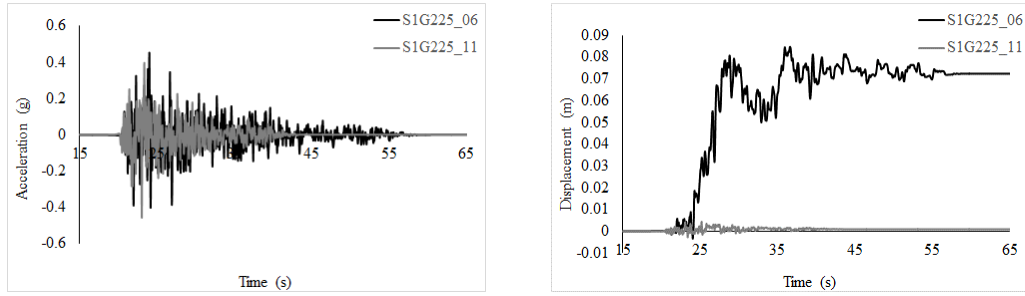


Figure 4.18. Ground acceleration and displacement demand related to Table 4.12

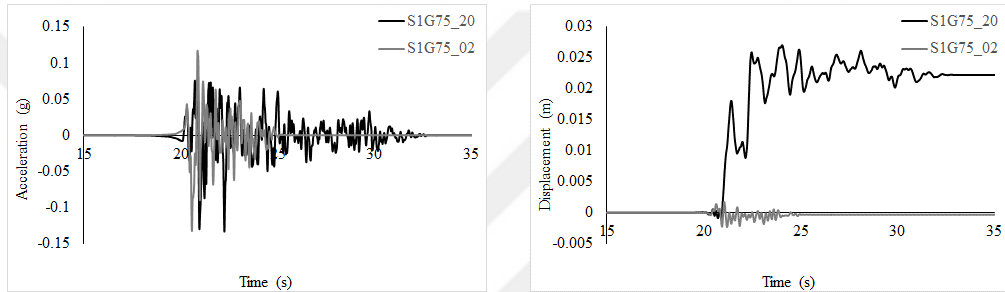


Figure 4.19. Ground acceleration and displacement demand related to Table 4.13

According to Table 4.11 and Figure 4.17, displacement demand resulted from GM 07 is 5.04 times that from GM 13 although PGAs are the same (Ratio=1.02). Effective duration plays an important role to cause this considerable difference in displacement demands with the ratio of 2.59. According to the results of Table 4.12 and Figure 4.18, GM 06 produces displacement demand, which is 19.47 times the one produced by GM 11 although PGAs are the same (Ratio=1.02). Effective duration is relatively effective with the ratio of 1.45 herein. Comparing GM 20 with GM 02 in Table 4.13 and Figure 4.19 indicates that, effective duration with the ratio of 2.59 is quite effective to cause this considerable demand ratio (11.68).

These unexpected observations are evident for RF2C, MU2B and MU3C according to Figures 4.3-4.8. Tables 4.11-4.13 and Figure 4.17-4.19 indicate that, effective duration is an effective parameter for these three ESDOFs. The reason is again high

degradation characteristics of these three models. They are exposed to effective duration more than other models as mentioned previously. These unexpected observations in Figures 4.3-4.8 (i.e. remarkable difference between displacement demands resulted from the ground motions with similar PGAs) are more evident for Site 1 than Site 2 and 3 due to short distance to NAFZ and soft soil conditions.

Another important observation in Figures 4.17-4.19 is the large residual displacement regarding ground motions resulting in higher demands. Such large residual displacement generally means severe damage to structures or even collapse. According to Figure 4.16, these unexpected observations occur in 475-year (low hazard rate), 225-year (intermediate hazard rate) and 75-year (high hazard rate) regarding RF2C, MU2B and MU3C, respectively. In other words, these unexpected observations exist in the most critical hazard levels of each ESDOF which may be close to the collapse state of the structure. Due to the arguments above, the displacement demands of RF2C, MU2B and MU3C related to Site 1 do not fit the bilinear regression models in an agreeable manner, as mentioned previously.

4.5 The Effect of Seismic Parameters (Other than Effective Duration) on Displacement Demands Resulted from Some Ground Motions with Similar PGAs

The effects of seismic parameters other than effective duration on displacement demands resulted from the same ground motions as the ones in Section 4.4.3 are studied in this section. The parameters which are effective in addition to duration, are PGV, PSa (T_1) and spectrum intensity (SI). PSa (T_1) is spectral acceleration at fundamental period of the considered ESDOF. Spectrum intensity (SI) is defined as the integral of pseudo-velocity spectrum from $T=0.1$ s to $T=2.5$ s (Housner, 1963). This parameter shows the energy content of the ground motion and is defined as follows:

$$SI = \int_{T=0.1}^{T=2.5} PSv(T)dT \quad (4.9)$$

Tables 4.14-4.16 show the same ground motions as the ones in Section 4.4.3 along with their PGV, PSa (T_1) and SI. The third row in Tables 4.14-4.16 is the ratio of the ground motion with more demand to the one with less demand in terms of PSa (T_1),

PGV, SI and resulted displacement demand. Figures 4.20-4.22 exhibit Tables 4.14-4.16 in the graphical form.

Table 4.14. Two ground motions as examples which are shown inside elliptic in Figure 4.16 regarding building sub-class RF2C

GM ID	PGV (cm/s)	SI (cm)	PSa (T=0.7 s) (g)	Max. Disp.(m)
S1G475_13	58.97	240.78	0.80	0.11
S1G475_07	78.11	267.27	1.16	0.54
Ratio	1.32	1.11	1.45	5.04

Table 4.15. Two ground motions as examples which are shown inside elliptic in Figure 4.16 regarding building sub-class MU2B

GM ID	PGV (cm/s)	SI (cm)	PSa (T=0.115 s) (g)	Max. Disp.(m)
S1G225_11	61.76	150.98	0.69	0.004
S1G225_06	58.99	138.38	1.20	0.085
Ratio	0.96	0.92	1.73	19.47

Table 4.16. Two ground motions as examples which are shown inside elliptic in Figure 4.16 regarding building sub-class MU3C

GM ID	PGV (cm/s)	SI (cm)	PSa (T=0.173 s) (g)	Max. Disp.(m)
S1G75_02	14.14	41.69	0.28	0.002
S1G75_20	12.30	46.87	0.31	0.03
Ratio	0.87	1.12	1.12	11.68

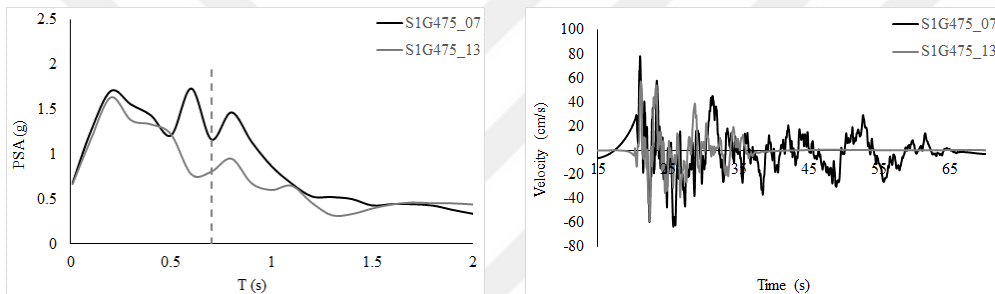


Figure 4.20. Pseudo-acceleration spectrum and ground velocity related to Table 4.14 (dashed grey line shows the fundamental period of RF2C)

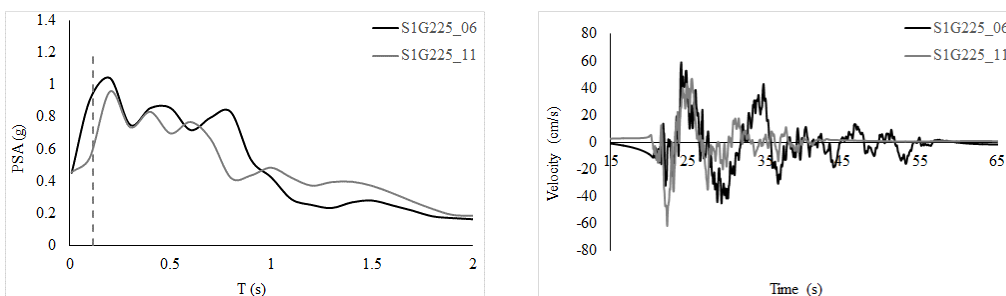


Figure 4.21. Pseudo-acceleration spectrum and ground velocity related to Table 4.15 (dashed grey line shows the fundamental period of MU2B)

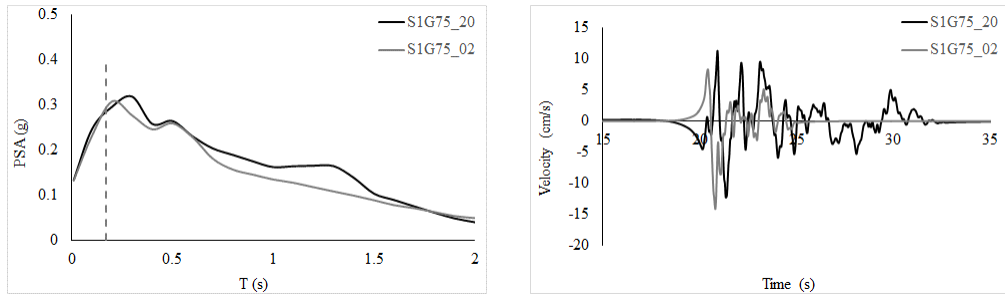


Figure 4.22. Pseudo-acceleration spectrum and ground velocity related to Table 4.16 (dashed grey line shows the fundamental period of MU3C)

According to Table 4.14, displacement demand resulted from GM 07 is 5.04 times that from GM 13 although PGAs are the same (Ratio=1.02). PSa is important herein with the ratio of 1.45. PGV and SI are slightly important with the ratios of 1.32 and 1.11, respectively. Table 4.15 shows that, the ratios related to SI and PGV of these ground motions are close to unity (The ratios are 0.92 and 0.96, respectively). However, PSa seems to be effective with the ratio of 1.73. Comparing GM 20 with GM 02 in Table 4.16 indicates that, PSa and SI are slightly important related to this case (the ratio is 1.12 for both).

Tables 4.14-4.16 as well as Figures 4.20-4.22 indicate that, PSa (T_1) is the effective parameter for all three ESDOFs. PGV is only important for RF2C because this parameter is related to medium-to-long-period intensity. SI is effective regarding RF2C and MU3C. Because these two models have fundamental periods much longer than $T=0.1$ s, that becomes more critical for SI. As the structural models under study in this section are the weakest ones, their fundamental period may increase (elongate) so that SI and PGV may become more important for their seismic response. As it was mentioned previously, Site 1 is more exposed to this observation than the other two sites. The reason may be also soft soil of this site which have larger fundamental period than stiff ones. Therefore the importance of SI and PGV becomes more apparent. This section puts forward the effects of PGV, SI and PSa (T_1) on structural demands resulted from the ground motions with similar PGAs but these effects are not as remarkable as effective duration.

4.6 ESDOF Response Statistics with Structural Variability

In Section 4.3, mean values of T , μ and η are used to model ESDOFs. As it was mentioned previously, these three parameters are random variables with mean and standard deviation since they affect the fragility functions more than other parameters. In this section, the probabilistic distributions of these parameters are taken into account for modeling ESDOFs using Latin Hypercube Sampling (LHS) method. Then displacement demand variations with respect to PGA are re-exhibited after considering structural variability.

4.6.1 Latin Hypercube Sampling Methodology

Latin Hypercube Sampling method is adopted in this section to sample the random variables. LHS methodology is developed by McKay et al. (1979) and is preferred by several authors (Ayyub and Lai, 1989; Erberik, 2008a; Askan, 2015). This approach is based on capturing the whole probabilistic distribution in a constrained manner with a smaller sample size when compared to the Monte Carlo Method. Another advantage of this approach is that it can sample multiple random variables, which is required in this study. If it is assumed that there are K random variables denoted by X_k , then the whole range of X_k is divided into N portions with equal marginal probabilities of $1/N$. Therefore, cumulative probability of n^{th} ($n=1, 2, \dots, N$) portion is obtained as follows:

$$P_n = \left(\frac{1}{N}\right)U_n + \left(\frac{n-1}{N}\right) \quad (4.10)$$

where U_n is a random number between 0 and 1. After calculating P_n through Equation 4.10, the final sample is obtained using inverse cumulative distribution function (F^{-1}).

$$X_{kn} = F_X^{-1}(P_n), \quad k = 1, 2, \dots, K \text{ and } n = 1, 2, \dots, N \quad (4.11)$$

where X_{kn} is sample input for n^{th} portion and k^{th} random variable. This process is repeated for K random variables so there is a matrix of samples with dimension of $K \times N$.

4.6.2 Demand Predictive Equations

In this section, 20 samples are derived using LHS which represent the probabilistic distribution of T , μ and η . The time history analyses of Section 4.3 are repeated for 20 models regarding each ESDOF group. Response statistics of ESDOFs are shown in Figures 4.23-4.28 as well as demand prediction equations. The scatters and prediction equations related to Section 4.3 (without structural variability) are also exhibited in grey. Bilinear predictive models are preferred for the ESDOFs with bilinear models in Section 4.3.



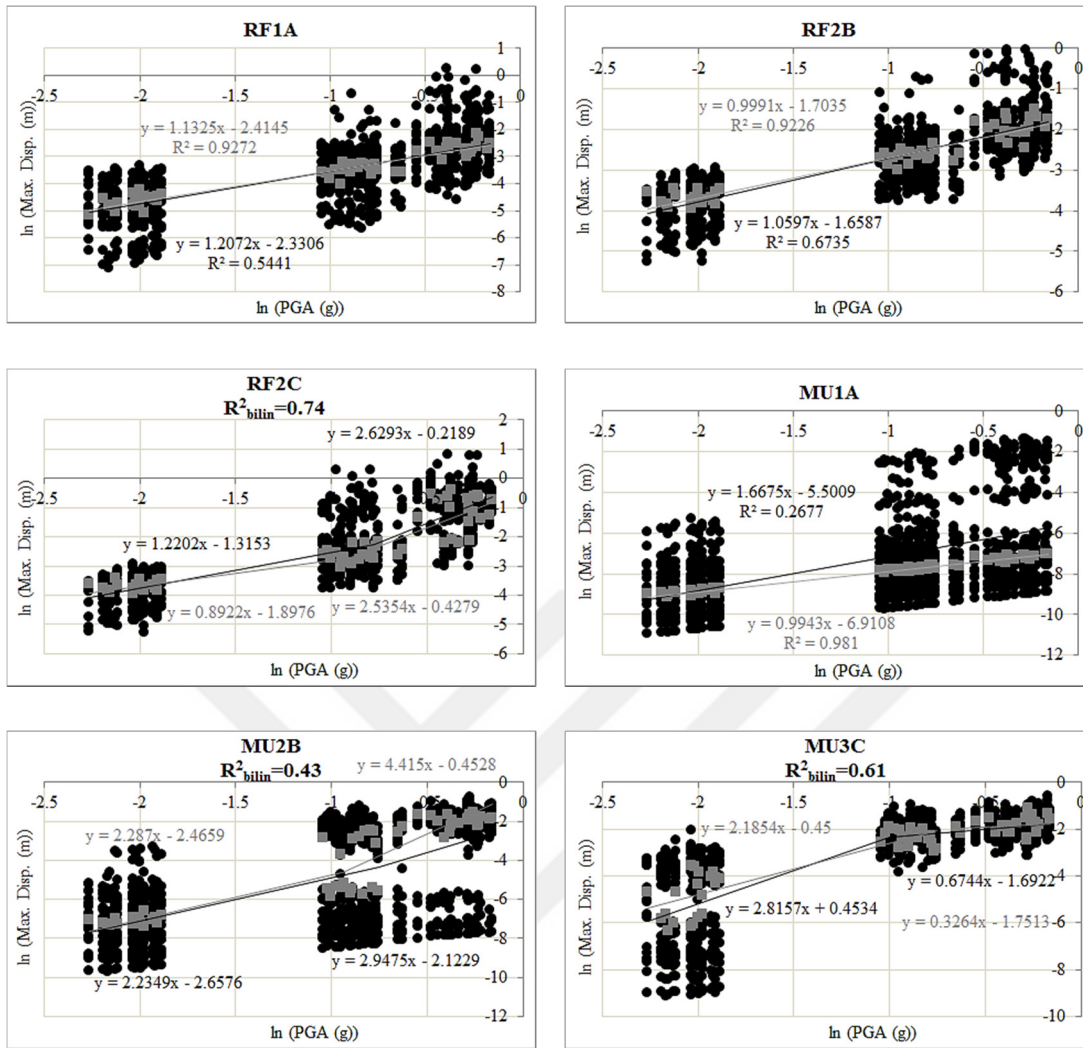


Figure 4.23. Variation of maximum displacement demand with respect to PGA and the predictive regression models for Site 1 using generic site amplification

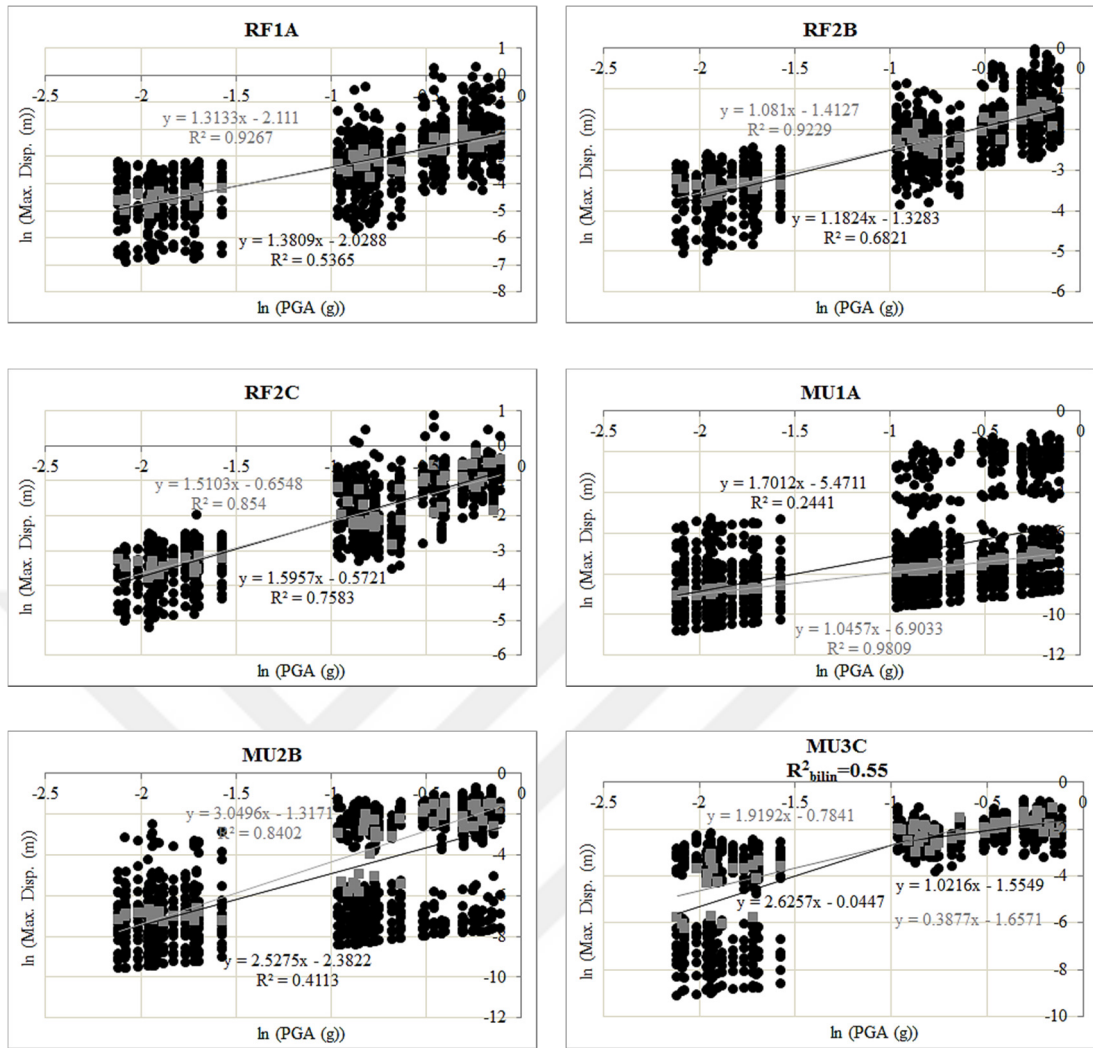


Figure 4.24. Variation of maximum displacement demand with respect to PGA and the predictive regression models for Site 1 using theoretical site amplification

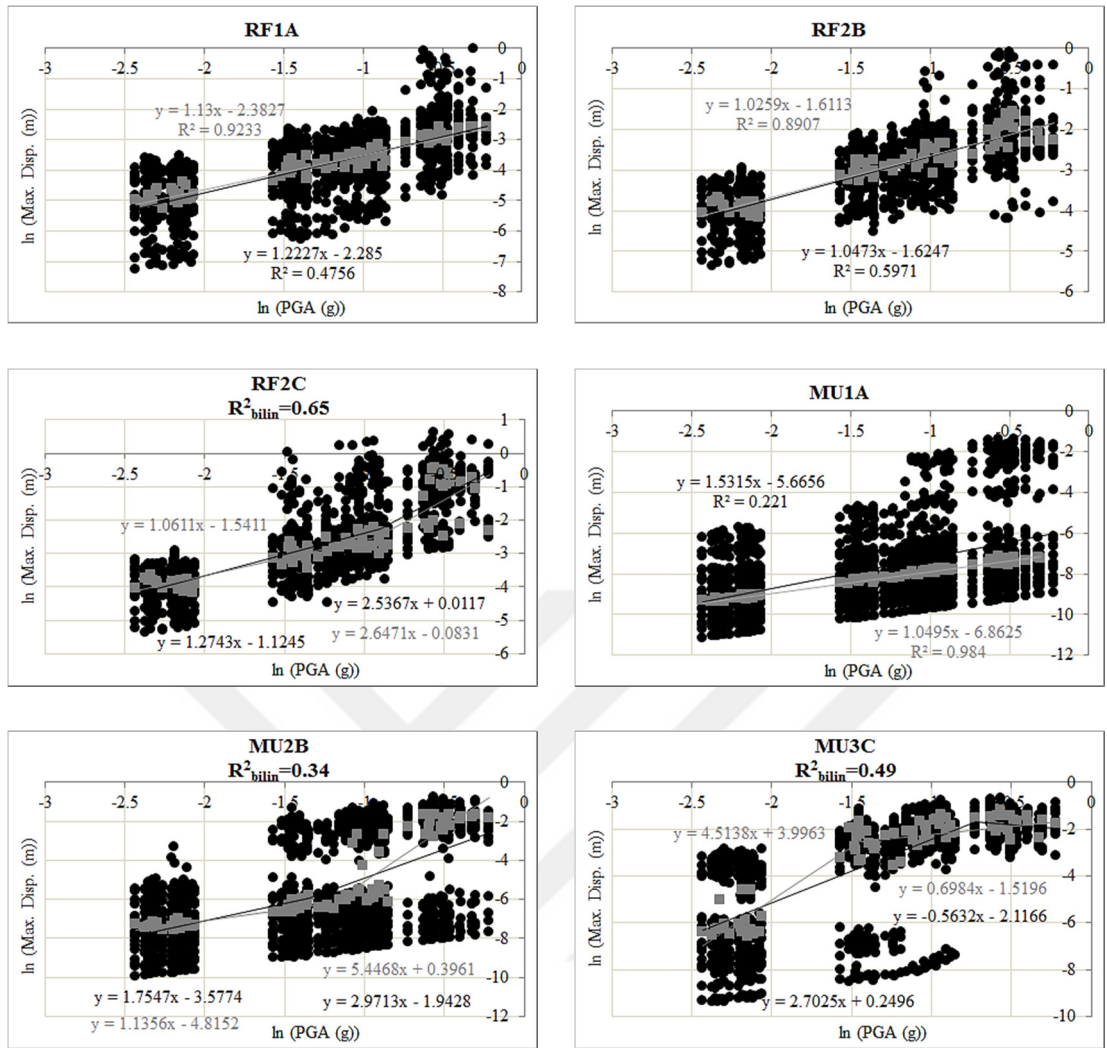


Figure 4.25. Variation of maximum displacement demand with respect to PGA and the predictive regression models for Site 2 without near-field forward directivity

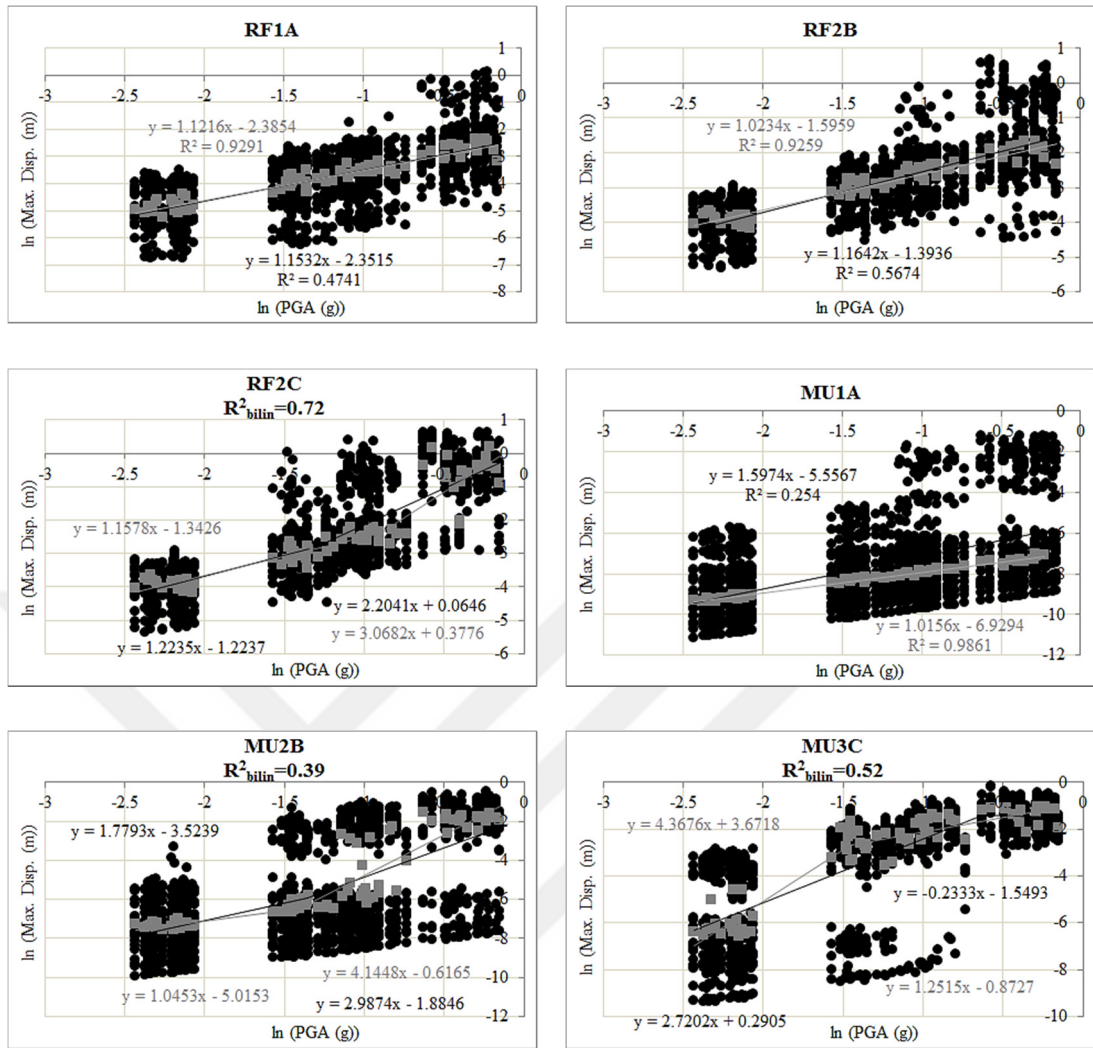


Figure 4.26. Variation of maximum displacement demand with respect to PGA and the predictive regression models for Site 2 with near-field forward directivity

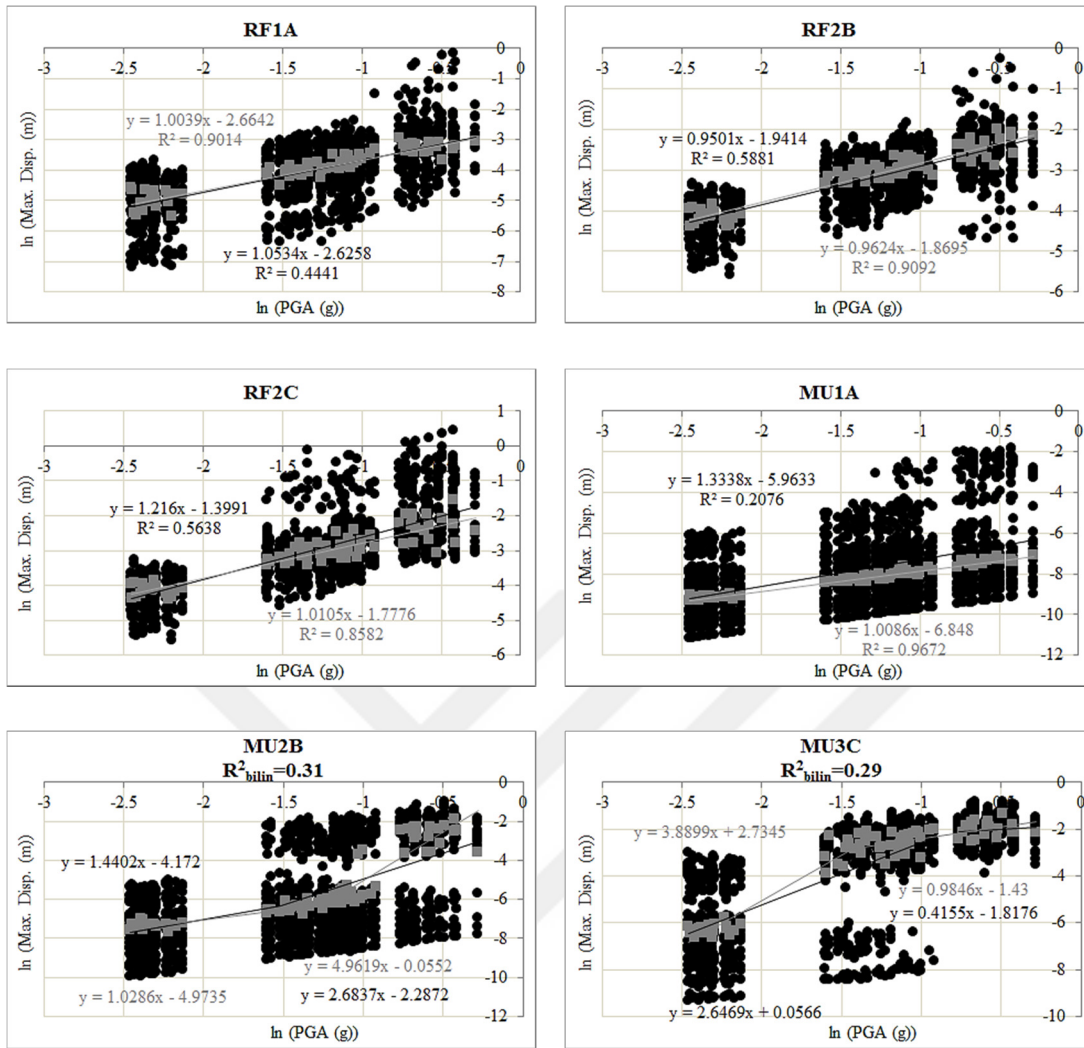


Figure 4.27. Variation of maximum displacement demand with respect to PGA and the predictive regression models for Site 3 using generic site amplification

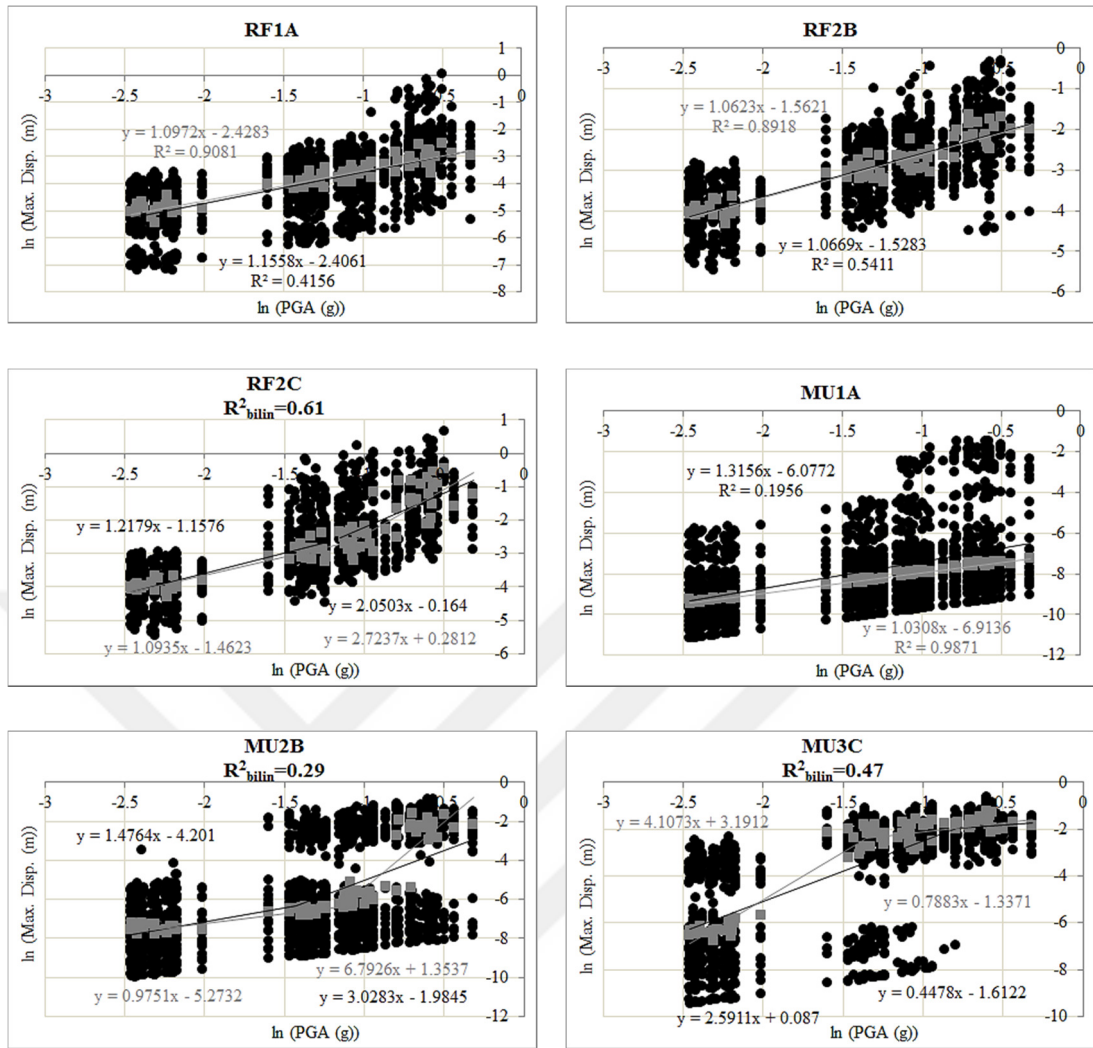


Figure 4.28. Variation of maximum displacement demand with respect to PGA and the predictive regression models for Site 3 using theoretical site amplification

Figures 4.23-4.28 indicate that, the median demands remain almost unchanged after considering structural variability for building sub-classes RF1A and RF2B. However, there is significant increase in median demands after considering structural variability regarding the building sub-class MU1A. Because the periods longer than mean period which cause larger displacement demands, are associated with larger spectral accelerations compared to the periods shorter than mean period regarding MU1A sub-class.

Considering structural variability generally reduces the median displacement demands of MU2B for larger PGAs regarding the whole sites. It generally reduces

the median displacement demands of MU3C for smaller PGAs regarding Site 1 and for larger PGAs regarding Site 2 and Site 3. The previous discussion regarding MU1A is not valid for MU2B and MU3C due to the period of T=0.2 seconds after which the spectral accelerations begin to decrease.

The slopes of two lines of the bilinear predictive models are similar to each other in the case of structural variability contrary to those of predictive models without structural variability especially for MU3C and MU2B. In other words, bilinear predictive models of ESDOFs with structural variability are close to linear especially for MU3C and MU2B, most probably due to large number of data while considering structural variability.

Figures 4.23-4.28 show median regression models, however, dispersion of regression models is not present in the figures. Dispersion of predictive model is defined as logarithmic uncertainty ($\beta_{D/IM}$) related to predicted demand given intensity measure, which is computed through the following equation according to Wen et al. (2004) and Hueste and Bai (2007):

$$\beta_{D/IM} = \sqrt{\ln\left(1 + \frac{\sum [\ln(D_{obs}) - \ln(\hat{D})]^2}{n - 2}\right)} \quad (4.12)$$

In this equation, D_{obs} is the observed displacement demand, \hat{D} is the median demand which is estimated from regression analyses and n is the sample size. Tables 4.17 and 4.18 represent $\beta_{D/IM}$ values regarding regression models, without and with structural variability, respectively. Dispersions are calculated for each line separately, regarding bilinear models.

Table 4.17. Logarithmic uncertainty ($\beta_{D/IM}$) regarding regression models, without structural variability (Section 4.3)

	RF1A	RF2B	RF2C	MU1A	MU2B	MU3C
Site 1/Generic	0.23	0.21	0.18,0.51	0.1	0.56,0.80	0.63,0.33
Site 1/Theoretical	0.25	0.21	0.41	0.1	0.77	0.69,0.3
Site 2/Without near-field	0.20	0.23	0.21,0.64	0.08	0.20,0.82	0.63,0.43
Site 2/With near-field	0.21	0.19	0.20,0.60	0.08	0.18,0.83	0.62,0.45
Site 3/Generic	0.23	0.19	0.26	0.12	0.19,0.70	0.41,0.36
Site 3/Theoretical	0.22	0.23	0.23,0.51	0.07	0.19,0.75	0.47,0.35

Table 4.18. Logarithmic uncertainty ($\beta_{D/IM}$) regarding regression models, with structural variability

	RF1A	RF2B	RF2C	MU1A	MU2B	MU3C
Site 1/Generic	0.70	0.50	0.60,0.63	1.27	1.24,1.30	1.21,0.47
Site 1/Theoretical	0.74	0.51	0.54	1.27	1.26	1.27,0.43
Site 2/Without near-field	0.72	0.52	0.62,0.70	1.22	1.16,1.38	1.19,0.47
Site 2/With near-field	0.71	0.63	0.56,0.74	1.23	1.15,1.38	1.19,0.49
Site 3/Generic	0.67	0.48	0.62	1.15	1.02,1.33	1.15,0.51
Site 3/Theoretical	0.75	0.57	0.61,0.72	1.16	1.1,1.38	1.21,0.52

According to Tables 4.17 and 4.18, taking structural variability into account considerably increases dispersion values. This observation is expected because number of data (n in Equation 4.12) is increased to a great extent. This increase in

dispersions is regarded as a shortcoming of structural variability because R^2 's of predictive demand models of ESDOFs with structural variability are quite small. However, taking structural variability into account has the advantage of considering the whole range of the most effective structural parameters. The dispersions of demand prediction equations specify the shape of fragility functions in Chapter 5.

4.7 Main Findings of Chapter 4

In this chapter, displacement demand prediction equations are developed for different ESDOF models with and without structural variability and different sites. The following observations are made in this chapter:

- The structures with high degradation characteristics (i.e. RF2C, MU2B and MU3C) require bilinear regression models in most of the cases.
- Residual analyses with respect to PGA, magnitude and distance show that the regression models are adequate in terms of PGA. Thus, it is decided that there is no need to add magnitude and distance to the predictive model.
- Residual analyses with respect to effective duration indicate that, there is no need to insert this parameter into the predictive model.
- Ground motion effective duration is shown to affect the displacement demands within PGA bins of the structures with high degradation characteristics more than those of the other structures. This impact is more obvious at near-field sites (Site 1 and 3).
- Effective duration affects different displacement demands of ground motions with similar PGAs regarding the structures with high degradation characteristics. This unexpected observation is obvious for Site 1 more than the other two sites due to the critical situation of this site.
- PGA, SI and PSa (T_1) are shown to affect displacement demands resulted from some ground motions with similar PGAs regarding the structures with high degradation characteristics. However, the effect of these parameters is observed to be less than effective duration for the ground motions under study.
- Structural variability increases the median demands of MU1A. However, it reduces the median demands of MU3C and MU2B for specific PGA ranges.

The median demands of RF1A and RF2B do not change so much after considering structural variability.

- The dispersions of demand prediction equations which specify the shape of fragility curves, are amplified when structural variability is considered.

This chapter has the following contributions:

- The demand prediction equations make fragility calculations (as presented in Chapter 5) significantly more practical.
- The effect of seismic parameters such as duration on structural demands is inspected via demand-PGA scatters along with demand predictive models in a straightforward manner.
- Ground motion simulation used in this dissertation facilitates the investigation of ground motion duration effect on seismic demand of structures. The regional characteristics of the duration effect could be inspected as well.



CHAPTER 5

SENSITIVITY ANALYSIS OF FRAGILITY FUNCTIONS

5.1 Introduction

In this chapter, the demand predictive models of ESDOFs, which were obtained in Chapter 4, are used to calculate fragility functions. Reliability formulation is applied to compute fragility functions based on median and dispersion properties of displacement demand. The effects of site conditions, forward directivity pulse model, alternative site amplification functions and structural variability on fragility curves are inspected in Sections 5.3, 5.4, 5.5 and 5.6, respectively. The main goal of this chapter is to observe the sensitivity of fragility curves to some regional seismological parameters related to the proposed regional hazard assessment. In Section 5.7, discontinuous fragility curves due to bilinear demand regression models are modified into continuous curves. In section 5.8, structural damage is estimated using fragility functions for two different ground motion scenarios. The sensitivity of estimated damage to seismological and structural parameters is also quantified in Section 5.8.

5.2 Methodology

Structural fragility is defined as exceedance probability of any damage limit state as a function of ground motion intensity measure. In this study, the fragility functions are derived using a well-known reliability formulation as follows (Ang and Tang, 1975):

$$P(LS_i | GMIP) = 1 - \Phi\left(\frac{\ln(\hat{C}) - \ln(\hat{D})}{\sqrt{\beta_C^2 + \beta_{D/IM}^2 + \beta_M^2}}\right) \quad (5.1)$$

where $P(LS_i | GMIP)$ is probability of exceeding the i^{th} limit state for a given ground motion intensity parameter (GMIP). Φ is the symbol for cumulative standard

normal distribution. \hat{D} and $\beta_{D/IM}$ are median displacement demand and corresponding uncertainty in logarithmic terms, respectively. These two parameters are estimated from regression analyses in Chapter 4. Parameters \hat{C} and β_c are median displacement capacity and its dispersion in logarithmic terms for the i^{th} limit state, respectively. Values of parameter \hat{C} are derived from Askan et al. (2015) as shown in Table 5.1. During the determination of limit state values for mean displacement capacity, previous studies in the literature have been considered (Akkar et al., 2005; Erberik, 2008a; Erberik, 2008b; Ay and Erberik, 2008) together with some engineering judgment. Accordingly, the displacement capacity values for RC frame models were obtained by assuming 0.2%, 1% and 2% interstory drift values for each limit state (i.e. LS1, LS2 and LS3), respectively and then converting these values to spectral displacement for the ESDOF models as given in Table 5.1. For masonry models, the mean displacement capacity values differ with the number of stories and the corresponding interstory drift values range between 0.02%-0.05%, 0.1%-0.5% and 0.3%-0.6% for limit states LS1, LS2 and LS3, respectively.

Table 5.1. Mean values of the displacement limit states for the considered ESDOF models (Askan et al., 2015)

Building class	limit state	Mean Sd (cm)
RF1A	LS1 (low damage)	1.55
	LS2 (intermediate damage)	6.7
	LS3 (high damage)	12.4
RF2B	LS1 (low damage)	2
	LS2 (intermediate damage)	8.1
	LS3 (high damage)	15.2
RF2C	LS1 (low damage)	1.65
	LS2 (intermediate damage)	7.11
	LS3 (high damage)	14.3
MU1A	LS1 (low damage)	0.071
	LS2 (intermediate damage)	0.249
	LS3 (high damage)	1.542
MU2B	LS1 (low damage)	0.141
	LS2 (intermediate damage)	0.368
	LS3 (high damage)	1.667
MU3C	LS1 (low damage)	0.105
	LS2 (intermediate damage)	0.516
	LS3 (high damage)	1.875

β_C parameter is assumed from the literature. Wen et al. (2004) stated that the value of $\beta_C=0.3$ is an appropriate measure for limit states which are derived from pushover analysis. This is also the average of dispersion values which are used by Erberik (2008a). Besides, Ramamoorthy et al. (2008) used $\beta_C=0.3$ during the generation of fragility curves in their study. Therefore capacity dispersion is assumed to be 0.3 in this study.

β_M is epistemic portion of uncertainty related to modeling. The most important source of epistemic uncertainty is the idealization of buildings as ESDOFs. This

parameter is also obtained from the literature. Wen et al. (2004) compared fragility curves of RC frames for $\beta_M=0.2, 0.3$ and 0.4 and observed no significant difference. Then they used the value of 0.3 for this parameter. Ellingwood et al. (2007) assumed $\beta_M=0.2$ for fragility calculations. In this study, modeling uncertainty is assumed to be 0.3 .

Regarding the bilinear demand prediction equations which were defined in Chapter 4, Equation 5.1 is applied for each line segment separately leading to discontinuous fragility functions. The main reason of discontinuous fragility curves is different \hat{D} and $\beta_{D/IM}$ values in Equation 5.1 for two line segments regarding bilinear demand prediction equations. This discontinuity is not tangible from the engineering point of view hence it is better to fit a continuous fragility curve to discontinuous ones using a lognormal fitting model.

5.3 The Effect of Site Condition on Fragility Curves

In this section, fragility functions are calculated for three sites, according to the procedures which were described in the previous section. Generic site amplification is considered for Site 1 and Site 3 and near-field effect is disregarded for Site 2 in this section. Predictive demand models of Section 4.3 are applied in this section so structural variability is disregarded (Figures 4.3, 4.5, 4.7 and Table 4.17). Fragility curves of Site 1 are regarded as benchmark and fragility curves of other two sites are compared with them. The main goal of these comparisons is to study the effects of distance to NAFZ (Site 1 versus Site 2) and site class (Site 1 versus Site 3) on fragility functions. Figures 5.1 and 5.2 show the aforementioned comparisons.

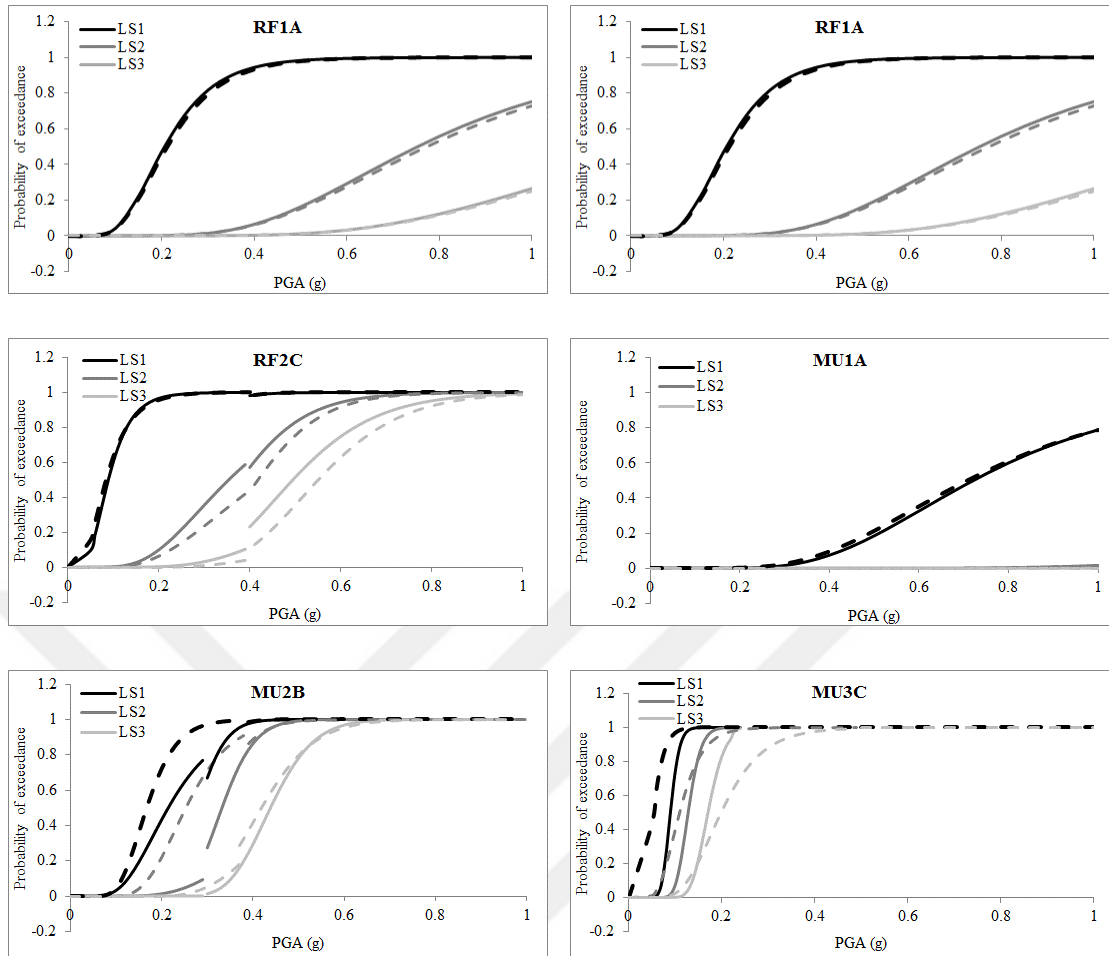


Figure 5.1. Fragility curves related to Site 2 (solid line) and Site 1 (dashed line)

Figure 5.1 exhibits that, Site 1 produces larger fragilities than Site 2 for MU2B as well as the first and the second limit states of MU3C. Because finite-fault model leads to higher high-frequency motions at close sites due to high stress concentrations. Assatourians and Atkinson (2007) investigated this point closely and concluded that high-frequency portion of spectrum is enhanced near high-stress patches on the fault.

Fragility curves of two sites are approximately coincident for RF1A and RF2B. Regarding RF2C, fragility of Site 2 becomes more critical especially for the second and the third limit states. One of the effective parameters herein is ground motion duration. As it was mentioned in Chapter 3, duration model consists of source and

distance terms. According to this model, duration becomes longer by increasing distance. Duration parameter has catastrophic impact on deficient structures more than other structures, as it was shown in Chapter 4. The fragility functions are observed to be dependent on site conditions in this study due to different regional parameters of selected ground motions at different sites.

Fragility curves related to bilinear models (RF2C, MU2B and MU3C) are observed to be discontinuous. Because there are two different demand models for two line segments. Although median demand models of two line segments are the same at intersection point, demand dispersions are different for them. This difference in $\beta_{D/IM}$ for two line segments leads to jumps in fragility curves. This discontinuity is not very obvious for MU3C because failure occurs in PGA values less than intersection point. This means that, the second line segment which has a lower slope, does not play an important role for this model.

It is notable that, these jumps are not physically reasonable but they appear due to mathematical reasons as were explained previously. Therefore it is more logical to fix them in practical situations. Ramamoorthy et al. (2006, 2008) encountered similar jumps in fragility curves because of developing bilinear predictive demand models. The authors proposed a lognormal function to obtain a continuous fragility curve. This lognormal fitting model as well as its applications in fragility functions of this study are explained in Section 5.7.

Another important observation of Figure 5.1 is related to MU1A. Fragility curves of LS2 and LS3 are very close to zero for this ESDOF model. This is due to the fact that mean displacement capacity of MU1A model is very high so LS2 and LS3 are not excited at all for the given range of PGA. In this model, the probability curves of LS1 for two sites are approximately coincident.

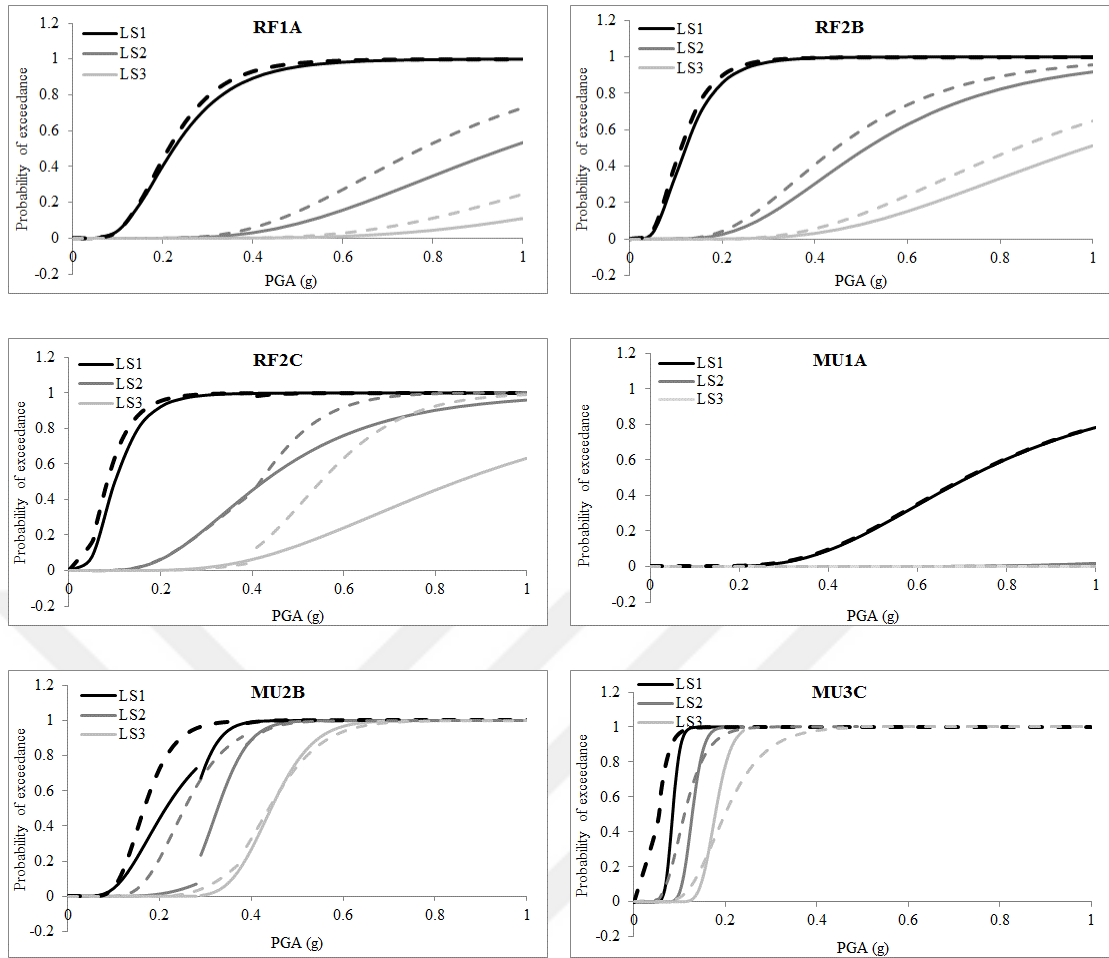


Figure 5.2. Fragility curves related to Site 3 (solid line) and Site 1 (dashed line)

The comparison of the fragility curve sets in Figure 5.2 reveals that RF sub-class on soft soil (Site 1) are more fragile than the ones on stiff soil (Site 3). The difference in fragilities even becomes more significant for deficient sub-class (i.e. RF2C). This trend is in accordance with the field observations after major earthquakes in which most of the deficient RC frame buildings in districts with soft soil condition have either experienced severe damage or collapse. For masonry buildings, the trend seems to be different due to the dynamic characteristics of these building sub-classes. Since masonry buildings are generally rigid structures, it may be expected that they are influenced when they reside on stiff soil conditions, especially if they have been constructed in a non-engineered manner.

5.4 The Effect of Near-Field Forward Directivity on Fragility Curves

In this section, the effect of near-field forward directivity is investigated on the fragility curves related to Site 2. The predictive demand models of Figure 4.6 are used to derive fragility functions and they are compared with the ones in Figure 5.1. Figure 5.3 shows the effect of forward directivity model on fragility curves.

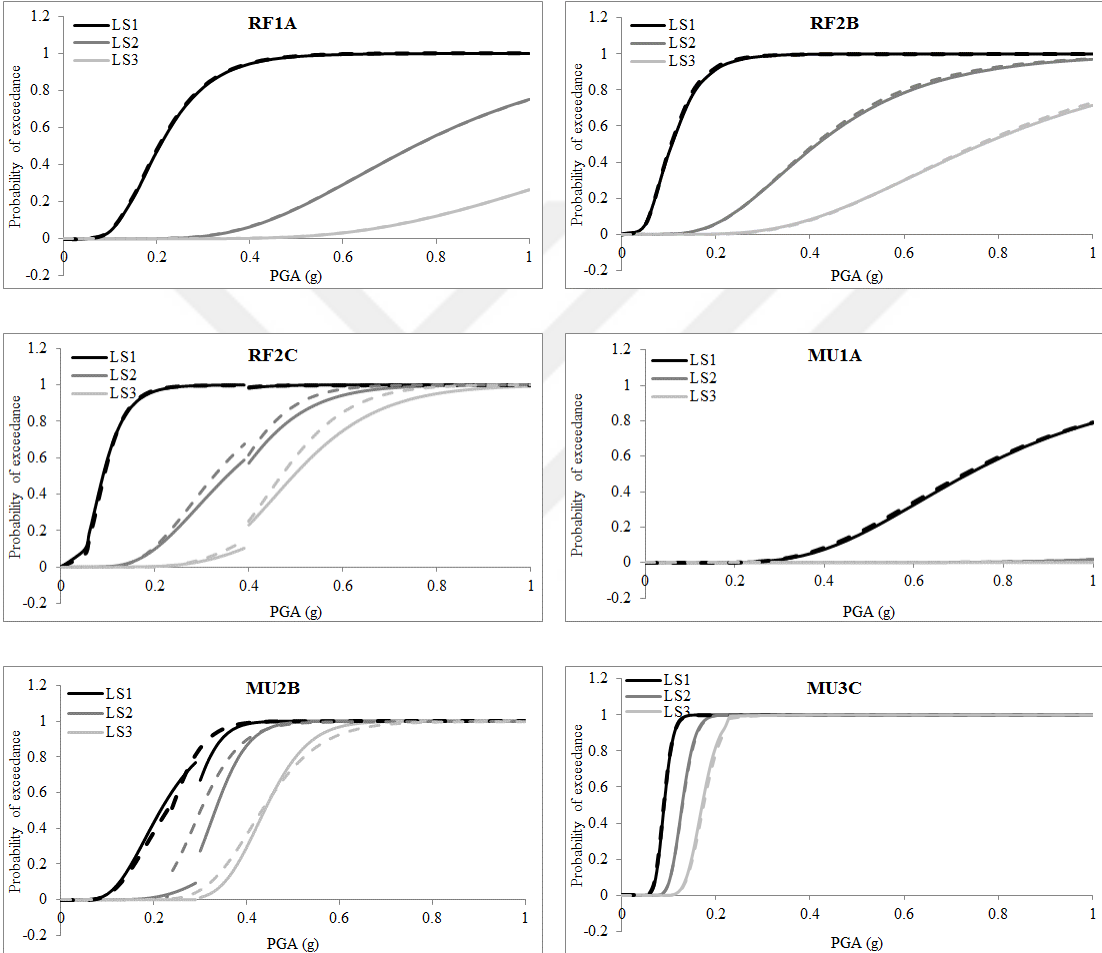


Figure 5.3. Fragility curves related to Site 2 with (dashed line) and without (solid line) near-field forward directivity

According to Figure 5.3, structural models are not affected from the analytical pulse model simulating the forward directivity effect except for RF2C and MU2B. The impact of forward directivity on these two models can be regarded as minor.

According to Chapter 3, forward directivity analytical pulse (Mavroeidis and Papageorgiou, 2003) is applied for ground motions with magnitude larger than $M_w=6$ since Equation 3.9, which is used to estimate pulse amplitude, is valid for magnitude range of 6 to 8. Because there is lack of historical ground motions with pulse-like behavior and magnitude smaller than 6. Therefore minimum pulse period is 1.25 seconds according to Equation 3.5 which is above the fundamental period range of ESDOF models in this study. The reason for RF2C and MU2B being affected very slightly is that, these models have high deterioration characteristics. The reason for MU3C not being affected is that, this model experiences failure at very low PGA levels (less than 0.2 g).

In order to verify the above observation, 13 March 1992 Erzincan earthquake, ERC station recording is simulated with and without forward directivity pulse model. This ground motion was applied in Chapter 3 to calibrate input pulse parameters. This ground motion is used for nonlinear time history analyses and displacement demand history of each ESDOF is plotted with and without near-field effects. Figure 5.4 illustrates these comparisons.

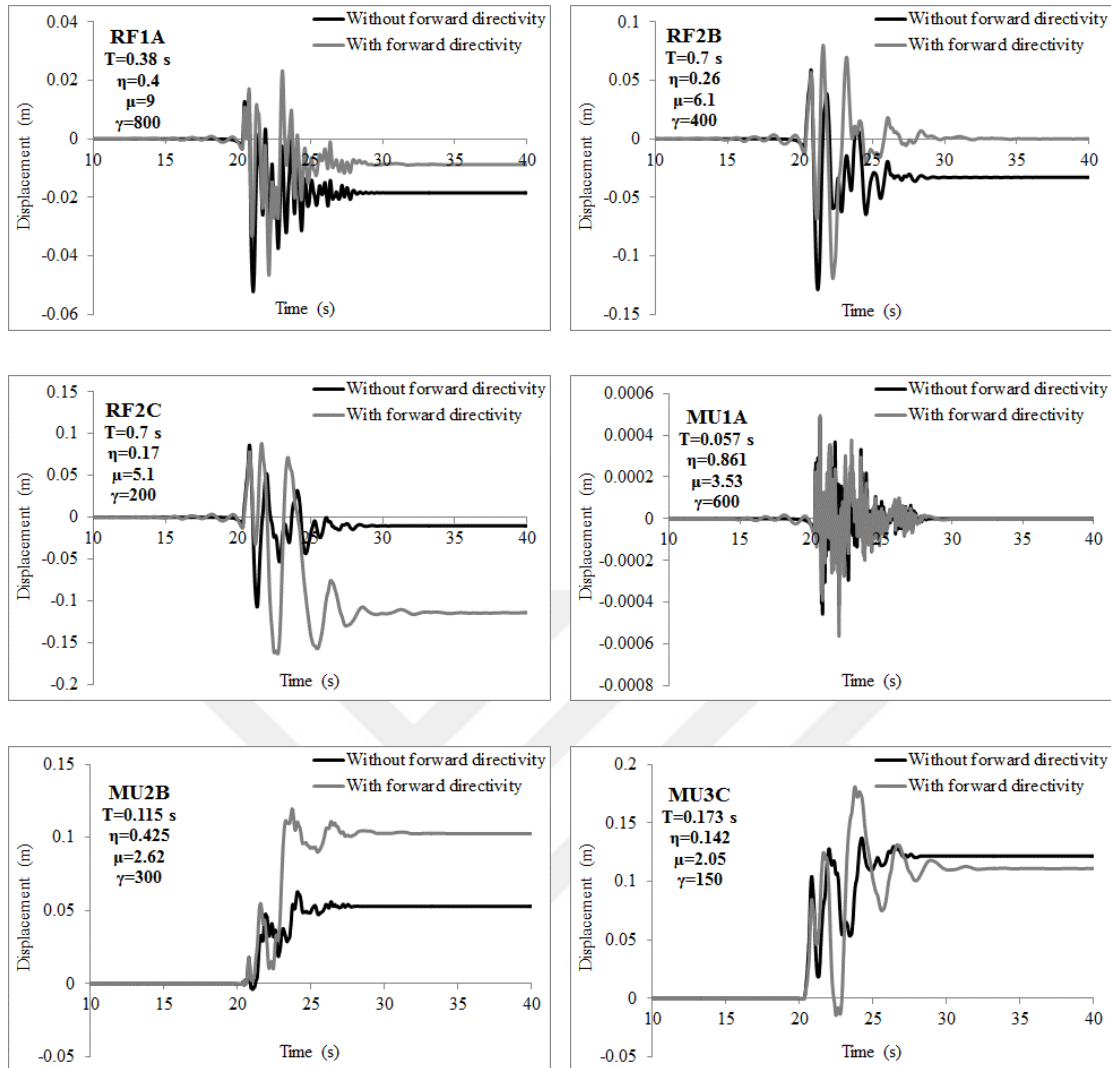


Figure 5.4. Displacement demand histories of ESDOFs using 13 March 1992 Erzincan, ERC recording with and without near-field forward directivity

Figure 5.4 confirms the observations about fragility curves. Forward directivity model has an effect on MU2B and RF2C only. Therefore near-field long-period pulse model in this study, does not influence typical low-rise and mid-rise residential buildings modeled as ESDOFs in a significant manner.

5.5 The Effect of Site Amplification Functions on Fragility Curves

In this section, fragility functions of Site 1 and 3 are recomputed using theoretical site amplification. The predictive demand models of Figures 4.4 and 4.8 are taken

into account in this section. Fragility curves are compared with the ones using generic site amplification which were shown in Section 5.3. Figures 5.5 and 5.6 illustrate those comparisons regarding Site 1 and 3, respectively.

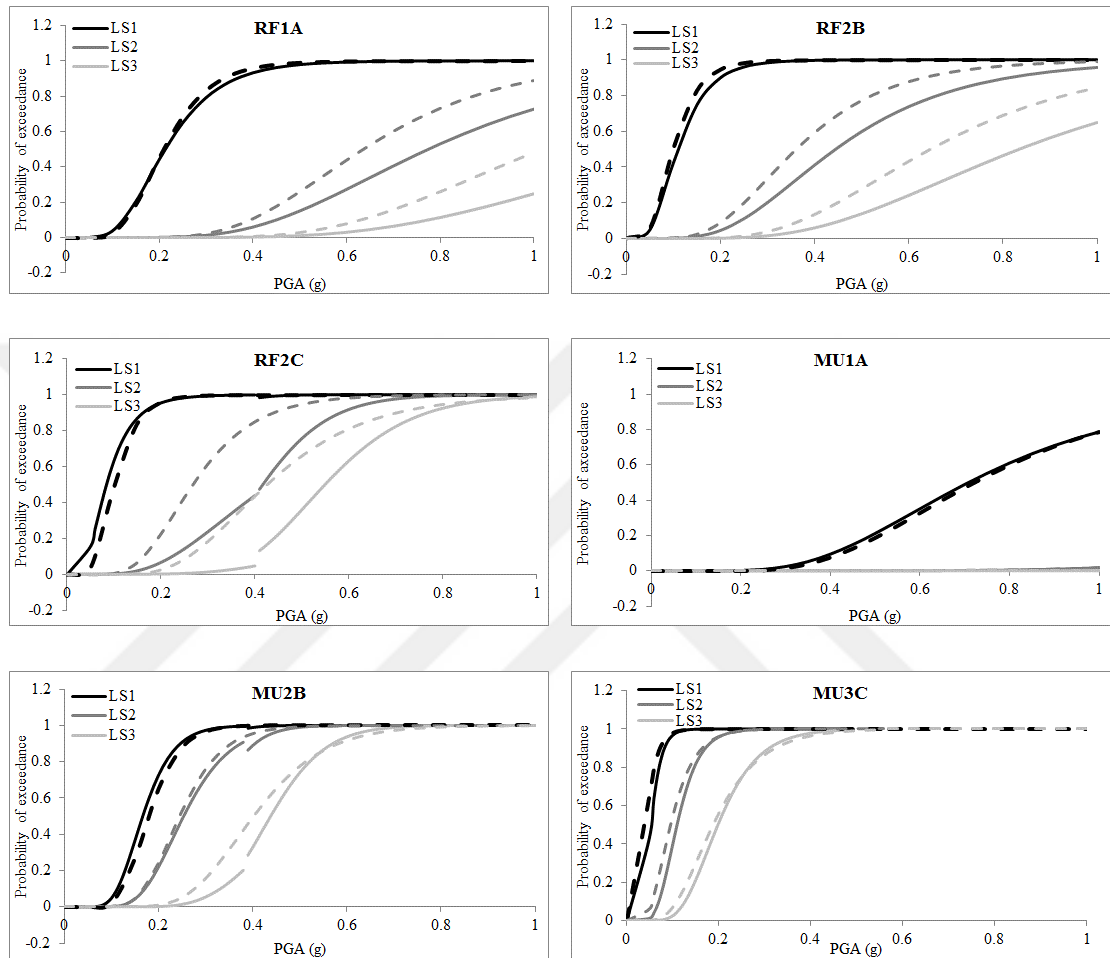


Figure 5.5. Fragility curves related to Site 1 using generic (solid line) and theoretical (dashed line) site amplification function

Figure 5.5 indicates that, theoretical site amplification increases seismic fragility functions for RC frames, considerably. This increase becomes more apparent for the second and third limit states of RF2C because of its severe deterioration characteristics. The effect of theoretical site function on masonry models is not as considerable as RC frame models, even it decreases fragilities for some limit states.

The main reason is that, theoretical site amplification has complex behavior and considerably larger peaks than generic site function for long periods (Figure 3.16).

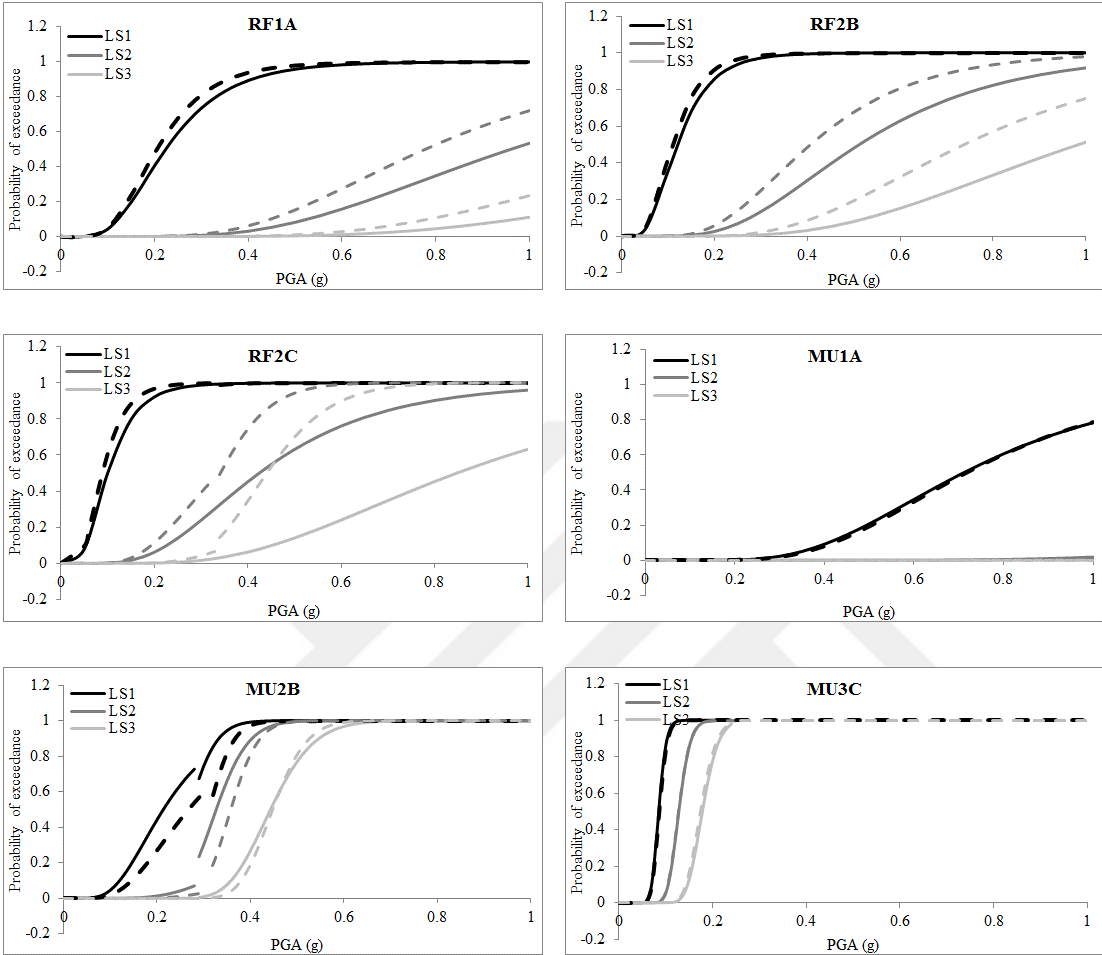


Figure 5.6. Fragility curves related to Site 3 using generic (solid line) and theoretical (dashed line) site amplification function

The results of Figure 5.6 related to Site 3 are to some extent similar to Figure 5.5 of Site 1. Considerable and negligible differences between fragility curves are observed regarding RC frames and masonry models, respectively. Theoretical site amplification increases seismic fragility functions of RF2C model for Site 3 much more than Site 1. The difference between theoretical and generic site amplifications at low frequencies of Site 3 is more than that of Site 1. Besides, the structures with

high deterioration are affected by detailed site response more than other structural models.

5.6 The Effect of Structural Variability on Fragility Curves

In Section 4.6, structural variability of each ESDOF model was taken into account using the LHS method. In this section, predictive demand models of Section 4.6, Figures 4.23-4.28 and Table 4.18 are used to derive fragility functions. The obtained fragility curves are compared with the ones related to ESDOF models without structural variability in Sections 5.3, 5.4 and 5.5. Figures 5.7-5.12 exhibit the impact of structural variability on fragility curves.

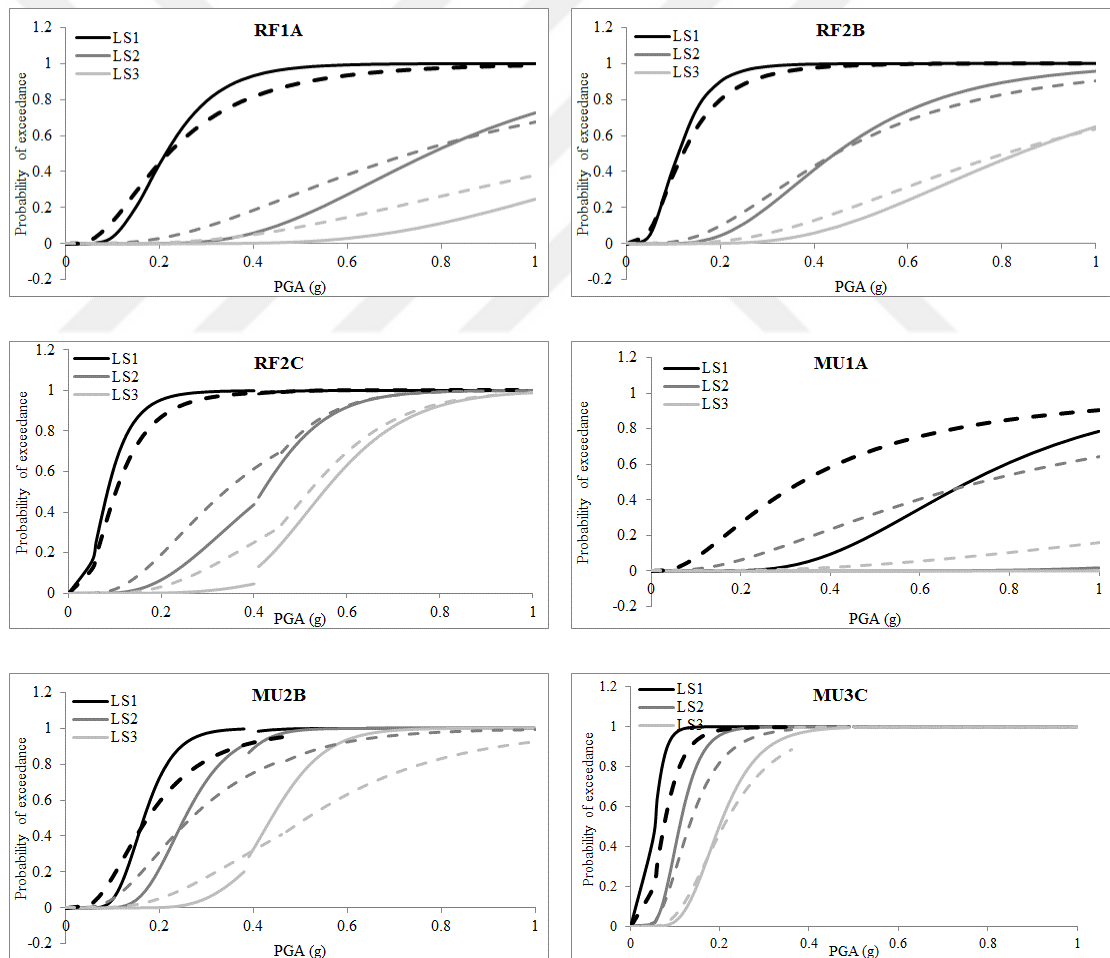


Figure 5.7. Fragility curves related to Site 1 using generic site amplification without (solid line) and with (dashed line) structural variability

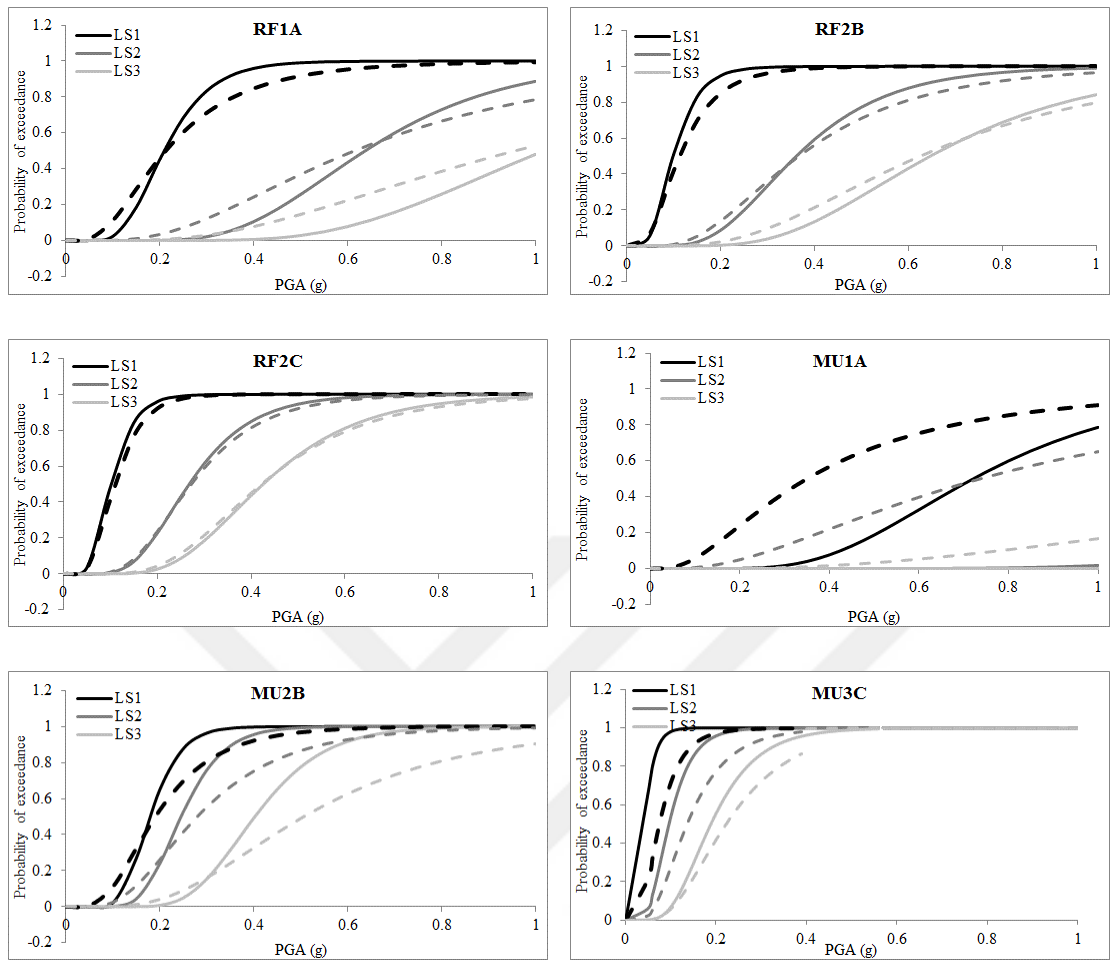


Figure 5.8. Fragility curves related to Site 1 using theoretical site amplification without (solid line) and with (dashed line) structural variability

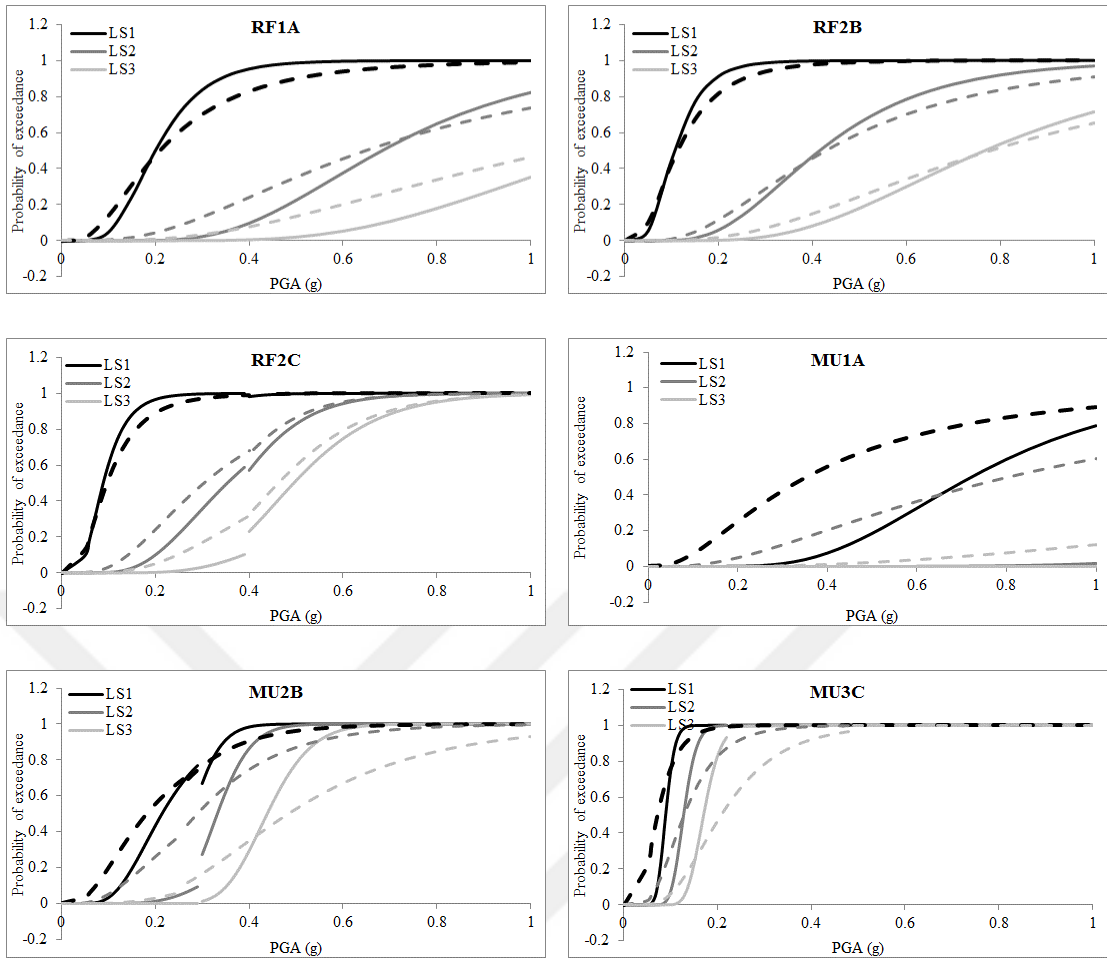


Figure 5.9. Fragility curves related to Site 2 without near-field forward directivity without (solid line) and with (dashed line) structural variability

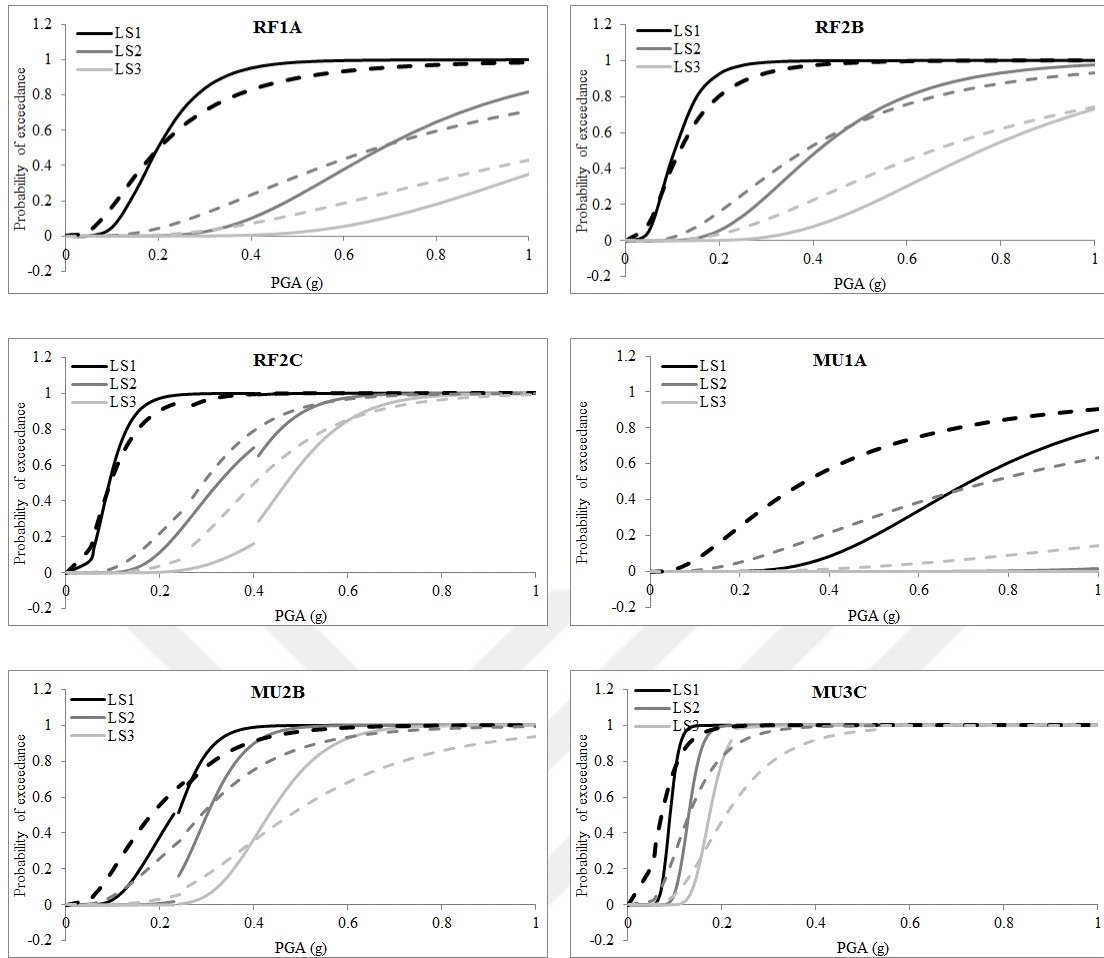


Figure 5.10. Fragility curves related to Site 2 with near-field forward directivity without (solid line) and with (dashed line) structural variability

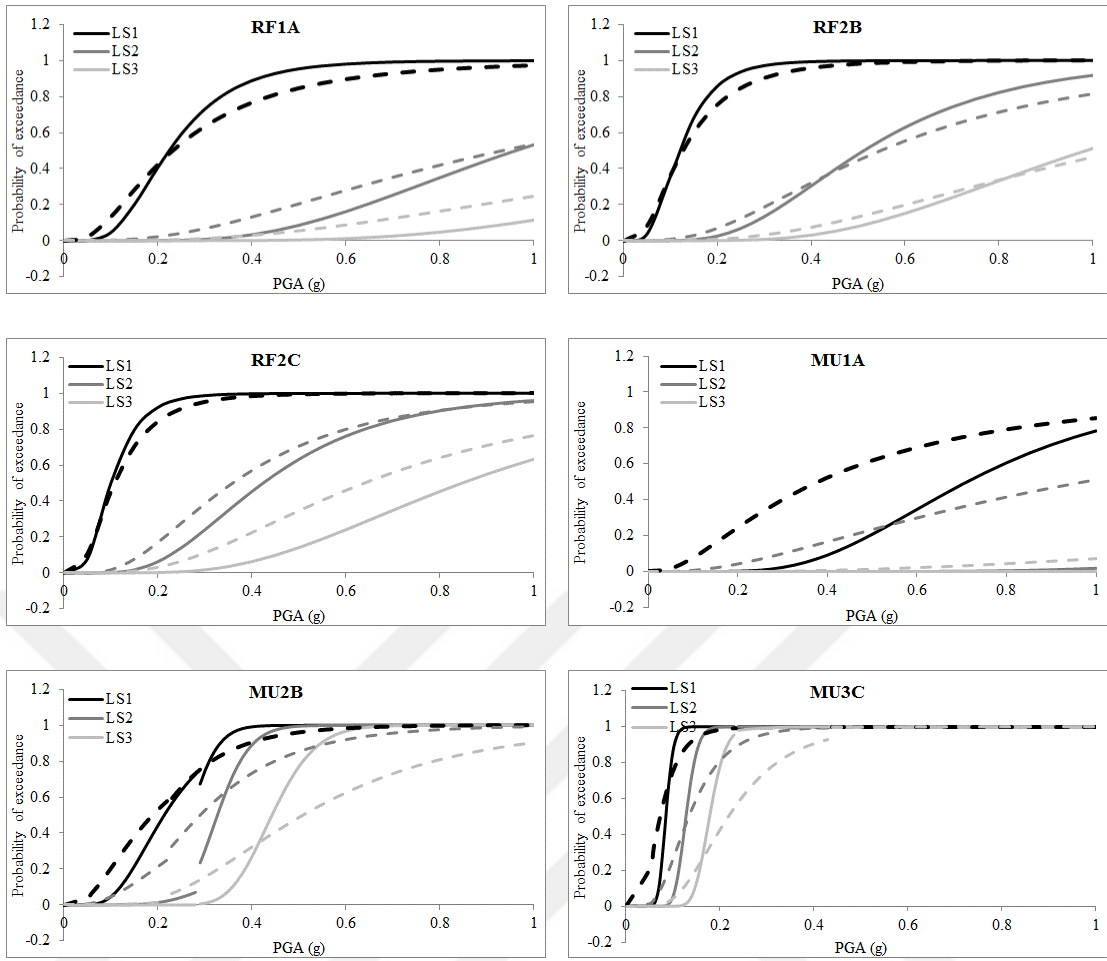


Figure 5.11. Fragility curves related to Site 3 using generic site amplification without (solid line) and with (dashed line) structural variability

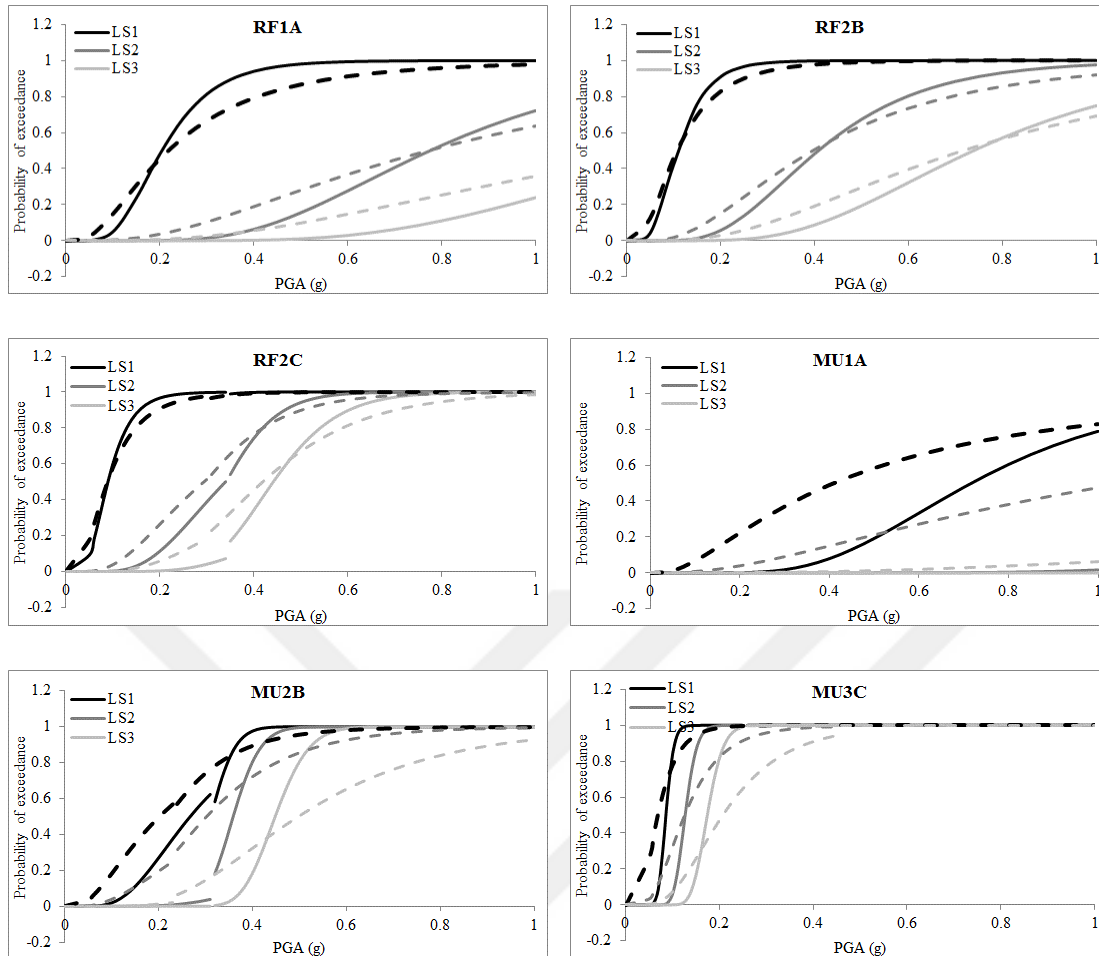


Figure 5.12. Fragility curves related to Site 3 using theoretical site amplification without (solid line) and with (dashed line) structural variability

It is observed that, presence of structural variability has a notable impact on seismic fragility of MU1A model more than the other models. MU1A model that represents well-designed 1 story masonry buildings with a very short mean period ($T=0.06$ seconds), a high mean yielding capacity ($\eta=0.86$) and a limited mean ductility factor ($\mu=3.5$). For such a rigid structure with small variation in one of the parameters can cause a drastic change in the displacement response of the model. It is not easy to predict the change in seismic demand of the model beforehand, but this ESDOF model becomes more vulnerable to seismic action after considering structural variability. The fragility functions are generally reduced for larger PGA values after executing structural variability, regarding MU2B and MU3C. This decrease is more

obvious for MU2B than MU3C. The effect of structural variability on RC frames is less evident than masonry buildings due to the previous discussions about MU1A. In nearly all of the cases, the slopes of the fragility curves seem to be flatter when compared to their counterparts that have been generated without considering structural variability. This is expected due to the increase in logarithmic uncertainty parameter ($\beta_{D/IM}$) due to presence of structural variability which is reflected in Tables 4.17 and 4.18.

5.7 Continuous Fragility Functions

As it was mentioned in the previous sections, fragility functions related to bilinear demand predictive models are discontinuous. The main reason of this discontinuity is two different dispersions for two line segments which is not reasonable from engineering point of view. Therefore it is recommended to fit a continuous fragility function to these separate curves. Ramamoorthy et al. (2006, 2008) proposed a lognormal function as follows to estimate the continuous fragility curve:

$$\hat{F}(PGA) = \Phi\left(\frac{\ln(PGA) - \gamma_1}{\gamma_2}\right) \quad (5.2)$$

where $\hat{F}(PGA)$ is continuous fragility function. γ_1 and γ_2 are unknown parameters which are estimated using nonlinear regression analysis by fitting $\hat{F}(PGA)$ on the calculated fragility curves. In this study, MATLAB program is used to fit a nonlinear curve with functional formulation of Equation 5.2 on derived fragility curves from the previous sections. Figures 5.13-5.18 show original discontinuous fragility functions as well as fitted continuous fragility curves. Structural variability is neglected in the following figures.

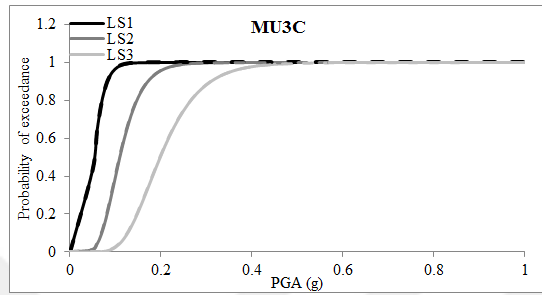
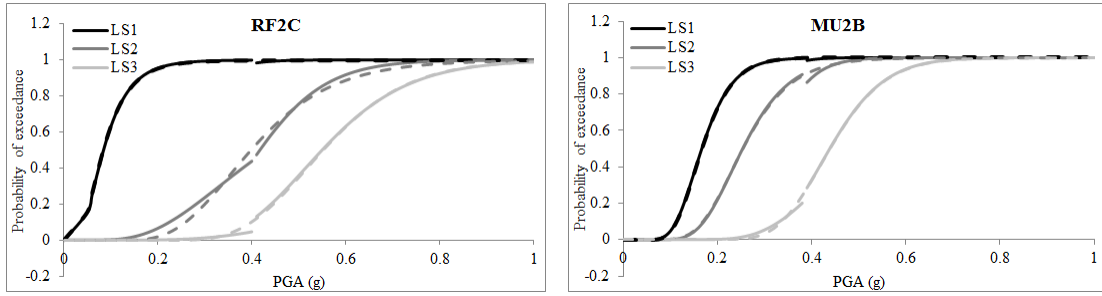


Figure 5.13. Continuous fitted fragility curves (dashed line) and discontinuous original fragility curves (solid line) for Site 1 using generic site amplification (without structural variability)

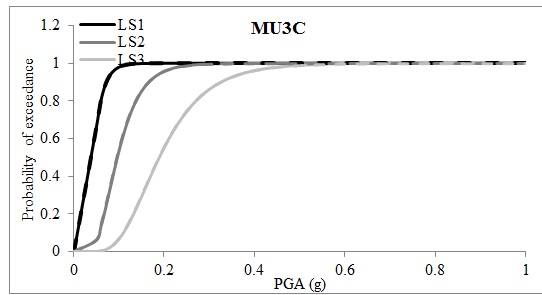


Figure 5.14. Continuous fitted fragility curves (dashed line) and discontinuous original fragility curves (solid line) for Site 1 using theoretical site amplification (without structural variability)

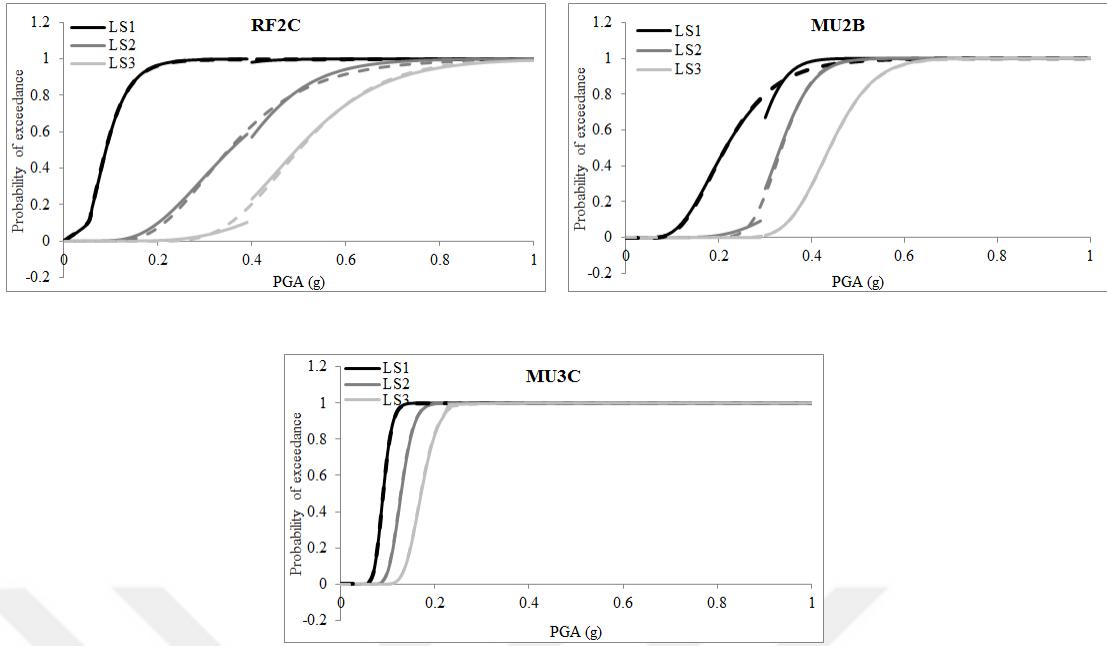


Figure 5.15. Continuous fitted fragility curves (dashed line) and discontinuous original fragility curves (solid line) for Site 2 without near-field forward directivity (without structural variability)

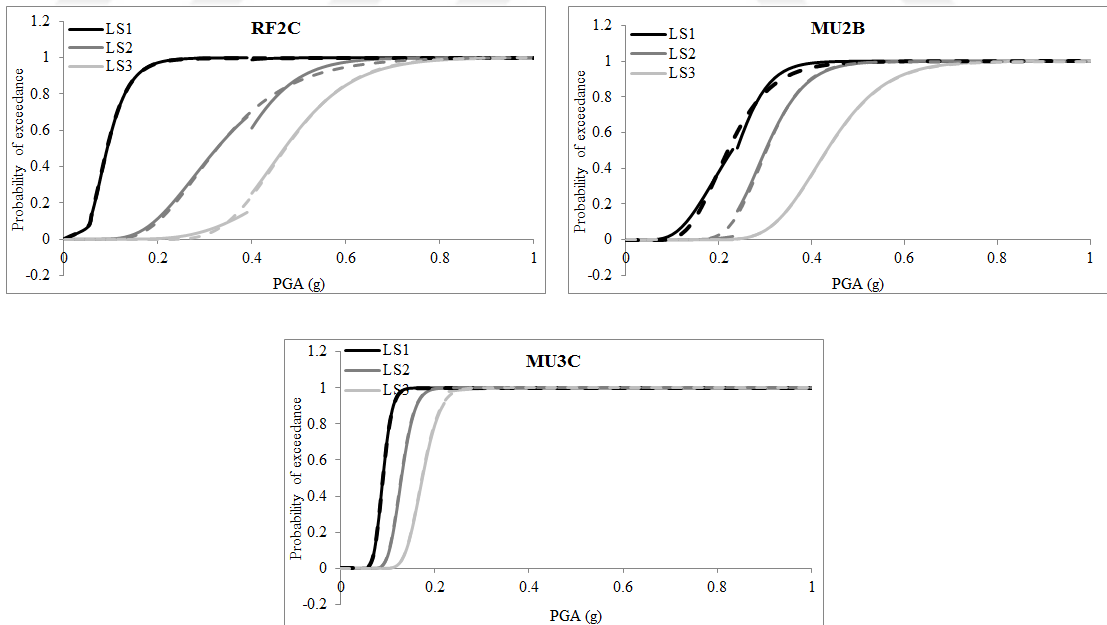


Figure 5.16. Continuous fitted fragility curves (dashed line) and discontinuous original fragility curves (solid line) for Site 2 with near-field forward directivity (without structural variability)

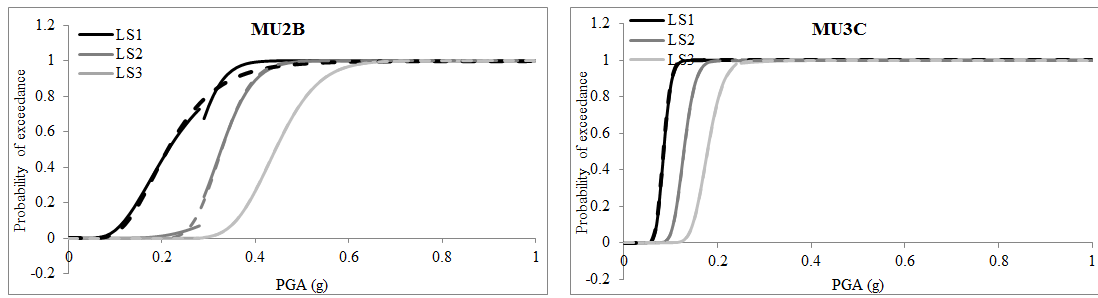


Figure 5.17. Continuous fitted fragility curves (dashed line) and discontinuous original fragility curves (solid line) for Site 3 using generic site amplification (without structural variability)

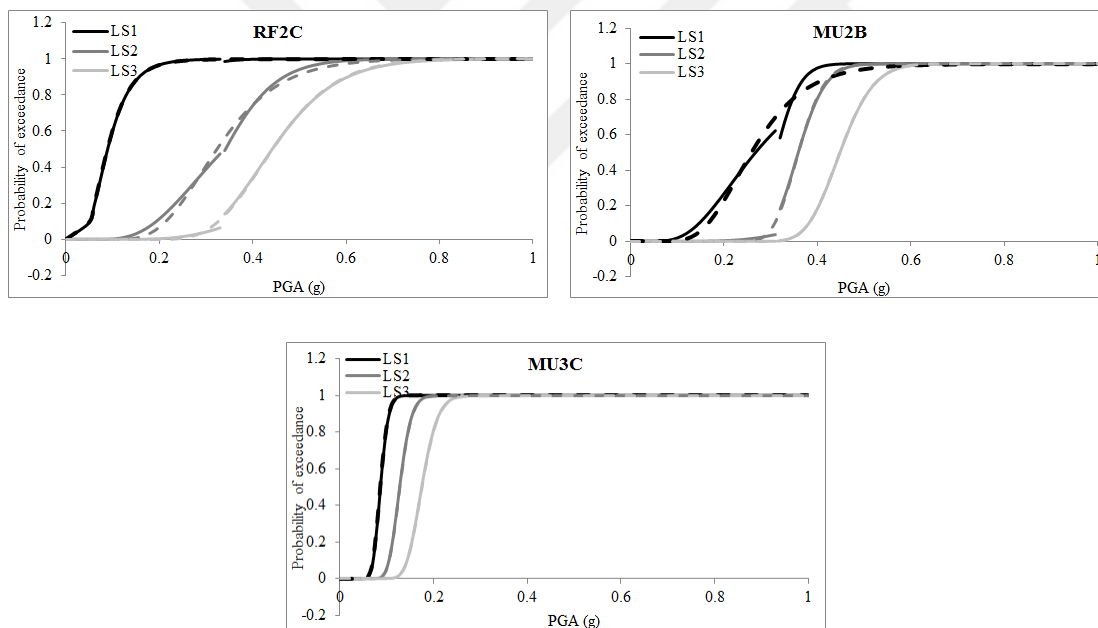


Figure 5.18. Continuous fitted fragility curves (dashed line) and discontinuous original fragility curves (solid line) for Site 3 using theoretical site amplification (without structural variability)

As it is observed from the Figures 5.13-5.18, fitted and original fragility curves for MU3C are exactly identical as discontinuity occurs after failure for this ESDOF model. Fitted and original fragility functions for MU2B exhibit minor differences for Site 2 and Site 3. The slopes of two lines related to the prediction equations of MU2B are quite different at Site 2 and 3 (Figures 4.5-4.8). Hence two separate fragility curves do not actually follow an individual lognormal function regarding this model and these sites. Fitted and original fragility functions for RF2C match closely especially for LS1 and LS3.

Figures 5.19-5.24 represent fragility functions after considering structural variability.

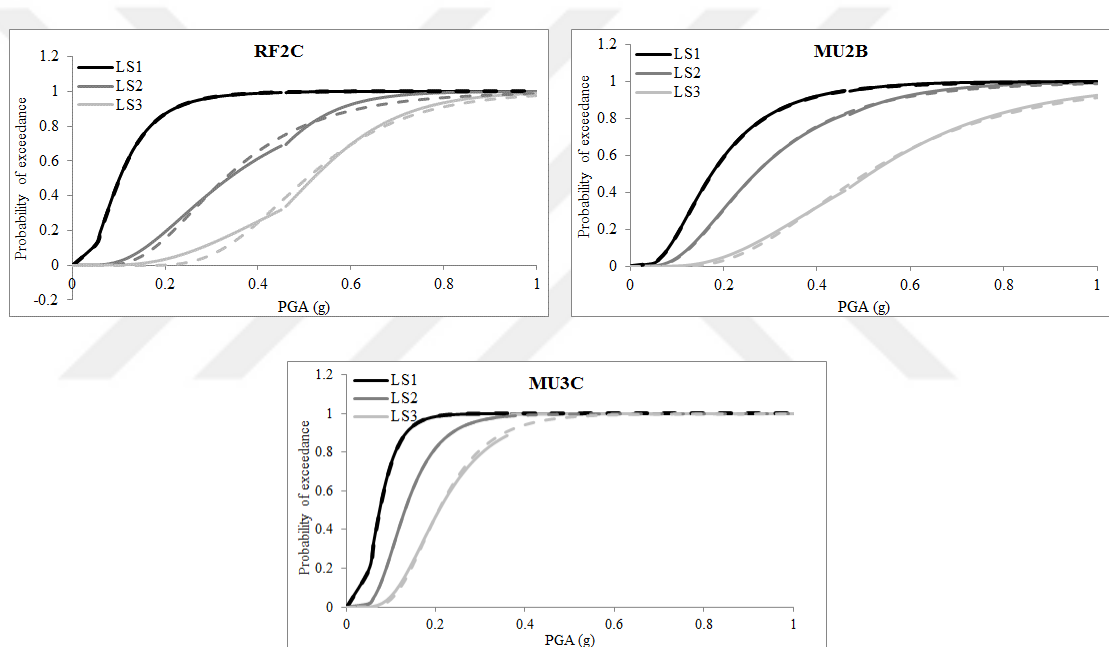


Figure 5.19. Continuous fitted fragility curves (dashed line) and discontinuous original fragility curves (solid line) for Site 1 using generic site amplification (with structural variability)

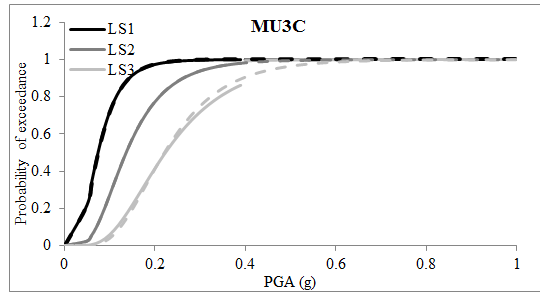


Figure 5.20. Continuous fitted fragility curves (dashed line) and discontinuous original fragility curves (solid line) for Site 1 using theoretical site amplification (with structural variability)

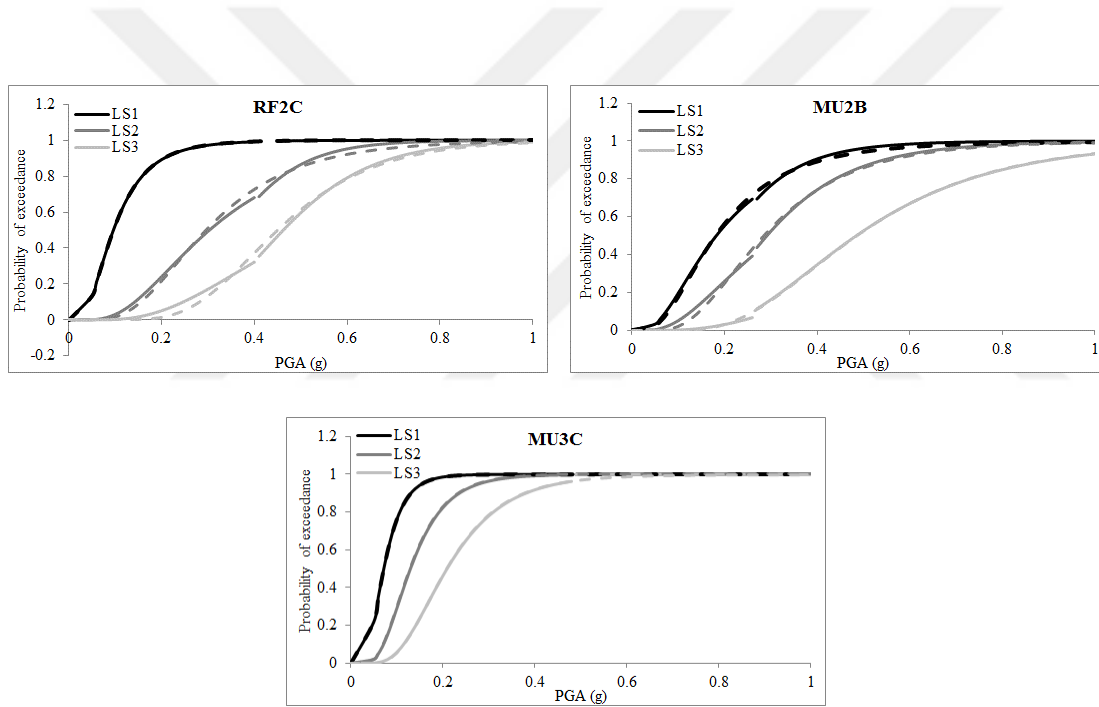


Figure 5.21. Continuous fitted fragility curves (dashed line) and discontinuous original fragility curves (solid line) for Site 2 without near-field forward directivity (with structural variability)

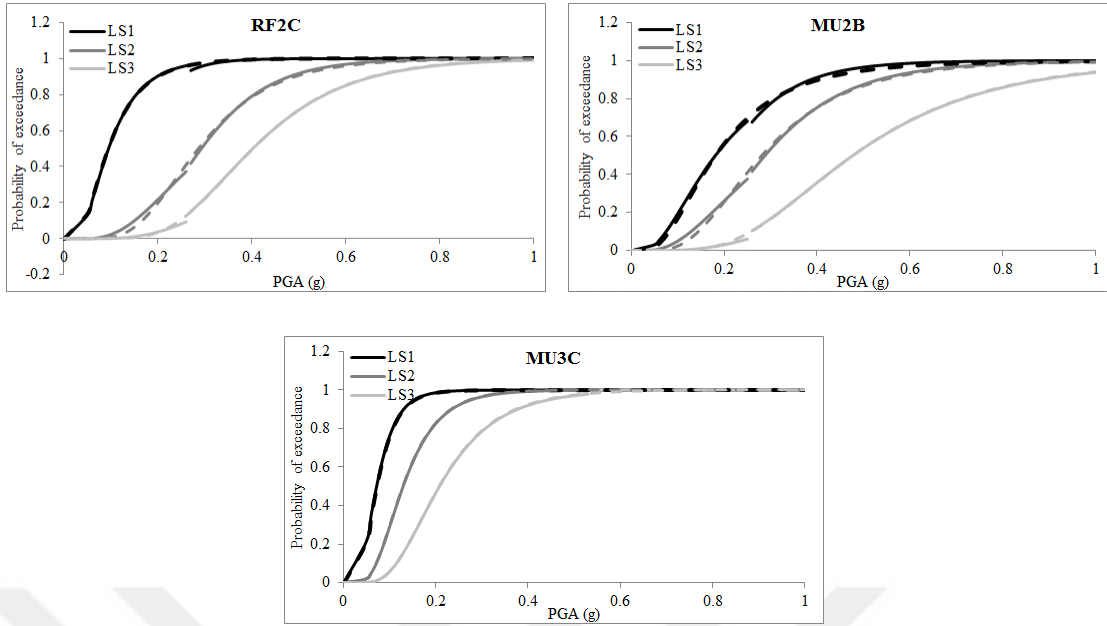


Figure 5.22. Continuous fitted fragility curves (dashed line) and discontinuous original fragility curves (solid line) for Site 2 with near-field forward directivity (with structural variability)

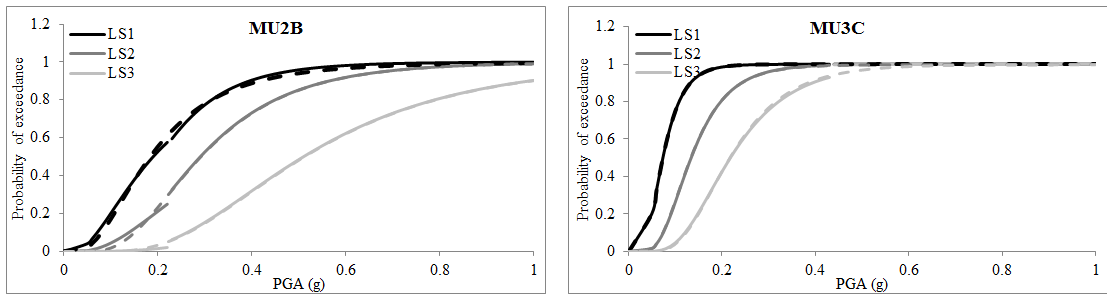


Figure 5.23. Continuous fitted fragility curves (dashed line) and discontinuous original fragility curves (solid line) for Site 3 using generic site amplification (with structural variability)

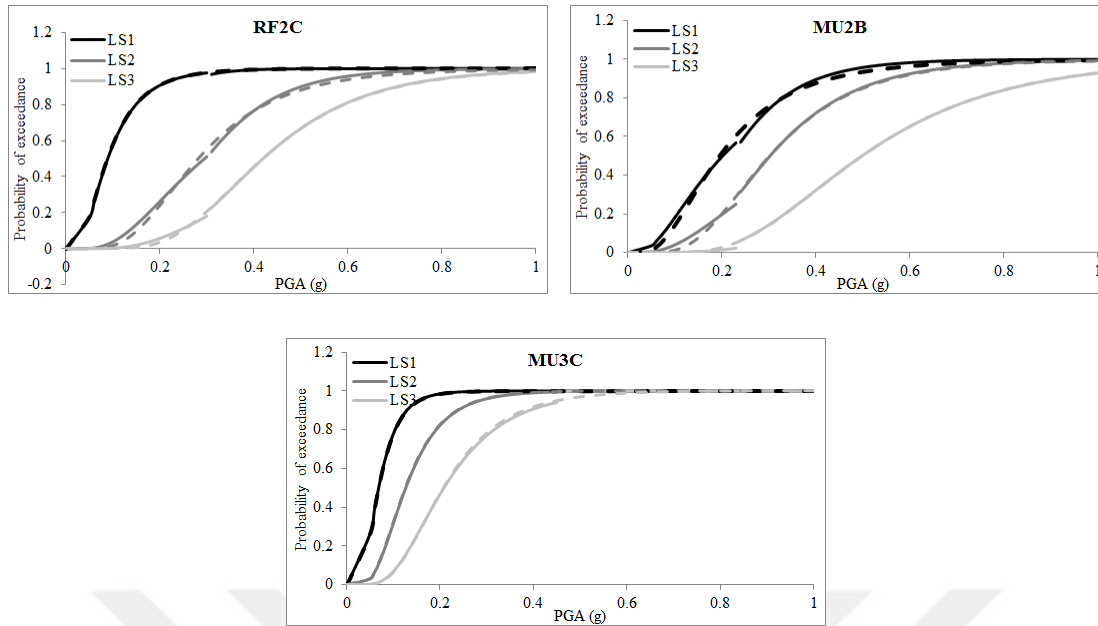


Figure 5.24. Continuous fitted fragility curves (dashed line) and discontinuous original fragility curves (solid line) for Site 3 using theoretical site amplification (with structural variability)

According to Figures 5.19-5.24, MU3C model exhibits an excellent match between continuous and discontinuous fragility curves similar to the case without structural variability. The estimated fragility function provides a better fit to the original one after applying structural variability, regarding MU2B model. Although discontinuous fragility functions are more accurate, estimated continuous functions are recommended to be used in practical situations since they are more physically meaningful.

5.8 Sensitivity of Estimated Damage to Seismological and Structural Parameters

In this section, the sensitivity of fragility curves to different parameters are quantified for a single ground motion scenario. The main aim of this section is to express the sensitivity of fragility curves in a more tangible manner. For this purpose, damage state probabilities are calculated from fragility functions of the previous sections for None, Light, Moderate and Severe damage states (DSs). Continuous fragility functions, which were defined in Section 5.7, are applied in this

section regarding bilinear demand models. Figure 5.25 shows damage state definitions with respect to fragility curves in this study. Dashed line shows estimated PGA value related to the ground motion scenario under consideration. Mean damage ratio (MDR) is then calculated using damage state probabilities according to Equation 5.3.

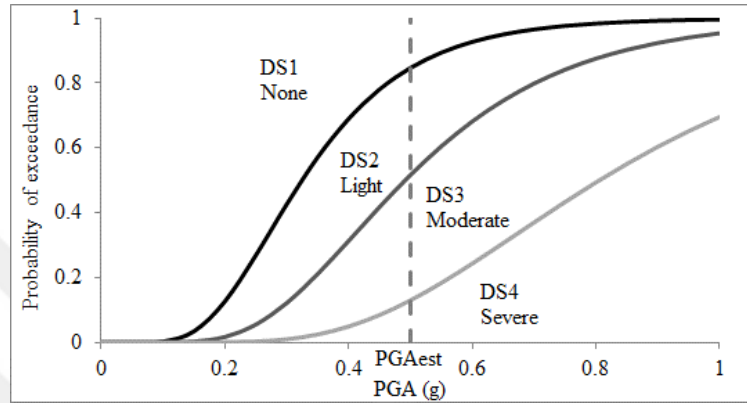


Figure 5.25. Damage state definitions on fragility functions in this study.

$$\text{MDR} = \sum_{i=1}^4 P(\text{DS}_i) \cdot \text{CDR}(\text{DS}_i) \quad (5.3)$$

where $P(\text{DS}_i)$ is the probability of i^{th} damage state which is obtained from the fragility curves as seen in Figure 5.25. CDR is central damage ratio corresponding to each damage state. Gurpinar et al. (1978) estimated CDRs as in Table 5.2 based on expert opinions and the previous studies. The severe and collapse damage states in Table 5.2 are combined and the mean CDR is used for severe damage state in this study.

Table 5.2. CDR values in this study (Adapted from Gurpinar et al., 1978)

Damage State	CDR (%)
None	0
Light	5
Moderate	30
Severe	70
Collapse	100

5.8.1 The Effect of Site Amplification and Forward Directivity Pulse on Estimated Damage due to 13 March 1992 Erzincan Earthquake

In this sub-section, the simulated ground motions from 13 March 1992 Erzincan earthquake at Site 1, 2 and 3 are employed. Generic and theoretical site amplifications are used for Site 1 and Site 3. The ground motion at Site 2 is simulated with and without near-field forward directivity pulse. The PGA values, which are obtained from the simulated motions, are applied to estimate damage state probabilities from fragility functions regarding each ESDOF model (with and without structural variability). MDR values for each case are then calculated according to Equation 5.3 and Table 5.2.

Figures 5.26, 5.27 and 5.28 exhibit MDR variations of different cases from a reference case related to Site 1, Site 2 and Site 3, respectively. In Figures 5.26-5.28, the abbreviations S1, S2, S3, T, G, wp, wop, w-sv and wo-sv stand for Site 1, Site 2, Site 3, theoretical site amplification, generic site amplification, with forward directivity pulse, without forward directivity pulse, with structural variability and without structural variability.

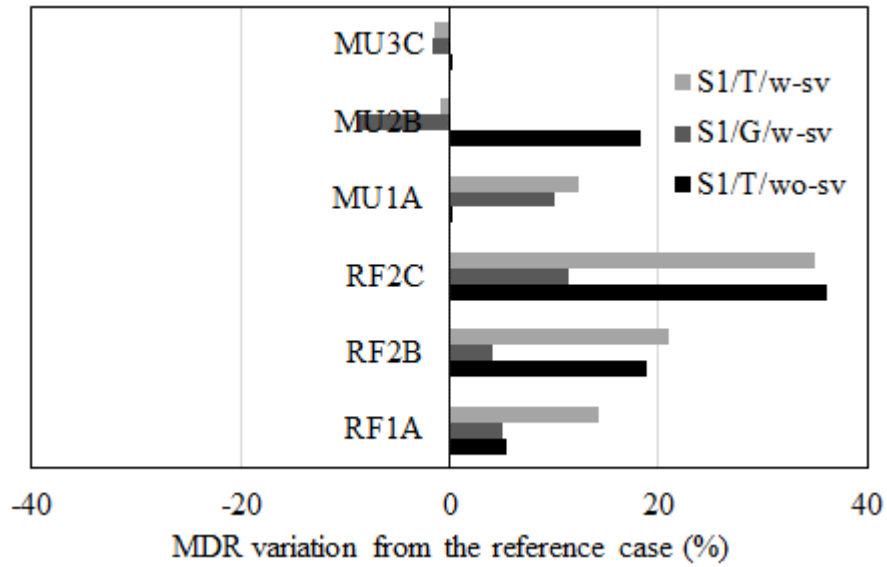


Figure 5.26. MDR variation of three cases related to Site 1 from the reference case which is Site 1 using generic site amplification and without structural variability (S1/G/wo-sv)

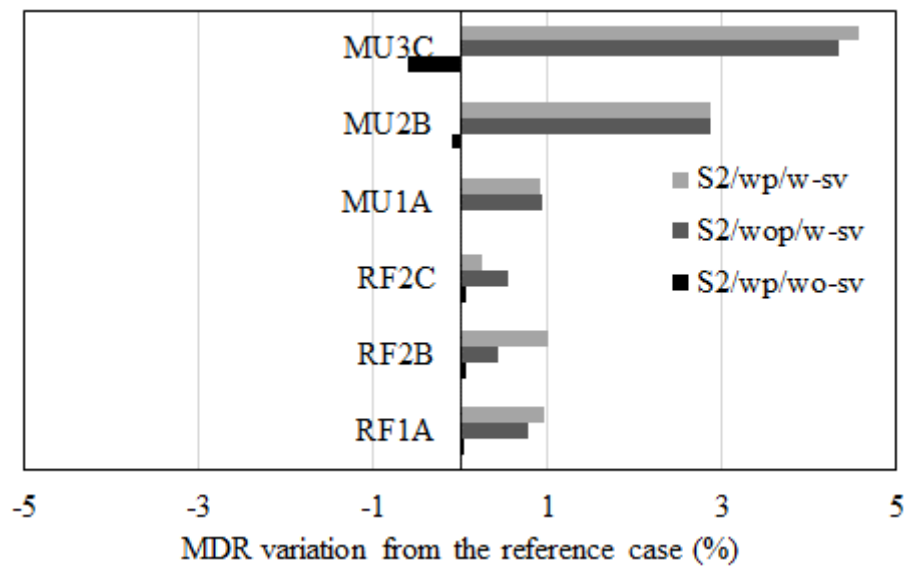


Figure 5.27. MDR variation of three cases related to Site 2 from the reference case, which is Site 2 without forward directivity pulse and without structural variability (S2/wop/wo-sv)

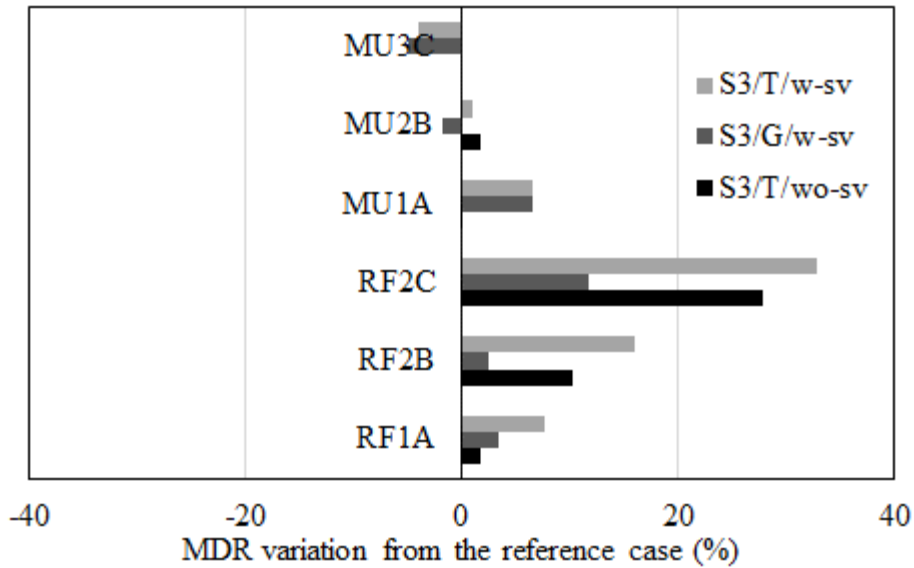


Figure 5.28. MDR variation of three cases related to Site 3 from the reference case, which is Site 3 using generic site amplification and without structural variability (S3/G/wo-sv)

Figure 5.26 indicates that, theoretical site amplification increases estimated damage of the whole ESDOFs. This increase is considerable for RF2C and negligible for MU1A and MU3C. This observation is also valid after applying structural variability. It means that, theoretical site amplification is more critical than generic one for the whole ESDOFs with and without structural variability. Structural variability leads to larger MDRs for the whole ESDOFs except for MU2B and MU3C. The observations related to Figure 5.28 of Site 3 are almost similar to Figure 5.26 of Site 1. The most important difference is that, MDR variation of MU2B with respect to theoretical site amplification and structural variability becomes smaller for Site 3.

Figure 5.27 shows that MDR variations due to forward directivity pulse are negligible (less than 1%). Structural variability leads to larger damage ratios for all of the structural models. The MDR differences of MU2B and MU3C due to structural variability is more than other ESDOF models.

5.8.2 The Effect of Site Condition on Estimated Damage due to Ground Motion Scenario with a Specified PGA

In this sub-section, the effect of site condition (site location and site class) on estimated damage is examined. In order to eliminate the differences in hazard levels regarding different sites, a ground motion scenario with a specified PGA(=0.4 g) is utilized to estimate MDRs. Figure 5.29 shows MDR errors of Site 2 and Site 3 from Site 1 for the ESDOF models with and without structural variability. MDR error is acquired from the variation of two MDR values divided by the smallest MDR. Generic site amplification is taken into account herein and near-field forward directivity is disregarded for Site 2.

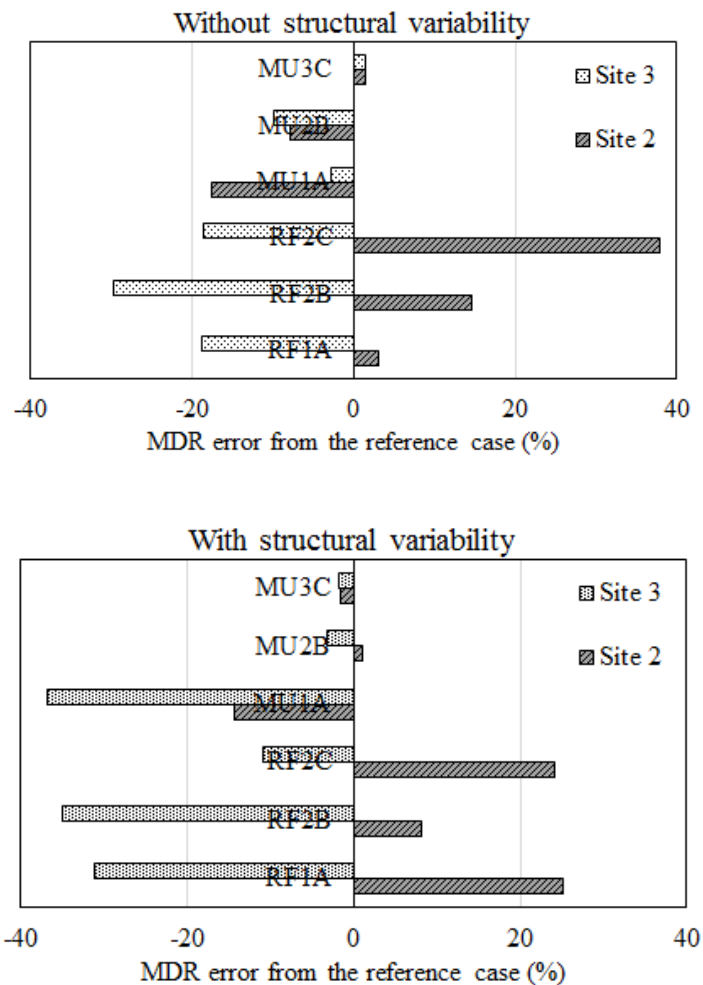


Figure 5.29. MDR error of Site 2 and 3 from Site 1 for PGA=0.4 g

It is obvious from Figure 5.29 that, estimated damage related to Site 1 is smaller than Site 2 for RC frames and it is larger than Site 3 regarding the whole ESDOF models except for MU3C without structural variability. Fragility functions in Section 5.3 related to Site 1 and 2, are almost the same regarding RF1A, RF2B and MU1A. However MDRs of those two sites are different according to Figure 5.29. The reason for this discrepancy is that, damage ratios of those ESDOF models are so small such that the variance between MDRs becomes more obvious in terms of error. The sensitivity of RC frames to site location and site class is more obvious than masonry buildings according to Figure 5.29.

Structural variability reduces the sensitivity of RF2C and MU2B and it grows the sensitivity of RF1A to site conditions. The sensitivity of MU1A and RF2B to Site 3 becomes larger after considering structural variability. However the sensitivity of the aforementioned models to Site 2 is reduced after considering structural variability. The effect of site conditions on MU3C is negligible for both cases of structural variability due to failure of this model at this PGA level.

5.9 Main Findings of Chapter 5

The sensitivity of fragility functions to regional seismicity parameters and structural variability is studied in this chapter. The use of ground motion simulations in this study helps to investigate the effect of site conditions (site class and site location), detailed local site response and near-field forward directivity pulse on building fragility functions in a practical way. The following observations are made:

- Theoretical site amplification produces larger fragility functions for RC frames especially the one with severe degradation characteristics (i.e. RF2C).
- Near-field forward directivity analytical pulse model does not have a considerable effect on structural models in this study. The pulse period is dependent on magnitude according to this pulse model and there are not adequate historical pulse-like ground motions with magnitude less than 6. Hence the analytical forward directivity model of Mavroeidis and Papageorgiou (2003) produces long-period pulse (longer than 1.25 second).

- Following the previous observation, it is believed that the ESDOF approximation in this study also leads to the insensitivity to the pulses with longer periods. In case of MDOF modeling, structural models with similar fundamental periods could behave differently under the same pulse.
- The fragility functions of Site 1 are larger than Site 3 mostly for RC frames (longer periods) and they are larger than Site 2 mostly for masonry buildings (shorter periods), regarding ESDOFs without structural variability. The main reason for dependency of fragility curves to site conditions in this study is the regional properties of simulated ground motions which are selected at different sites.
- The effect of structural variability on fragility functions is more evident for masonry buildings especially MU1A than RC frames due to short period, high yielding capacity and limited ductility of masonry models.
- The proposed continuous fragility curves provide an agreeable fit to discontinuous curves regarding bilinear demand predictive models.
- In order to realize the sensitivity of fragility functions in a quantified manner, mean damage ratios resulted from ground motion scenarios are compared for different cases. Results show the extent of sensitivity of fragility curves to the studied seismological and structural parameters.



CHAPTER 6

CONCLUSIONS, CONTRIBUTIONS AND FUTURE WORK

6.1 Summary

In this dissertation, a novel approach is proposed to estimate regional seismic hazard using simulated ground motions. Instead of using ground motion prediction equations, stochastic simulation methodologies are applied to calculate ground motion amplitudes. These approaches consider ground motion randomness in calculations and produce agreeable results for high-frequency region (higher than 1 Hertz). Additionally, they do not necessitate detailed velocity models which are essential for alternative techniques and do not exist for most regions in Turkey.

Point-source simulation methodology is used for areal seismic zones while finite-fault model based on dynamic corner frequency is implemented for fault zones. The input simulation parameters which involve geometric spreading, quality factor, high frequency decay factor and ground motion duration are taken from the literature. Stress drop and fault dimensions of finite-fault simulation method are derived from empirical relationships. The only parameter which is calibrated in this study is stress drop of point-source simulation.

Erzincan region in eastern Turkey is selected as the case study area. Three sites are selected in this region according to their different distances from NAFZ, different soil conditions and different rupture directivity characteristics. Monte Carlo simulation methodology is applied to achieve the temporal and spatial distribution of events within the boundaries of seismic zones. Moment magnitude of each event is attained using Gutenberg-Richter recurrence model. The seismic hazard results obtained at three sites are compared to those from traditional PSHA to see the differences in between. The variance of simulated ground motion amplitudes from

the corresponding median values of GMPE are plotted against simulated ground motion amplitudes. These variance scatter plots are useful to figure out the discrepancies between two seismic hazard approaches. The effect of near-field forward directivity analytical pulse is investigated on seismic hazard functions of Site 2. Two alternative site amplification functions are inspected in this study: generic site amplification and theoretical site amplification. The hazard functions resulting from the theoretical transfer function with and without soil nonlinearity are compared to those of generic site amplification for Site 1 and Site 3.

Next, the ground motion time histories are selected according to the proposed UHS with different site amplification and forward directivity models. 20 ground motions are selected correspondingly for each return period of 2475, 475, 225 and 75 years. The ground motions are selected from the simulated ground motion database which is used to construct UHS. The selected ground motions have minimum deviation from the target spectrum (UHS), thus they provide an agreeable match.

The results of the proposed seismic hazard methodology can be useful for regional seismic damage and loss estimations. This point is inspected in this thesis through parametric analyses where the sensitivity of seismic fragility functions to site conditions, near-field forward directivity and site amplification functions are investigated. In order to generate building fragility functions, the selected ground motions are used to conduct nonlinear time history analyses of certain residential building types in Erzincan. These typical residential building types in Erzincan have been idealized as equivalent single degree of freedom systems. Maximum displacement demands resulting from time history analyses of these ESDOFs are shown as a function of earthquake intensity, which is PGA, in this dissertation.

Two alternative approaches are followed in seismic fragility analyses by using the selected ESDOF models. In the first approach, ESDOF models with mean values of period (T), yielding strength ratio (η) and ductility ratio (μ) are considered (i.e. structural variability is disregarded). In the second approach, the probabilistic distributions of those structural parameters are obtained by using the Latin Hypercube Sampling (LHS) method (i.e. structural variability is regarded). Then, demand prediction equations are developed for each ESDOF with and without structural variability; for each site with different site amplifications; as well as near-

field forward directivity models. Standard least square regression methodology is applied to calculate the regression coefficients and uncertainties. Some of these predictive models are linear while some others are bilinear in log-log scale. The residual plots of regression models with respect to PGA, magnitude, distance and duration are investigated as well.

Fragility functions of ESDOF models with and without structural variability are constructed for three sites with different site amplification and near-field forward directivity models. Fragility functions of structural models with bilinear trend are not continuous due to difference in dispersions of two linear segments. In order to fix this discontinuity, a lognormal nonlinear curve is fitted on discontinuous fragility curves to be used in practical situations.

In order to quantify the sensitivity of fragility curves to seismic and structural parameters, mean damage ratios (MDRs) of the ESDOFs (with and without structural variability) are calculated for a ground motion scenario. 13 March 1992 Erzincan earthquake is utilized to study the effect of site amplification models, near-field forward directivity pulse and structural variability on the calculated MDRs for each site. In order to compare MDR values between sites, a second scenario with a fixed $PGA=0.4$ g is taken into consideration.

6.2 Conclusions

The main observations of this dissertation are as follows:

- Classical PSHA generally yields larger spectral ordinates as compared to the proposed study due to the wide aleatory variability involved. This wide aleatory variability arises from the large sigma values in GMPEs and wide range of standard deviations in PSHA.
- Regarding the site in the close vicinity of NAFZ and located on soft soil, the proposed study yields slightly larger response spectra for low annual exceedance rates (2% and 10% exceedance probability in 50 years) and for periods less than 0.5 second due to major events. It is well known that the attenuation (ground motion prediction) models are not effective in predicting the major events at short source-to-site distances due to the inherent lack of

those data. Besides, in the proposed study, the finite-fault simulation yields enhanced high-frequency ground motions at close distances.

- After implementing the forward directivity pulse model, spectral ordinates related to return periods of 2475 and 475 years for natural periods of larger than 1 second are amplified. The contribution of high duration ground motions decreases considerably especially for 2475 years, regarding the aforementioned natural periods and return periods.
- Theoretical site amplification without soil nonlinearity (small input rock motion) is observed to increase the ground motion amplitudes for larger periods as compared to generic site amplification.
- As observed in soft soil, the spectral ordinates of the proposed UHS with 475-year return period are larger than those of design spectrum.
- The spectral ordinates of the proposed UHS with 475-year return period and the ones of design spectrum are almost consistent at site with stiff soil. This observation and the previous one highlight the significance of site amplification in seismic design strategies.
- Theoretical site amplification with soil nonlinearity (large input rock motion) remarkably underestimates ground motion amplitudes for smaller periods. The underestimation is more considerable for soft soil than stiff soil.
- The selected ground motions with respect to the proposed UHS provide an agreeable match to target spectrum. This point is proved by calculating root mean square error (RMSE) of the median ground motions with respect to the proposed UHS (target spectrum). In most of the cases, RMSEs are shown to be less than or equal to 0.05. Hence, scaling is not required in this study.
- Among the ESDOF models that represent common building sub-classes in the region, structural types with high degradation characteristics, require bilinear predictive demand model in most of the cases. Modifying linear models into bilinear ones for these cases improves the behavior of prediction equations in terms of R^2 .
- Residual plots in terms of PGA exhibit no observable trend lines. This observation indicates that the predictive demand equation is adequate in terms of PGA.

- The dependency of residuals on magnitude is observed to be more than the corresponding dependency on distance. However this dependency is not remarkably high (i.e. R^2 values of trend lines are less than 10 %) so these parameters are not added to the predictive equations.
- The dependency of residuals from predictive demand models on effective duration is not sufficiently considerable to be added to the model but this parameter is effective regarding ESDOF models with severe degradation characteristics.
- In order to observe the impact of effective duration on seismic demand in detail, displacement demands are divided into different PGA bins. It is observed that, effective duration is more likely to cause destructive effect on deficient structures.
- Some ground motions with similar PGAs are observed to yield considerably different displacement demands. This observation is mostly related to close site and soft soil and is valid for deficient structural models. Ground motion effective duration, acceleration response spectrum at fundamental period, PGV and spectrum intensity are the seismic parameters which might be effective regarding this observation.
- The fragility functions of masonry buildings are affected by implementing structural variability more than RC frame buildings. This is mainly due to the very short mean fundamental period (i.e. a very steep slope for the initial stiffness of the considered hysteresis model) together with very limited displacement ductility capacity (i.e. a very narrow margin in the nonlinear behavior range from yielding to collapse) of these building sub-classes.
- The near-field site produces larger fragility functions than the far-field one generally for masonry buildings due to the enhanced high-frequency simulated ground motion at close distance. The fragilities of far-field site are above those of near-field one regarding RC frames with severe degradation characteristics due to longer ground motion duration related to far-field site.
- The soft soil produces larger fragility functions than the stiff soil mostly for RC frame building classes due to the effects of soft soil on long-period structures.

- Theoretical site amplification (without soil nonlinearity) is more critical than generic one in terms of fragility curves for RC frame buildings. The effect of theoretical site amplification is more evident for deficient structure and stiff soil. The main reason is that the fundamental period of stiff site (from theoretical amplification) is close to the period of mid-rise RC frame buildings.
- Near-field forward directivity pulse does not have a considerable impact on residential buildings considered within the scope of this study. The main reason is that, analytical pulse model, which is implemented in this dissertation, produces long-period pulse (longer than 1.25 seconds) due to pulse period and magnitude empirical relationship. Thus the pulse did not excite the building models (with mean fundamental periods much shorter than the pulse period) sufficiently to yield severely damaging effects.
- The lognormal fitting function provides an agreeable fit to the original discontinuous fragility function in most of the cases.
- Structural variability increases the mean damage ratios of ESDOF models except for building classes MU3C and MU2B related to Site 1 and Site 3, regarding the 13 March 1992 Erzincan earthquake.
- For the scenario event with $PGA=0.4g$, RC frame building classes which are assumed to be located at near-field site display less damage than the ones assumed to be located at far-field site.
- For the scenario event with $PGA=0.4g$, the building classes assumed to be located at soft soil display larger mean damage ratios in comparison with stiff soil except for MU3C. The impact of soft soil on estimated damage is more obvious for RC frame buildings due to closer fundamental periods of the site and the structures.

6.3 Contributions to the Literature

The main advantages, achievements and contributions of this study to the literature are listed as follows:

- The implementation of anticipated ground motions in the region via detailed source and site-related parameters at selected sites show that PSHA could be modified to include regional and complex seismicity parameters.

- The proposed methodology has the advantage of considering regional and local seismicity parameters such as path effects (including anelastic attenuation, geometric spreading, and duration) as well as site factors such as amplification and high frequency decay (in the form of the kappa factor) which is not the case in classical PSHA.
- The proposed approach could be employed effectively in areas of sparse networks, scarce data and incomplete catalogs where GMPEs may not produce acceptable results.
- UHS from the proposed methodology is derived from the individual recordings of scenario earthquakes whereas classical UHS is the envelope of multiple earthquakes. Thus, the proposed approach produces more physical spectral ordinates.
- The seismic wave characteristics are involved in the proposed seismic hazard study whereas GMPEs in traditional PSHA deal with a single spectral ordinate rather than full seismic waves.
- The proposed approach benefits from both probabilistic seismic hazard and ground motion simulation methodologies which is a less-studied issue.
- The proposed approach in this study facilitates implementation of detailed site response inside probabilistic seismic hazard studies. It is difficult, however, to account for such site response models via traditional PSHA as the site parameters are usually coarsely included in GMPEs.
- The effect of near-field forward directivity is implemented in seismic hazard calculations in a straightforward manner via an analytical pulse model.
- The effect of ground motion duration on regional seismic hazard and seismic demand of structures could be inspected via ground motion simulation methods in this study.
- This study proposes a complete earthquake catalog consistent with the regional seismicity as the historical catalogs are generally incomplete both temporally and spatially.
- The complete simulated ground motion database in this study results in a simple and reliable ground motion selection with regional properties.
- Ground motion scaling is avoided in this study; hence, the inherent ground motion randomness is preserved.

- The demand predictive models make fragility calculations more practical through the reliability formulation in this study. Besides, these predictive models provide the opportunity to study the effect of seismic parameters (such as duration) on structural demands.
- The proposed approach helps to study the effect of site conditions (site location and site class) on fragility functions. Such a detailed sensitivity analysis is usually not possible with fragility functions derived from the recorded ground motions due to insufficient data at different sites.
- The effect of detailed site amplification and near-field forward directivity is investigated on fragility functions. Such a sensitivity analysis would be difficult with the fragility functions derived from classical PSHA.

6.4 Limitations and Future Work

The proposed approach in this dissertation has the following limitations:

- The stochastic simulation methodology which is used in this study is mostly efficient for frequencies larger than one Hertz. Therefore the selected simulated ground motions from the proposed study must be applied with caution for high-rise structures (or for structures with fundamental periods longer than one second.)
- The proposed seismic hazard assessment requires more computational effort than classical PSHA due to vast number of ground motion simulations.
- Analytical forward directivity pulse model used in this study is associated with the long-period region of spectrum hence it does not excite the building models which are considered in this study.
- The building classes are represented by ESDOF models to estimate seismic damage in regional scale. Actually, this is the most practical solution if regional damage estimation is performed by fragility analysis through a vast number of structural simulations, which is not feasible by using MDOF models. However, the use of ESDOF models are based on some gross assumptions like the structure should be regular and uniform in both plan and elevation so that the fundamental mode response is dominant, local response is not taken into consideration, etc.

The following arguments are recommended for future studies:

- Hybrid simulation methodologies might be used in ground motion simulations to overcome the deficiency of stochastic models in low-frequency region.
- The proposed study may be generalized to different regions of Turkey leading to a more global seismic hazard map.
- Further investigations on data and models are required regarding forward directivity pulses to inspect the building classes which are vulnerable to forward directivity near-field effect.
- Further building classes and structural types might be considered for nonlinear time history analyses and derivation of fragility functions.
- The fragility functions might be derived with respect to other intensity parameters such as PGV.
- The fragility functions of typical structures can also be modeled as multiple degree of freedom (MDOF) systems to include complex structural effects.



REFERENCES

Abrahamson, N. A. (2000). Effects of rupture directivity on probabilistic seismic hazard analysis. Sixth International Conference on Seismic Zonation: Managing Earthquake Risk in the 21st Century, Palm Springs, CA.

Abrahamson, N. A. and Silva, W. (2008). Summary of the Abrahamson & Silva NGA Ground-Motion Relations. *Earthquake Spectra*, 24(1), 67-97.

Akansel, V. H., Ameri, G., Askan, A., Caner, A., Erdil, B., Kale, Ö. and Okuyucu, D. (2014). The 23 October 2011 Mw 7.0 Van (Eastern Turkey) Earthquake: Characteristics of Recorded Strong Ground Motions and Post Earthquake Condition Assessment of Infrastructure and Cultural Heritage. *Earthquake Spectra*, 30(2), 657-682.

Aki, K. (1967). Scaling law of seismic spectrum. *Journal of Geophysical Research*, 72(4), 1217-1231.

Aki, K. (1980). Attenuation of Shear-waves in the Lithosphere for Frequencies from 0.05 to 25 Hz. *Physics of the Earth and Planetary Interiors*, 29(2), 195-196.

Akkar, S., Sucuoglu, H. and Yakut, A. (2005). Displacement-Based Fragility Functions for Low- and Mid-rise Ordinary Concrete Buildings. *Earthquake Spectra*, 21(4), 901-927.

Akkar, S. and Bommer, J. (2010). Empirical Equations for the Prediction of PGA, PGV and Spectral Accelerations in Europe, the Mediterranean Region and the Middle East. *Seismological Research Letters*, 81(2), 195-206.

Akkar, S. and Cagnan, Z. (2010). A Local Ground-Motion Predictive Model for Turkey, and Its Comparison with Other Regional and Global Ground-Motion Models. *Bulletin of Seismological Society of America*, 100(6), 2978-2995.

Alavi, B. and Krawinkler, H. (2000). Considering of Near-Fault Ground Motion Effect in Seismic Design. 12th World Conference of Earthquake Engineering, Auckland, New Zealand.

Ambraseys, N. N., Douglas, J., Sarma, S. K. and Smit, P. M. (2005). Equations for the Estimation of Strong Ground Motions from Shallow Crustal Earthquakes Using Data from Europe and the Middle East: Horizontal Peak Ground Acceleration and Spectral Acceleration. *Bulletin of Earthquake Engineering*, 3, 1-53.

Anderson, J. and Hough, S. E. (1984). A Model for the Shape of the Fourier Amplitude Spectrum of Acceleration at High Frequencies. *Bulletin of Seismological Society of America*, 74(5), 1969-1993.

Ang, A. H. S. and Tang, W. H. (1975). *Probability Concepts in Engineering Planning and Design*. John Wiley and sons, Inc., Vol 2.

Ansal, A., Akinci, A., Gultrera, G., Erdik, M., Pessina, V., Tonuk, G. and Ameri, G. (2009). Loss Estimation in Istanbul Based on Deterministic Earthquake Scenarios of the Marmara Sea Region (Turkey). *Soil Dynamics and Earthquake Engineering*, 29, 699-709.

Arias (1970). A Measure of Earthquake Intensity. *Seismic Design for Nuclear Power Plants*. Hansen, R. MIT press, 438-483.

ASCE (2005). Seismic Design Provisions of ASCE. Structural Engineering Institute.

Askan, A., Sisman, F. N. and Ugurhan, B. (2013). Stochastic Strong Ground Motion Simulations in Sparsely-Monitored Regions: A Validation and Sensitivity Study on the 13 March 1992 Erzincan (Turkey) Earthquake. *Soil Dynamics and Earthquake Engineering*, 55, 170-181.

Askan, A., Asten, M., Erberik, M.A., Erkmen, C., Karimzadeh, S., Kılıç, N., Şişman, F.N. and Yakut, A. (2015). Estimation of Potential Seismic Damage in Erzincan. Project TUJJB-UDP-01-12, no. 6.

Assatourians, K. and Atkinson, G. (2007). Modeling Variable-Stress Distribution with the Stochastic Finite-Fault Technique. *Bulletin of Seismological Society of America*, 96(7), 1935-1949.

Assatourians, K. and Atkinson, G. (2013). EqHaz: An Open-Source Probabilistic Seismic-Hazard Code Based on the Monte Carlo Simulation Approach. *Seismological Research Letters*, 84(3), 516-524.

Atkinson, G. and Boore, D. (1995). Ground Motion Relations for Eastern North America. *Bulletin of Seismological Society of America*, 85(1), 17-30.

Atkinson, G., Assatourians, K., Boore, M. D., Campbell, K. W. and Motazedian, D. (2009). A Guide to Differences between Stochastic Point-Source and Stochastic Finite-Fault Simulations. *Bulletin of the Seismological Society of America*, 99(6), 3192-3201.

Ay, B. O. and Erberik, M. A. (2008). Vulnerability of Turkish Low-Rise and Mid-Rise Reinforced Concrete Frame Structures. *Journal of Earthquake Engineering*, 12(S2), 2-11.

Ay, B. O. (2012). A Proposed Ground Motion Selection and Scaling Procedures for Structural Systems. PhD Thesis, Middle East Technical University.

Ay, B. O. and Akkar, S. (2012). A Procedure on Ground Motion Selection and Scaling for Nonlinear Response of Simple Structural Systems. *Earthquake Engineering and Structural Dynamics*, 41(12), 1693-1707.

Ayyub, B. M. and Lai, K. (1989). Structural Reliability Assessment Using Latin Hypercube Sampling. 5th International Conference on Structural Safety and Reliability, San Francisco, United States.

Bai, J.-W., Gardoni, P. and Hueste, M. B. (2011). Story-Specific Demand Models and Seismic Fragility Estimates for Multi-Story Buildings. *Structural Safety*, 33, 96-107.

Baker, J. W. (2011). Conditional Mean Spectrum: Tool for Ground-Motion Selection. *Journal of Structural Engineering*, 137(3), 322-331.

Beresnev, I. and Atkinson, G. M. (1997). Modeling Finite-Fault Radiation from the wn Spectrum. *Bulletin of Seismological Society of America*, 87, 67-84.

Beresnev, I. and Atkinson, G. (1998a). FINSIM - a FORTRAN Program for Simulating Stochastic Acceleration Time Histories from Finite Faults. *Seismological Research Letters*, 69, 27-32.

Beresnev, I. and Atkinson, G. (1998b). Stochastic Finite-Fault Modeling of Ground Motions from the 1994 Northridge, California Earthquake. I. Validation on Rock Sites. *Bulletin of Seismological Society of America*, 88(6), 1392-1401.

Beresnev, I. A., Atkinson, G. M., Johnson, P. A. and Field, E. H. (1998). Stochastic Finite-Fault Modeling of Ground Motions from the 1994 Northridge, California,

Earthquake. II. Widespread Nonlinear Response at Soil Sites. *Bulletin of Seismological Society of America*, 88(6), 1402-1410.

Bolt, B. A. (1973). Duration of Strong Motion. 5th World Conference of Earthquake Engineering, Rome, Italy.

Bommer, J. and Martinez-Pereira, A. (1999). The Effective Duration of Earthquake Strong Motion. *Journal of Earthquake Engineering*, 3(2), 127-172.

Bommer, J. and Acevedo, B. (2004). The Use of Real Earthquake Accelerograms as Input to Dynamic Analysis. *Journal of Earthquake Engineering*, 8(1), 43-91.

Bommer, J. and Crowley, H. (2006). The Influence of Ground-Motion Variability in Earthquake Loss Modelling. *Bulletin of Earthquake Engineering*, 4, 231-248.

Boore, D. (1983). Stochastic Simulation of High-Frequency Ground Motions Based on Seismological Models of the Radiated Spectra. *Bulletin of Seismological Society of America*, 73(6), 1865-1894.

Boore, D. and Atkinson, G. (2008). Ground-Motion Prediction Equations for the Average Horizontal Component of PGA, PGV, and 5%-Damped PSA at Spectral Periods between 0.01 s and 10.0 s. *Earthquake Spectra*, 24(1), 99-138.

Boore, M. D. and Joyner, W. B. (1997). Site Amplifications for Generic Rock Sites. *Bulletin of the Seismological Society of America*, 87(2), 327-341.

Boore, M. D. (2003). Simulation of Ground Motion Using the Stochastic Method. *Pure and Applied Geophysics*, 160(3-4), 635-676.

Boore, M. D. (2009). Comparing Stochastic Point-Source and Finite-Source Ground-Motion Simulations: SMSIM and EXSIM. *Bulletin of the Seismological Society of America*, 99(6), 3202-3216.

Boore, M. D. (2013). The Uses and Limitations of the Square-Root-Impedance Method for Computing Site Amplification. *Bulletin of Seismological Society of America*, 103(4), 2356-2368.

Bray, J. and Rodriguez-Marek, A. (2004). Characterization of Forward-Directivity Ground Motions in the Near-Fault Region. *Soil Dynamics and Earthquake Engineering*, 24, 815-828.

Brune, J. (1970). Tectonic Stress and the Spectra of Seismic Shear Waves from Earthquakes. *Journal of Geophysical Research*, 75(26), 4997-5009.

Brune, J. (1971). Correction to "Tectonic Stress and the Spectra of Seismic Shear Waves from Earthquakes". *Journal of Geophysical Research*, 76(20), 5002.

Calvi, G. M. (1999). A Displacement-Based Approach for Vulnerability Evaluation of Classes of Buildings. *Journal of Earthquake Engineering*, 3(3), 411-438.

Calvi, G. M., Pinho, R., Magenes, G., Bommer, J., Restrepo-Velez, L. F. and Crowley, H. (2006). Development of Seismic Vulnerability Assessment Methodologies over the Past 30 Years. *ISET Journal of Earthquake Technology*, 43(3), 75-104.

Campbell, K. W. and Bozorgnia, Y. (2008). NGA Ground Motion Model for the Geometric Mean Horizontal Component of PGA, PGV, PGD and 5% Damped Linear Elastic Response Spectra for Periods Ranging from 0.01 to 10 s. *Earthquake Spectra*, 24(1), 139-171.

Cao, T., Petersen, M. D., Cramer, C. H., Topozada, T. R., Reichle, M. S. and Davis, J. F. (1999). The Calculation of Expected Loss Using Probabilistic Seismic Hazard. *Bulletin of Seismological Society of America*, 89(4), 867-876.

Cartwright, D. E. and Longuet-Higgins, M. S. (1956). The Statistical Distribution of the Maxima of a Random Function. *Proceedings of the Royal Society of London*, 237(1209), 212-232.

Celik, O. C. and Ellingwood, B. R. (2010). Seismic Fragilities for Non-Ductile Reinforced Concrete Frames – Role of Aleatoric and Epistemic Uncertainties. *Structural Safety*, 32, 1-12.

Chiou, B. S. J. and Youngs, R. R. (2008). An NGA Model for the Average Horizontal Component of Peak Ground Motion and Response Spectra. *Earthquake Spectra*, 24(1), 173-215.

Chopra, S., Kumar, D., Choudhury, P. and Yadav, R. B. S. (2012). Stochastic Finite Fault Modelling of Mw 4.8 Earthquake in Kachchh, Gujarat, India. *Journal of Seismology*, 16, 435-449.

Collins, K., Wen, Y. K. and Foutch, D. A. (1996). Dual-Level Seismic Design: A Reliability-Based Methodology. *Earthquake Engineering and Structural Dynamics*, 25, 1433-1467.

Cornell, C. A. (1968). Engineering Seismic Risk Analysis. *Bulletin of the Seismological Society of America*, 58(5), 1583-1606.

Cramer, C. H. (2006). Quantifying the Uncertainty in Site Amplification Modeling and Its Effects on Site-Specific Seismic-Hazard Estimation in the Upper Mississippi Embayment and Adjacent Areas. *Bulletin of Seismological Society of America*, 96(6), 2008-2020.

Crowley, H., Pinho, R. and Bommer, J. (2004). A Probabilistic Displacement-based Vulnerability Assessment Procedure for Earthquake Loss Estimation. *Bulletin of Earthquake Engineering*, 2(2), 173-219.

Crowley, H., Bommer, J., Pinho, R. and Bird, J. (2005). The Impact of Epistemic Uncertainty on an Earthquake Loss Model. *Earthquake Engineering and Structural Dynamics*, 34(14), 1653-1685.

Crowley, H. and Bommer, J. (2006). Modelling Seismic Hazard in Earthquake Loss Models with Spatially Distributed Exposure. *Bulletin of Earthquake Engineering*, 4(3), 249-273.

Datta, D. and Ghosh, S. (2008). Uniform Hazard Spectra Based on Park-Ang Damage Index. *Journal of Earthquake and Tsunami*, 2(3), 241-258.

Demartinos, K. and Faccioli, E. (2012). Probabilistic Seismic Performance Assessment of Classes of Buildings Using Physics-Based Simulations and Ground-Motion Prediction Equations. *Journal of Earthquake Engineering*, 16(1), 40-60.

Deniz, A. (2006). Estimation of Earthquake Insurance Premium Rates Based on Stochastic Methods. MS Thesis, Middle East Technical University.

Eads, L., Miranda, E., Krawinkler, H. and Lignos, D. G. (2013). An efficient method for estimating the collapse risk of structures in seismic regions. *Earthquake Engineering and Structural Dynamics*, 42, 25-41.

Ellingwood, B. R., Celik, O. C. and Kinali, K. (2007). Fragility Assessment of Building Structural Systems in Mid-America. *Earthquake Engineering and Structural Dynamics*, 36, 1935-1952.

Erberik, M. A. and Elnashai, A. S. (2004). Fragility Analysis of Flat-Slab Structures. *Engineering Structures*, 26(7), 937-948.

Erberik, M. A. (2008a). Fragility-Based Assessment of Typical Mid-Rise and Low-Rise RC Buildings in Turkey. *Engineering Structures*, 30(5), 1360-1374.

Erberik, M. A. (2008b). Generation of Fragility Curves for Turkish Masonry Buildings Considering In-Plane Failure Modes. *Earthquake Engineering and Structural Dynamics*, 37(3), 387-405.

Farsangi, E., Rezvani, F., Talebi, M. and Hashemi, S. (2014). Seismic Risk Analysis of Steel-MRFs by Means of Fragility Curves in High Seismic Zones. *Advances in Structural Engineering*, 17(9)

Frankel, A. (1993). Three-Dimensional Simulations of the Ground Motions in the San Bernardino Valley, California ,for Hypothetical Earthquakes on the San Andreas Fault. *Bulletin of Seismological Society of America*, 83, 1020-1041.

Frankel, A., Mueller, C., Barnhard, T., Perkins, D., Leyendecker, E. V., Dickman, N., Hanson, S. and Hopper, M. (1996). National Seismic-Hazard Maps: Documentation June 1996. US Geological Survey, Open-File Report 96-532.

Gencturk, B., Elshani, A. S. and Song, J. (2008). Fragility Relationships for Populations of Woodframe Structures Based on Inelastic Response. *Journal of Earthquake Engineering*, 12(S2), 119-128.

Ghofrani, H., Atkinson, G., Goda, K. and Assatourians, K. (2013). Stochastic Finite-Fault Simulations of the 2011 Tohoku, Japan, Earthquake. *Bulletin of Seismological Society of America*, 103(2B), 1307-1320.

Graves, R. W. and Pitarka, A. (2010). Broadband Ground-Motion Simulation Using a Hybrid Approach. *Bulletin of Seismological Society of America*, 100(5A), 2095-2123.

Gu, P. and Wen, Y. K. (2007). A Record-Based Method for the Generation of Tridirectional Uniform Hazard-Response Spectra and Ground Motions Using the Hilbert-Huang Transform. *Bulletin of Seismological Society of America*, 97(5), 1539-1556.

Gurpinar, A., Abalı, M., Yucemen, M. S. and Yesilcay, Y. (1978). Feasibility of Mandatory Earthquake Insurance in Turkey. Earthquake Engineering Research Center, Report No. 78-05.

Hanks, T. C. and Kanamori, H. (1979). A Moment Magnitude Scale. *Journal of Geophysical Research*, 84(B5), 2348-2350.

Hanks, T. C. and McGuire, R. K. (1981). The Character of High-frequency Strong Ground Motion. *Bulletin of Seismological Society of America*, 71(6), 2071-2095.

Hartzell, S. H. (1978). Earthquake Aftershocks as Green's Functions. *Geophysical Research Letters*, 5(1), 1-4.

Haselton, C. B. (2009). Evaluation of Ground Motion Selection and Modification Methods: Predicting Median Interstory Drift Response of Buildings. Pacific Earthquake Engineering Research Centre, 2009/1.

Hashash, Y. and Moon, S. (2011). Site Amplification Factors for Deep Deposits and their Application in Seismic Hazard Analysis for Central U.S. University of Illinois at Urbana-Champaign.

Heaton, T. (1990). Evidence for and Implications of Self-Healing Pulses of Slip in Earthquake Rupture. *Physics of the Earth and Planetary Interiors*, 64(1), 1-20.

Herrmann, R. B. (1985). An Extension of Random Vibration Theory Estimates of Strong Ground Motion to Large Distances. *Bulletin of Seismological Society of America*, 75(5), 1447-1453.

Hisada, Y. (2008). Broadband Strong Motion Simulation in Layered Half-Space Using Stochastic Green's Function Technique. *Journal of Seismology*, 12(2), 265-279.

Housner, G. W. (1963). The Behavior of Inverted Pendulum Structures during Earthquakes. *Bulletin of Seismological Society of America*, 53(2), 403-417.

Hueste, M. B. and Bai, J.-W. (2007). Seismic Retrofit of a Reinforced Concrete Flat-Slab Structure: Part II Seismic Fragility Analysis. *Engineering Structures*, 29, 1178–1188.

Ibarra, L. and Krawinkler, H. (2005). Global Collapse of Frame Structures under Seismic Excitations. The John A. Blume Earthquake Engineering Center, Stanford University, Rep. No. TB 152.

Ibarra, L., Medina, R. and Krawinkler, H. (2005). Hysteretic Models that Incorporate Strength and Stiffness Deterioration. *Earthquake Engineering and Structural Dynamics*, 34, 1489-1511.

Idriss, I. M. (2008). An NGA Empirical Model for Estimating the Horizontal Spectral Values Generated By Shallow Crustal Earthquakes. *Earthquake Spectra*, 24(1), 217-242.

Jayaram, N., Lin, T. and Baker, J. W. (2011). A Computationally Efficient Ground-Motion Selection Algorithm for Matching a Target Response Spectrum Mean and Variance. *Earthquake Spectra*, 27(3), 797-815.

Jeon, J., Park, J. and DesRoches, R. (2015). Seismic Fragility of Lightly Reinforced Concrete Frames with Masonry Infills. *Earthquake Engineering and Structural Dynamics*, 44(11), 1783-1803.

Jeong, S. H. and Elnashai, A. S. (2007). Probabilistic Fragility Analysis Parameterized by Fundamental Response Quantities. *Engineering Structures*, 29(6), 1238-1251.

Joyner, W. B., Warrick, R. E. and Fumal, T. E. (1981). The Effect of Quaternary Alluvium on Strong Ground Motion in the Coyote Lake, California, Earthquake of 1979. *Bulletin of Seismological Society of America*, 71, 1333-1349.

Joyner, W. B. and Boore, D. (1986). On Simulating Large Earthquakes by Green's Function Addition of Smaller Earthquakes. *Earthquake Source Mechanics*. Das, S., Boatwright, J. and Scholz, C. H., 37, 269–274.

Kadaş, K. (2006). Influence of Idealized Pushover Curves on Seismic Response. MSc Thesis, Middle East Technical University.

Kale, Ö. and Akkar, S. (2013). A New Procedure for Selecting and Ranking Ground-Motion Prediction Equations (GMPEs): The Euclidean Distance-Based Ranking (EDR) Method. *Bulletin of Seismological Society of America*, 103(2A), 1069–1084.

Kalkan, E. and Gulkan, P. (2005). Discussion of an Attenuation Relationship Based on Turkish Strong Motion Data and Iso-Acceleration Map of Turkey by Ulusay et al., 2004. *Engineering Geology*, 79, 288-290.

Karaca, H. (2014). Estimation of Potential Earthquake Losses for the Evaluation of Earthquake Insurance Risks. PhD Thesis, Middle East Technical University.

Kempton, J. and Stewart, J. P. (2006). Prediction Equations for Significant Duration of Earthquake Ground Motions Considering Site and Near-Source Effects. *Earthquake Spectra*, 22(4), 985-1013.

Khaheshi Banan, K., Kolaj, M., Motazedian, D., Sivathayalan, S., Hunter, J. A., Crow, H. L., Pugin, A. J., Brooks, G. R. and Pyne, M. (2012). Seismic Site Response Analysis for Ottawa, Canada: A Comprehensive Study Using Measurements and Numerical Simulations. *Bulletin of Seismological Society of America*, 102(5), 1976-1993.

Kottke, A. and Rathje, E. M. (2008). A Semi-Automated Procedure for Selecting and Scaling Recorded Earthquake Motions for Dynamic Analysis. *Earthquake Spectra*, 24(4), 911-932.

Kramer, S. L. (1996). *Geotechnical Earthquake Engineering*. Prentice Hall, Inc., Upper Saddle River.

Krawinkler, H., Medina, R. and Alavi, B. (2003). Seismic Drift and Ductility Demands and their Dependence on Ground motions. *Engineering Structures*, 25(5), 637-653.

Lignos, D. G. and Krawinkler, H. (2011). Deterioration Modeling of Steel Components in Support of Collapse Prediction of Steel Moment Frames under Earthquake Loading. *Journal of Structural Engineering*, 137(11), 1291-1302.

Lignos, D. G. and Krawinkler, H. (2012). Sidesway Collapse of Deteriorating Structural Systems under Seismic Excitations. The John A. Blume Earthquake Engineering Research Center, Stanford University, Rep.No.TB 177.

Luco, N., Ellingwood, B. R., Hamburger, R. O., Hooper, J. D., Kimball, J. K. and Kircher, C. A. (2007). Risk-Targeted versus Current Seismic Design Maps for the Conterminous United States. SEAOC 2007 Convention Proceedings. Squaw Creek, California, Structural Engineers Association.

Mavroeidis, G. P. and Papageorgiou, A. S. (2003). A Mathematical Representation of Near-Fault Ground Motions. *Bulletin of Seismological Society of America*, 93(3), 1099-1131.

McGuire, R. K. and Arabasz, W. J. (1990). *An Introduction to Probabilistic Seismic Hazard Analysis*. Society of Exploration Geophysics, Vol 1.

McGuire, R. K. (2004). Seismic Hazard and Risk Analysis. Earthquake Engineering Research Institute.

McKay, M. D., Beckman, R. J. and Conover, W. J. (1979). A Comparison of Three Methods for Selecting Values of Input Variables in the Analysis of Output from a Computer Code. *Technometrics*, 21(2), 239-245.

Mena, B., Mai, P. M., Olsen, K. B., Purvance, M. and Brune, J. (2010). Hybrid Broadband Ground-Motion Simulation Using Scattering Green's Functions: Application to Large-Magnitude Events. *Bulletin of Seismological Society of America*, 100(5A), 2143-2162.

Metin, A. (2006). Inelastic Deformation Demands on Moment-Resisting Frame Structures. MSc Thesis, Middle East Technical University.

Moghaddam, H., Fanaie, N. and Motazedian, D. (2010). Estimation of Stress Drop for Some Large Shallow Earthquakes Using Stochastic Point Source and Finite Fault Modeling. *Scientia Iranica*, 17(3), 217-235.

Mohammadioun, B. and Serva, L. (2001). Stress Drop, Slip Type, Earthquake Magnitude, and Seismic Hazard. *Bulletin of Seismological Society of America*, 91(4), 604-707.

Motazedian, D. and Atkinson, G. M. (2005). Stochastic Finite-Fault Modeling Based on a Dynamic Corner Frequency. *Bulletin of Seismological Society of America*, 95(3), 995-1010.

Musson, R. M. W. (2000). The Use of Monte Carlo Simulations for Seismic hazard Assessment in the U.K. *Anadali Di Geofisica*, 43(1), 1-9.

Naeim, F. and Lew, M. (1995). On the Use of Design Spectrum Compatible Time Histories. *Earthquake Spectra*, 11(1), 111-127.

Nakamura, Y. (1989). A Method for Dynamic Characteristics Estimation of Subsurface Using Microtremor on the Ground Surface. Railway Technical Research Institute, no. 30.

Nicknam, A., Abbasnia, R., Bozorgnasab, M. and Eslamian, Y. (2010). Synthesizing Broadband Time-Histories at Near Source Sites; Case Study, 2003 Bam Mw6.5 Earthquake. *Journal of Earthquake Engineering*, 14(6), 898-917.

Nogoshi, M. and Igarashi, T. (1971). On the Amplitude Characteristics of Microtremor. Part II. *Journal of Seismological Society of Japan*, 24, 26-40.

Novikova, E. I. and Trifunac, M. D. (1994). Duration of Strong Ground Motion in terms of Earthquake Magnitude, Epicentral Distance, Site Condition and Site Geometry. *Earthquake Engineering and Structural Dynamics*, 23, 1023-1043.

Olsen, K. B., Archuleta, R. J. and Matarrese, J. R. (1996). Three-Dimensional Simulation of a Magnitude 7.75 Earthquake on the San Andreas Fault. *Science*, 270, 1628-1632.

Ozmen, H. B., Inel, M., Meral, E. and Bucakli, M. (2010). Vulnerability of Low And Mid-Rise Reinforced Concrete Buildings in Turkey. 14th European Conference on Earthquake Engineering, Ohrid, Macedonia.

Padgett, J. E. and DesRoches, R. (2007). Sensitivity of Seismic Response and Fragility to Parameter Uncertainty. *Journal of Structural Engineering*, 133(12), 1710-1718.

Papoulia, J., Fahjan, Y. M., Hutchings, L. and Novikova, T. (2015). PSHA for Broad-Band Strong Ground-Motion Hazards in the Saronikos Gulf, Greece, from Potential Earthquake with Synthetic Ground Motions. *Journal of Earthquake Engineering*, 19(4), 624-648.

Pejovic, J. and Jankovic, S. (2015). Seismic fragility assessment for reinforced concrete high-rise buildings in Southern Euro-Mediterranean zone. *Bulletin of Earthquake Engineering*, 1-28.

Ramamoorthy, S. K., Gardoni, P. and Bracci, J. M. (2006). Probabilistic Demand Models and Fragility Curves for Reinforced Concrete Frames. *Journal of Structural Engineering*, 132(10), 1563-1572.

Ramamoorthy, S. K., Gardoni, P. and Bracci, J. M. (2008). Seismic Fragility and Confidence Bounds for Gravity Load Designed Reinforced Concrete Frames of Varying Height. *Journal of Structural Engineering*, 134(4), 639-650.

Raschke, M. (2014). Insufficient Statistical Model Development of Ground-Motion Relations for Regions with Low Seismicity. *Bulletin of Seismological Society of America*, 104(2), 1002-1005.

Rodriguez-Perez, Q., Ottemoller, L. and Castro, P. R. (2012). Stochastic Finite-Fault Ground-Motion Simulation and Source Characterization of the 4 April 2010 Mw 7.2 El Mayor-Cucapah Earthquake. *Seismological Research Letters*, 83(2), 235-249.

Rohmer, J., Douglas, J., Bertil, D., Monfort, D. and Sedan, O. (2014). Weighing the Importance of Model Uncertainty against Parameter Uncertainty in Earthquake Loss Assessments. *Soil Dynamics and Earthquake Engineering*, 58, 1-9.

Roumelioti, Z., Kiratzi, A. and Theodulidis, N. (2004). Stochastic Strong Ground-Motion Simulation of the 7 September 1999 Athens (Greece) Earthquake. *Bulletin of Seismological Society of America*, 94(3), 1036-1052.

Rupakhety, R., Sigurðsson, S. U. and Sigbjörnsson, R. (2012). Response Spectral Model for Forward-Directivity Ground Motion in the Near-Fault Area. *15th World Conference on Earthquake Engineering*, Lisbon.

Saragoni, G. R. and Hart, G. C. (1974). Simulation of Artificial Earthquakes. *Earthquake Engineering and Structural Dynamics*, 2(3), 249-267.

Schnabel, P. B., Lysmer, J. and Seed, H. B. (1972). SHAKE: A Computer Program for Earthquake Response Analysis of Horizontally Layered Sites. *Earthquake Engineering Research Center, University of California, Berkeley, UCB/EERC-72/12*,.

Shahi, S. K. and Baker, J. W. (2011). An Empirically Calibrated Framework for Including the Effects of Near-Fault Directivity in Probabilistic Seismic Hazard Analysis. *Bulletin of the Seismological Society of America*, 101(2), 742–755.

Shapira, A. and Eck, T. V. (1993). Synthetic Uniform-Hazard Site Specific Response Spectrum. *Natural Hazards*, 8, 201-215.

Shoja-Taheri, J. and Ghofrani, H. (2007). Stochastic Finite-Fault Modeling of Strong Ground Motions from the 26 December 2003 Bam, Iran, Earthquake. *Bulletin of Seismological Society of America*, 97(6), 1950-1959.

Shome, N., Cornell, C. A., Bazzurro, P. and Carballo, E. (1998). Earthquakes, Records, and Nonlinear Responses. *Earthquake Spectra*, 14(3), 469-499.

Silva, V., Crowley, H., Pinho, R. and Varum, H. (2013). Extending Displacement-Based Earthquake Loss Assessment (DBELA) for the computation of Fragility Curves. *ENGSTRUCT*, 56, 343-356.

Somerville, P. G., Sen, M. and Cohee, B. (1991). Simulations of Strong Ground Motions Recorded during the 1985 Michoacan, Mexico and Valparaiso. *Bulletin of Seismological Society of America*, 81(1), 1-27.

Somerville, P. G. (1998). Development of an Improved Ground Motion Representation for Near Fault Ground Motions. SMIP98 Seminar on Utilization of Strong-Motion Data, Oakland, CA.

Thenhaus, P. C. and Campbell, K. W. (2003). Seismic Hazard Analysis. Earthquake Engineering Handbook. Chan, W. F. and Scawthorn, C. CRC Press.

TSC (2007). Turkish Seismic Code. Ministry of Public Works and Settlement Government of Republic of Turkey.

UBC (1997). Uniform Building Code. International Code Council.

Ugurhan, B. and Askan Gundogan, A. (2010). Stochastic Strong Ground Motion Simulation of the 12 November 1999 Düzce (Turkey) Earthquake Using a Dynamic Corner. Bulletin of Seismological Society of America, 100(4), 1498-1512.

Ugurhan, B., Askan Gundogan, A. and Erberik, M. A. (2011). A Methodology for Seismic Loss Estimation in Urban Regions Based on Ground-Motion Simulations. Bulletin of Seismological Society of America, 101(2), 701-725.

Ugurhan, B., Askan, A., Akinci, A. and Malagnini, L. (2012). Strong-Ground-Motion Simulation of the 6 April 2009 L'Aquila, Italy, Earthquake. Bulletin of Seismological Society of America, 102(4), 1429-1445.

Wells, D. L. and Coppersmith, K. J. (1994). New Empirical Relationships among Magnitude, Rupture Length, Rupture Width, Rupture Area and Surface Displacement. Bulletin of the Seismological Society of America, 84(4), 974-1002.

Wen, Y. K. and Wu, C. L. (2001). Uniform Hazard Ground Motions for Mid-America Cities. Earthquake Spectra, 17(2), 359-384.

Wen, Y. K., Ellingwood, B. R. and Bracci, J. M. (2004). Vulnerability Function Framework for Consequence-based Engineering. MAE Center Project DS-4 Report.

Whitman , R. V. (1973). Damage Probability Matrices for Prototype Buildings. MIT.

Wu, C. L. and Wen, Y. K. (2000). Earthquake Ground Motion Simulation and Reliability Implications. Department of Civil and Environmental Engineering, University of Illinois at Urbana-Champaign, no. 630.

Yalcinkaya, E. (2005). Stochastic Finite-Fault Modeling of Ground Motions from the June 27, 1998 Adana-Ceyhan Earthquake. *Earth Planets Space*, 57, 107-115.

Zafarani, H., Noorzad, A., Ansari, A. and Bargi, K. (2009). Stochastic Modeling of Iranian Earthquakes and Estimation of Ground Motion for Future Earthquakes in Greater Tehran. *Soil Dynamics and Earthquake Engineering*, 29, 722-741.



APPENDIX A

SELECTED GROUND MOTIONS

In this appendix, selected ground motion recordings which were derived in Chapter 3 are listed with their main characteristics. These ground motions were used in Chapter 4 to perform nonlinear time history analysis of ESDOFs. The ground motion parameters which are shown in this appendix, are moment magnitude (M), closest distance to rupture (R_{rup}), PGA, PGV, effective duration (time span between 5% and 95 % of arias intensity) and spectrum intensity (SI).

Table A.1 displays selected ground motions with the aforementioned parameters. In this table, the abbreviations G, T, wonf and wnf stand for generic site amplification, theoretical site amplification, without near-field forward directivity pulse and with near-field forward directivity pulse, respectively.

Ground motion ID (GM ID) consists of site of interest (S1: Site 1, S2: Site 2, and S3: Site 3). The second part of GM ID is site amplification or near-field forward directivity model which might be G, T, wonf or wnf. After site amplification or forward directivity model, return period is stated in years. The last part of ground motion ID is ground motion number which varies between 1 and 20 for each case.

Table A.1. Selected ground motions in this dissertation and their main characteristics

GM ID	Return Period (years)	M	R _{rup} (km)	PGA (g)	PGV (cm/s)	Effective Duration (s)	SI (cm)
S1G475_01	475	7.6	6.77	0.77	77.01	8.34	264.2
S1G475_02	475	7.9	7.71	0.76	102.67	22.31	280.4
S1G475_03	475	6.5	2.67	0.86	73.45	4.79	282.4
S1G475_04	475	7.5	9.13	0.58	91.94	17.09	277.0
S1G475_05	475	7.1	5.82	0.80	96.48	5.09	255.7
S1G475_06	475	6.8	2.01	0.80	93.21	3.95	250.5
S1G475_07	475	7.9	11.93	0.68	78.11	26.07	267.3
S1G475_08	475	7.9	11.93	0.79	80.07	26.21	241.0
S1G475_09	475	7.1	7.10	0.68	53.07	8.01	230.6
S1G475_10	475	7.5	9.68	0.64	64.60	14.99	268.7
S1G475_11	475	7.5	9.68	0.69	81.71	15.89	232.8
S1G475_12	475	7.9	9.69	0.76	58.56	8.72	222.3
S1G475_13	475	7.2	12.16	0.67	58.97	10.07	240.8
S1G475_14	475	6.9	4.44	0.78	117.96	4.87	280.7
S1G475_15	475	6.9	4.07	0.76	63.90	5.13	221.0
S1G475_16	475	7.4	12.36	0.72	86.78	13.54	227.8
S1G475_17	475	7.5	9.59	0.75	75.63	13.98	243.3
S1G475_18	475	7.5	9.59	0.69	96.13	13.11	310.4
S1G475_19	475	7.6	7.52	0.62	95.37	8.22	242.2
S1G475_20	475	7.6	7.52	0.84	154.75	7.44	282.3
S1G225_01	225	6.6	4.92	0.47	45.02	4.22	142.5
S1G225_02	225	7.1	11.14	0.43	65.17	8.80	148.1
S1G225_03	225	6.9	14.72	0.39	40.51	8.82	143.8
S1G225_04	225	7.1	13.22	0.43	49.14	9.57	150.0
S1G225_05	225	6.9	10.40	0.44	55.38	7.41	161.9
S1G225_06	225	7.7	17.11	0.45	58.99	18.98	138.4
S1G225_07	225	7.6	16.80	0.54	55.59	13.80	163.6
S1G225_08	225	7.6	16.80	0.41	73.63	13.40	166.0
S1G225_09	225	7.2	17.33	0.36	48.79	10.18	162.5
S1G225_10	225	7.4	17.31	0.41	48.51	13.94	137.7
S1G225_11	225	7.3	20.53	0.46	61.76	13.06	151.0
S1G225_12	225	6.9	14.72	0.37	47.31	8.62	137.2
S1G225_13	225	6.5	9.48	0.39	45.22	3.80	141.3
S1G225_14	225	7.9	15.44	0.38	60.52	16.02	160.8
S1G225_15	225	7.0	7.68	0.47	47.96	5.76	147.7
S1G225_16	225	7.0	11.38	0.35	43.65	9.06	160.1
S1G225_17	225	7.2	10.77	0.41	49.43	9.35	145.3

Table A.1 (Continued)

S1G225_18	225	7.1	10.01	0.52	65.22	8.02	149.1
S1G225_19	225	7.1	14.80	0.46	46.60	9.96	154.0
S1G225_20	225	6.8	6.26	0.39	38.27	5.69	139.4
S1G75_01	75	7.2	49.77	0.15	17.36	12.85	44.6
S1G75_02	75	6.0	14.45	0.13	14.14	3.06	41.7
S1G75_03	75	6.2	17.43	0.15	12.50	3.83	50.2
S1G75_04	75	7.0	44.91	0.14	13.65	12.52	41.7
S1G75_05	75	6.6	24.24	0.12	15.25	5.81	45.3
S1G75_06	75	7.0	48.58	0.12	18.27	13.19	51.0
S1G75_07	75	6.6	27.91	0.14	17.90	7.20	51.3
S1G75_08	75	6.4	18.12	0.14	14.97	5.08	45.3
S1G75_09	75	6.6	22.95	0.15	12.43	5.59	49.1
S1G75_10	75	6.6	28.87	0.15	19.94	7.64	50.4
S1G75_11	75	6.2	17.43	0.14	11.04	4.17	41.7
S1G75_12	75	7.4	67.85	0.13	23.78	17.69	45.7
S1G75_13	75	6.5	20.61	0.15	15.76	5.00	47.9
S1G75_14	75	6.2	20.47	0.14	13.36	3.07	47.6
S1G75_15	75	6.6	29.42	0.12	11.26	7.15	38.6
S1G75_16	75	6.6	30.08	0.12	14.13	6.34	40.6
S1G75_17	75	6.6	30.08	0.11	14.57	5.87	40.6
S1G75_18	75	6.3	19.82	0.10	12.40	3.45	45.2
S1G75_19	75	6.7	27.02	0.13	12.91	7.63	44.9
S1G75_20	75	6.7	29.88	0.13	12.30	7.66	46.9
S1T475_01	475	7.5	9.59	0.78	83.52	14.13	302.7
S1T475_02	475	7.6	7.52	0.74	100.94	8.21	337.3
S1T475_03	475	7.3	5.37	0.67	73.94	8.32	320.3
S1T475_04	475	7.7	5.15	0.78	104.06	6.42	301.8
S1T475_05	475	6.9	4.44	0.66	108.43	5.88	284.8
S1T475_06	475	6.5	0.43	0.74	112.84	3.98	325.4
S1T475_07	475	7.5	9.28	0.90	77.21	7.94	328.9
S1T475_08	475	7.6	6.88	0.74	89.28	5.35	334.1
S1T475_09	475	7.6	7.51	0.80	138.44	7.90	297.0
S1T475_10	475	7.5	9.19	0.84	116.88	16.53	358.6
S1T475_11	475	7.5	9.71	0.64	93.58	15.93	345.9
S1T475_12	475	7.3	6.81	0.82	80.75	5.44	325.1
S1T475_13	475	7.5	9.71	0.66	75.91	16.91	258.7
S1T475_14	475	7.9	12.25	0.79	79.03	27.20	363.4
S1T475_15	475	6.5	2.68	0.86	85.97	4.50	352.5
S1T475_16	475	7.1	5.96	0.79	94.23	6.07	286.0
S1T475_17	475	7.9	12.25	0.63	68.91	25.47	316.5
S1T475_18	475	7.9	12.72	0.60	72.23	11.53	280.6
S1T475_19	475	6.3	0.46	0.87	61.30	3.05	280.5
S1T475_20	475	7.5	12.08	0.60	65.28	8.28	313.9

Table A.1 (Continued)

S1T225_01	225	6.9	11.53	0.53	51.79	5.14	218.9
S1T225_02	225	6.7	10.13	0.39	57.95	4.48	189.6
S1T225_03	225	6.5	9.21	0.47	47.06	3.79	193.1
S1T225_04	225	7.6	16.80	0.53	51.71	14.80	191.2
S1T225_05	225	7.4	17.31	0.44	63.05	13.45	211.9
S1T225_06	225	7.3	14.07	0.40	54.55	10.05	219.4
S1T225_07	225	7.0	7.68	0.44	49.23	8.39	197.8
S1T225_08	225	7.3	10.82	0.47	62.03	8.25	198.6
S1T225_09	225	6.9	13.54	0.51	54.18	7.39	175.2
S1T225_10	225	6.0	1.98	0.46	59.28	2.04	180.8
S1T225_11	225	7.7	15.80	0.44	64.30	23.99	215.7
S1T225_12	225	7.7	17.46	0.42	62.13	10.71	215.3
S1T225_13	225	7.6	16.80	0.38	67.61	14.45	193.0
S1T225_14	225	7.4	20.26	0.43	42.24	14.56	204.5
S1T225_15	225	6.5	9.48	0.42	43.55	4.78	165.2
S1T225_16	225	7.1	6.37	0.43	62.79	10.12	204.2
S1T225_17	225	7.1	10.76	0.47	51.18	9.41	200.7
S1T225_18	225	7.3	14.07	0.42	49.07	11.36	180.6
S1T225_19	225	6.9	9.10	0.46	49.10	7.12	199.9
S1T225_20	225	6.9	12.08	0.45	42.82	6.31	170.3
S1T75_01	75	7.2	55.99	0.16	17.15	10.50	60.6
S1T75_02	75	6.5	32.48	0.18	17.98	7.04	56.4
S1T75_03	75	6.4	15.64	0.15	15.85	6.24	57.2
S1T75_04	75	6.7	27.68	0.18	17.99	6.99	59.5
S1T75_05	75	7.0	43.51	0.18	18.39	9.42	65.1
S1T75_06	75	7.1	42.95	0.14	17.89	12.20	61.1
S1T75_07	75	6.6	27.91	0.15	16.17	6.76	51.5
S1T75_08	75	7.1	52.34	0.18	18.06	11.23	54.1
S1T75_09	75	7.3	50.43	0.14	19.21	15.98	66.0
S1T75_10	75	6.4	18.12	0.14	17.14	5.11	57.1
S1T75_11	75	5.7	10.55	0.14	12.22	2.00	54.0
S1T75_12	75	6.6	24.24	0.12	16.07	5.70	55.0
S1T75_13	75	6.8	26.80	0.13	13.08	9.35	58.7
S1T75_14	75	7.0	37.40	0.14	23.96	9.56	66.7
S1T75_15	75	6.3	15.13	0.15	16.35	4.62	65.7
S1T75_16	75	7.2	55.18	0.14	22.46	12.99	59.1
S1T75_17	75	6.5	32.33	0.21	22.05	4.74	67.0
S1T75_18	75	6.5	22.50	0.17	18.06	4.35	62.4
S1T75_19	75	7.3	57.96	0.13	19.96	17.71	59.1
S1T75_20	75	6.6	27.91	0.12	14.02	6.64	56.2
S2wonf2475_01	2475	7.7	13.89	0.62	87.15	14.35	252.8
S2wonf2475_02	2475	6.8	6.34	0.63	103.34	4.74	273.3
S2wonf2475_03	2475	7.9	10.78	0.61	79.81	10.98	243.9

Table A.1 (Continued)

S2wonf2475_04	2475	7.8	9.58	0.57	91.55	8.88	269.1
S2wonf2475_05	2475	7.5	11.01	0.55	65.88	15.45	232.6
S2wonf2475_06	2475	7.2	7.96	0.67	95.50	9.97	257.7
S2wonf2475_07	2475	7.5	9.19	0.56	86.15	11.57	262.1
S2wonf2475_08	2475	7.7	8.67	0.63	82.46	19.12	265.2
S2wonf2475_09	2475	7.7	6.54	0.60	73.01	8.27	279.5
S2wonf2475_10	2475	7.7	12.80	0.57	77.67	23.94	230.8
S2wonf2475_11	2475	7.7	10.21	0.54	72.99	18.52	224.5
S2wonf2475_12	2475	7.7	8.67	0.74	79.06	18.84	265.5
S2wonf2475_13	2475	7.6	13.41	0.73	63.36	19.16	232.9
S2wonf2475_14	2475	6.7	5.69	0.60	50.76	4.17	208.9
S2wonf2475_15	2475	7.8	9.58	0.80	93.15	9.32	236.5
S2wonf2475_16	2475	7.2	14.77	0.60	77.82	10.77	220.5
S2wonf2475_17	2475	7.8	12.84	0.57	73.66	12.90	275.8
S2wonf2475_18	2475	7.6	11.13	0.48	85.15	9.23	200.7
S2wonf2475_19	2475	7.2	7.96	0.68	101.42	10.13	288.7
S2wonf2475_20	2475	7.3	8.49	0.53	92.76	8.61	232.5
S2wonf475_01	475	6.9	12.68	0.35	53.81	6.84	141.8
S2wonf475_02	475	7.6	21.92	0.36	64.01	13.95	160.4
S2wonf475_03	475	6.6	12.33	0.36	46.07	4.82	155.4
S2wonf475_04	475	7.7	21.84	0.41	47.23	10.73	167.8
S2wonf475_05	475	7.6	23.44	0.36	82.11	12.09	153.9
S2wonf475_06	475	7.6	20.99	0.32	68.20	18.34	157.8
S2wonf475_07	475	7.4	21.48	0.38	46.65	15.70	166.5
S2wonf475_08	475	7.6	21.64	0.41	42.19	13.40	153.8
S2wonf475_09	475	6.7	13.79	0.42	36.71	5.59	139.4
S2wonf475_10	475	7.4	25.49	0.33	45.66	13.62	148.6
S2wonf475_11	475	7.6	23.25	0.34	47.98	19.90	162.7
S2wonf475_12	475	7.9	32.01	0.39	72.51	29.77	172.0
S2wonf475_13	475	6.5	10.88	0.43	47.29	4.26	143.8
S2wonf475_14	475	7.8	24.06	0.38	58.50	28.12	146.5
S2wonf475_15	475	6.9	12.68	0.33	39.73	7.53	136.8
S2wonf475_16	475	7.6	20.99	0.42	44.65	18.14	165.4
S2wonf475_17	475	7.7	19.53	0.39	57.81	12.70	147.5
S2wonf475_18	475	7.7	17.29	0.36	54.03	13.43	174.9
S2wonf475_19	475	7.4	22.15	0.41	67.81	13.02	168.5
S2wonf475_20	475	7.6	23.25	0.34	40.32	21.44	154.4
S2wonf225_01	225	7.8	41.03	0.25	34.38	16.72	114.3
S2wonf225_02	225	7.9	39.27	0.23	42.44	20.69	117.0
S2wonf225_03	225	7.9	39.27	0.23	34.19	20.29	112.5
S2wonf225_04	225	7.3	28.11	0.25	26.44	16.37	97.3
S2wonf225_05	225	7.1	20.59	0.26	33.84	9.60	97.7
S2wonf225_06	225	7.0	15.67	0.30	27.10	12.74	102.5

Table A.1 (Continued)

S2wonf225_07	225	7.2	23.49	0.26	27.52	15.77	103.8
S2wonf225_08	225	6.4	13.00	0.29	31.68	3.88	114.6
S2wonf225_09	225	7.3	40.29	0.23	36.54	10.30	108.0
S2wonf225_10	225	7.4	37.81	0.22	35.44	14.17	103.8
S2wonf225_11	225	7.2	24.69	0.24	37.95	12.49	100.4
S2wonf225_12	225	7.3	35.83	0.29	38.10	14.20	108.5
S2wonf225_13	225	7.6	43.75	0.24	31.24	18.71	113.5
S2wonf225_14	225	7.5	41.59	0.24	37.90	16.89	103.2
S2wonf225_15	225	7.3	32.59	0.21	25.21	16.11	101.2
S2wonf225_16	225	7.3	26.60	0.26	41.51	13.56	105.1
S2wonf225_17	225	6.8	17.60	0.28	28.48	6.72	109.5
S2wonf225_18	225	7.6	32.00	0.24	26.81	18.01	99.2
S2wonf225_19	225	6.6	14.14	0.26	22.86	6.77	86.9
S2wonf225_20	225	7.2	23.59	0.23	28.88	12.45	106.7
S2wonf75_01	75	6.4	31.60	0.10	8.68	4.14	38.4
S2wonf75_02	75	6.8	43.97	0.13	10.99	8.25	37.0
S2wonf75_03	75	5.9	13.23	0.12	9.10	3.08	35.6
S2wonf75_04	75	7.1	59.86	0.11	13.45	13.32	42.0
S2wonf75_05	75	6.1	23.64	0.12	9.66	3.22	37.3
S2wonf75_06	75	6.5	32.05	0.12	10.26	5.51	36.2
S2wonf75_07	75	6.9	48.63	0.11	15.40	8.81	37.9
S2wonf75_08	75	6.3	30.06	0.13	8.88	3.68	35.4
S2wonf75_09	75	6.4	31.68	0.09	9.29	4.65	36.5
S2wonf75_10	75	6.2	24.72	0.10	11.25	2.93	37.6
S2wonf75_11	75	7.0	57.84	0.12	14.70	10.64	37.1
S2wonf75_12	75	6.9	51.23	0.10	11.23	10.11	43.2
S2wonf75_13	75	6.2	25.32	0.12	11.29	3.88	40.1
S2wonf75_14	75	6.1	20.75	0.12	14.16	2.87	42.1
S2wonf75_15	75	6.6	37.96	0.09	10.38	6.39	36.8
S2wonf75_16	75	6.8	40.53	0.10	10.79	7.81	39.5
S2wonf75_17	75	6.6	40.76	0.10	13.31	4.78	40.4
S2wonf75_18	75	6.1	22.43	0.11	12.90	4.13	42.0
S2wonf75_19	75	6.2	22.17	0.11	9.56	5.44	37.3
S2wonf75_20	75	6.7	41.27	0.10	11.66	7.33	38.3
S2wnf2475_01	2475	6.8	6.34	0.75	91.48	5.00	326.9
S2wnf2475_02	2475	7.8	9.58	0.54	125.22	8.88	276.5
S2wnf2475_03	2475	7.7	6.54	0.57	156.31	9.58	311.3
S2wnf2475_04	2475	7.8	9.58	0.62	146.07	9.05	268.7
S2wnf2475_05	2475	7.7	12.80	0.76	94.43	23.94	294.9
S2wnf2475_06	2475	7.3	13.48	0.67	100.61	12.92	290.3
S2wnf2475_07	2475	7.7	8.67	0.80	119.05	19.24	277.3
S2wnf2475_08	2475	7.5	11.01	0.86	74.64	14.57	264.9
S2wnf2475_09	2475	7.3	8.35	0.68	146.18	10.08	315.7

Table A.1 (Continued)

S2wnf2475_10	2475	7.6	10.31	0.62	116.59	10.34	342.0
S2wnf2475_11	2475	7.7	10.21	0.76	89.70	18.20	329.6
S2wnf2475_12	2475	7.5	8.59	0.76	140.53	15.43	302.4
S2wnf2475_13	2475	7.2	7.96	0.68	101.42	10.13	288.7
S2wnf2475_14	2475	7.1	6.11	0.84	105.34	7.87	293.1
S2wnf2475_15	2475	7.9	10.78	0.65	121.79	11.12	256.5
S2wnf2475_16	2475	6.7	8.92	0.71	88.54	5.44	260.0
S2wnf2475_17	2475	6.8	6.34	0.81	134.32	4.15	365.1
S2wnf2475_18	2475	7.5	8.59	0.79	105.23	15.66	322.0
S2wnf2475_19	2475	7.6	13.41	0.62	101.76	21.19	285.9
S2wnf2475_20	2475	7.2	7.96	0.67	95.50	9.97	257.7
S2wnf475_01	475	7.4	22.15	0.41	67.81	13.02	168.5
S2wnf475_02	475	7.9	20.12	0.38	58.31	14.23	202.4
S2wnf475_03	475	6.9	12.68	0.44	64.96	6.92	182.1
S2wnf475_04	475	7.7	26.80	0.45	48.16	20.82	179.2
S2wnf475_05	475	7.5	18.13	0.37	51.63	16.81	175.1
S2wnf475_06	475	7.9	32.01	0.39	72.51	29.77	172.0
S2wnf475_07	475	7.8	20.26	0.34	56.81	14.82	177.4
S2wnf475_08	475	7.7	20.72	0.43	61.24	18.06	182.6
S2wnf475_09	475	7.9	24.26	0.32	55.19	14.27	192.3
S2wnf475_10	475	6.3	7.49	0.48	62.29	2.25	171.3
S2wnf475_11	475	7.4	21.48	0.38	49.75	16.44	175.0
S2wnf475_12	475	7.7	21.84	0.41	47.23	10.73	167.8
S2wnf475_13	475	7.9	22.02	0.36	78.12	14.24	202.2
S2wnf475_14	475	7.7	17.29	0.36	54.03	13.43	174.9
S2wnf475_15	475	7.2	15.44	0.34	42.36	10.76	183.7
S2wnf475_16	475	7.4	21.48	0.38	46.65	15.70	166.5
S2wnf475_17	475	7.5	18.13	0.32	38.33	15.23	164.9
S2wnf475_18	475	7.9	29.21	0.33	52.24	23.79	195.4
S2wnf475_19	475	7.8	29.12	0.37	63.02	18.84	164.3
S2wnf475_20	475	7.7	17.29	0.35	74.08	15.30	178.2
S2wnf225_01	225	7.8	41.03	0.25	34.38	16.72	114.3
S2wnf225_02	225	7.9	39.27	0.23	42.44	20.69	117.0
S2wnf225_03	225	7.9	39.27	0.23	34.19	20.29	112.5
S2wnf225_04	225	7.3	28.11	0.25	26.44	16.37	97.3
S2wnf225_05	225	7.1	20.59	0.26	33.84	9.60	97.7
S2wnf225_06	225	7.0	15.67	0.30	27.10	12.74	102.5
S2wnf225_07	225	7.2	23.49	0.26	27.52	15.77	103.8
S2wnf225_08	225	6.4	13.00	0.29	31.68	3.88	114.6
S2wnf225_09	225	7.3	40.29	0.23	36.54	10.30	108.0
S2wnf225_10	225	7.4	37.81	0.22	35.44	14.17	103.8
S2wnf225_11	225	7.2	24.69	0.24	37.95	12.49	100.4
S2wnf225_12	225	7.3	35.83	0.29	38.10	14.20	108.5

Table A.1 (Continued)

S2wnf225_13	225	7.6	43.75	0.24	31.24	18.71	113.5
S2wnf225_14	225	7.5	41.59	0.24	37.90	16.89	103.2
S2wnf225_15	225	7.3	32.59	0.21	25.21	16.11	101.2
S2wnf225_16	225	7.3	26.60	0.26	41.51	13.56	105.1
S2wnf225_17	225	6.8	17.60	0.28	28.48	6.72	109.5
S2wnf225_18	225	7.6	32.00	0.24	26.81	18.01	99.2
S2wnf225_19	225	6.6	14.14	0.26	22.86	6.77	86.9
S2wnf225_20	225	7.2	23.59	0.23	28.88	12.45	106.7
S2wnf75_01	75	6.4	31.60	0.10	8.68	4.14	38.4
S2wnf75_02	75	6.8	43.97	0.13	10.99	8.25	37.0
S2wnf75_03	75	5.9	13.23	0.12	9.10	3.08	35.6
S2wnf75_04	75	7.1	59.86	0.11	13.45	13.32	42.0
S2wnf75_05	75	6.1	23.64	0.12	9.66	3.22	37.3
S2wnf75_06	75	6.5	32.05	0.12	10.26	5.51	36.2
S2wnf75_07	75	6.9	48.63	0.11	15.40	8.81	37.9
S2wnf75_08	75	6.3	30.06	0.13	8.88	3.68	35.4
S2wnf75_09	75	6.4	31.68	0.09	9.29	4.65	36.5
S2wnf75_10	75	6.2	24.72	0.10	11.25	2.93	37.6
S2wnf75_11	75	7.0	57.84	0.12	14.70	10.64	37.1
S2wnf75_12	75	6.9	51.23	0.10	11.23	10.11	43.2
S2wnf75_13	75	6.2	25.32	0.12	11.29	3.88	40.1
S2wnf75_14	75	6.1	20.75	0.12	14.16	2.87	42.1
S2wnf75_15	75	6.6	37.96	0.09	10.38	6.39	36.8
S2wnf75_16	75	6.8	40.53	0.10	10.79	7.81	39.5
S2wnf75_17	75	6.6	40.76	0.10	13.31	4.78	40.4
S2wnf75_18	75	6.1	22.43	0.11	12.90	4.13	42.0
S2wnf75_19	75	6.2	22.17	0.11	9.56	5.44	37.3
S2wnf75_20	75	6.7	41.27	0.10	11.66	7.33	38.3
S3G2475_01	2475	7.6	8.01	0.52	80.90	7.52	193.3
S3G2475_02	2475	7.3	9.19	0.51	62.74	9.75	193.0
S3G2475_03	2475	7.4	11.43	0.51	99.90	12.70	179.5
S3G2475_04	2475	7.7	13.13	0.56	63.69	7.57	161.1
S3G2475_05	2475	6.9	4.43	0.59	60.52	6.08	191.9
S3G2475_06	2475	7.8	11.53	0.61	89.34	20.82	219.3
S3G2475_07	2475	7.1	5.29	0.55	54.71	8.99	159.3
S3G2475_08	2475	7.4	10.71	0.49	69.76	16.31	183.5
S3G2475_09	2475	7.7	8.60	0.66	70.57	10.37	175.5
S3G2475_10	2475	7.0	4.48	0.56	70.23	5.81	213.0
S3G2475_11	2475	7.5	7.89	0.56	67.85	16.18	194.8
S3G2475_12	2475	7.4	10.71	0.51	45.68	16.24	173.8
S3G2475_13	2475	7.1	9.36	0.51	75.65	9.94	187.4
S3G2475_14	2475	7.4	10.71	0.52	52.88	14.73	156.9
S3G2475_15	2475	7.2	11.03	0.60	76.68	10.79	199.0

Table A.1 (Continued)

S3G2475_16	2475	7.1	8.94	0.75	42.04	7.70	164.9
S3G2475_17	2475	7.6	11.89	0.47	55.29	8.66	182.8
S3G2475_18	2475	7.9	13.66	0.65	56.63	27.62	184.4
S3G2475_19	2475	7.3	10.42	0.48	55.59	8.06	172.5
S3G2475_20	2475	6.9	4.43	0.66	70.10	6.47	212.2
S3G475_01	475	7.2	14.22	0.32	53.01	11.55	128.1
S3G475_02	475	7.4	19.99	0.31	41.37	11.98	133.6
S3G475_03	475	7.7	22.76	0.31	42.07	22.14	122.6
S3G475_04	475	7.5	21.16	0.28	40.12	16.92	124.3
S3G475_05	475	7.7	15.73	0.36	37.98	13.12	114.7
S3G475_06	475	6.8	5.91	0.33	49.37	5.21	113.4
S3G475_07	475	7.6	16.70	0.37	45.66	12.97	116.0
S3G475_08	475	6.5	5.82	0.32	34.73	4.69	112.6
S3G475_09	475	6.8	11.11	0.37	31.04	5.36	122.0
S3G475_10	475	7.4	14.12	0.34	49.78	12.07	132.0
S3G475_11	475	7.3	19.83	0.39	49.43	12.36	133.7
S3G475_12	475	7.6	14.15	0.33	44.19	15.48	112.1
S3G475_13	475	7.3	17.96	0.36	36.35	13.14	120.5
S3G475_14	475	7.4	14.12	0.34	47.47	12.16	127.0
S3G475_15	475	7.8	18.42	0.40	43.59	17.27	125.4
S3G475_16	475	7.3	15.53	0.33	24.58	11.23	100.3
S3G475_17	475	7.4	19.99	0.35	37.63	13.45	122.7
S3G475_18	475	7.4	15.84	0.33	44.08	11.31	127.5
S3G475_19	475	7.9	23.37	0.34	54.48	15.89	135.5
S3G475_20	475	7.9	23.37	0.26	48.34	17.02	110.6
S3G225_01	225	7.5	26.80	0.26	33.01	17.08	100.2
S3G225_02	225	7.7	32.43	0.26	47.48	14.44	93.8
S3G225_03	225	7.3	20.25	0.31	19.87	12.37	85.7
S3G225_04	225	7.5	36.32	0.23	30.61	16.54	84.9
S3G225_05	225	7.5	34.00	0.24	45.85	18.57	86.8
S3G225_06	225	7.7	27.70	0.23	26.84	17.47	80.2
S3G225_07	225	7.1	20.78	0.23	25.73	10.24	87.4
S3G225_08	225	7.3	19.88	0.28	23.90	11.43	93.7
S3G225_09	225	6.5	13.06	0.29	22.31	5.10	83.3
S3G225_10	225	7.4	29.98	0.29	31.43	13.87	86.7
S3G225_11	225	6.6	11.84	0.22	24.74	5.54	84.3
S3G225_12	225	6.8	16.85	0.23	22.78	6.48	83.2
S3G225_13	225	7.5	28.79	0.20	30.65	16.94	85.8
S3G225_14	225	6.7	16.30	0.25	23.64	5.93	84.6
S3G225_15	225	7.0	20.18	0.20	23.44	12.05	76.4
S3G225_16	225	7.3	25.80	0.25	28.22	11.94	80.2
S3G225_17	225	7.5	28.79	0.21	30.14	15.25	101.4
S3G225_18	225	7.3	23.12	0.26	27.75	12.57	95.5

Table A.1 (Continued)

S3G225_19	225	7.2	15.95	0.25	36.98	10.11	90.7
S3G225_20	225	7.8	22.33	0.29	34.01	14.64	85.6
S3G75_01	75	6.3	23.09	0.09	10.00	3.83	30.6
S3G75_02	75	6.4	18.43	0.10	10.90	5.15	29.2
S3G75_03	75	6.3	19.46	0.10	8.14	4.97	28.6
S3G75_04	75	6.5	32.01	0.11	8.50	5.33	31.0
S3G75_05	75	6.6	33.54	0.09	8.40	7.30	27.7
S3G75_06	75	6.7	37.43	0.09	9.80	7.30	32.6
S3G75_07	75	6.4	24.92	0.11	7.07	5.71	29.4
S3G75_08	75	6.8	44.32	0.09	10.97	9.14	30.7
S3G75_09	75	6.7	35.91	0.11	6.82	8.34	29.7
S3G75_10	75	6.7	42.34	0.10	10.62	7.14	34.3
S3G75_11	75	6.7	42.72	0.09	10.30	5.28	34.5
S3G75_12	75	6.9	43.17	0.12	12.22	7.89	32.4
S3G75_13	75	6.0	14.92	0.10	12.09	3.30	31.3
S3G75_14	75	6.7	38.59	0.10	9.49	8.91	33.2
S3G75_15	75	6.3	19.46	0.10	8.80	4.79	33.0
S3G75_16	75	6.3	20.53	0.09	9.28	4.43	27.6
S3G75_17	75	6.6	27.80	0.11	11.39	5.13	33.3
S3G75_18	75	6.3	24.78	0.11	9.36	3.37	33.7
S3G75_19	75	6.1	17.96	0.09	7.65	2.14	29.9
S3G75_20	75	6.8	44.77	0.09	7.60	8.59	25.6
S3T2475_01	2475	7.3	8.20	0.55	63.02	6.56	234.5
S3T2475_02	2475	6.9	4.43	0.53	103.79	6.71	282.9
S3T2475_03	2475	7.4	11.43	0.49	100.76	13.38	237.1
S3T2475_04	2475	7.7	6.94	0.56	66.58	16.07	287.4
S3T2475_05	2475	7.3	8.12	0.65	83.04	6.16	255.0
S3T2475_06	2475	7.3	9.19	0.46	71.30	9.52	266.3
S3T2475_07	2475	7.5	7.89	0.56	79.26	16.61	261.1
S3T2475_08	2475	7.1	6.72	0.51	81.82	7.12	231.6
S3T2475_09	2475	7.7	8.60	0.57	79.34	10.29	247.9
S3T2475_10	2475	7.6	8.01	0.55	73.67	7.91	270.4
S3T2475_11	2475	7.1	8.94	0.73	52.92	8.76	227.4
S3T2475_12	2475	7.8	11.53	0.57	100.50	19.91	283.6
S3T2475_13	2475	7.0	4.48	0.58	87.06	4.80	281.7
S3T2475_14	2475	7.9	13.66	0.61	83.96	26.81	270.7
S3T2475_15	2475	7.3	10.42	0.50	67.87	7.58	256.0
S3T2475_16	2475	7.7	8.60	0.56	74.74	10.84	263.4
S3T2475_17	2475	7.1	6.72	0.45	70.15	5.95	248.4
S3T2475_18	2475	7.7	6.94	0.55	99.34	17.32	258.5
S3T2475_19	2475	7.0	4.48	0.50	87.83	6.12	305.4
S3T2475_20	2475	6.9	4.43	0.50	85.29	6.02	283.9
S3T475_01	475	7.4	19.55	0.38	34.94	14.48	157.9

Table A.1 (Continued)

S3T475_02	475	7.5	21.16	0.33	61.25	17.59	161.6
S3T475_03	475	7.8	18.42	0.38	42.67	18.66	170.0
S3T475_04	475	7.7	15.39	0.34	57.70	9.37	152.6
S3T475_05	475	7.0	9.66	0.42	41.58	9.00	167.2
S3T475_06	475	7.2	14.22	0.32	59.10	11.54	165.5
S3T475_07	475	7.3	19.83	0.37	50.99	12.36	166.8
S3T475_08	475	7.4	14.12	0.34	50.75	12.61	170.2
S3T475_09	475	6.9	9.75	0.35	45.19	8.24	148.3
S3T475_10	475	6.5	4.23	0.33	38.86	4.07	137.1
S3T475_11	475	6.8	11.11	0.34	34.06	5.38	161.0
S3T475_12	475	6.9	9.75	0.45	37.06	8.37	138.0
S3T475_13	475	7.7	14.31	0.39	93.35	12.74	198.1
S3T475_14	475	6.5	5.90	0.34	52.37	3.12	177.8
S3T475_15	475	7.9	13.65	0.35	63.73	14.78	188.7
S3T475_16	475	7.3	17.96	0.34	39.71	13.78	165.8
S3T475_17	475	7.8	10.79	0.36	39.24	11.18	179.4
S3T475_18	475	6.2	4.34	0.39	30.96	3.89	137.6
S3T475_19	475	7.4	19.55	0.33	40.41	14.08	136.7
S3T475_20	475	7.4	15.84	0.32	49.62	11.97	167.8
S3T225_01	225	6.7	16.30	0.25	30.26	5.73	123.1
S3T225_02	225	7.5	26.80	0.27	47.64	18.25	139.1
S3T225_03	225	7.3	23.12	0.24	26.12	13.03	123.8
S3T225_04	225	7.6	25.80	0.20	36.14	19.36	127.8
S3T225_05	225	7.1	16.38	0.27	39.38	11.73	114.0
S3T225_06	225	7.3	27.09	0.23	40.38	14.11	129.8
S3T225_07	225	7.2	16.86	0.28	46.38	13.73	131.5
S3T225_08	225	7.3	27.09	0.29	41.64	13.98	123.7
S3T225_09	225	7.5	34.61	0.26	28.36	14.41	125.8
S3T225_10	225	7.3	23.66	0.25	24.89	12.37	128.4
S3T225_11	225	7.1	19.99	0.26	43.56	10.43	141.2
S3T225_12	225	7.5	28.87	0.25	55.34	14.64	126.4
S3T225_13	225	7.6	24.73	0.26	41.36	21.16	132.6
S3T225_14	225	7.7	19.40	0.35	31.93	14.88	115.3
S3T225_15	225	7.5	26.80	0.23	33.81	18.83	131.6
S3T225_16	225	7.8	24.37	0.29	45.86	17.23	129.8
S3T225_17	225	7.8	24.37	0.27	55.08	20.91	126.1
S3T225_18	225	7.3	19.88	0.28	31.68	11.77	113.4
S3T225_19	225	6.7	13.53	0.29	27.30	6.98	118.1
S3T225_20	225	7.7	38.30	0.25	35.66	20.52	133.1
S3T75_01	75	6.9	43.17	0.09	12.53	8.57	40.8
S3T75_02	75	6.0	14.92	0.09	14.16	3.30	41.4
S3T75_03	75	6.4	24.92	0.11	9.83	5.74	42.1
S3T75_04	75	6.1	17.96	0.10	8.72	2.09	42.5

Table A.1 (Continued)

S3T75_05	75	6.3	24.78	0.11	11.59	3.45	45.1
S3T75_06	75	7.0	55.25	0.10	11.01	12.93	43.5
S3T75_07	75	7.0	48.32	0.11	11.83	12.63	45.1
S3T75_08	75	6.9	43.17	0.10	12.61	8.44	41.9
S3T75_09	75	6.9	43.25	0.11	9.92	8.66	47.1
S3T75_10	75	6.6	28.69	0.09	12.24	5.73	46.5
S3T75_11	75	6.8	39.19	0.09	10.35	8.46	40.2
S3T75_12	75	7.1	55.34	0.11	13.01	12.84	46.5
S3T75_13	75	6.3	19.46	0.09	10.17	4.85	41.0
S3T75_14	75	6.7	45.78	0.09	12.10	5.78	43.1
S3T75_15	75	6.7	33.45	0.10	9.74	6.12	44.2
S3T75_16	75	6.7	37.43	0.09	11.40	7.35	46.8
S3T75_17	75	7.0	48.32	0.11	15.42	14.27	48.5
S3T75_18	75	7.3	61.89	0.13	17.06	17.17	43.8
S3T75_19	75	6.9	42.53	0.09	11.88	8.43	48.0
S3T75_20	75	7.1	58.24	0.11	7.78	11.07	41.1

APPENDIX B

RESIDUAL PLOTS OF DEMAND PREDICTION EQUATIONS

Figures B.1-B.6 show the residual scatters of demand predictive models for ESDOFs without structural variability with respect to moment magnitude (M_w), closest distance to rupture (R_{rup}) and effective duration (which is shown as duration in the figures) for the three sites with different site amplification and near-field forward directivity models.

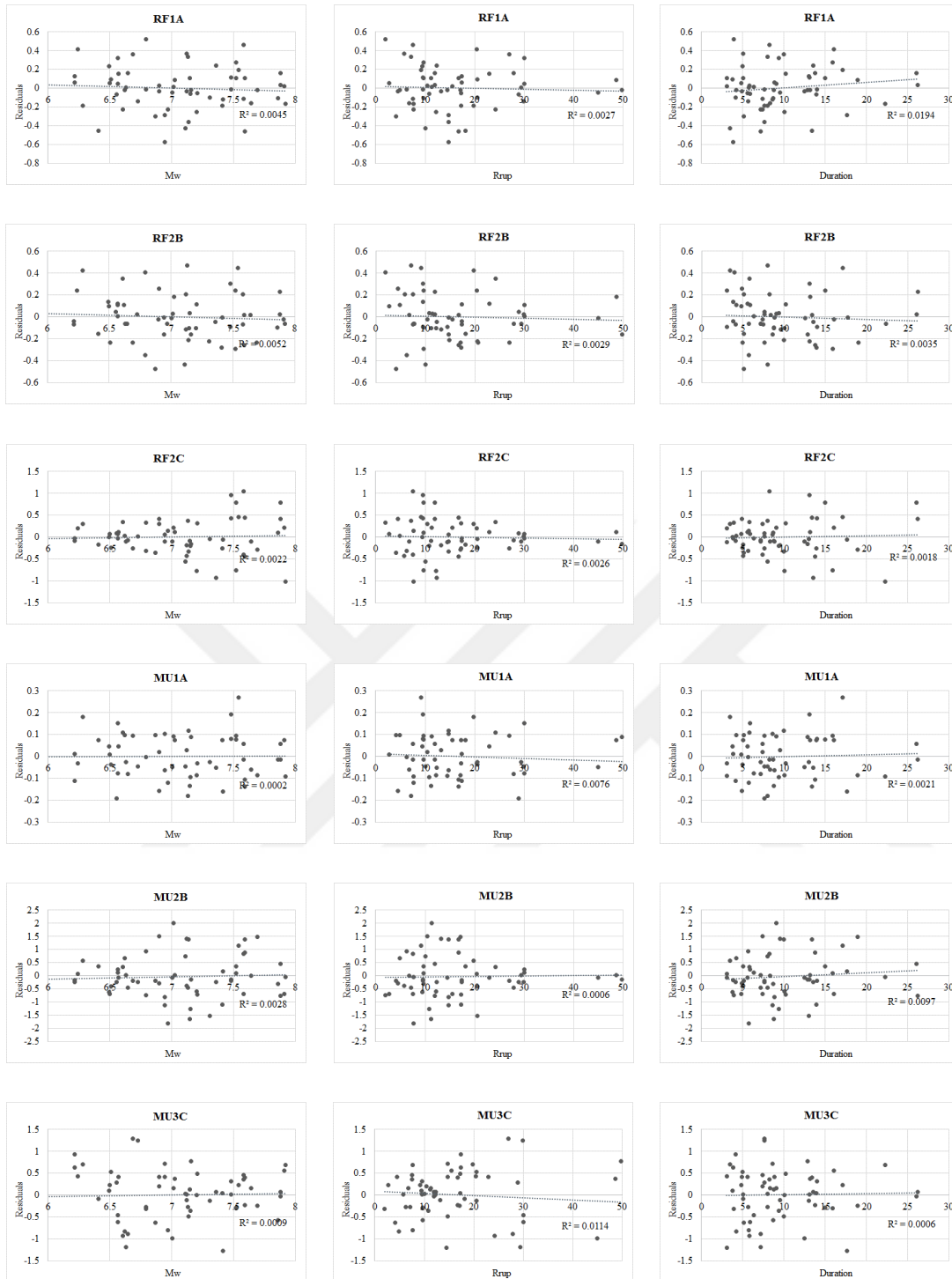


Figure B.1. Residual plots related to predictive models of Figure 4.3 with respect to magnitude, distance (km) and duration (s) (Site 1 generic site amplification).

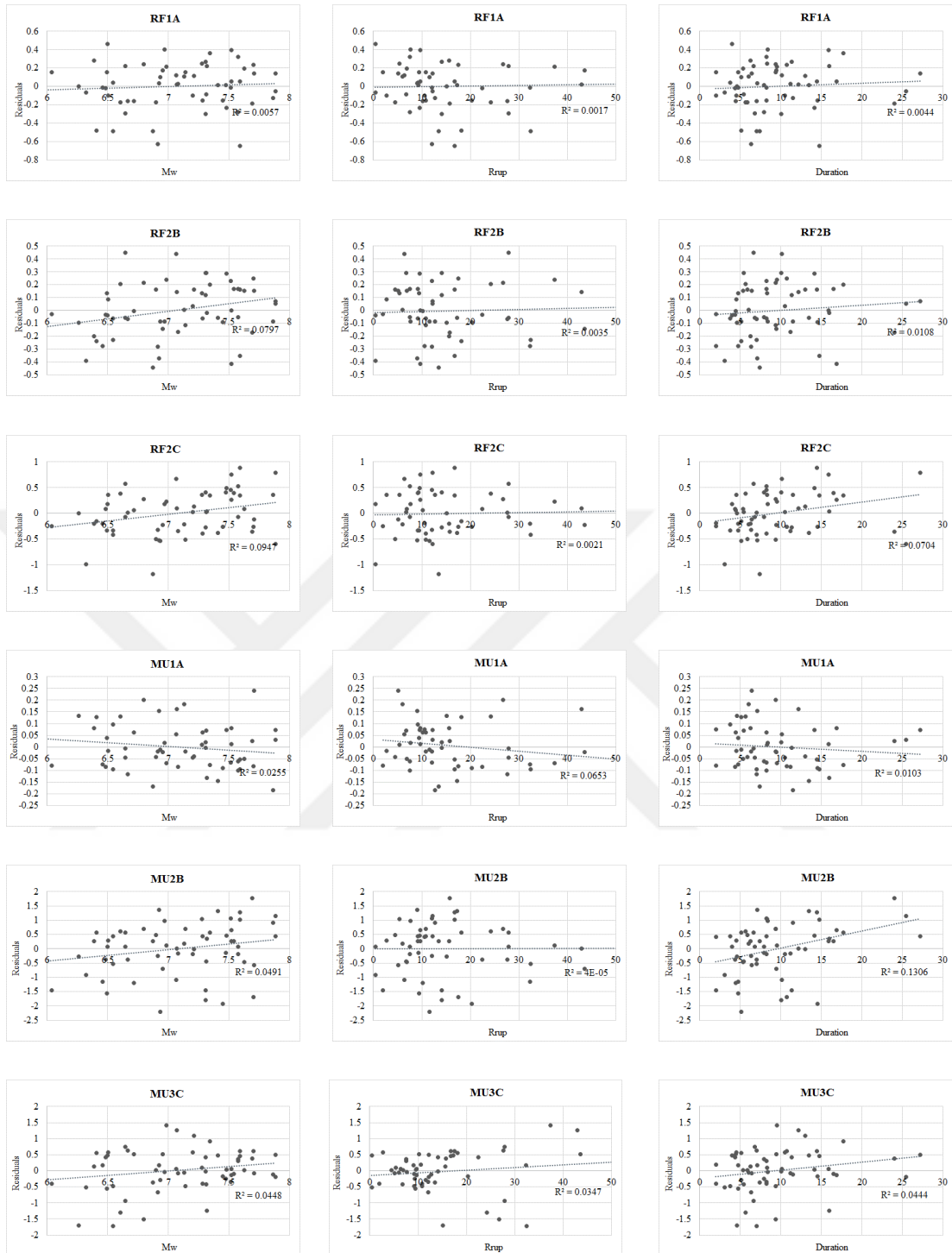


Figure B.2. Residual plots related to predictive models of Figure 4.4 with respect to magnitude, distance (km) and duration (s) (Site 1 theoretical site amplification).

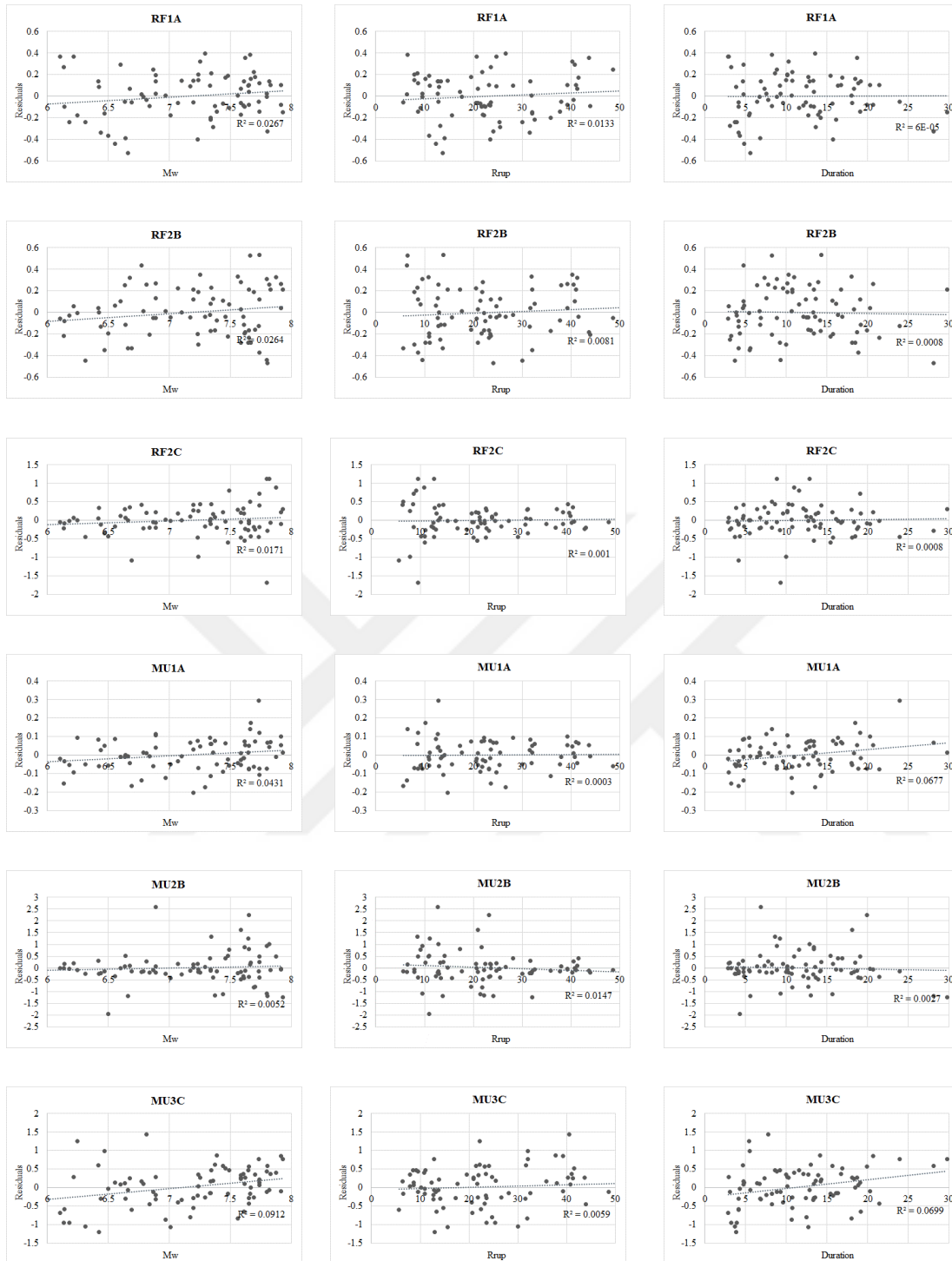


Figure B.3. Residual plots related to predictive models of Figure 4.5 with respect to magnitude, distance (km) and duration (s) (Site 2 without near-field forward directivity).

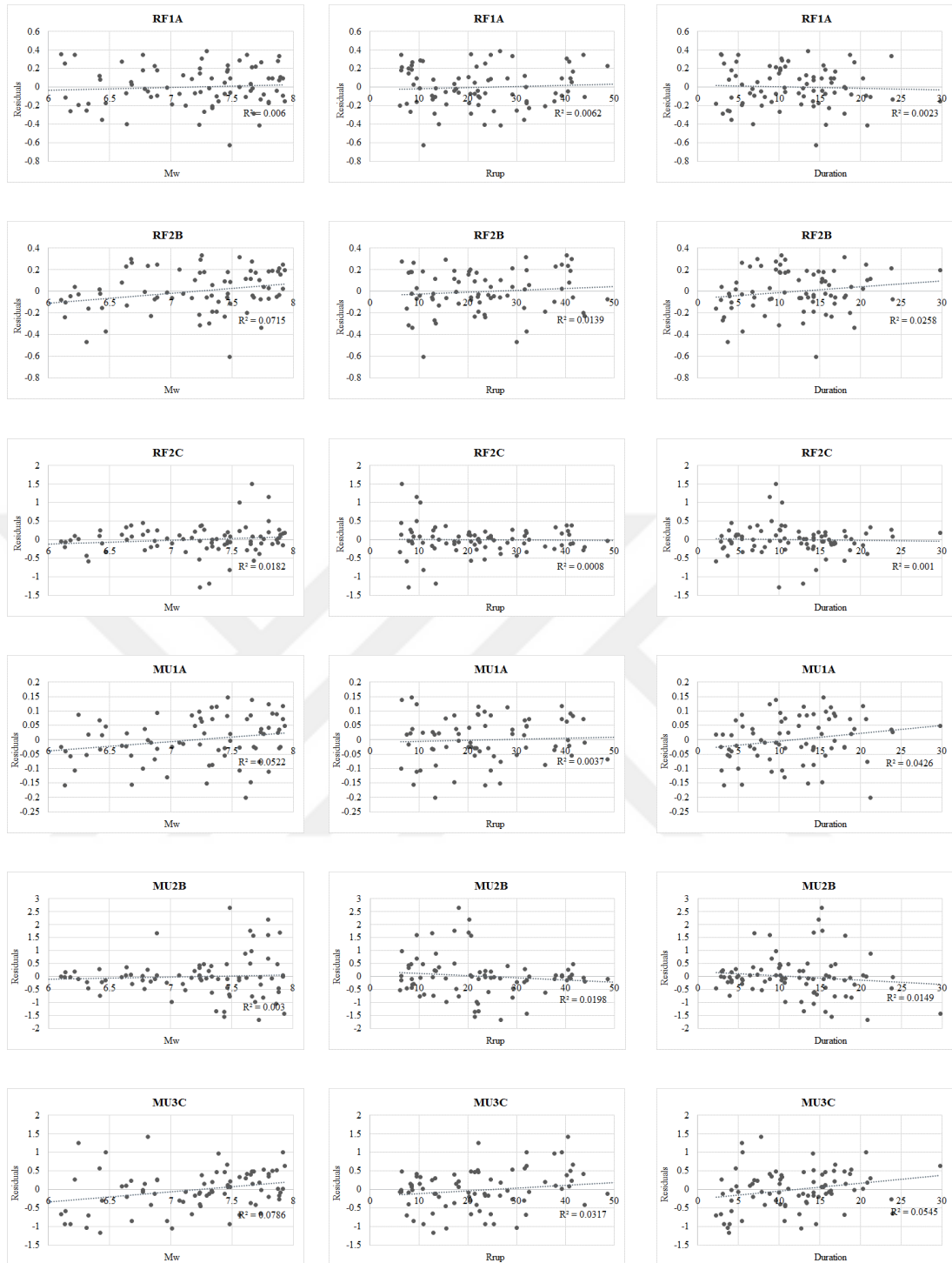


Figure B.4. Residual plots related to predictive models of Figure 4.6 with respect to magnitude, distance (km) and duration (s) (Site 2 with near-field forward directivity).

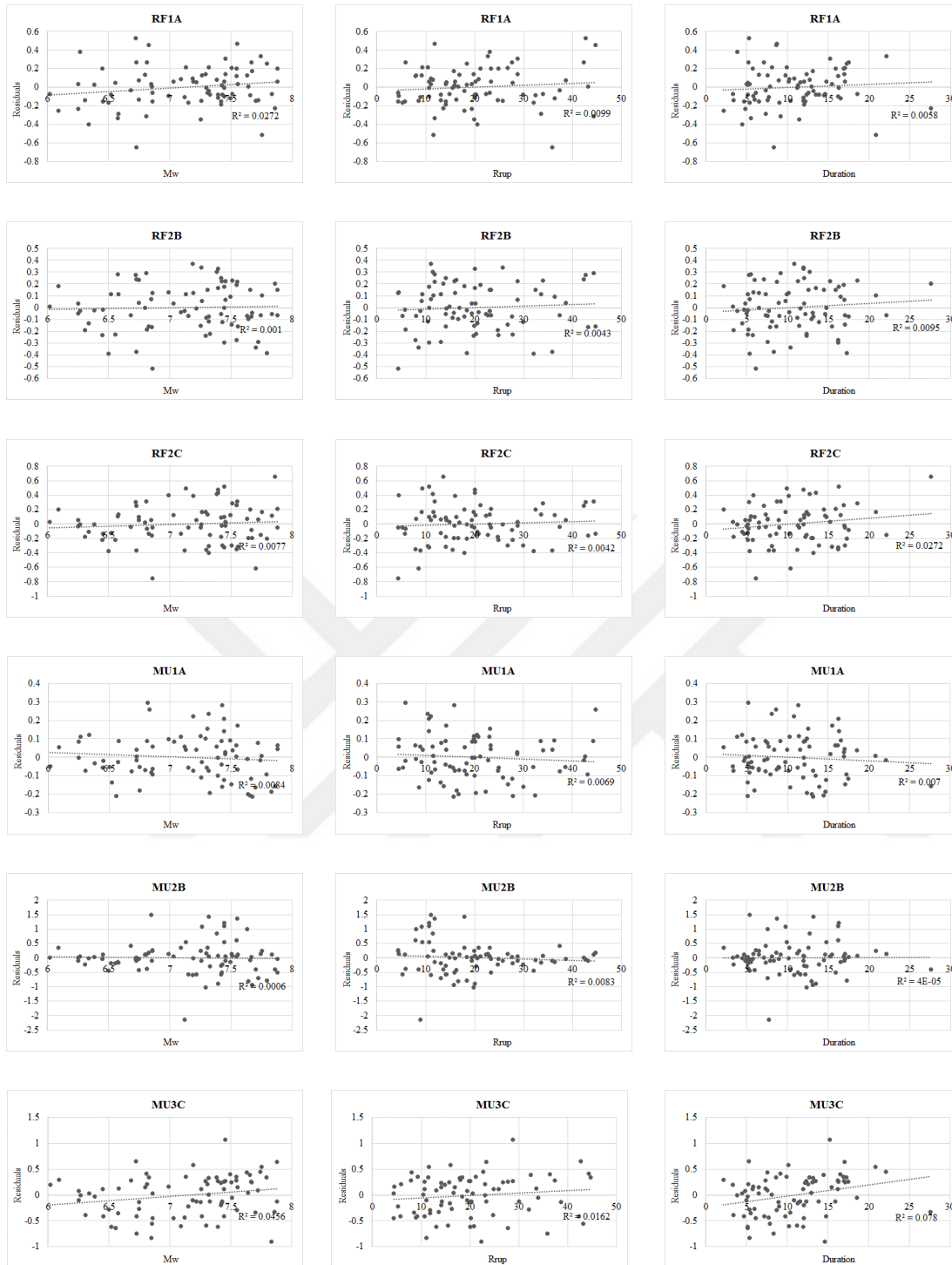


Figure B.5. Residual plots related to predictive models of Figure 4.7 with respect to magnitude, distance (km) and duration (s) (Site 3 using generic site amplification).

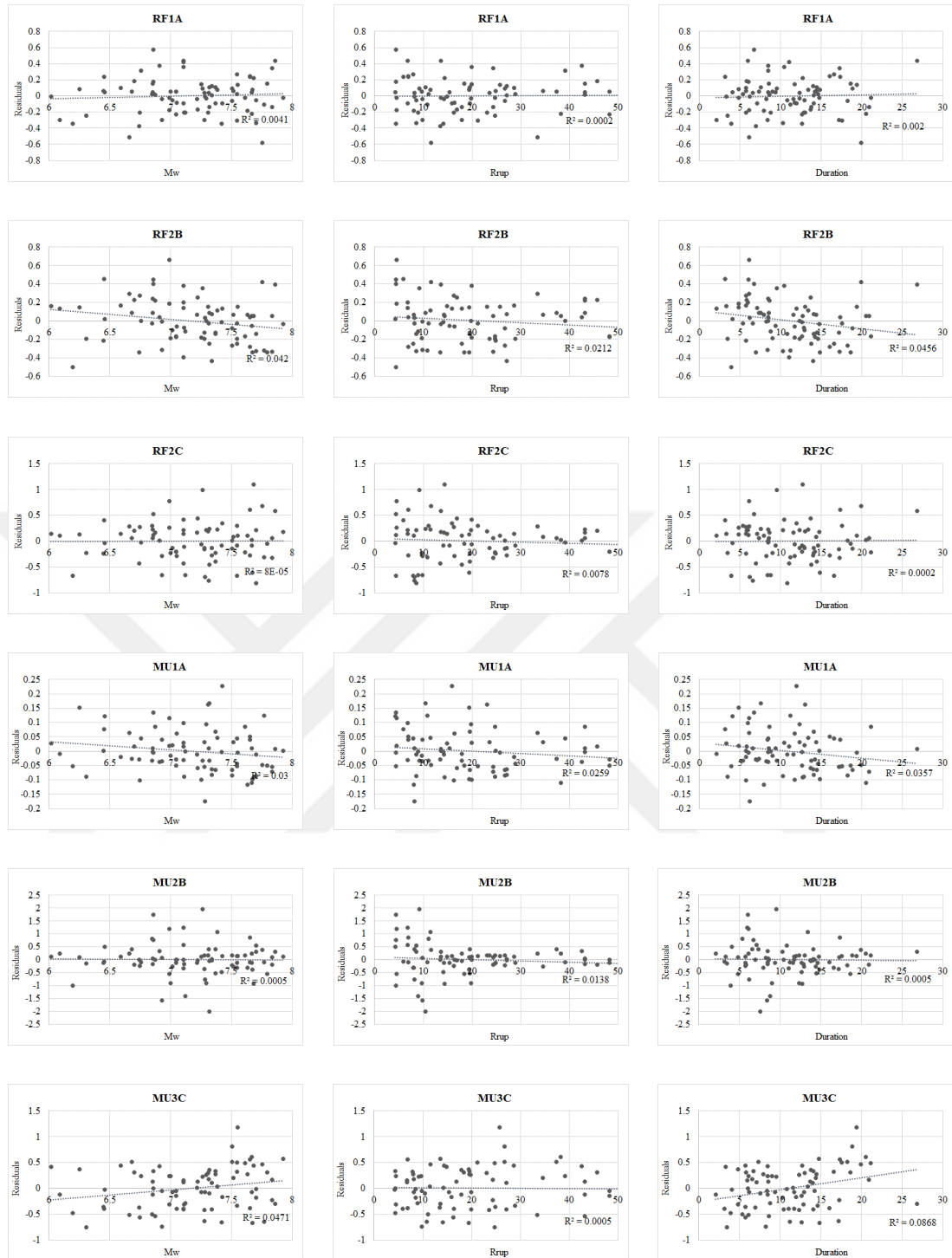


Figure B.6. Residual plots related to predictive models of Figure 4.8 with respect to magnitude, distance (km) and duration (s) (Site 3 using theoretical site amplification).



APPENDIX C

VARIATIONS OF DEMAND WITH RESPECT TO EFFECTIVE DURATION

Displacement demand versus effective duration scatter plots are shown in this appendix for the whole cases and different PGA bins. The trend lines and corresponding R^2 values for the scatters are also displayed along with the figures. R^2 values regarding different cases (three sites with different site amplification and forward directivity models and six SDOF groups) and different PGA bins are tabulated in Chapter 4. The scatter plots are exhibited regarding Site 1 using generic site amplification and MU3C as an example in Chapter 4. The scatters regarding the whole cases are shown in Figures C.1 to C.36. In these figures, PGA_m and std. dev stand for mean and standard deviation of PGAs inside each bin, respectively and effective duration is shown by “Duration”.

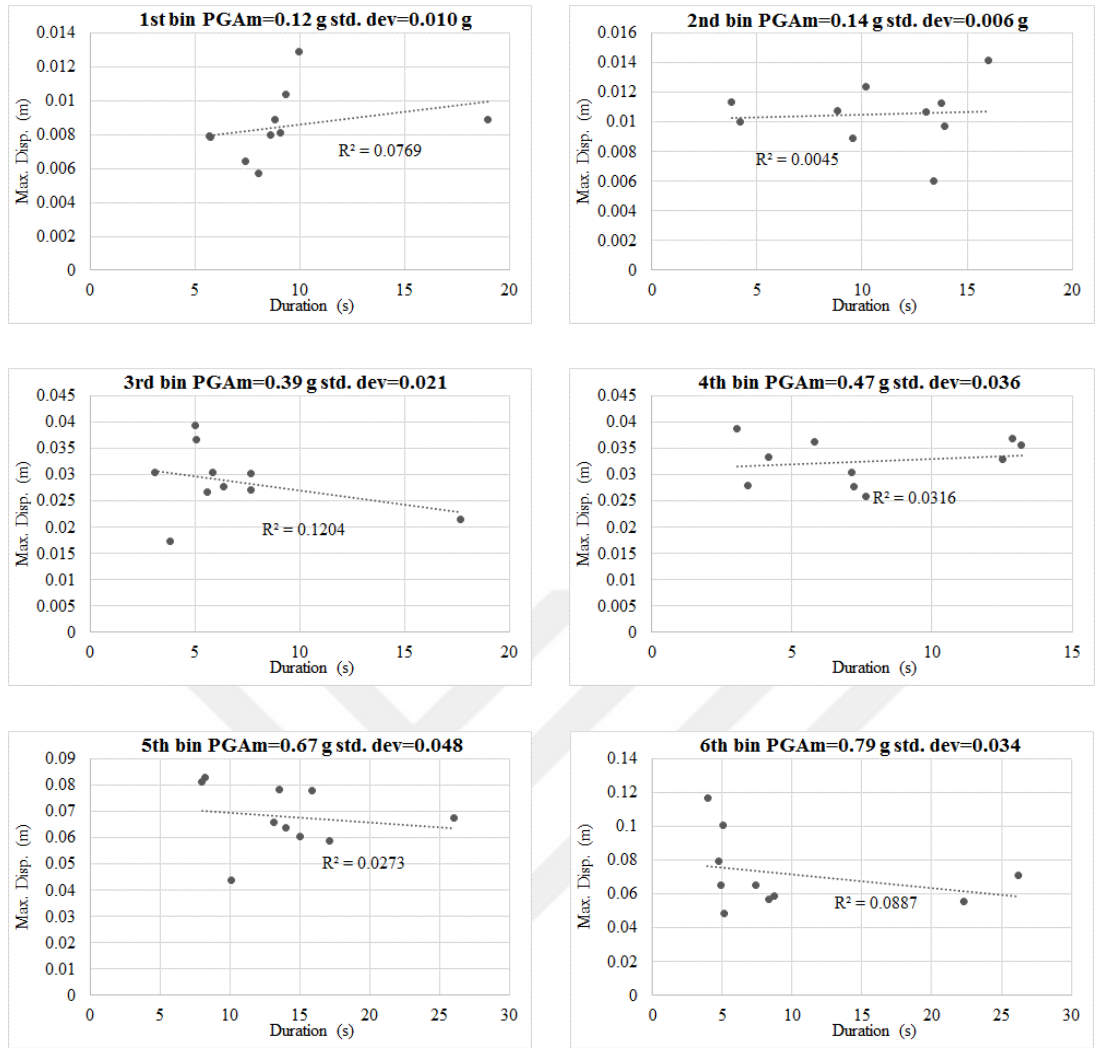


Figure C.1. Maximum displacement demand versus effective duration scatters for six PGA bins regarding Site 1 using generic site amplification and RF1A

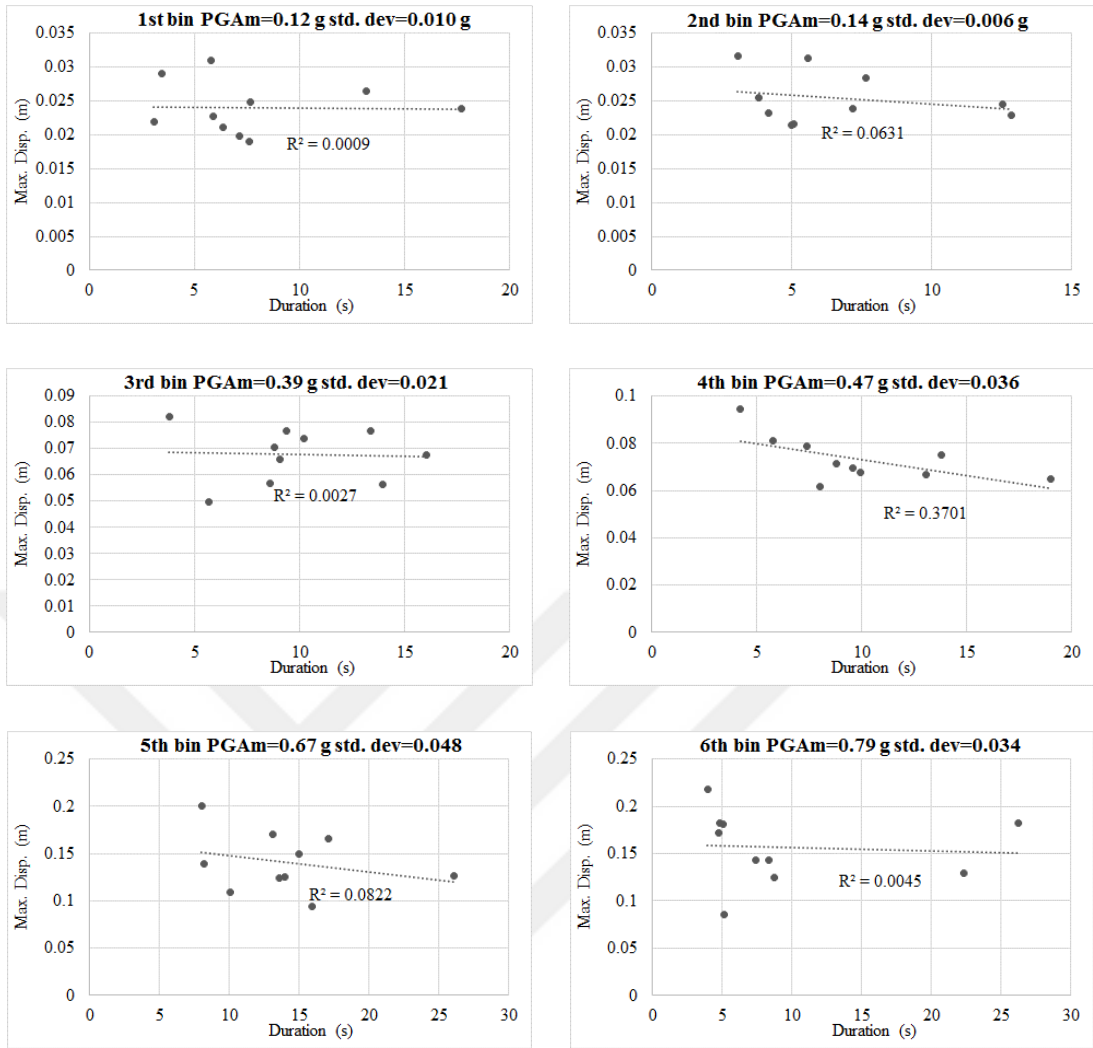


Figure C.2. Maximum displacement demand versus effective duration scatters for six PGA bins regarding Site 1 using generic site amplification and RF2B

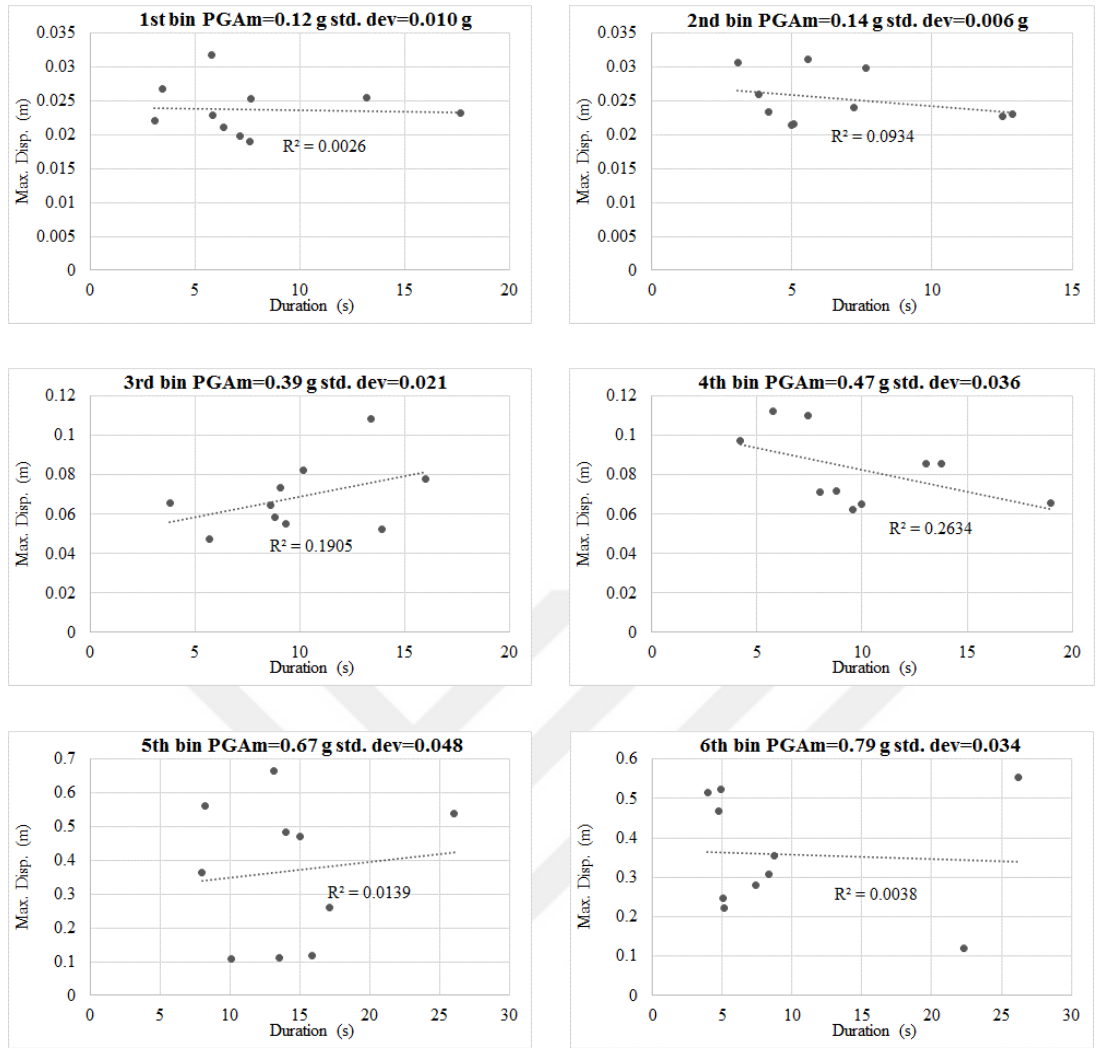


Figure C.3. Maximum displacement demand versus effective duration scatters for six PGA bins regarding Site 1 using generic site amplification and RF2C

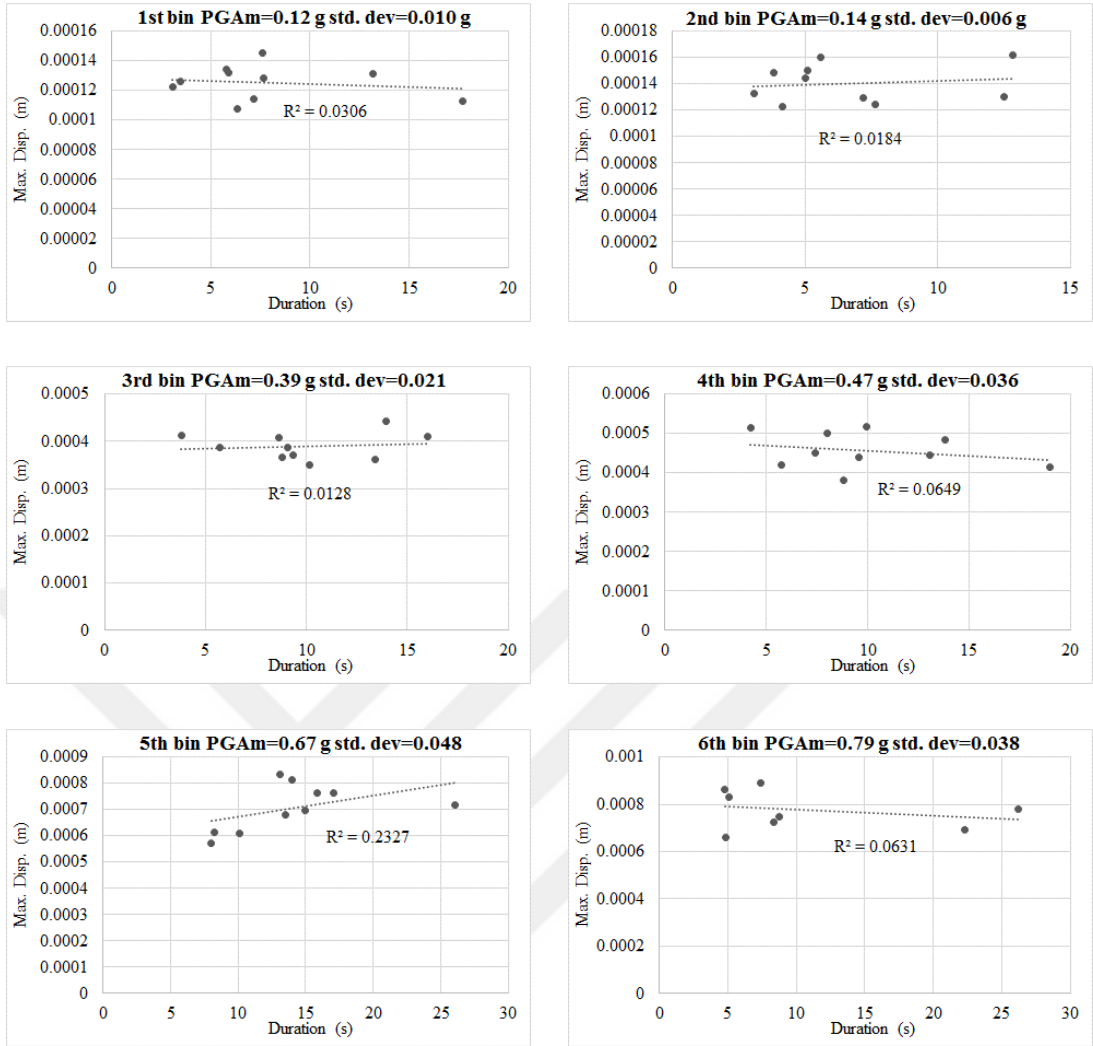


Figure C.4. Maximum displacement demand versus effective duration scatters for six PGA bins regarding Site 1 using generic site amplification and MU1A

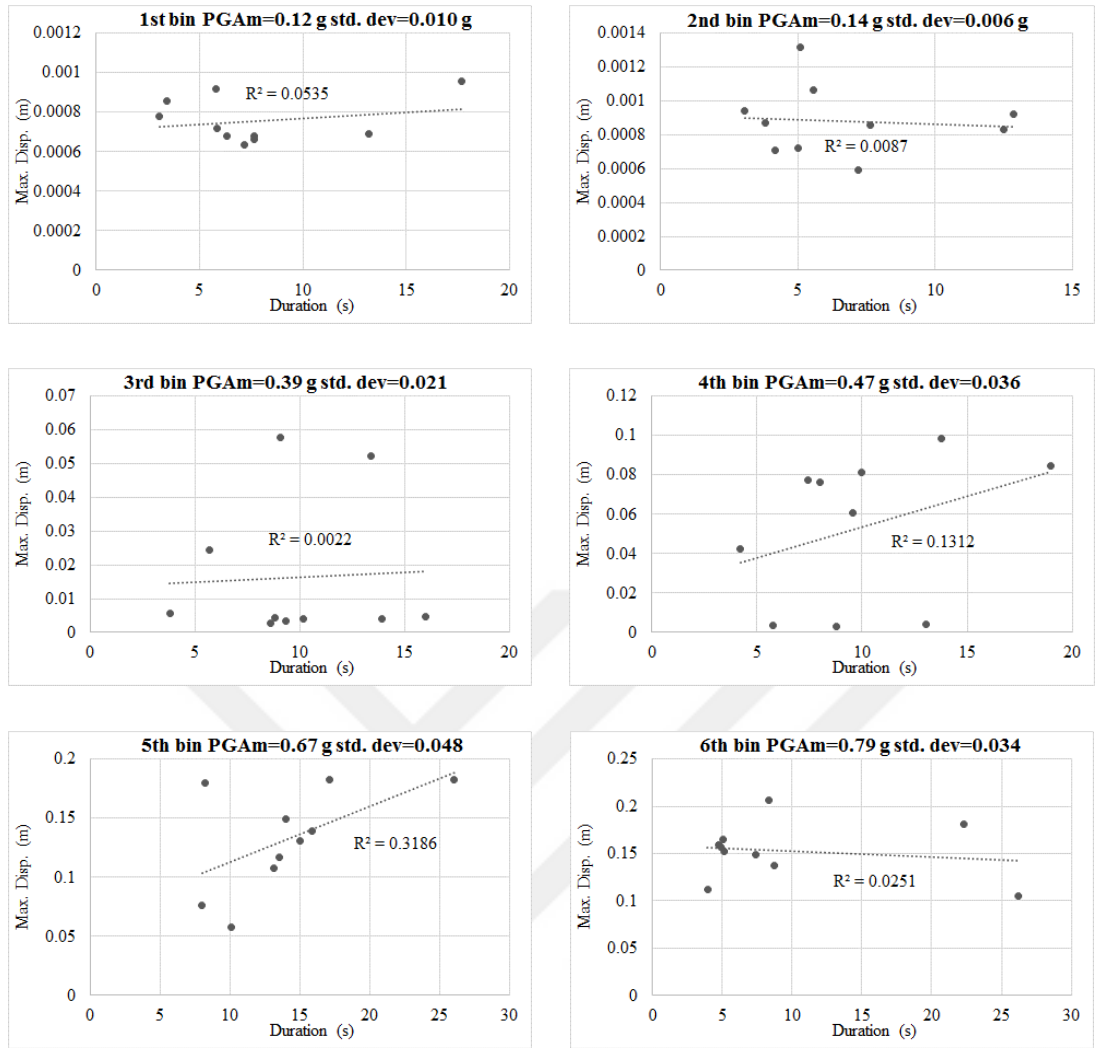


Figure C.5. Maximum displacement demand versus effective duration scatters for six PGA bins regarding Site 1 using generic site amplification and MU2B

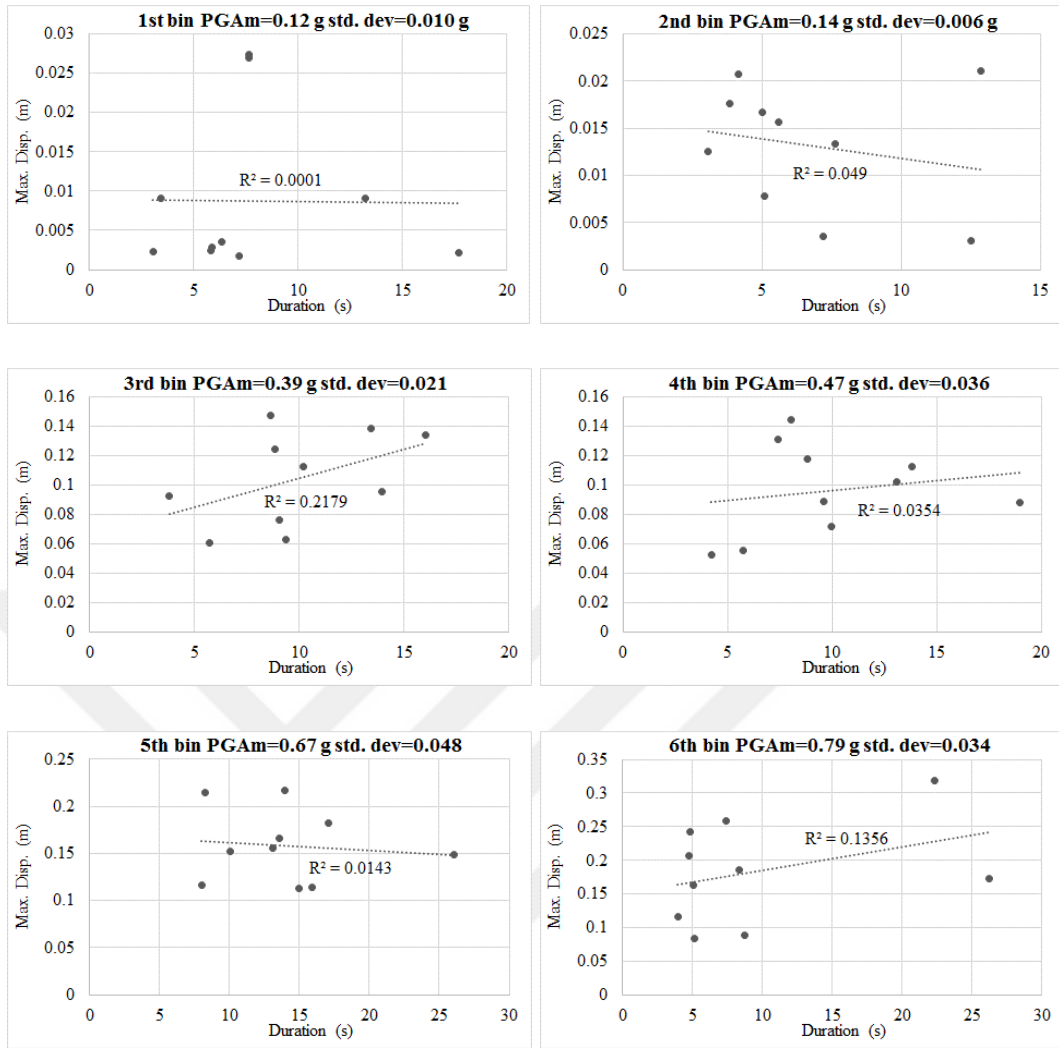


Figure C.6. Maximum displacement demand versus effective duration scatters for six PGA bins regarding Site 1 using generic site amplification and MU3C

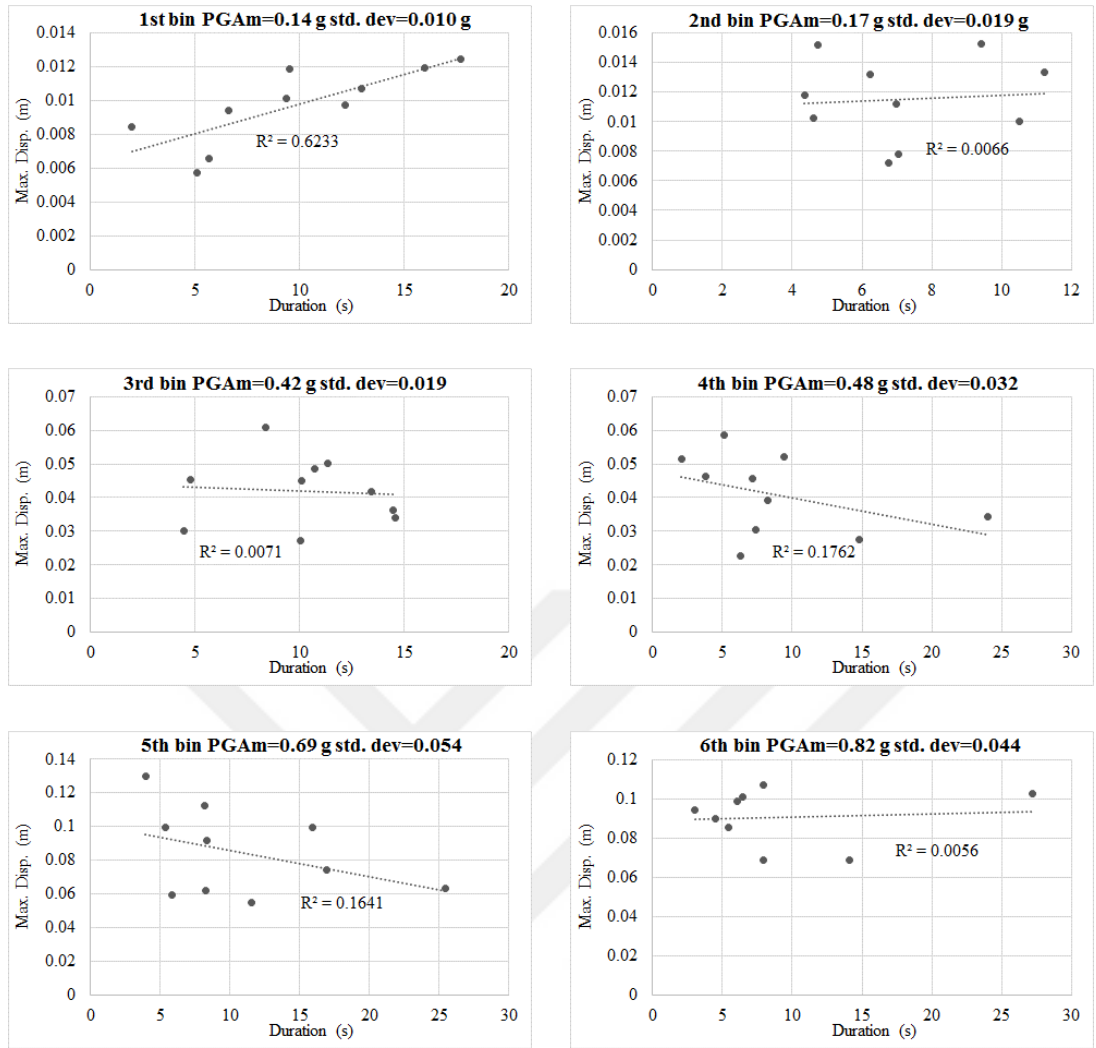


Figure C.7. Maximum displacement demand versus effective duration scatters for six PGAm bins regarding Site 1 using theoretical site amplification and RF1A

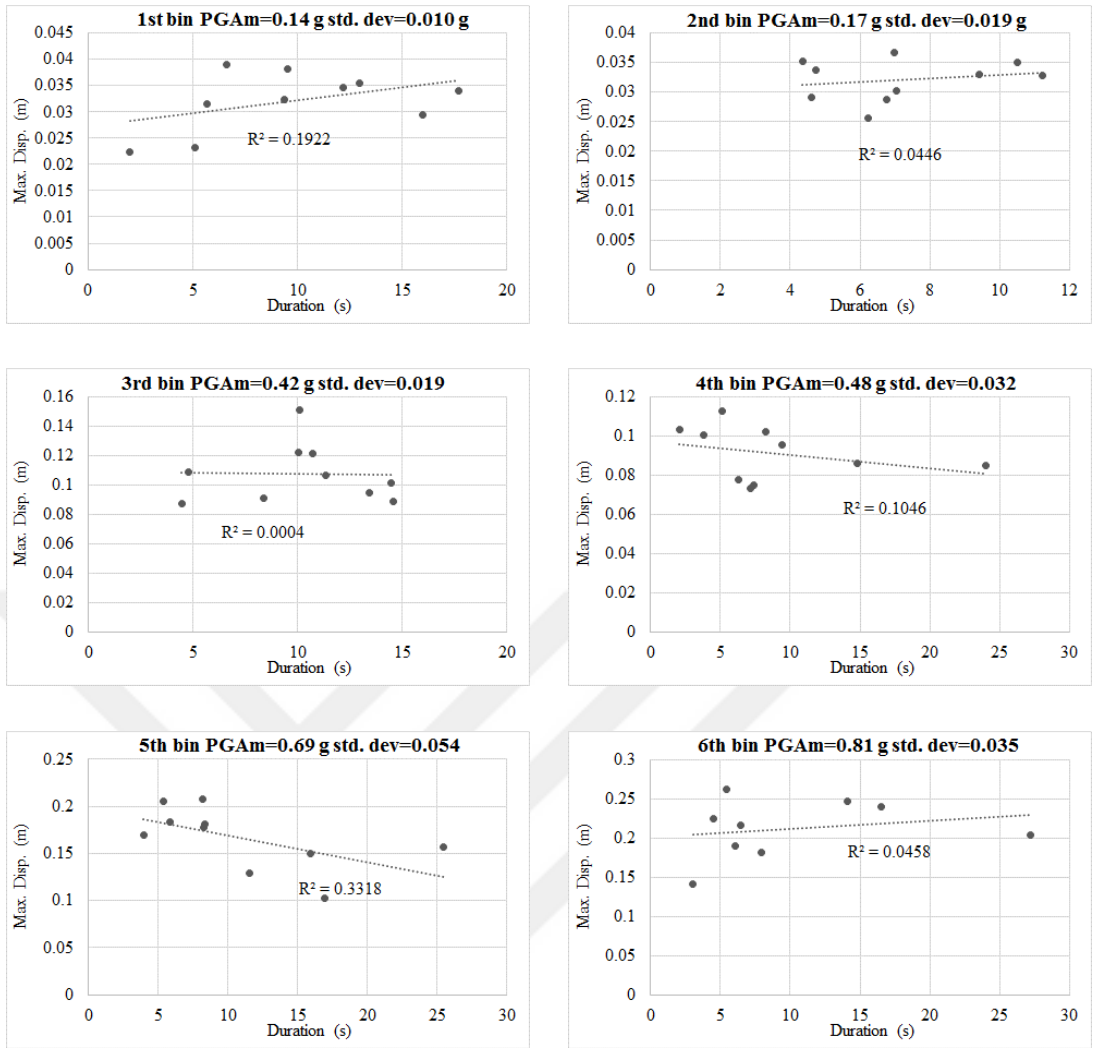


Figure C.8. Maximum displacement demand versus effective duration scatters for six PGA bins regarding Site 1 using theoretical site amplification and RF2B

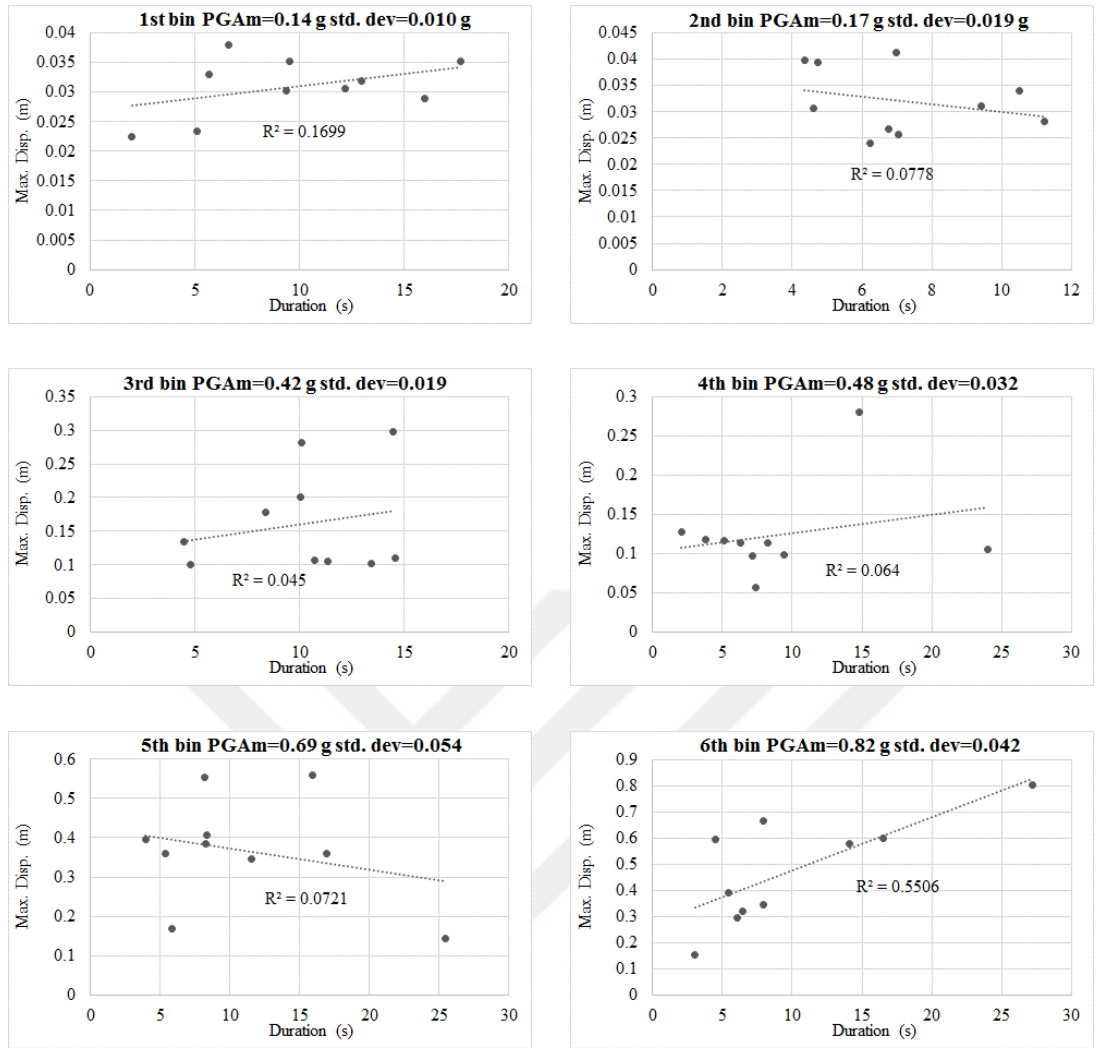


Figure C.9. Maximum displacement demand versus effective duration scatters for six PGAm bins regarding Site 1 using theoretical site amplification and RF2C

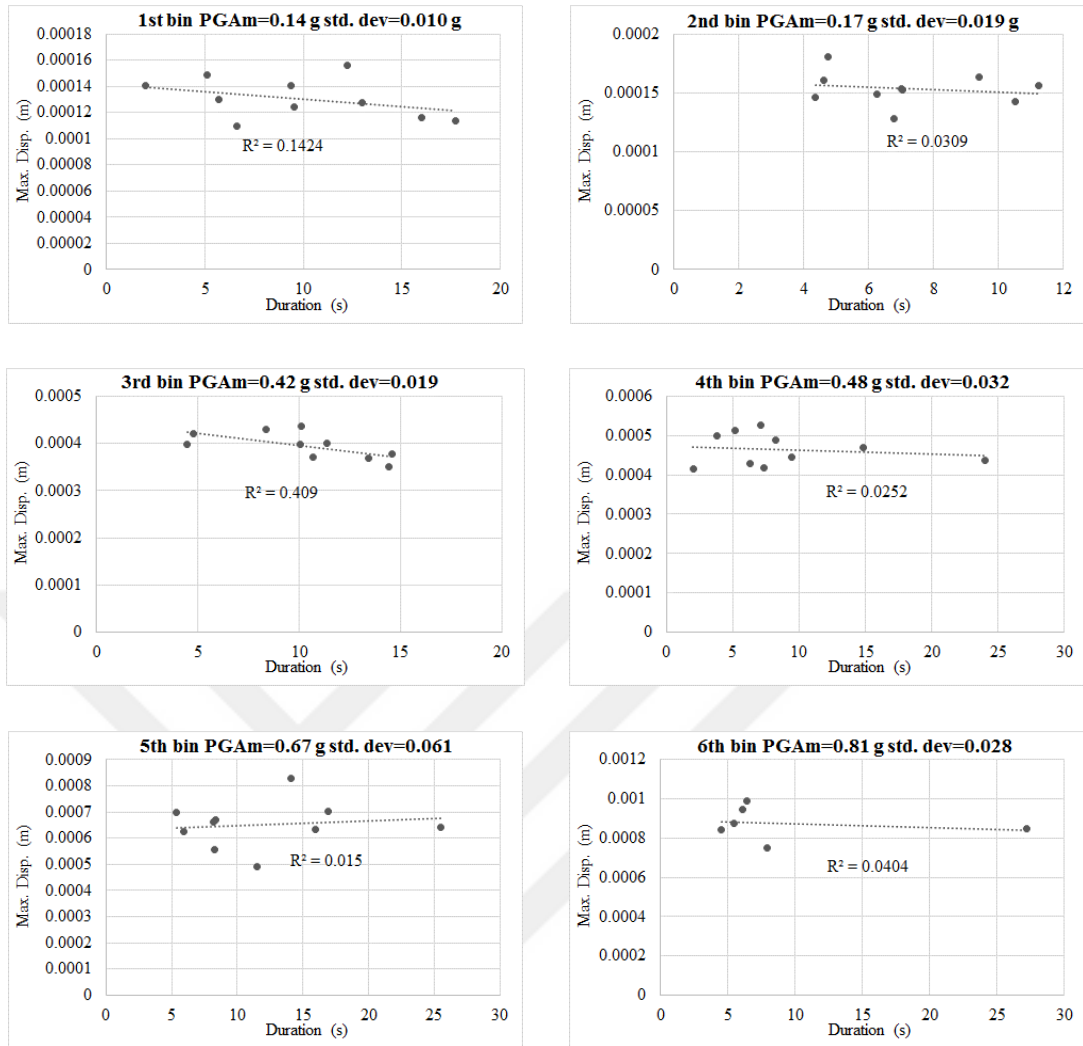


Figure C.10. Maximum displacement demand versus effective duration scatters for six PGA bins regarding Site 1 using theoretical site amplification and MU1A

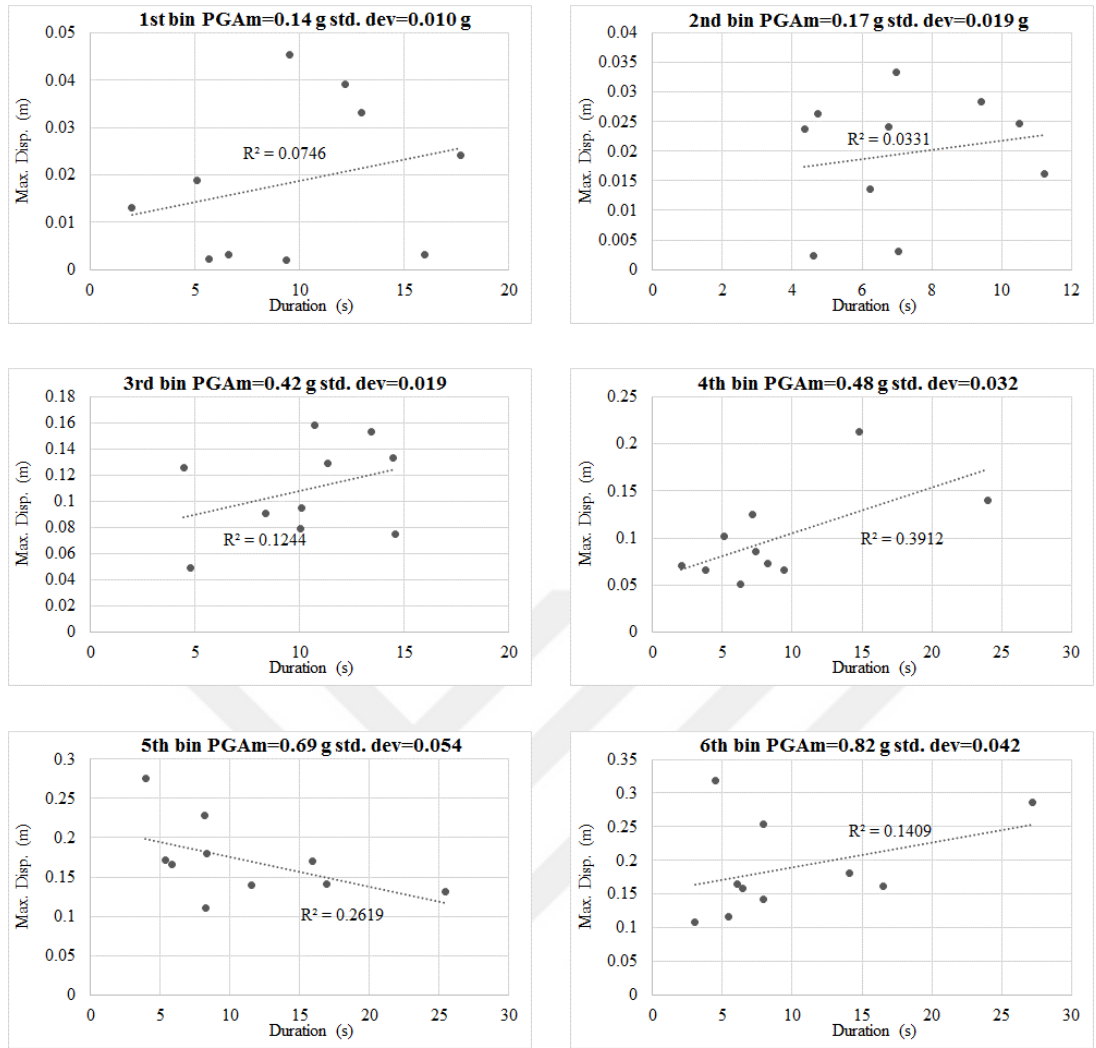


Figure C.11. Maximum displacement demand versus effective duration scatters for six PGA bins regarding Site 1 using theoretical site amplification and MU2B

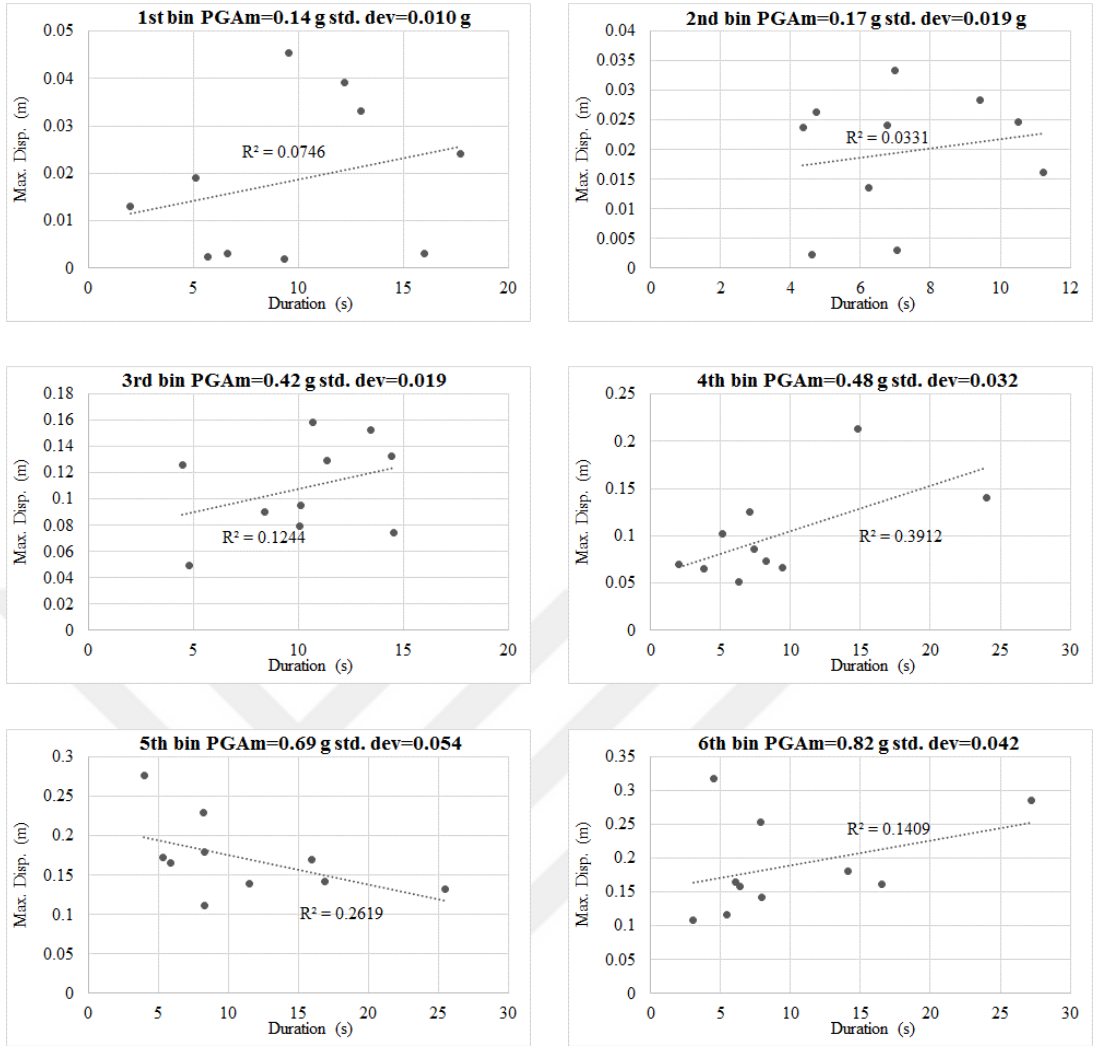


Figure C.12. Maximum displacement demand versus effective duration scatters for six PGA bins regarding Site 1 using theoretical site amplification and MU3C

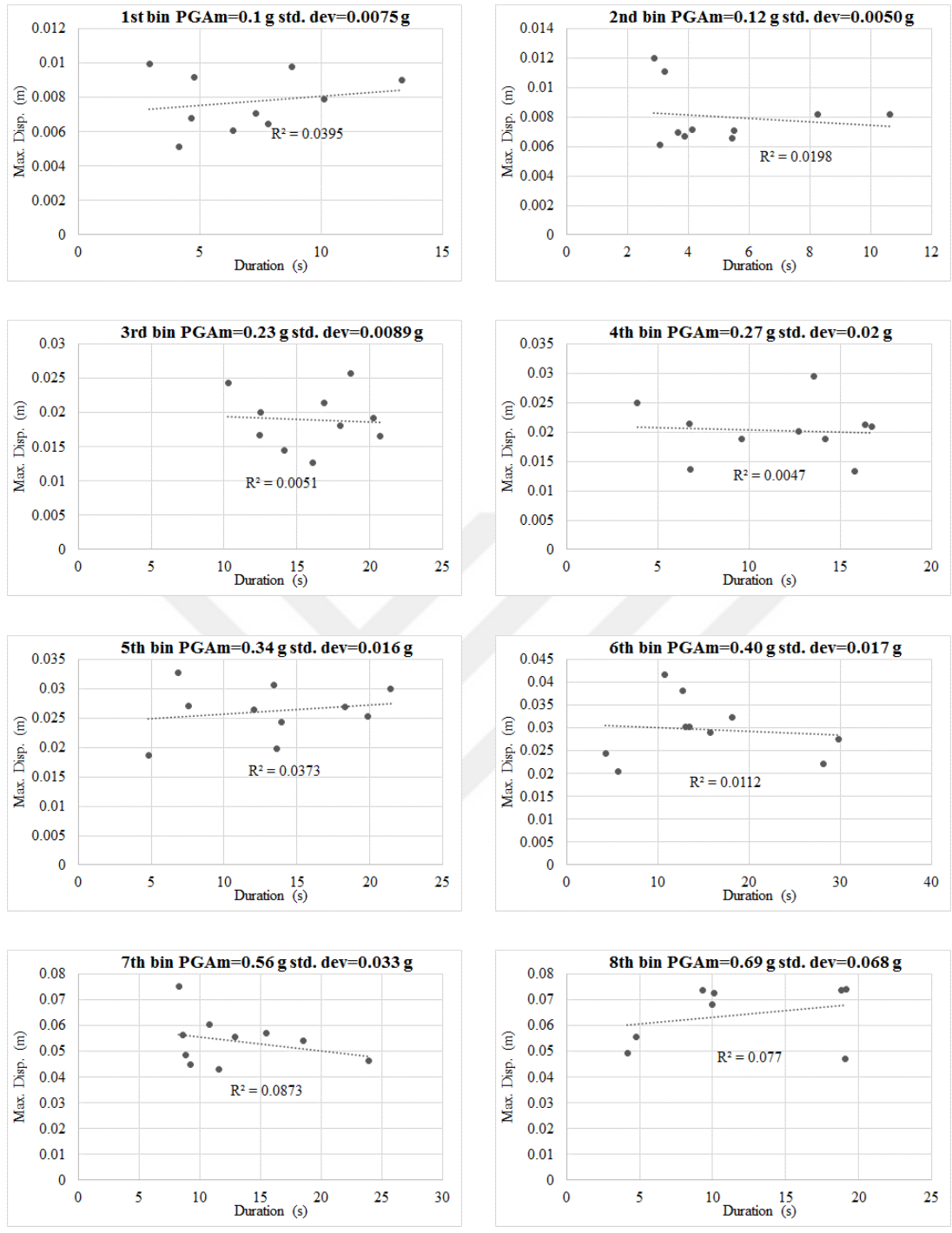


Figure C.13. Maximum displacement demand versus effective duration scatters for eight PGA bins regarding Site 2 without near-field forward directivity pulse and RF1A

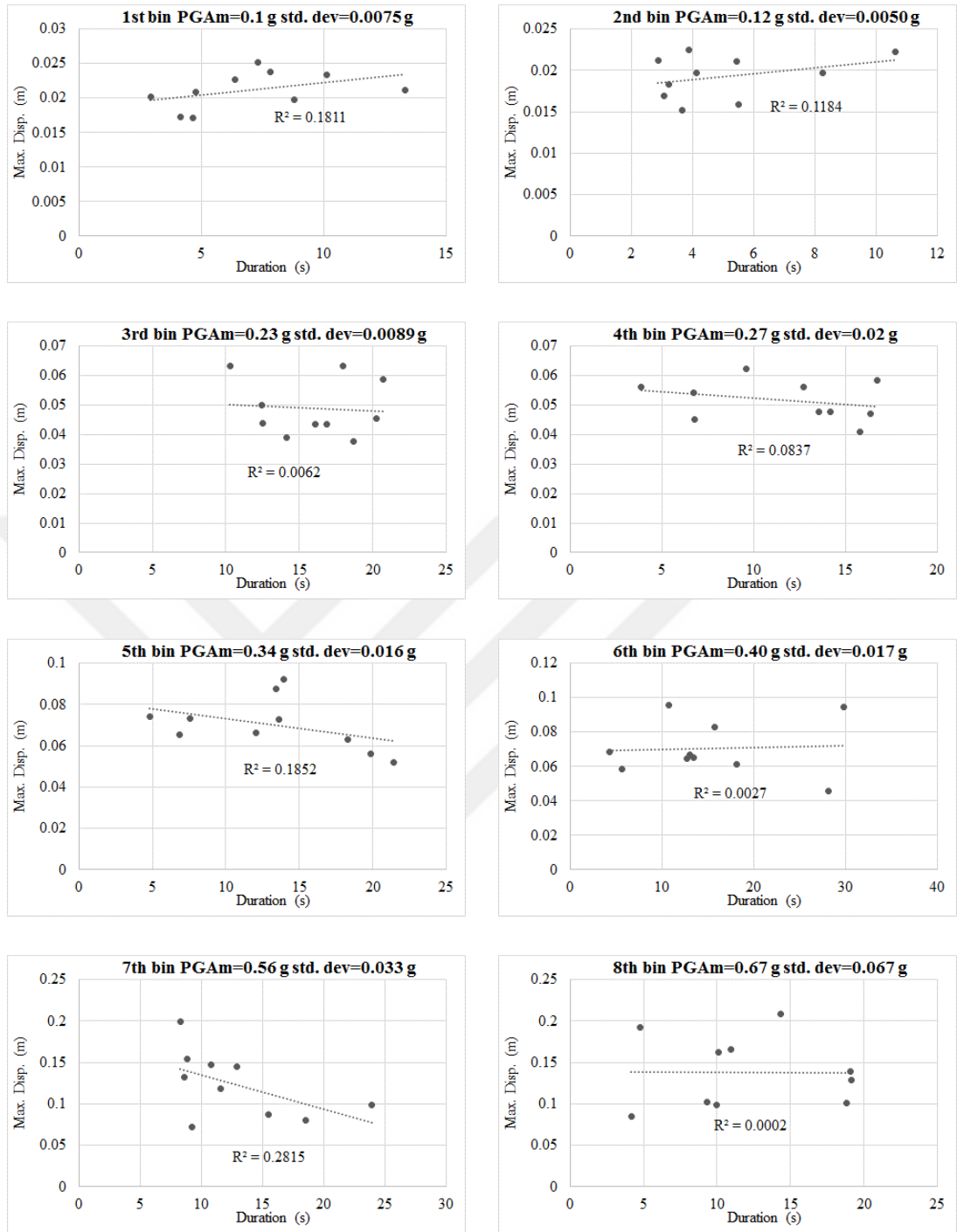


Figure C.14. Maximum displacement demand versus effective duration scatters for eight PGA bins regarding Site 2 without near-field forward directivity pulse and RF2B

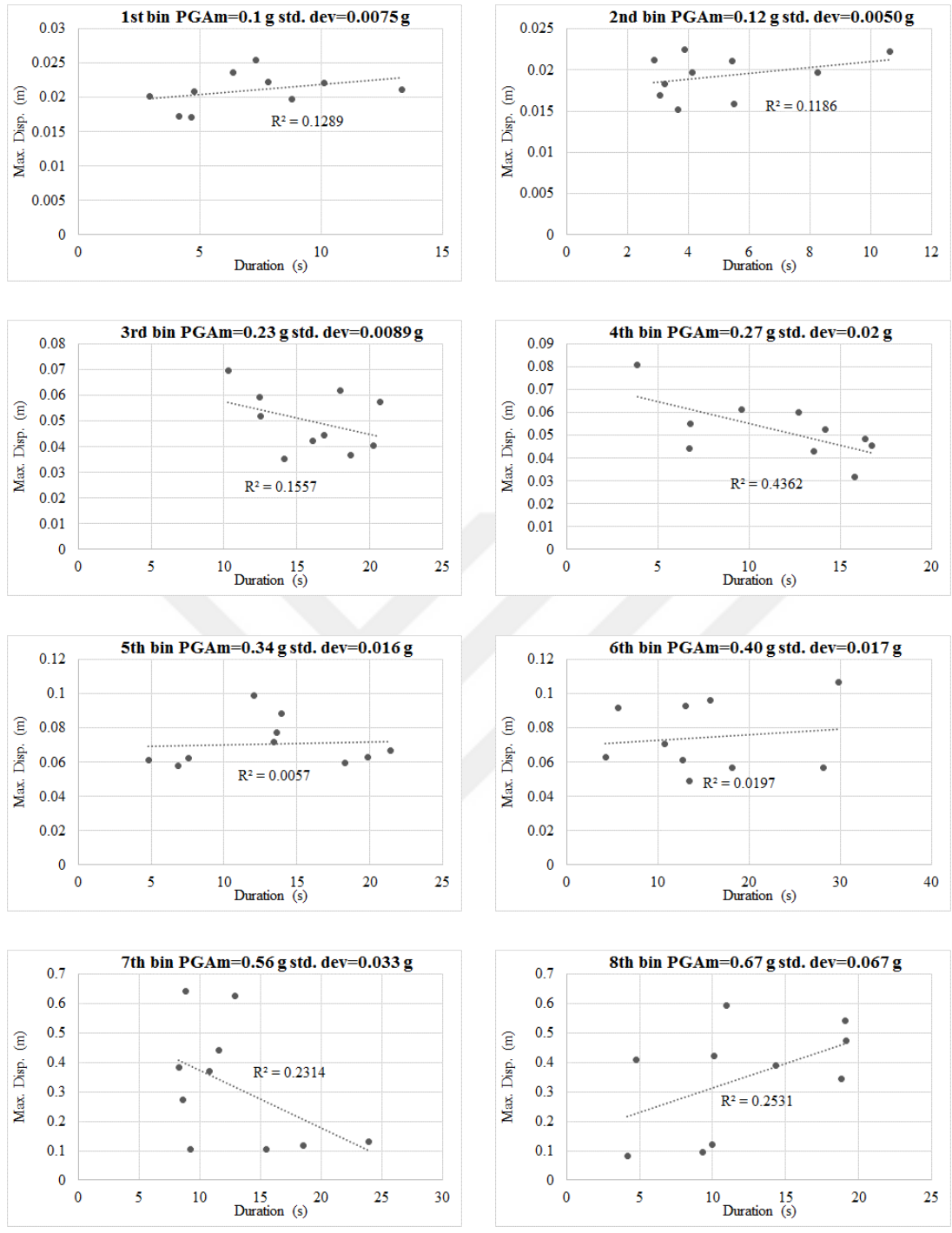


Figure C.15. Maximum displacement demand versus effective duration scatters for eight PGA bins regarding Site 2 without near-field forward directivity pulse and RF2C

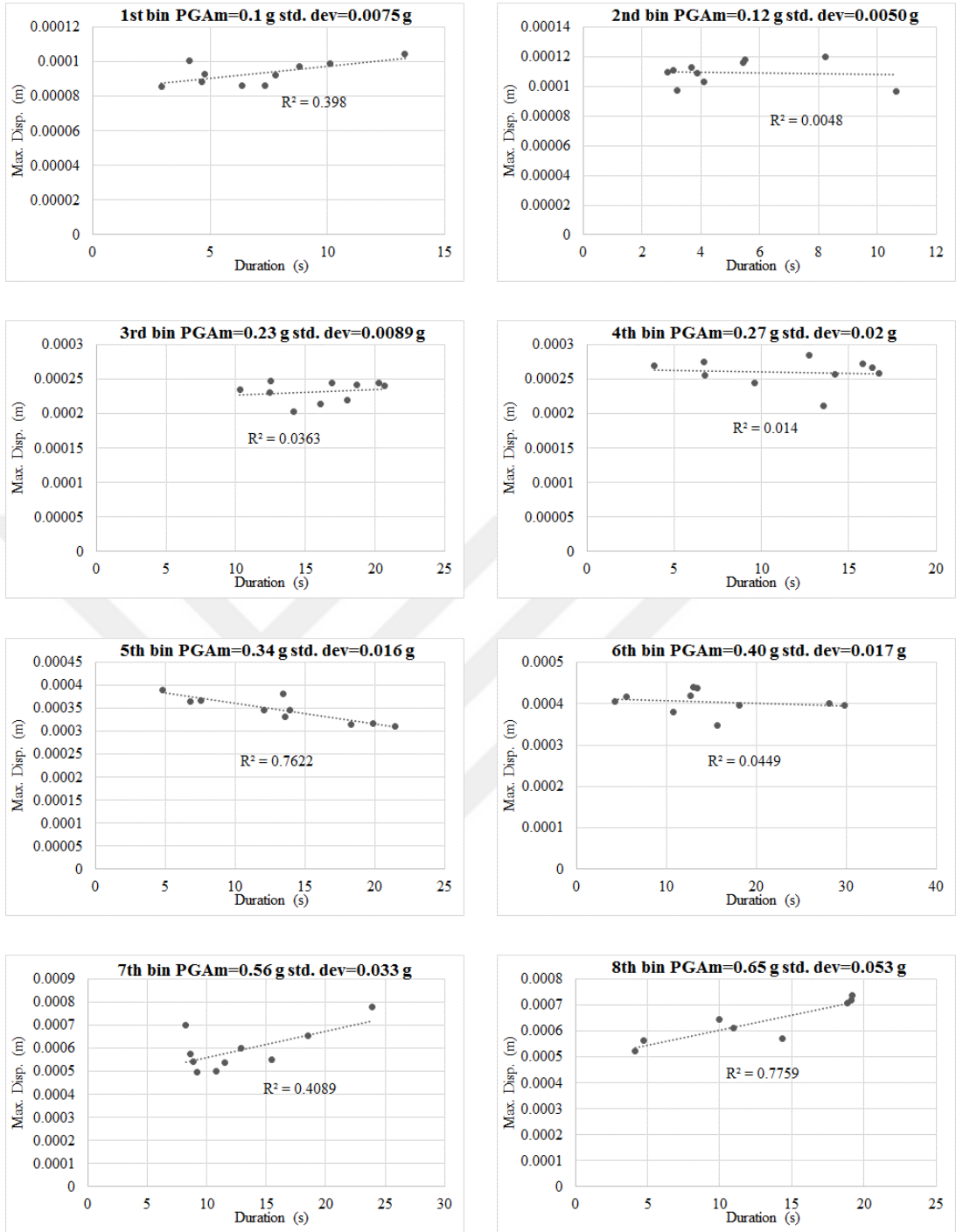


Figure C.16. Maximum displacement demand versus effective duration scatters for eight PGA bins regarding Site 2 without near-field forward directivity pulse and MU1A

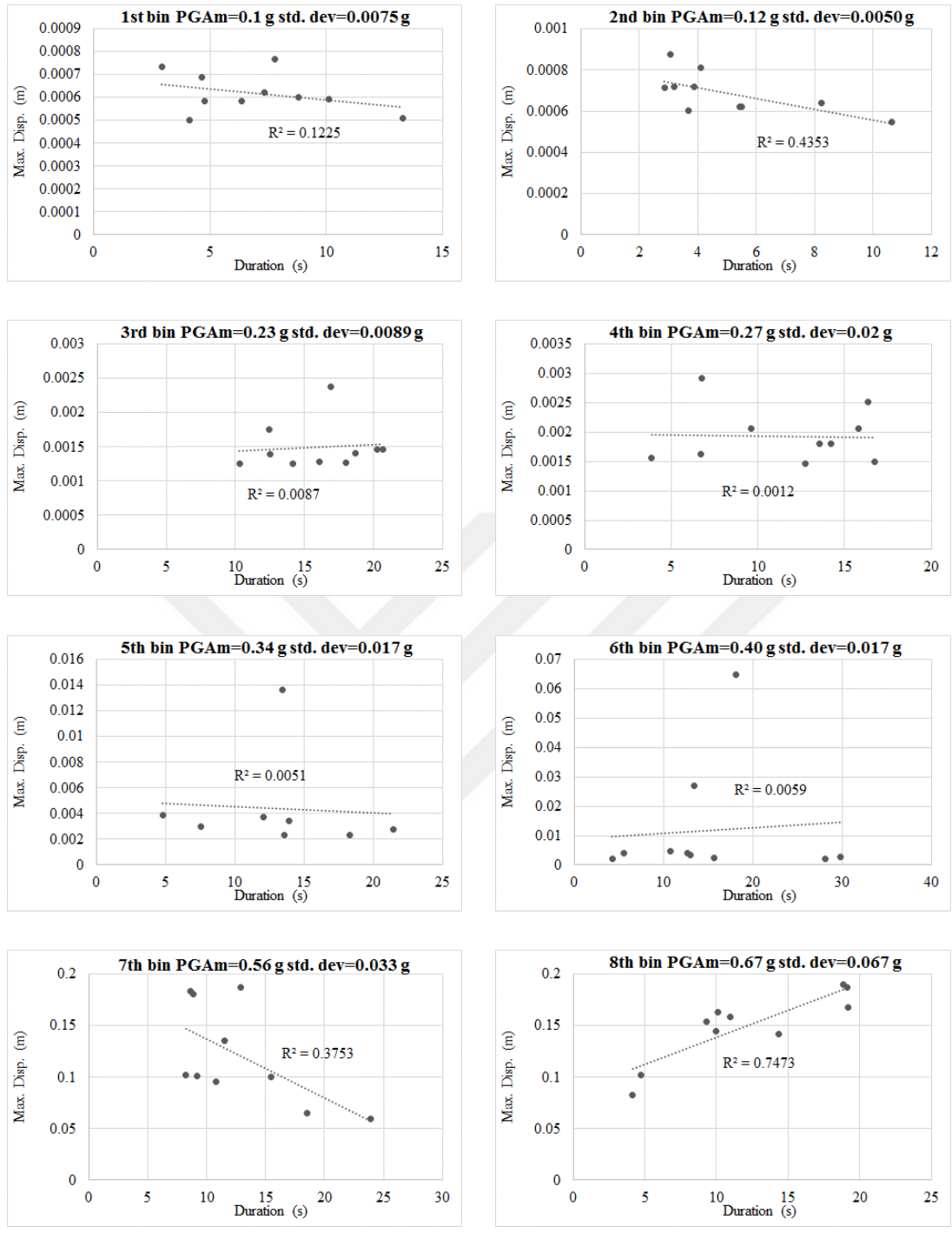


Figure C.17. Maximum displacement demand versus effective duration scatters for eight PGA bins regarding Site 2 without near-field forward directivity pulse and MU2B

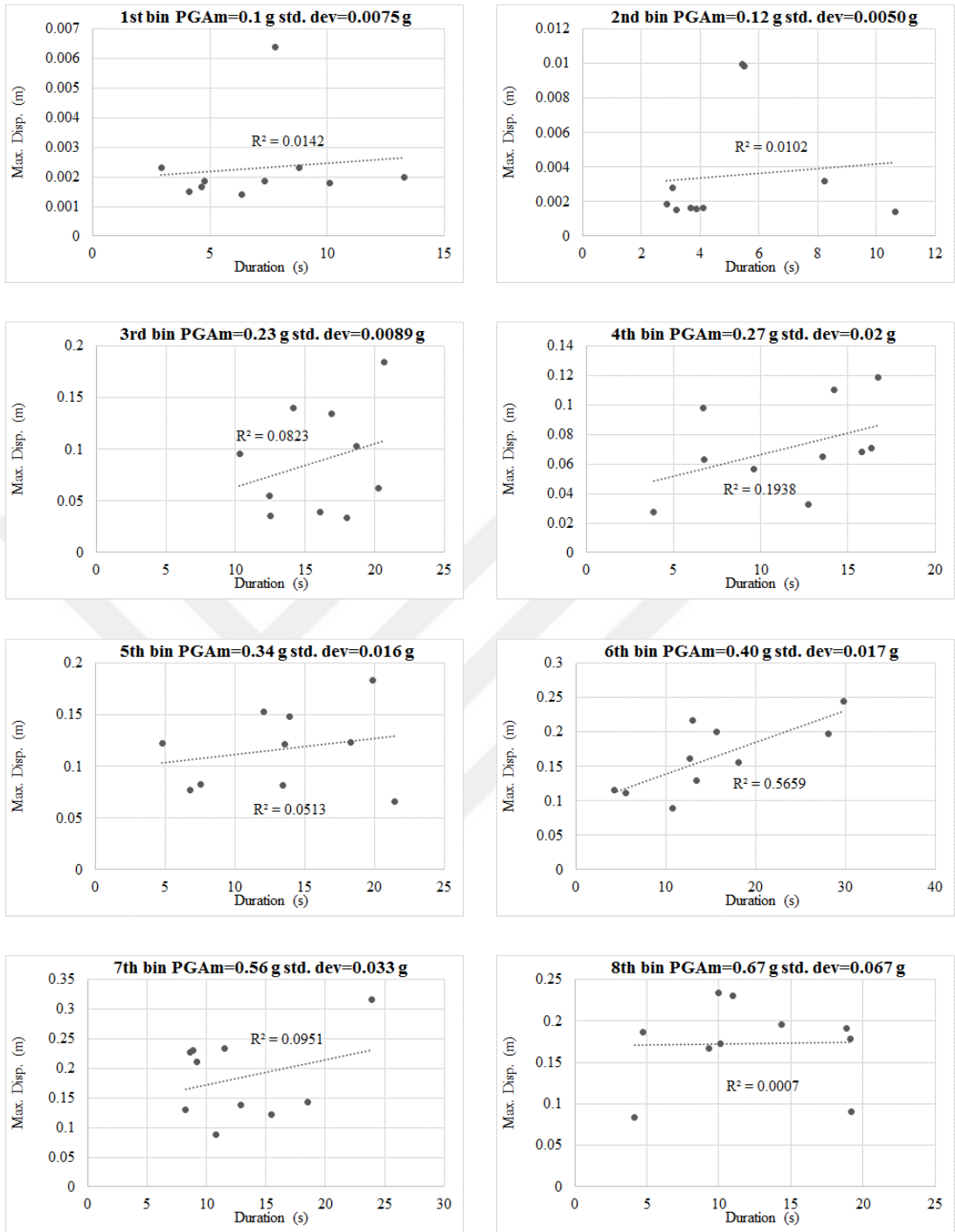


Figure C.18. Maximum displacement demand versus effective duration scatters for eight PGA bins regarding Site 2 without near-field forward directivity pulse and MU3C

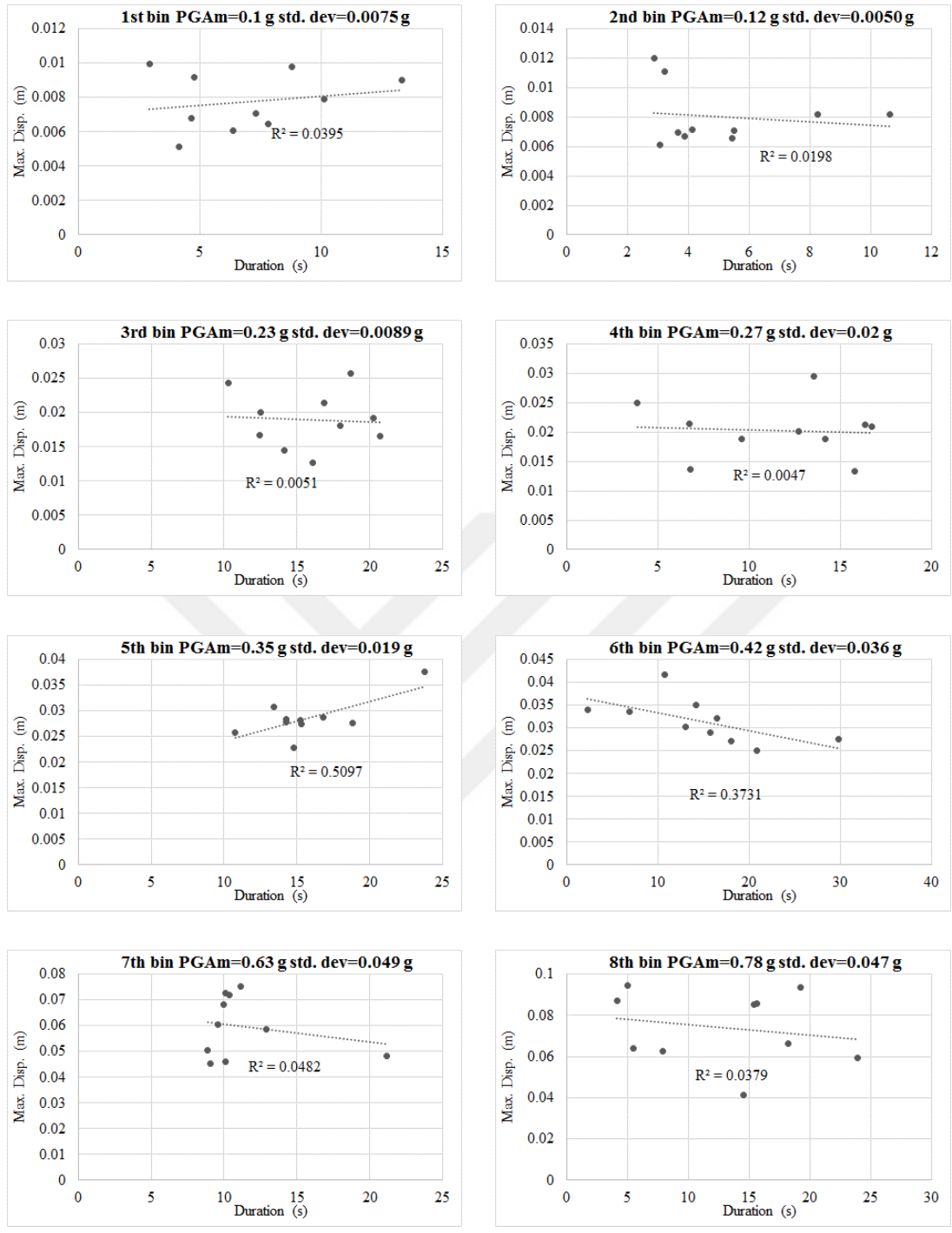


Figure C.19. Maximum displacement demand versus effective duration scatters for eight PGA bins regarding Site 2 with near-field forward directivity pulse and RF1A

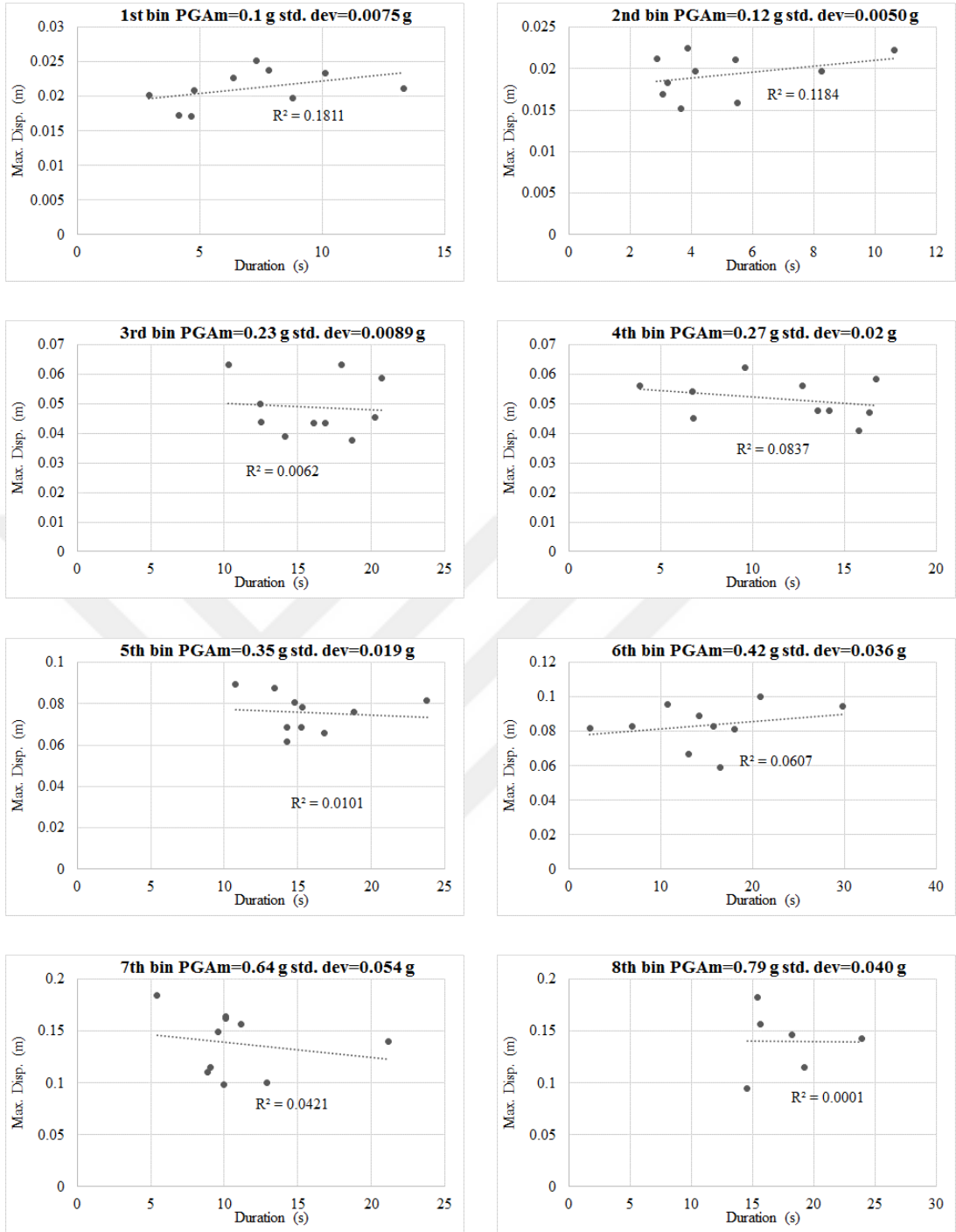


Figure C.20. Maximum displacement demand versus effective duration scatters for eight PGA bins regarding Site 2 with near-field forward directivity pulse and RF2B

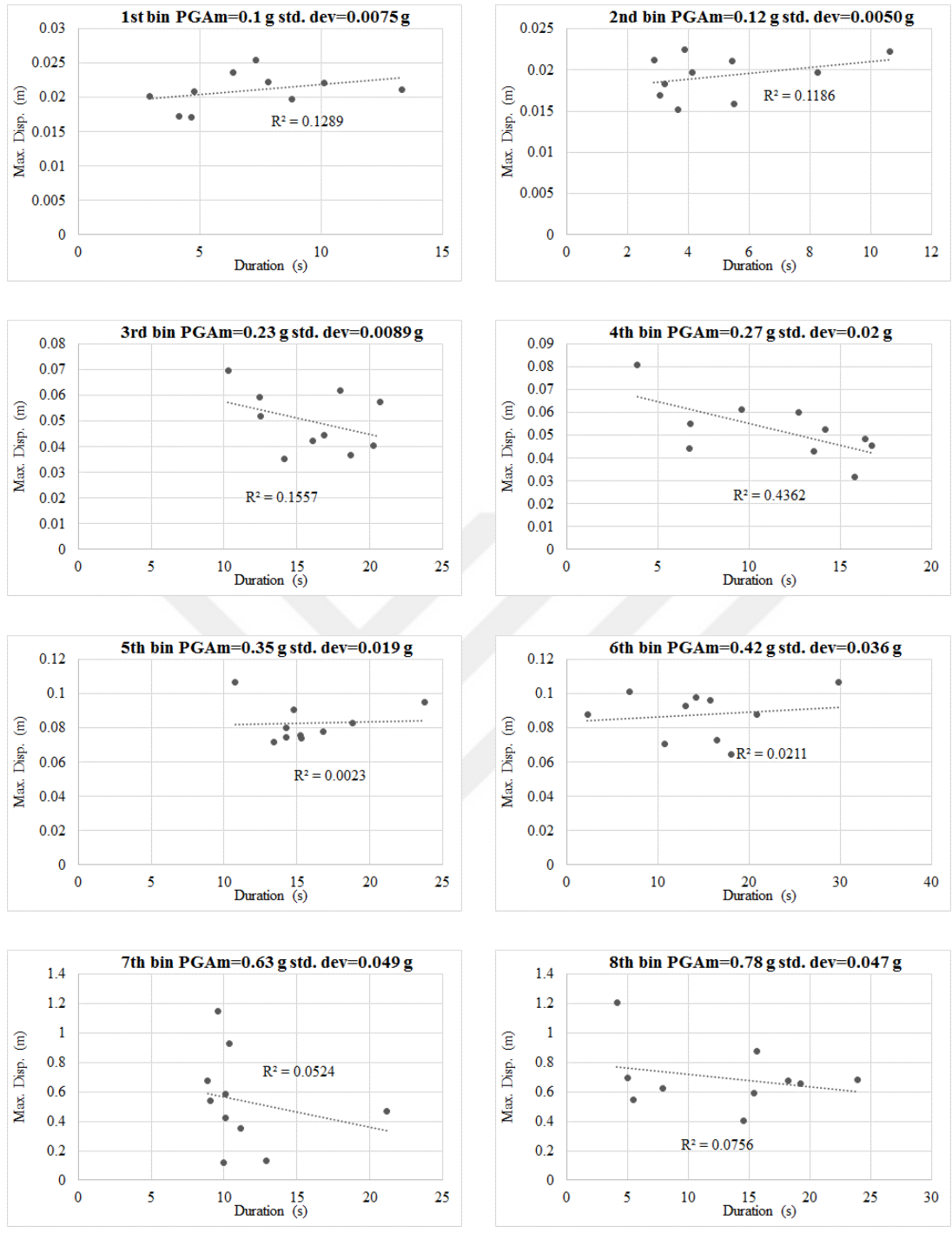


Figure C.21. Maximum displacement demand versus effective duration scatters for eight PGA bins regarding Site 2 with near-field forward directivity pulse and RF2C

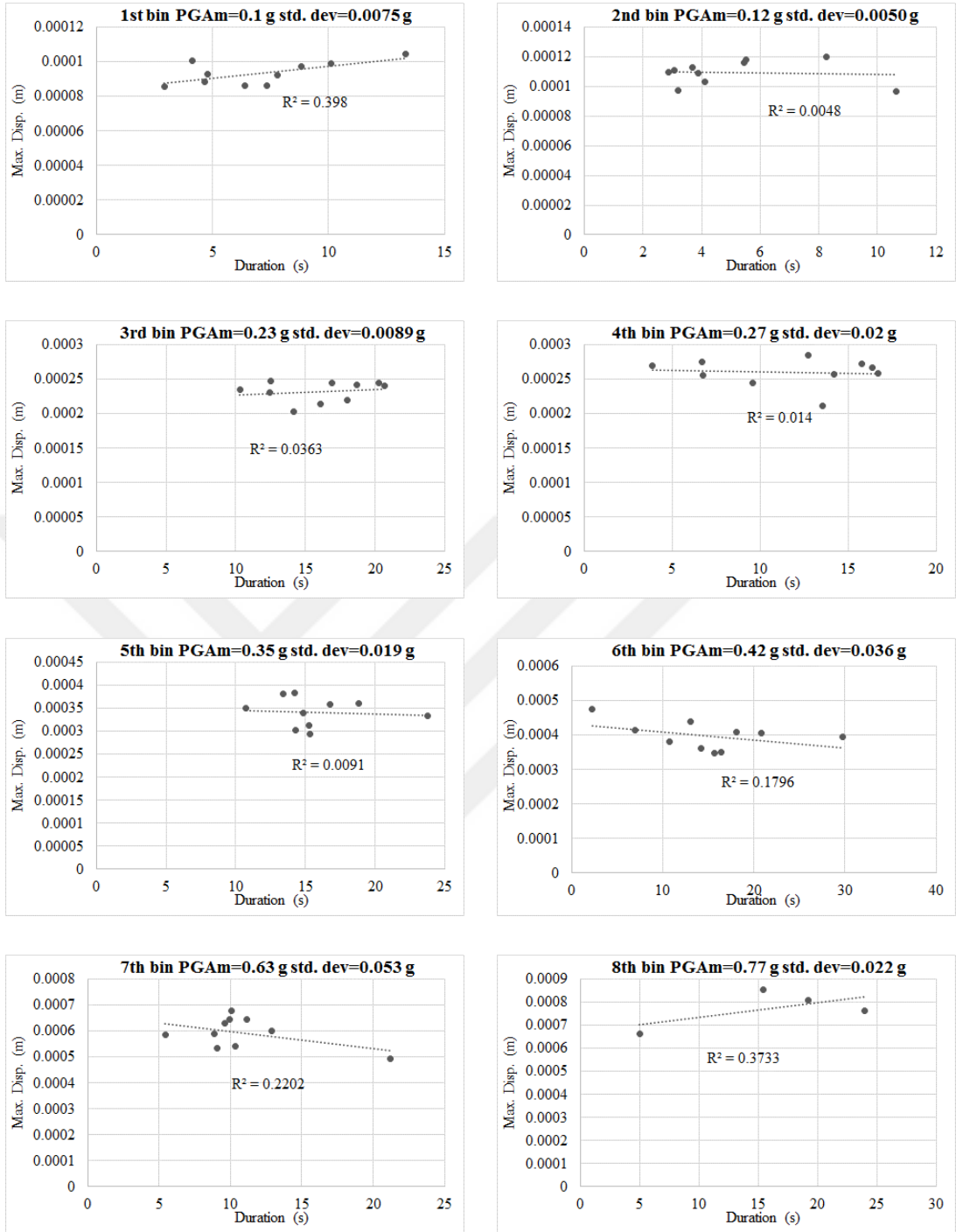


Figure C.22. Maximum displacement demand versus effective duration scatters for eight PGA bins regarding Site 2 with near-field forward directivity pulse and MU1A

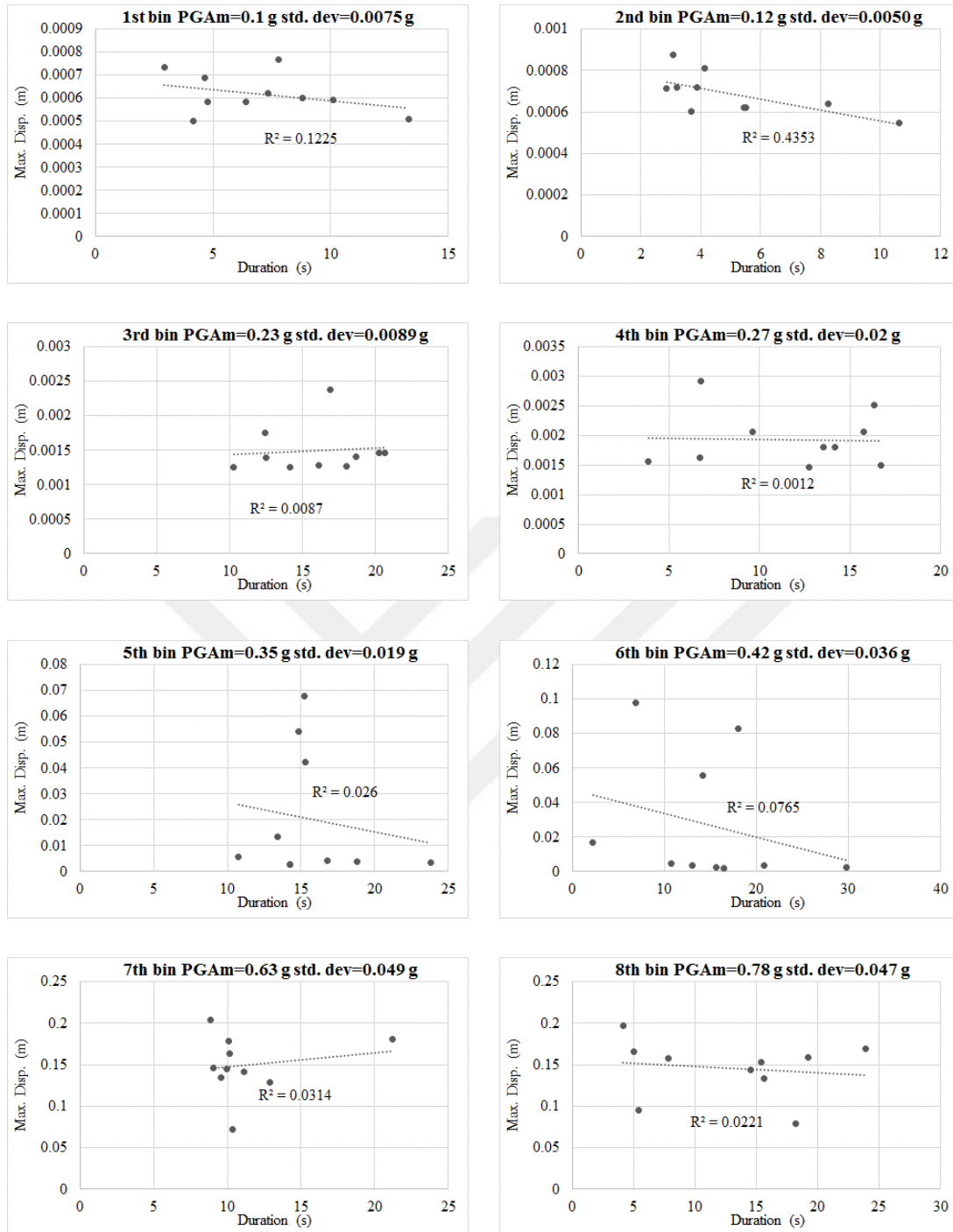


Figure C.23. Maximum displacement demand versus effective duration scatters for eight PGA bins regarding Site 2 with near-field forward directivity pulse and MU2B

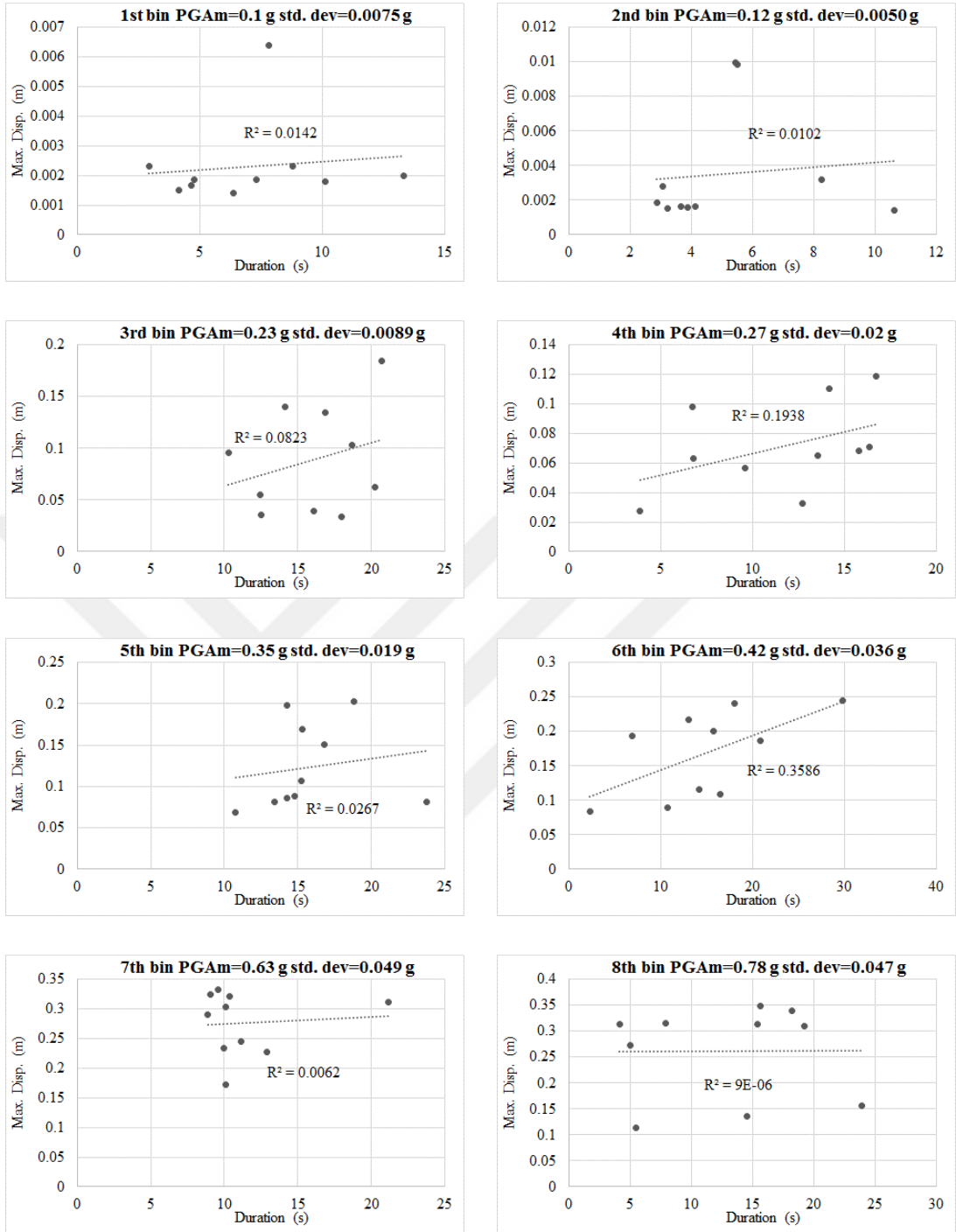


Figure C.24. Maximum displacement demand versus effective duration scatters for eight PGA bins regarding Site 2 with near-field forward directivity pulse and MU3C

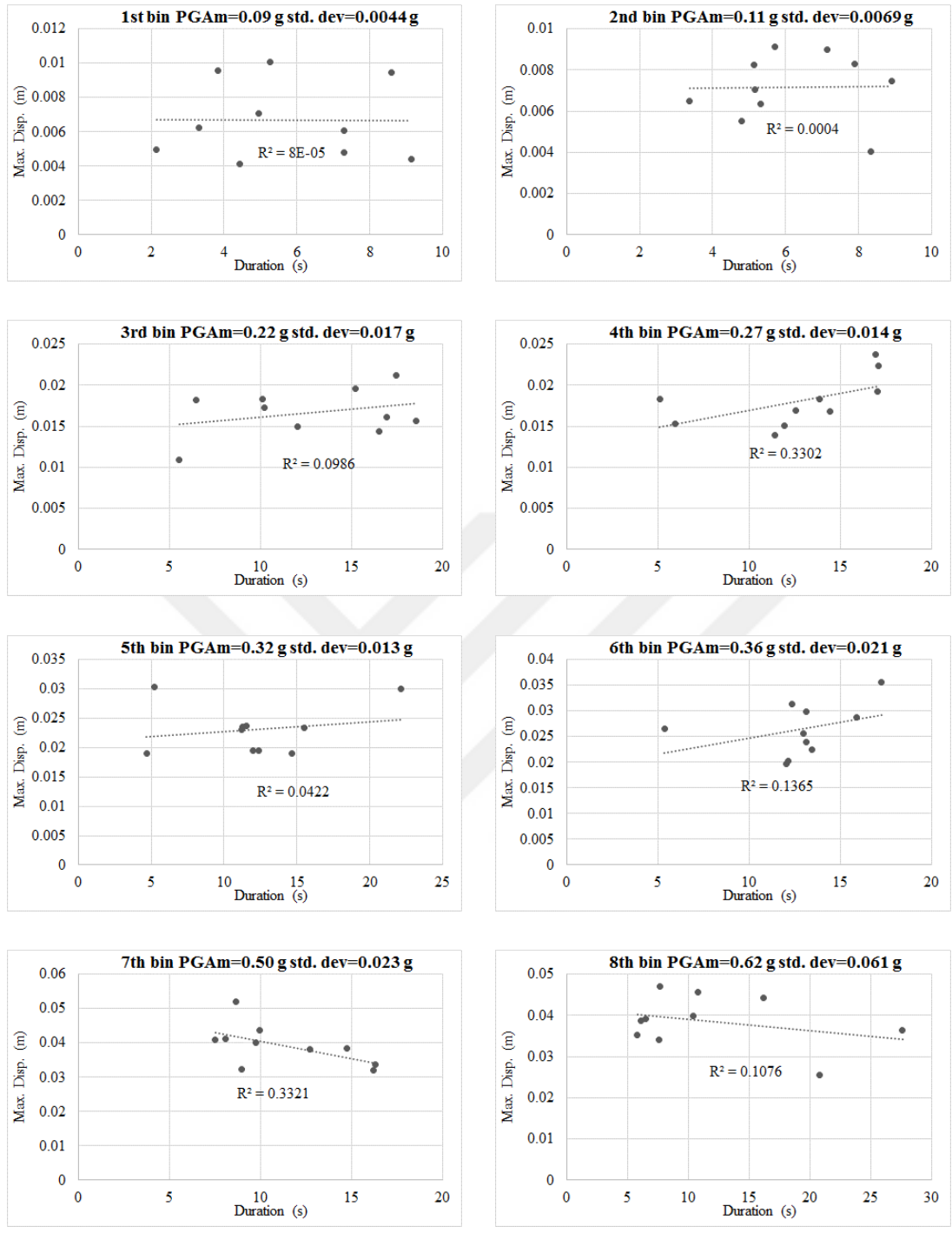


Figure C.25. Maximum displacement demand versus effective duration scatters for eight PGA bins regarding Site 3 using generic site amplification and RF1A

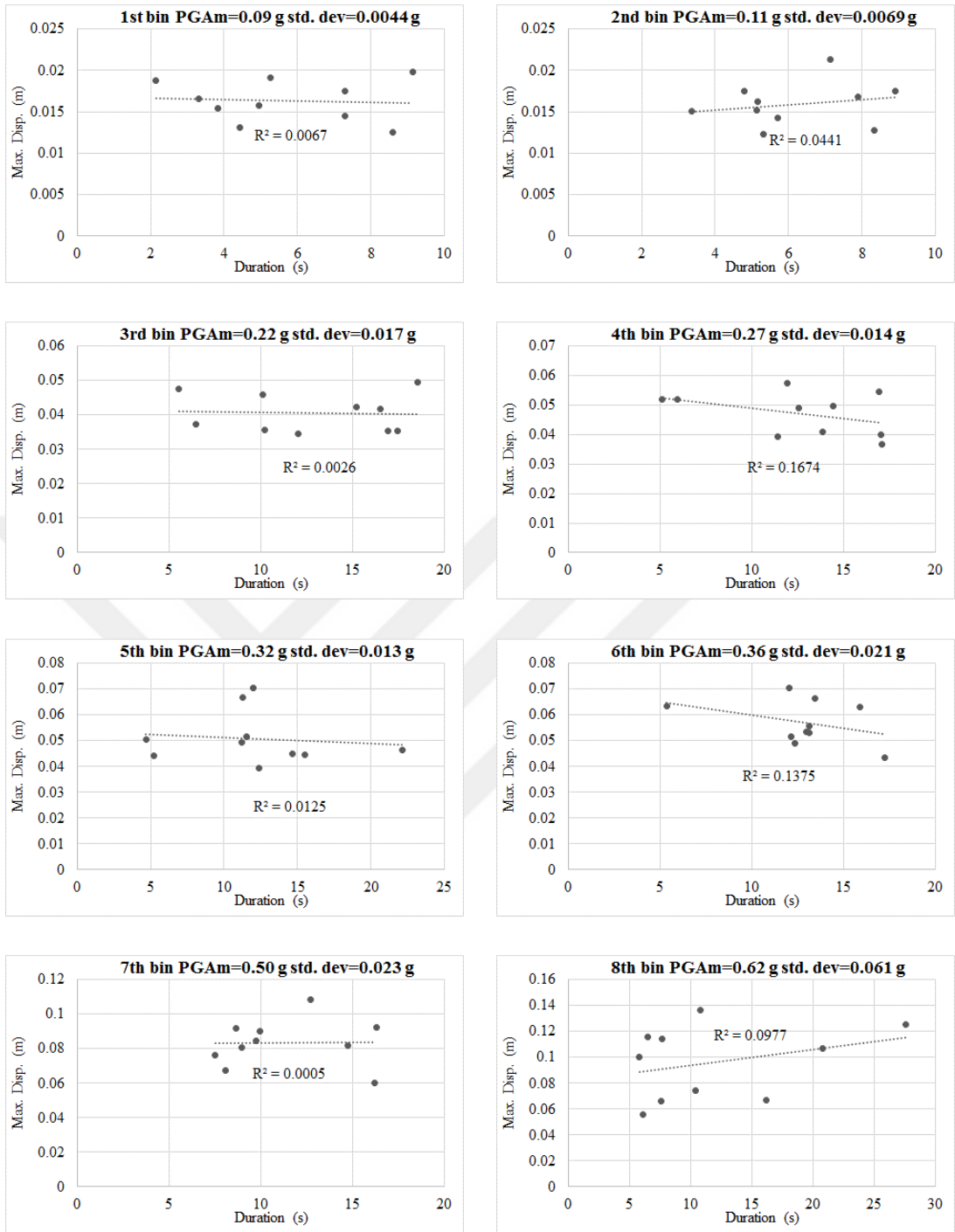


Figure C.26. Maximum displacement demand versus effective duration scatters for eight PGA bins regarding Site 3 using generic site amplification and RF2B

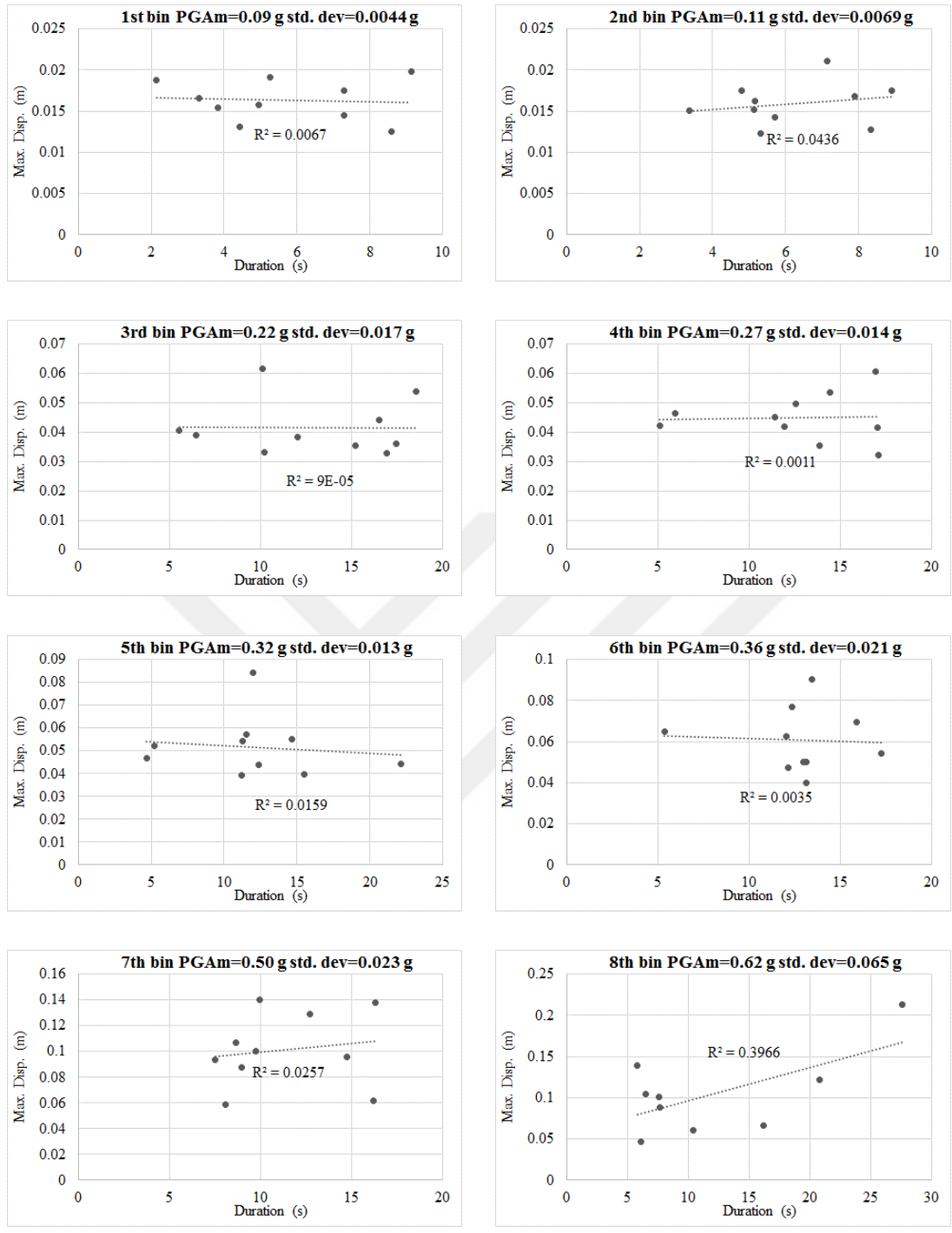


Figure C.27. Maximum displacement demand versus effective duration scatters for eight PGA bins regarding Site 3 using generic site amplification and RF2C

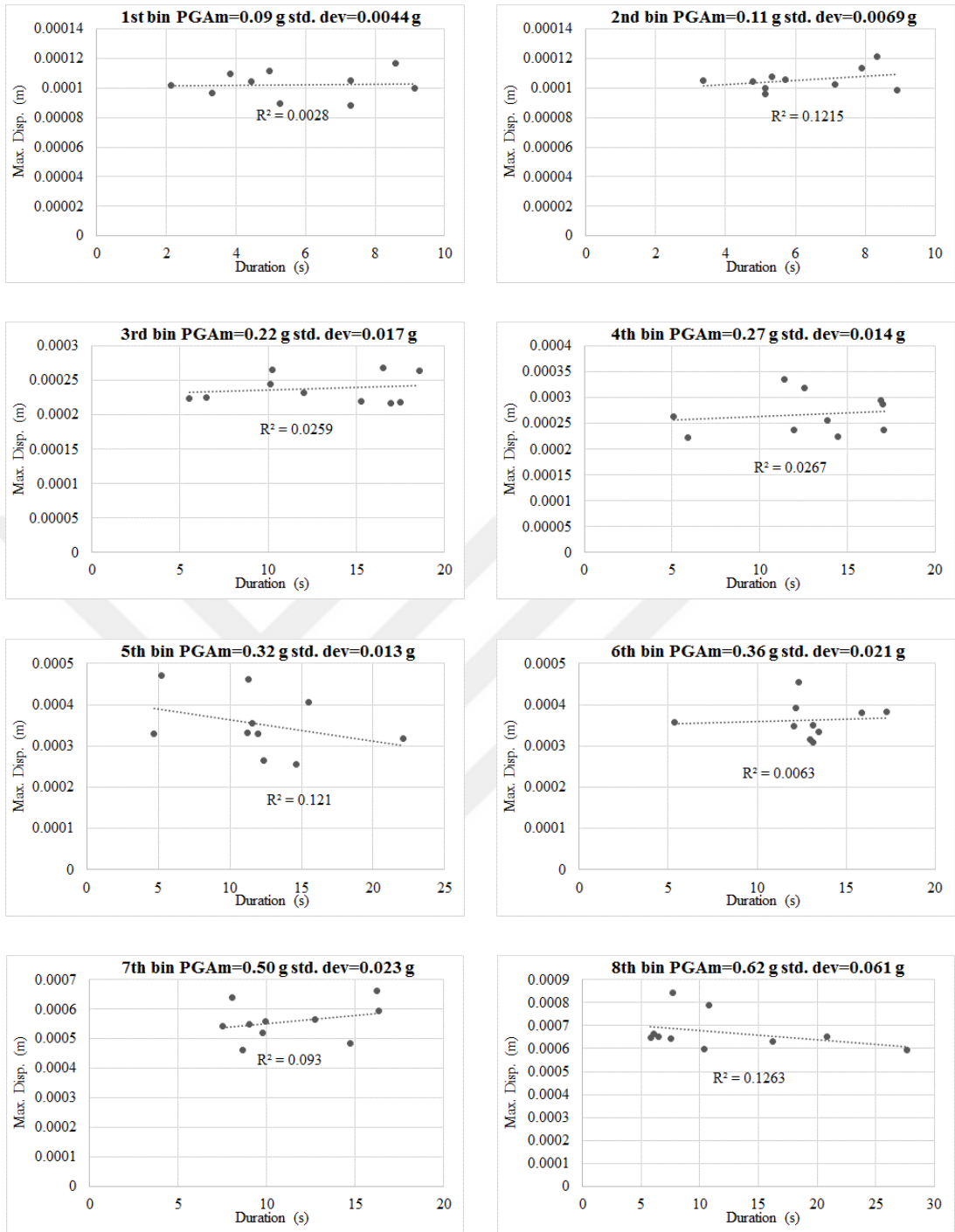


Figure C.28. Maximum displacement demand versus effective duration scatters for eight PGA bins regarding Site 3 using generic site amplification and MU1A

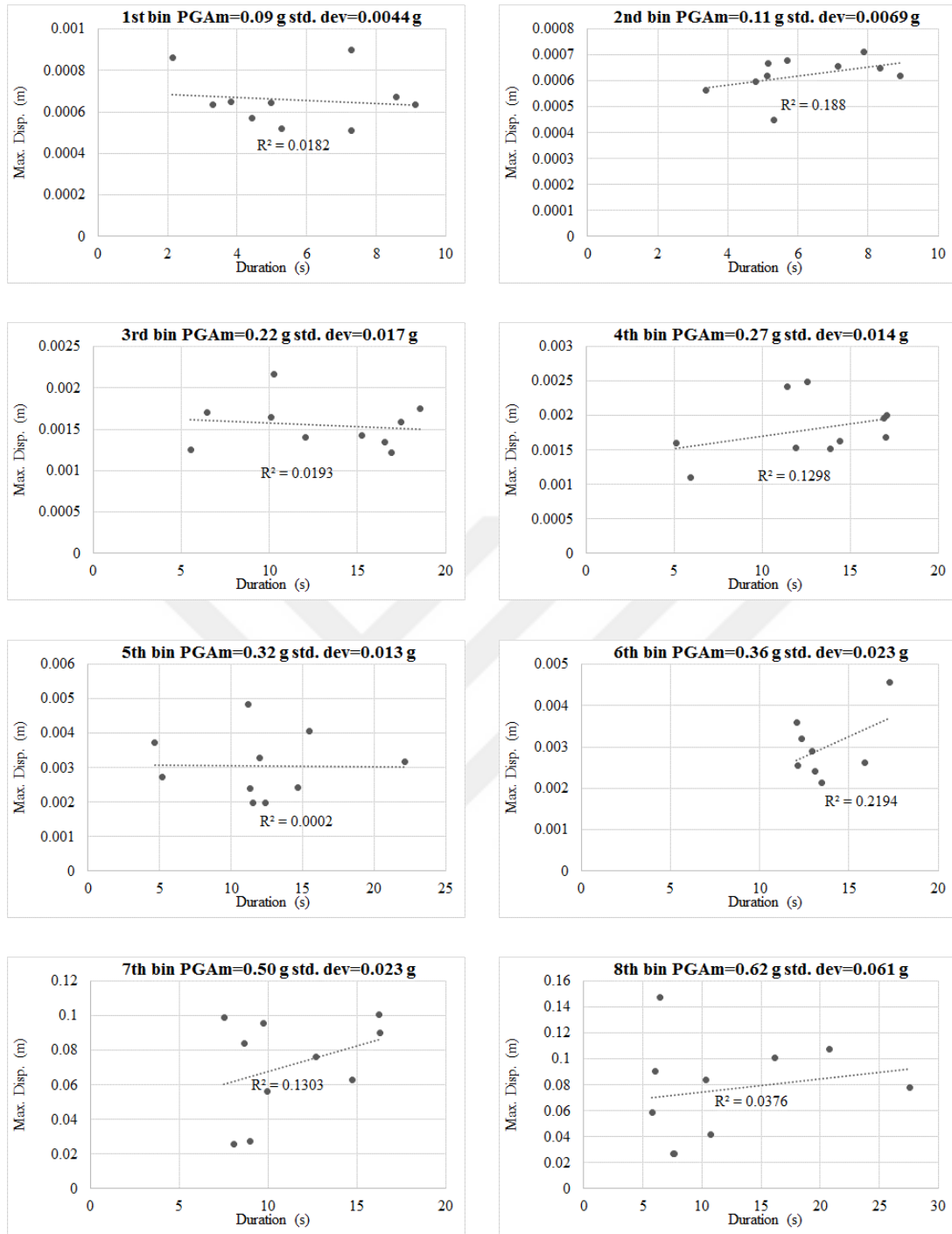


Figure C.29. Maximum displacement demand versus effective duration scatters for eight PGA bins regarding Site 3 using generic site amplification and MU2B

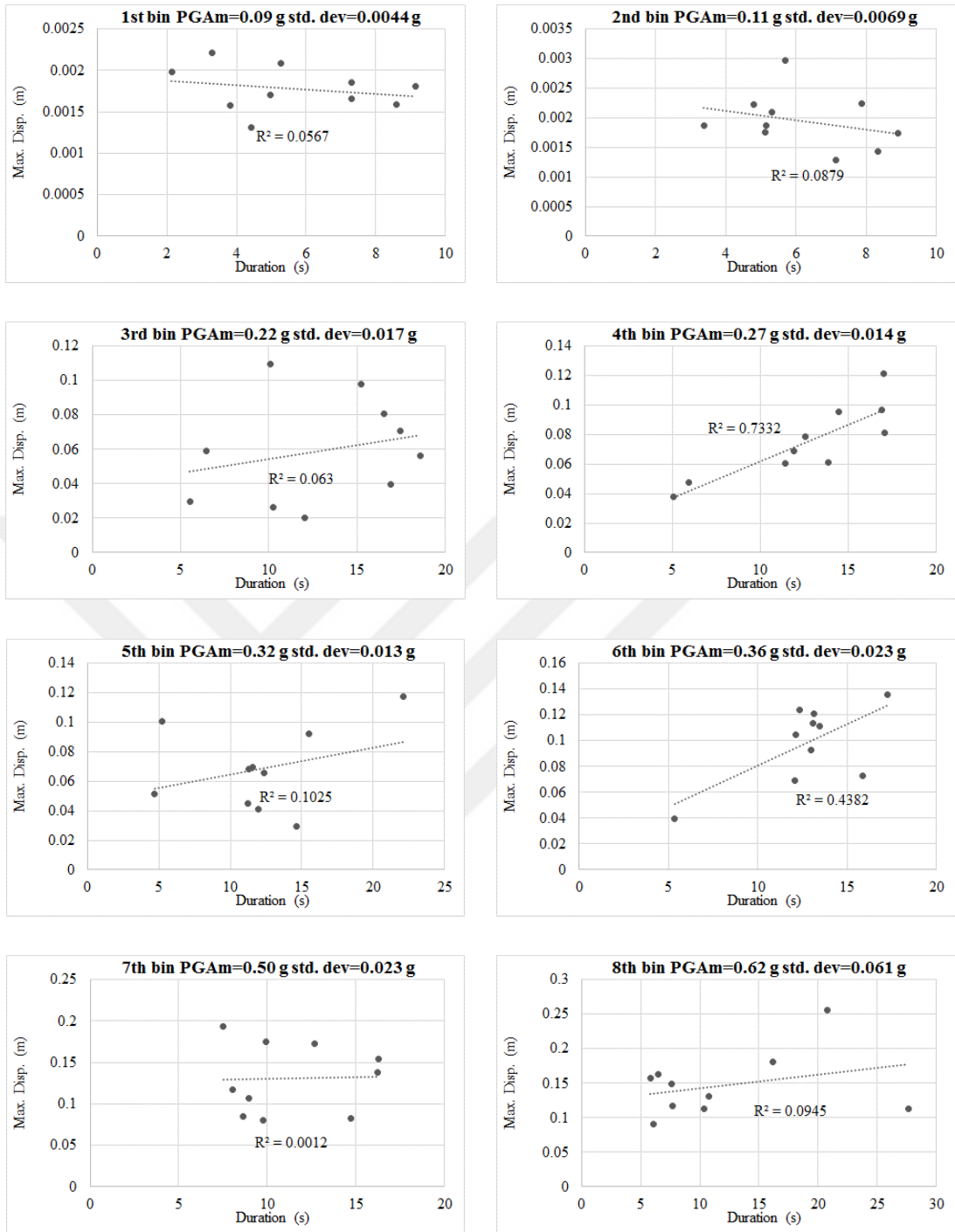


Figure C.30. Maximum displacement demand versus effective duration scatters for eight PGA bins regarding Site 3 using generic site amplification and MU3C

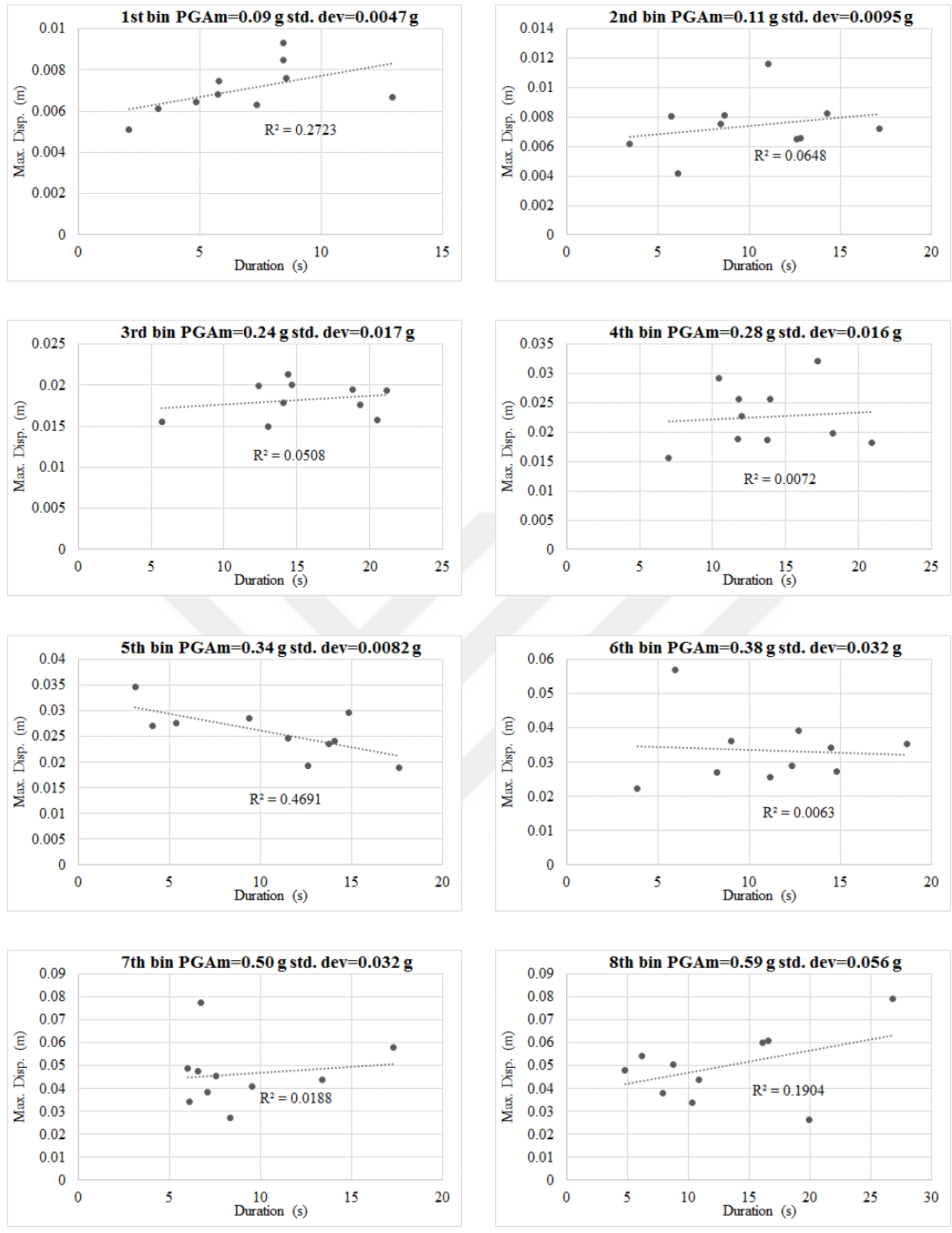


Figure C.31. Maximum displacement demand versus effective duration scatters for eight PGA bins regarding Site 3 using theoretical site amplification and RF1A

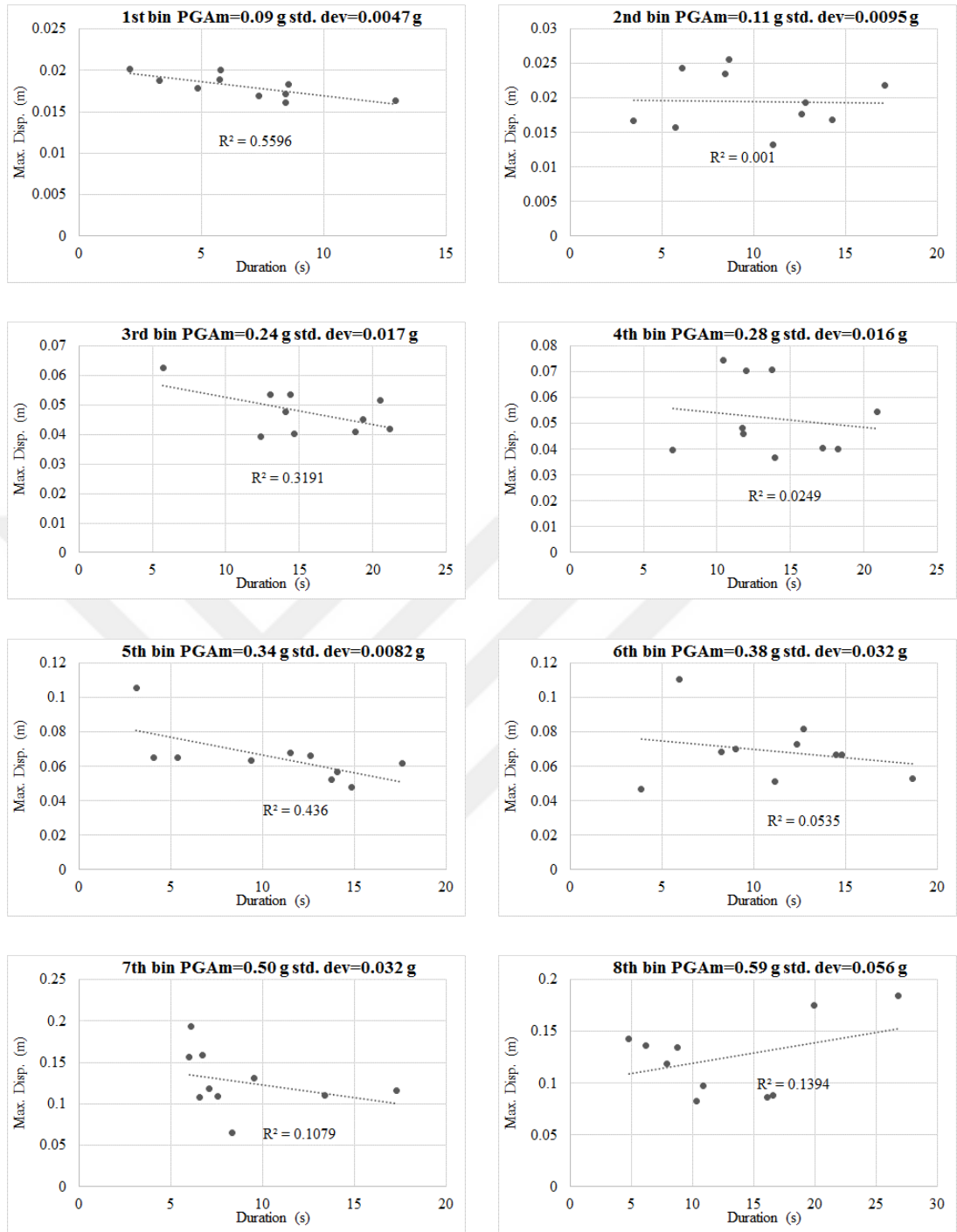


Figure C.32. Maximum displacement demand versus effective duration scatters for eight PGA bins regarding Site 3 using theoretical site amplification and RF2B

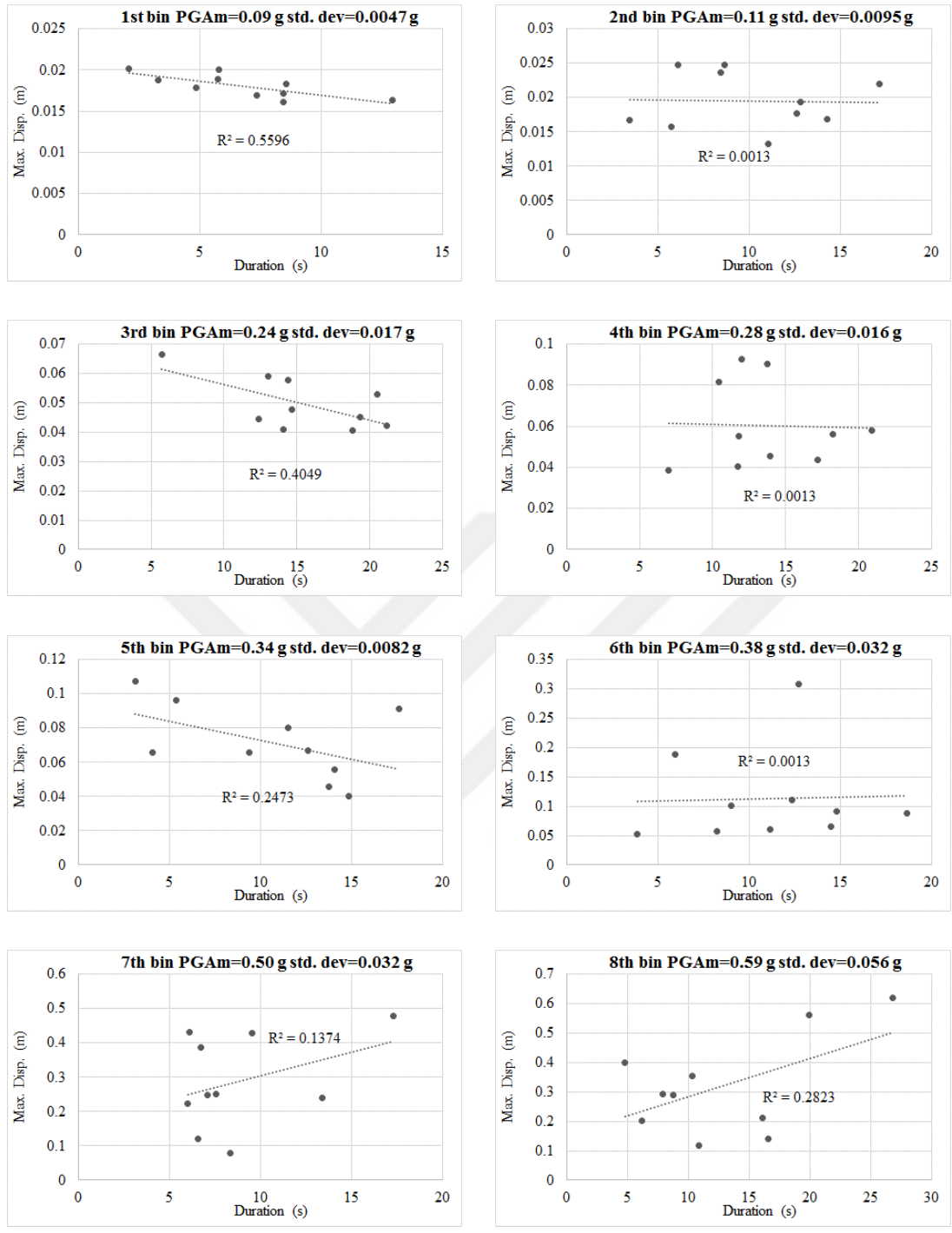


Figure C.33. Maximum displacement demand versus effective duration scatters for eight PGA bins regarding Site 3 using theoretical site amplification and RF2C

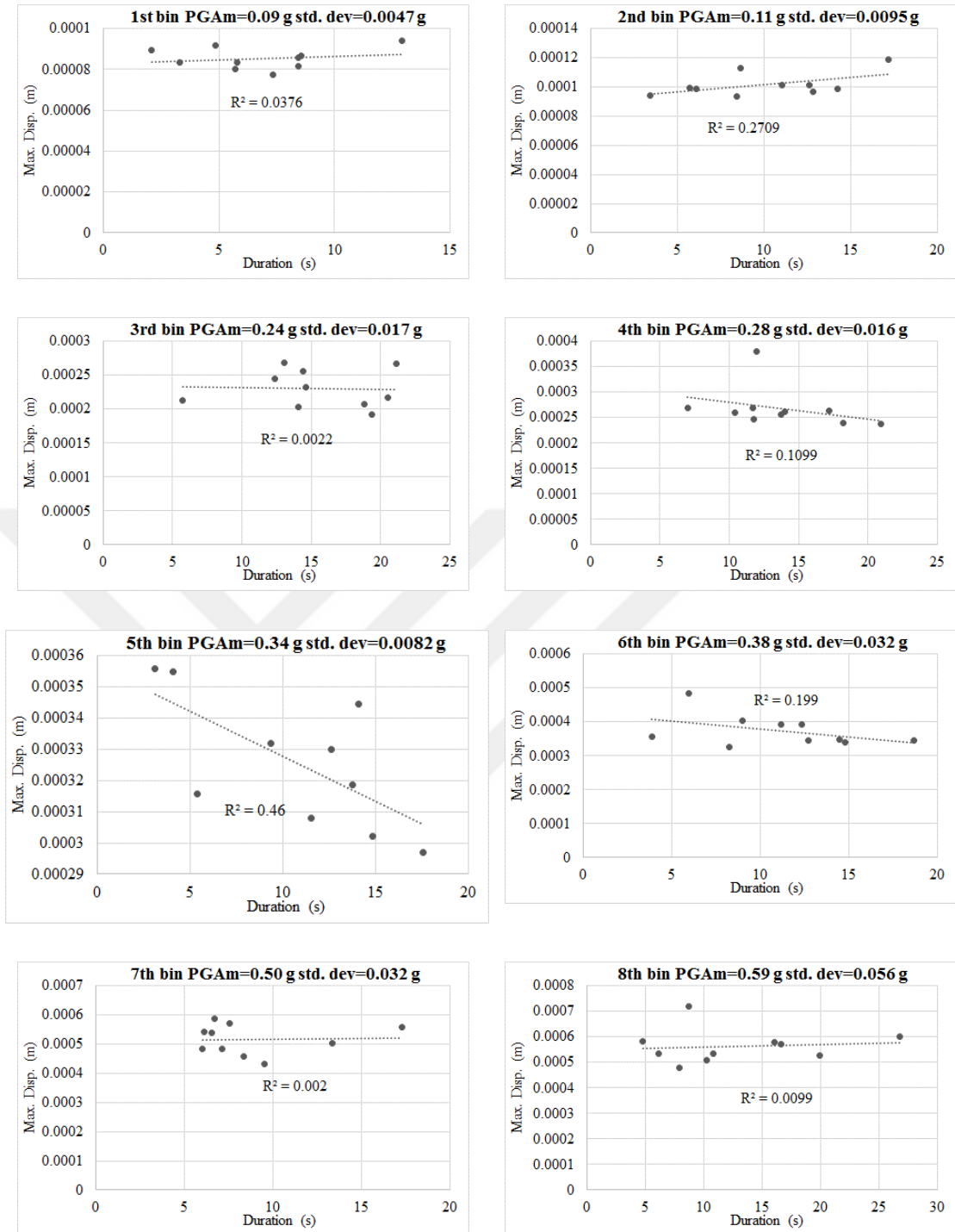


Figure C.34. Maximum displacement demand versus effective duration scatters for eight PGA bins regarding Site 3 using theoretical site amplification and MU1A

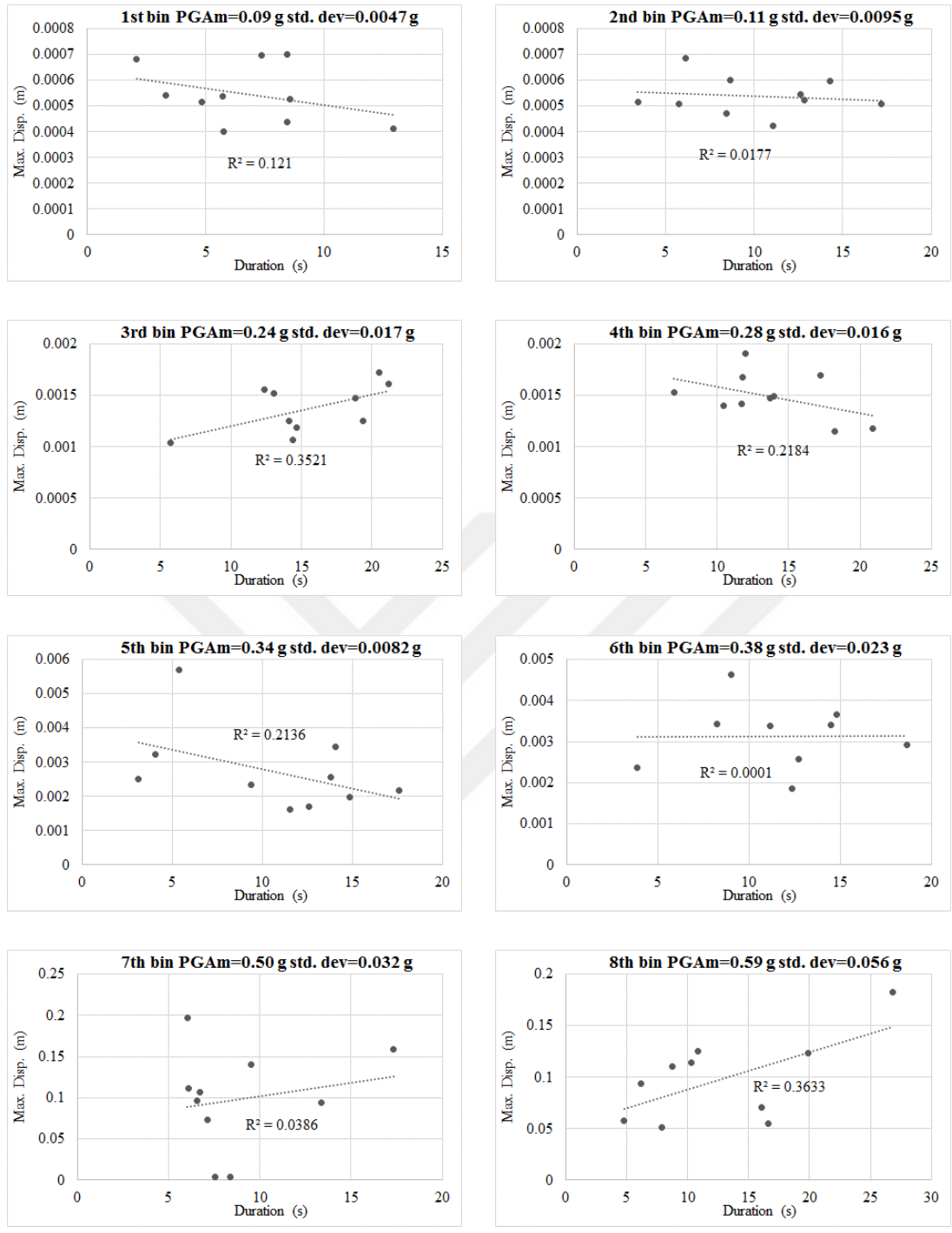


Figure C.35. Maximum displacement demand versus effective duration scatters for eight PGA bins regarding Site 3 using theoretical site amplification and MU2B

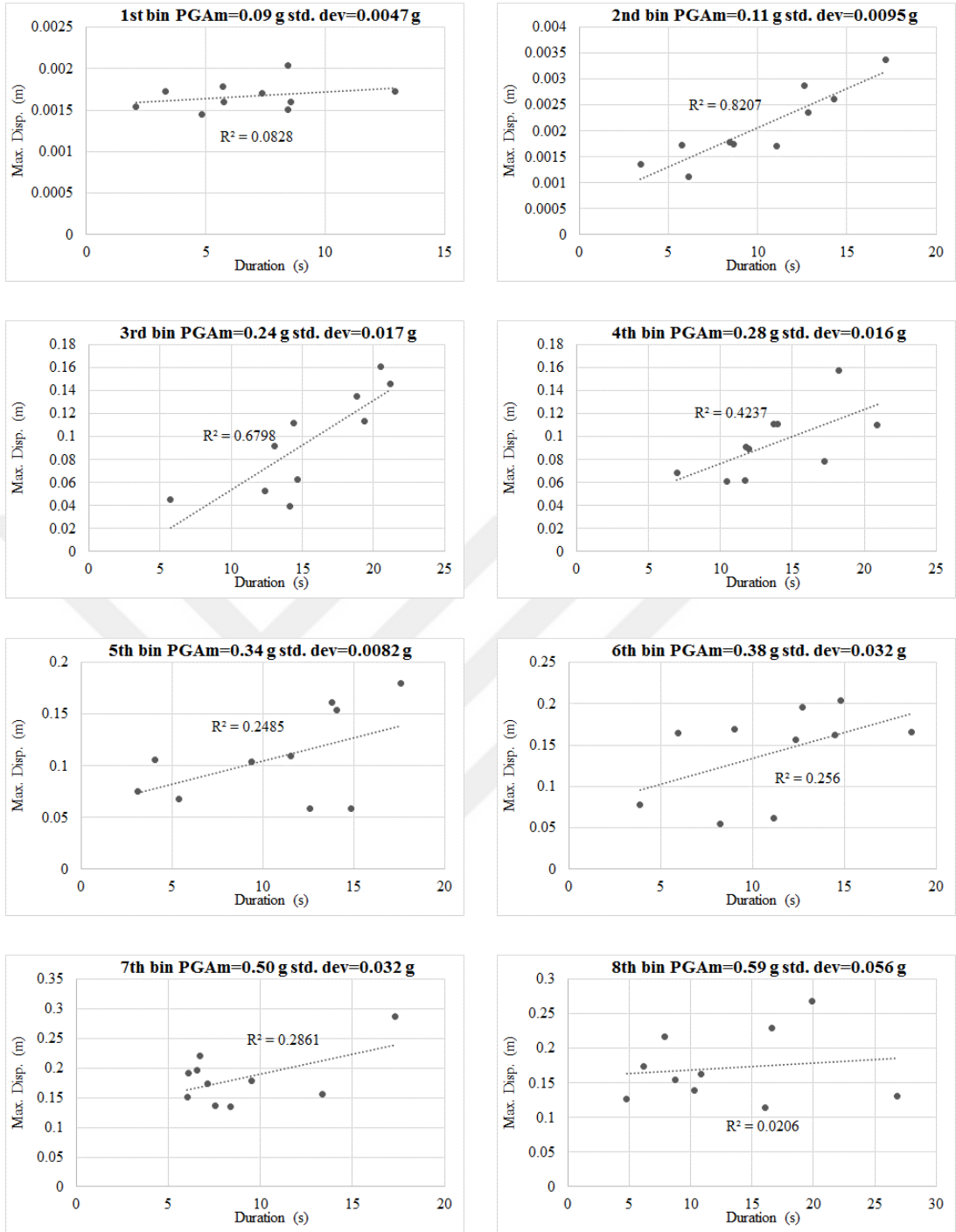


Figure C.36. Maximum displacement demand versus effective duration scatters for eight PGA bins regarding Site 3 using theoretical site amplification and MU3C



CURRICULUM VITAE

PERSONAL INFORMATION



- First Name: Aida
 - Surname: Azari Sisi
 - Place & Date of Birth: Tehran, Iran. 1985
- Nationality: Iranian

e_mail: aida.azarisisi@gmail.com

EDUCATION

2011 -2016 PhD in Earthquake Engineering, Department of Civil Engineering, [Middle East Technical University](#), Ankara, Turkey. GPA: 3.86/4

- **PhD Thesis Title:** "Derivation of Site-Specific UHS Based on Simulated Ground Motions and its Parametric Effects on Building Fragility"

Advisor: [Assoc. Prof. Dr. A. Askan Gündoğan](#)

Co-Advisor: [Assoc. Prof. Dr. M.A. Erberik](#)

2007 - 2010 M.Sc in Structural Engineering, Department of Civil Engineering, [Sahand University of Technology](#), Tabriz, Iran, GPA: 16.98/20

- **MS Thesis Title:** "Exact Dynamic Analysis of Asymmetric Thin-Walled Beam-Columns under Axial Load" Grade: 18.75/20

Advisor: [Assoc. Prof. Dr. B. Rafezy](#)

2003 – 2007 B.Sc in Civil Engineering, Department of Civil Engineering, [Tabriz University](#), Tabriz, Iran. GPA: 16.42/20

1999 – 2003 Mathematics and Physics Diploma, Bagherololum High School, Tabriz, Iran.

CURRENT RESEARCHES

- Strong ground motion data processing
- Strong ground motion database compilation
- Seismic damage assessment of structures
- Strong ground motion simulation
- Stochastic simulation of earthquake catalog
- Probabilistic seismic hazard analysis (PSHA)

RESEARCH INTERESTS

- Strong ground motion data collecting and processing
- Probability based seismic vulnerability assessment
- Performance-based earthquake engineering
- Synthetic strong ground motion
- Stochastic earthquake catalog generation
- Dynamic analysis of thin-walled beams
- Coupled vibration of wall-core structures

LANGUAGE PROFICIENCY

- Azerbaijani (Mother Tongue), Persian (Mother Tongue), English (Advanced), Turkish (Fluent), German (Intermediate)

COMPUTER SKILLS

Computer Programming Language: MATLAB, FORTRAN90

Engineering Software: SAP 2000, ETABS, AutoCAD, SAFE, OPENSEES, SeismoStruct, ANSYS

Seismological Software: SeismoSignal, EZFRISK, Utility Software for Data Processing (USDP)

General Software: Microsoft Office (Word, Excel, Power Point) & ...

WORK EXPERIENCE

- Project Engineer (2009-2010), Misho Construction Company, Tabriz, Iran.

AWARDS AND HONORS

- 2215- Graduate Scholarship Program for International Students (2012-2015), Scientific and Technological Research Council of Turkey (TUBITAK), Ankara, Turkey.
- Summer School on “Wave and Rupture Propagation with Realistic Velocity Structures” (2014), Southern California Earthquake Center (SCEC) and Earthquake Research Institute of the University of Tokyo, Los Angeles, USA.

JOURNAL ARTICLES

- D. M. Boore, **A. Azari Sisi** and S. Akkar, 2012. "Using Pad-Stripped Acausally Filtered Strong-Motion Data", Bulletin of the Seismological Society of America. Vol. 102, No. 2.
- S. Akkar, M.A. Sandıkkaya, M. Senyurt, **A. Azari Sisi**, B.O. Ay, P. Traversa, J. Douglas, F. Cotton, L. Luzi, B. Hernandez and S. Godey, 2014. "Reference Database for Seismic Ground-Motion in Europe (RESORCE) ", Bulletin of Earthquake

Engineering. Vol.12, Issue.3.

- **A. Azari Sisi**, A. Askan and M.A. Erberik, 2015. "Site-Specific Uniform Hazard Spectrum in Eastern Turkey Based on Simulated Ground Motions Including Near-field Directivity and Detailed Site Effects", Journal of Earthquake Engineering (Under review).

CONFERENCE PAPERS AND PRESENTATIONS

- **A. Azari Sisi** and B. Rafezy, 2010. "Exact Dynamic Analysis of Thin-Walled Beams under Distributed Axial Load", 5th National Congress on Civil Engineering, Mashhad, Iran.
- **A. Azari Sisi**, B. Rafezy and W.P. Howson, 2012. "Exact Stiffness and Frequency Relationships for a Doubly Asymmetric Bending-Torsion Thin-Walled Beam", 15th World Conference on Earthquake Engineering, Lisbon, Portugal.
- S.Akkar and **A. Azari Sisi**, 2013. "A Probabilistic Model for Strength Reduction Factor for Damage Assessment", 2nd Turkish Conference on Earthquake Engineering and Seismology (TDMSK), Hatay, Turkey.
- **A. Azari Sisi**, A.Askan and M. A. Erberik, 2014. "Site-specific Uniform Hazard Spectrum Based on Simulated Ground Motions", Second European Conference on Earthquake Engineering and Seismology (2ECEES), Istanbul, Turkey.
- **A. Azari Sisi**, A.Askan and M. A. Erberik, 2014. "A Parametric Study on Synthetic Uniform Hazard Spectrum of Erzincan, Turkey", Poster presentation, SCEC 2014 Summer School, Los Angeles, USA.
- **A. Azari Sisi**, A.Askan and M. A. Erberik, 2015. "Ground Motion Selection Based on a Synthetic Uniform Hazard Spectrum", 26th General Assembly of the International Union of Geodesy and Geophysics, Prague, Czech Republic.

- **A. Azari Sisi**, A.Askan and M. A. Erberik, 2016. "Simulation of 13 March 1992 Erzincan (Turkey) Earthquake Including a Near-field Forward Directivity Pulse Model: Implications for Earthquake Engineering", Oral presentation, Seismological Society of America, Reno, USA.
- **A. Azari Sisi**, A.Askan and M. A. Erberik, 2016. "Simulation of 13 March 1992 Erzincan (Turkey) Earthquake Including a Near-field Forward Directivity Pulse Model: Implications for Earthquake Engineering", Seismological Research Letters, SSA 2016 Annual Meeting Announcement. Vol.87, No.2B.

ACADEMIC ACTIVITIES AND TECHNICAL REPORTS

- "Seismic Ground Motion Assessment (SIGMA)", funded by French Electricity Company (EDF), Research Assistant, 2012-2013.
- "Research Infrastructures for Earthquake Hazard (NERA)", funded by the European Community FP7, Research Assistant, 2012.
- "Utility Software for Data Processing (USDP Version2)", Earthquake Engineering Research Centre, METU, Ankara, Turkey, Research Assistant, 2011-2013.
- "23 Ekim 2011 M_w 7.2 Van Depremi Sismik ve Yapısal Hasara İlişkin Saha Gözlemleri" , Report No: METU/EERC 2011-04, Earthquake Engineering Research Centre, METU, Ankara, Turkey, November 2011. (<http://eerc.metu.edu.tr/>)
- "A Report on the 19 May 2011 Kutahya-Simav Earthquake (Preliminary Report) ", Report No: METU/EERC 2011-02, in collaboration with Earthquake Engineering Research Centre, METU, and Disaster Management and Emergency Presidency (AFAD), Ankara, Turkey, June 2011. (<http://eerc.metu.edu.tr/>)

REFERENCES:

- **Dr. Ayşegül Askan Gündoğan**, Associate Professor

Middle East Technical University, Department of Civil
Engineering

aaskan@metu.edu.tr

- **Dr. Murat Altuğ Erberik**, Professor

Middle East Technical University, Department of Civil
Engineering

altug@metu.edu.tr

- **Dr. David Boore**, Geophysicist

U.S. Geological Survey

boore@usgs.gov

- **Dr. B. Rafezy**, Associate Professor

Sahand University of Technology, Department of Civil
Engineering

rafezyb@sut.ac.ir